Design and construction of an atomic clock on an atom chip

Friedemann Reinhard

To cite this version:

Friedemann Reinhard. Design and construction of an atomic clock on an atom chip. Atomic Physics [physics.atom-ph]. Université Pierre et Marie Curie - Paris VI, 2009. English. NNT : . tel-00414386

HAL Id: tel-00414386
https://theses.hal.science/tel-00414386

Submitted on 8 Sep 2009

LABORATOIRE KASTLER–BROSSEL
SYRTE – Observatoire de Paris

ÉCOLE DOCTORALE
Physique de la Région Parisienne
ED 107

THÈSE DE DOCTORAT DE L'UNIVERSITÉ DE PARIS VI
spécialité : Physique Quantique

présentée par
Friedemann Reinhard

pour obtenir le titre de
Docteur de l'université Paris VI – Pierre et Marie Curie

Sujet de Thèse :

Design and Construction of an Atomic Clock on an Atom Chip

Soutenue le 27 février 2009 devant le jury composé de :

M.	Christophe SALOMON	Président du jury
Mme.	Isabelle BOUCHOULE	Rapporteur
M.	Kurt GIBBLE	Rapporteur
M.	Jakob REICHEL	Directeur de thèse
M.	Peter ROSENBUSCH	Membre invité
M.	Vincent LORENT	Examinateur

Résumé Nous décrivons la conception et la construction d'une horloge atomique sur une puce à atomes, visant une stabilité de quelques 10^{-13} à 1s et une application en tant qu'étalon secondaire. Cette horloge est basée sur la transition à deux photons entre les sous-états hyperfins $|1,-1\rangle$ et $|2,1\rangle$ de l'état fondamental de l'atome ^{87}Rb. Elle interroge cette transition en effectuant une spectroscopie de type Ramsey, soit sur un nuage thermique d'atomes froids, soit sur un condensat de Bose–Einstein (BEC). Contrairement aux horloges à fontaines, ce nuage est magnétiquement piégé sur une puce à atomes.

Nous décrivons d'une part un modèle théorique de la stabilité d'horloge, d'autre part un montage expérimental dedié, capable de contrôler le champ magnétique à un niveau relatif de 10^{-5} et doté d'une puce hybride, qui contient des conducteurs à courant continu ainsi qu'un guide d'onde pour acheminer la microonde d'interrogation.

Mots clés Horloge atomique compacte, puce à atomes, horloge à atomes piégés, étalon secondaire, condensat de Bose–Einstein, courant ultra–stable

Abstract We describe the design and construction of an atomic clock on an atom chip, intended as a secondary standard, with a stability in the range of few 10^{-13} at 1s. This clock is based on a two-photon transition between the hyperfine states $|F=1, m_F=-1\rangle$ and $|2,1\rangle$ of the electronic ground state of the ^{87}Rb atom. This transition is interrogated using a Ramsey scheme, operating on either a cloud of thermal atoms or a Bose-Einstein condensate. In contrast to atomic fountain clocks, this clock is magnetically trapped on an atom chip.

We describe a theoretical model of the clock stability and the design and construction of a dedicated apparatus. It is able to control the magnetic field at the relative 10^{-5} level and features a hybrid atom chip, containing DC conductors as well as a microwave transmission line for the clock interrogation.

Keywords Compact atomic clock, atom chip, trapped atom clock, secondary standard, Bose–Einstein condensate, ultrastable current

Address

Laboratoire Kastler–Brossel
24, rue Lhomond
75231 Paris CEDEX 05

0.1 Remerciments

Je remercie avant tout Jakob Reichel, mon directeur de thèse. Il a pris le risque de m'embaucher, malgré le fait que j'avais suivi un Master en physique théorique. Ainsi, il m'a permis d'élargir mes connaissances nettement plus profondément qu'il me l'aurait été possible dans une thèse théorique.

Au quotidien, ma formation était assurée par Peter Rosenbusch, qui m'a encadré du montage de mon premier laser jusqu'à nos premiers atomes froids. Je lui dois tout autant et je suis sûr de ne jamais oublier les innombrables astuces qu'il a su me montrer pendant ces trois ans.

Il ne pourrait y avoir un meilleur co–thésard que Clément Lacroûte. Doté du même goût musical, théatral et sportif que moi, il a participé à cette aventure de montage de manip' dès le début. Je le remercie pour tout son soutien et je lui souhaite bon courage pour les derniers mètres de sa thèse.

J'ai eu la chance de soutenir ma thèse devant un jury exceptionel: Christophe Salomon, Isabelle Bouchoule, Kurt Gibble et Vincent Lorent. Je les remercie tous les quatre du temps qu'il m'ont consacré et de l'interêt, qu'ils ont ainsi montré pour mon travail. Je suis notamment reconnaissant à mes rapporteurs, Isabelle et Kurt, qui ont transformé cette évaluation de mon manuscrit en un vif échange scientifique. J'ai beaucoup profité de nos discussions.

Cette thèse s'est déroulée sous les drapeaux de deux laboratoires, le laboratoire Kastler–Brossel et le SYRTE à l'Observatoire de Paris. Je remercie leurs directeurs respectifs, Frank Laloë et Paul Indelicato au LKB, Philip Tuckey et Noël Dimarcq au SYRTE, de m'avoir acceuilli.

Une ambiance scientifique ambitieuse et un esprit acceuillant et ouvert dans ces laboratoires m'ont permis de discuter de mon travail avec de grands acteurs du domaine comme André Clairon, Alice Sinatra, Yvan Castin, Michèle Leduc, Christian Bordé, Peter Wolf, Sébastien Bize, Giorgio Santarelli, Michel Lours, Arnaud Landragin, Franck Perreira dos Santos, Pierre Lemonde, Roland Barillet, Pierre Uhrich, David Holleville, Stéphane Guerandel, Yann Lecoq et David Valat. Je tiens à les remercier de leur idées et leurs réactions.

Vers la fin de ma thèse, notre équipe a été rejointe par Fernando Ramirez–Martinez et Christian Deutsch. Je les remercie de leur soutien, qui m'a permis de commencer la rédaction de ma thèse tout en voyant l'expérience progresser. Je remercie également nos deux stagiaires succesifs, Lucas de Soultrait et David Fehrenbacher.

Pendant cette thèse, mes collègues de l'équipe des microcircuits à atomes m'ont appris tout autant que mes encadrants. Notamment, je remercie Philipp Treutlein, qui peut être considéré comme le véritable père scientifique de cette expérience et qui m'a conseillé sur des nombreuses questions en physique atomique et en conception à haute fréquence. Le nombre de fois où je le cite dans cette thèse en témoigne. Cette manip' ne marcherait pas sans la contribution essentielle de Tobias Schneider, qui a fabriqué la puce selon nos exigeances peu modestes et qui a conçu le modèle de base de notre blindage. La conception a été facilitée considérablement par le savoir–faire et les dossiers de commandes de Yves Colombes, Tilo Steinmetz et Felix Linke. Je remercie également tous les autres, Guilhem Dubois, Kenneth Maussang, Romain Long, Andreas Trottmann, Ed Marti, Thomas Liennard, Jürgen Volz, Roger Gehr, Yun Li, Jerome Éstève, Florian Haas, Vincent Dugrain, Benjamin Besga, Pascal Böhi, Stephan Camerer, Johannes Hoffrogge, David Hunger et Max Riedel.

Le chapître 1 de cette thèse ne serait pas le même sans la bibliothèque virtuelle de Francois-Xavier Esnault, qu'il m'a laissé utiliser gracieusement. Je le remercie vivement et je conseille sa thèse à tous les lecteurs qui souhaitent une introduction plus profonde que la mienne.

La physique expérimentale est injuste: Une phrase laconique comme "Nous utilisons un support en titane, asservi en temperature" peut cacher le travail laborieux de quelques dizaines de collaborateurs. Tout d'abord, il faut commander ces choses, une tâche primordiale mais peu gratifiante, qui a été gerée de la manière la plus gentille et efficace par notre équipe de gestion, Marine Pailler, Yertha Baïdomti, Pascale Baudoin, Véronique Benayoun, Catherine Laurent, Anne Thomson, Pascale Michel, Anne Queusel et Thérèse Ecolasse. Je remercie également Linda Krikorian, Thierry Tardieu et Monique Bonnamy, qui m'ont soutenu dans toute question d'administration du coté du LKB. Le pas suivant, la fabrication des diverses pièces sur mesure, a été énormément facilité par le soutien de notre équipe mécanique, Jean–Pierre Aoustin, Laurent Pelaye et Jean–Jacques Bousquet. L'interaction avec vous était un vrai plaisir. La partie la plus redoutée de la physique atomique est sans doute le montage du vide: Ce travail nous a été facilité beaucoup par l'aide d'Annie Gerard, que je remercie pour ce soutien. L'outil essentiel de la chasse au bruit de phase est l'électronique. Ici, j'ai profité énormément du savoir–faire de notre équipe d'éléctronique, Giorgio Santarelli, Michel Lours, Roland Barillet, Laurent Volodimer, Michel Dequin et Jose Pinto. Notamment, je les remercie de leur travail acharné pour mettre au point l'alimentation de courant 3A, qui est la base du chapitre 6 de cette thèse. Je remercie également Anton Scheich, l'électronicien de l'université de Munich. Je remercie également, non, je tire mon chapeau à notre équipe d'informatique, Pascal Blondé, David Cathelineau et Emmanuel Delor, qui ont su mettre en place un réseau qui marche avec la stabilité d'une bonne horloge. Du coté du LKB, je remercie Francis Hulin–Hubbard de son soutien pour tout ce qui concerne l'informatique.

C'est notamment grâce à mes collègues magnifiques que ces années resteront inoubliables pour moi, et il y en a plusieurs qui ont mérité une véritable place d'honneur sur mon compte Facebook:
J'ai beaucoup apprecié nos nombreuses séances d'escalade, rendues possibles par Florence Cornu. Je remercie tout ceux qui m'ont accompagné, Scott Crane, sans doute mon seul ami avec une adresse email navy.mil, Julien Le Gouet, auquel je suis en plus reconaissant de m'avoir acceuilli pendant mes candidatures à Boston, et Jacques Millo. Je lui souhaite bonne chance pour la rédaction de sa thèse, qui sera sans doute un chef d'oeuvre de la métrologie moderne.
Je remercie également mes adversaires sur les terrains du Badminton et du Jorkyball: Michael Petersen, Danois, donc imbattable, Thierry Botter, doté d'un tir trop fort pour mes lunettes en plastique, FX Esnault, Sam Dawkins et Amandine Proia.
J'ai également eu le plaisir de devenir leader d'un groupe de musique, les Jazzalobs. Je

remercie mes sidemen Loïc Duchayne (d), Clément Lacroûte (g), Rodolphe Boudot (b), Scott Crane (tb), Samuel Deleglise (sax) et Thomas Grange (f) ainsi que nos managers Emmanuel Vergnaud et Michel Poinse.
En plus de ces activités régulières, j'ai beaucoup aimé les discussions philosophiques, dégustations de vins et les sorties avec François Impens, Tanja Mehlstäubler, Thomas Levèque, Sinda Mejri, Philip Westergaard, Nicolas Rosetto, Stéphanie Perrin, Quentin Bodart, Olga Kozlova, Jérôme Lodewyck, Arnaud Lecallier, Haifeng Jiang, Frédéric Chapelet, Rodolphe Le Targat, Xavier Baillard, Alexandre Gauguet, Pacome Delva, Natascia Castagna, Christian Jentsch, Benjamin Canuel, François Narbonneau, Stephanie Perrin, Anders Brusch et Céline Vian.

Finalement et sourtout, je remercie mes parents pour tout leur soutien, sans lequel cette thèse n'aurait pas été possible.

Contents

Introduction

This thesis lies at the intersection between two young and intense areas of research: Atom chips and compact atomic clocks. Atom chips – magnetic traps created by microfabricated conductors – have made it possible to perform state–of–the–art experiments with ultracold atomic clouds in a compact setup. Even more, they have made it possible to build highly integrated atom–optical devices, reminiscent of the microchips of modern microelectronics. Compact atomic clocks, in turn, have enabled the development of satellite navigation systems and have therefore become commercially interesting devices.

In this thesis, both of these developments merge: We describe the construction of a novel atomic clock, which interrogates a hyperfine transition in magnetically trapped Rubidium atoms. It uses the atom chip technology as a tool to achieve competitive performance in a compact setup. In this way, it is the first atom chip experiment which is aiming at an application beyond the proof–of–principle level.

Atom chips – Applications for ultracold atoms When Bose–Einstein condensation was first observed in 1995 [1, 2], it must have seemed hardly realistic that the complex underlying technology could ever find a use in portable applications. Today, 14 years after this achievement, it is possible to write a thesis like the present one. This thesis, too, deals with the construction of a BEC machine, but with a completely different focus. The apparatus is compact and aims at a real–world application: a portable atomic clock.

Such experiments have become possible because of one major breakthrough, the advent of atom chip technology. The basic idea of this technology is to trap cold atoms in microscopic magnetic traps, created by microfabricated conductors. After a first proposal of 1995 [3], this idea has been pioneered in the late 1990s, when atoms were for the first time guided [4, 5] and trapped [6] on microchips. Inspired by this success, the term "atom chip" has been coined in [7] and BEC has been achieved in these traps in 2001 [8, 9].

This development has sparked a lot of creativity and has triggered a paradigm shift: The idea of integration had come into the world of cold atoms. Consequently, the 2000s have seen numerous theoretical proposals and experimental prototypes of new devices using cold atom technology.

On the scientific side, atom chips have been used to confine quantum gases in regimes that have been previously inaccessible. A remarkable example is the achievement of gases with reduced dimensionality. Atom chips have been used to create highly anisotropic traps, in which a quantum gas exhibits quasi–one–dimensional dynamics [10, 11, 12].

Another direction in basic research uses atom chips to couple cold atoms to solid–state quantum systems like mechanical nano–resonators [13, 14].

Closer to an application are studies which use the cold atoms as a surface probe. Being magnetically trapped, the cold cloud above the atom chip is inherently sensitive to magnetic fields produced by the surface. This has been used to study noise [15, 16, 17, 18] and static impurities [19, 18, 20] of the microfabricated conductors.

Maybe the most ambitious application is to use atom chips for quantum computing.

Indeed, appropriate gates have been proposed [21, 22] and state sensitive detection of single atoms can be realized [23, 24]. To date, the only missing step to meeting the DiVincenzo criteria [25] with an atom chip seems to be the deterministic preparation of single atoms, which is a subject of study in another experiment of our group.

Finally, the atom chip technology lends itself to two classical problems of metrology: Inertial sensors and atomic clocks. On the inertial sensor side, several prototypes of chip–based interferometers have been built over the last years [26, 27, 28], based on the interference of external quantum states ("matter waves"). Work on the atomic clock side has been less intense, but a proof–of–principle experiment has shown that a hyperfine transition in a magnetically trapped cloud on on atom chip can indeed be used to build a clock [29]. This thesis describes the first atom chip experiment which is intended to yield a competitive atomic clock. In doing so, it can be seen as a contribution to two active directions of research in the field of atomic clocks: the work towards compact clocks and the work towards clocks operating on trapped particles.

Towards compact clocks and trapped particle clocks Considerable effort is spent to improve the performance of compact secondary standard clocks, mostly because of their application in satellite navigation. These compact clocks can be further divided into several categories with a different bias towards either performance or compactness. Today's benchmark clocks in terms of *compactness* are miniaturized vapor cell clocks, which perform laser spectroscopy on a room–temperature Alkali metal vapor. These clocks, reaching a stability in the range of $10^{-11}\sqrt{\mathrm{s}}$, have been miniaturized to a volume of $10\mathrm{mm}^3$ [30]. They are intended as an alternative to quartz oscillators in high–end portable applications.

Today's benchmark compact clocks in terms of *performance* are liter–sized clocks which achieve a stability in the range of few $10^{-13}\sqrt{\mathrm{s}}$. These clocks are candidates for future satellite navigation systems and it is these specifications which are the long–term goal of the experiment described in this thesis. The best existing clocks with comparable performance operate on a cloud of trapped ions [31] or a laser–cooled, but untrapped, vapor of Alkali atoms [32].

At the same time, both primary and secondary standard clocks begin to exploit the advanced trapping techniques which have been devised over the last decades. Today's best optical clocks are based on single trapped ions [33] or neutral atoms, which are trapped in an optical lattice [34]. The latter technique contains a remarkable similarity to the clock described in this thesis: To avoid that the trapping potential shifts the clock transition, the lattice light is tuned to a "magic wavelength", where its lightshift is equal for both clock states. In much the same way, we tune the magnetic background field of our trap to a "magic field", where both atomic states see the same trapping potential (see below).

Our clock transition It is evident that atom chip technology can provide a compact setup to manipulate an atomic sample. It is less obvious why this sample could be used as a clock medium: A hyperfine transition of a trapped atom is inevitably shifted by the magnetic field of the trap and the mean–field shift of the trapped atomic cloud. Luckily, both shifts are strongly suppressed for one particular hyperfine transition: The two–photon transition between the hyperfine states $|1,-1\rangle$ and $|2,1\rangle$ of ^{87}Rb. To first order, both of these states have the same magnetic moment. Consequently, a magnetic field shifts each of the states in the same way (so that both can be trapped and, moreover, feel the same trapping potential). The *transition between these states*, however, is independent of the magnetic field, since the shift is common–mode for both states. Furthermore, the mean–field shift is small for this transition, since the inter– and intra–species scattering properties of both states are nearly equal.

These properties have first been explored in a series of experiments in the group of E. Cornell at Boulder. The first coherent transfer between two condensates of the clock states has been achieved in 1998 [35]. The system has subsequently been used to study demixing of a condensate [36] and has led to the discovery of spin waves [37, 38]. For this thesis, the most relevant study is one of the latest of this series, [39]. It studies the coherence of the system, which is found to be limited by dephasing due to variations of the mentioned frequency shifts over the atomic cloud. Since these shifts are small, coherence times of seconds can be obtained even in a magnetically trapped cloud.

For the work on atom chips, the potential of this result is twofold: Atoms in a long–lived coherent superposition of internal states can be used to sense external sources of decoherence, which could arise from the proximity of the room–temperature chip surface. On the other hand, the ability to prepare and manipulate a long–lived coherent system in a compact setup opens up new possibilities for miniaturized metrology devices. Both of these directions have been explored in our group. By a study along the former line of thought, the chip surface was found not to influence the coherence, even at micron distances. The same experiment has been run as a proof–of–principle atomic clock, achieving a stability of $1.7\cdot10^{-11}\sqrt{\mathrm{s}}$ [29]. In this thesis, we continue the latter approach, by designing and constructing a dedicated setup, which will improve this figure by one order of magnitude in the near future and by two orders of magnitude in the long term. The resulting setup will also be an attractive starting point for a chip–based inertial sensor, which could be implemented by spatially splitting the clock states between the Ramsey pulses.

Structure of the thesis The following chapters will discuss the details of the design and construction of the atomic clock on a chip. We have chosen a top–down structure, going from the global view of the experimental goal to the technical details.

- Chapter 1 reviews the theory of atomic clocks in general and introduces clock stability, the relevant figure of merit for a secondary standard like our clock. It gives an outlook onto the state of the art for both primary and, in more detail, secondary standards.

- The second key technology of this experiment are atom chips, which we discuss in chapter 2. Here, we take an engineering viewpoint and discuss in detail the theory of chip design. We show that a microtrap can be considered as composed of elementary two–dimensional fields rather than of wires, an approach which we have found to provide a helpful intuition.

- The theory of our clock is developed in 3. We review the descriptions of the interaction of an atom with the magnetic trapping field, of collisions in the atomic cloud and of the interaction of the atoms with the excitation pulses. We subsequently use these tools to develop a major result of this thesis: A prediction of the stability of the atomic clock on a chip. Finally, we present a simple model of the decoherence in our system, which predicts optimal parameters for the trap.
- Chapter 4 presents the experimental setup. A particular focus is put onto the control of the magnetic field, since this is a major challenge of this experiment. We describe in detail the magnetic shielding and the coils producing the offset fields.
- The chip is such a central part of the experiment that it deserves a chapter of its own, chapter 5. We describe our chip design in detail, with a special focus on the integration of the microwave transmission line, which drives the excitation pulses.
- We have invested a lot of effort into the electronics of the experiment, most notably the necessary control of electric currents with low noise and a high temporal stability. This work is presented in chapter 6. The main result of this work is the development of a dedicated power supply, capable of sourcing a constant current with both low noise and high temporal stability.
- Chapter 7 presents the first result of our setup. We demonstrate its high stability, by an analysis of the atomic lifetime and the fluctuations of the atom number. We conclude by a documentation of the first observation of the BEC phase transition.

1 Atomic clocks

To outsiders, the world of atomic clocks easily appears as a scientific ivory tower, keen to beat records of esoteric quantities like stability and exactitude with no apparent practical use. It is interesting to observe that the opposite is true and that clocks have often found applications in completely different areas.

The oldest example for this statement is probably Harrison's creative solution of the longitude problem. In the 17th century, measuring the longitudinal position of a ship was an unsolved problem (the latitude could be easily measured by a sextant). John Harrison (1693–1776), a british woodworker, finally solved the problem by constructing a precise clock, which was furthermore compact and robust enough to withstand the harsh environment of a ship. With this tool, ships could tell their longitude simply by measuring the time lag between local time and ship's time. [40]

In a similar way, the first quartz clocks in the 1930s unexpectedly led to a remarkable finding: That the earth's rotation was irregular [41]. This observation abruptly transformed clocks into geophysical instruments and ultimately led to a redefinition of the second. In 1967, when the more precise atomic clocks had emerged, the second was decoupled from astronomic quantities and defined as *"la durée de 9192631770 périodes de la radiation correspondant à la transition entre les deux niveaux hyperfins de l'état fondamental de l'atome de césium 133"* [42].

Atomic clocks, too, have found unexpected applications in other areas of science. Particularly spectacular examples are the observation of a signature of gravitational waves in the timing drift of a pulsar's radio–frequency pulses [43] or the search for a drift of fundamental constants [44]. Their most visible application to date clearly is the global positioning system (GPS), which is able to tell positions on earth with meter precision – from the run–time delays of a set of compact atomic clocks on orbiting satellites.

This thesis is a contribution to this latter field – the development of compact atomic clocks. To describe it in detail later on, we will use the typical vocabulary and definitions of atomic clocks, which we will introduce in this chapter. We discuss several categories of clocks and introduce the mathematical tools used to characterize their behaviour. We conclude the chapter by a survey of today's benchmark atomic clocks, with a particular focus on compact clocks.

Working principle An atomic clock measures time in much the same way as a ruler measures length. It measures an unknown time interval by comparing it to a periodic signal of known frequency. In this way, it performs in time what a ruler does in space by comparing an unknown length to a periodic pattern of stripes with a fixed and known spacing of one millimeter.

This approach to measure time consists essentially of two steps: The first is to generate a periodic signal of a fixed frequency. This signal must be extremely stable, in a sense which will be defined below, and its frequency must be very well known. This signal is then used as a reference for time, which can be done, e.g. by counting its cycles. In this work, we do not pay attention to this latter "clockwork", the techniques to measure time using a given periodic signal. Instead, we focus on the first task, to generate a highly stable periodic signal. An atomic clock generates this signal from an atomic transition, which we will assume to take place between two atomic states $|0\rangle$ (ground state) and $|1\rangle$ (excited state), separated by an energy $\hbar\omega_{\mathrm{at}}$. A continuous, high–precision signal can be generated from such a transition in several ways [45],[46]:

Active clocks In this kind of clock, the clock signal is generated directly by the radiation of the atomic transition. The most widespread implementation of this kind is the active hydrogen maser. This clock generates its output from a hyperfine transition in the electronic groundstate of hydrogen, by pumping the sample into the excited state and extracting the radiation of the transition by means of a resonant cavity.

Passive clocks In most of today's clocks, the atomic transition does not directly generate the signal. Instead, it is generated by a "flywheel" or "local oscillator", a continuously running signal generator, which may be less stable than the atomic transition. The frequency ω_{fw} of this generator is repeatedly measured by "interrogating" an atomic sample and subsequently corrected. This "interrogation" is performed by driving a spectroscopy on the atomic sample from the signal of the flywheel. This spectroscopy can be performed in several ways:

- **Continuous spectroscopy** In this technique, the flywheel signal is applied continuously to the atomic sample. The feedback to the flywheel is generated by monitoring some signature of the atomic resonance, e.g. the atomic absorption. This technique is used in Rubidium vapor cell clocks and CPT clocks (see below).
- **Rabi spectroscopy** In this technique, the atomic sample is placed in the state $|0\rangle$ and subsequently exposed to a pulse of the flywheel signal. During this pulse, Rabi oscillations of a frequency Ω will develop between the two states of the transition, so that the pulse drives the atomic system into a state $\cos(\Omega t)|0\rangle + \sin(\Omega t)|1\rangle$. Both the duration of the pulse and the power of the flywheel signal are experimentally controlled, such that Ωt is a measure of the detuning between the flywheel and the atomic resonance. The advantage of a pulsed interrogation is that preparation phases can be inserted between two interrogations. In this way, the properties of the atomic sample can be better controlled. In particular, it becomes possible to use laser–cooled samples, which are prepared between two pulses and it becomes possible to alter the configuration between subsequent measurements to evaluate systematic effects.
  This interrogation is used in some optical clocks [47].
- **Ramsey spectroscopy** This technique, too, is a pulsed scheme. Precisely, two separated pulses are applied to the atomic sample: A first one prepares a coherent superposition $(|0\rangle + i|1\rangle)/\sqrt{2}$. It follows a period T_R, during which the sample evolves freely. During this time, the superposition picks up a phase $\phi = (\omega_{\mathrm{fw}} - \omega_{\mathrm{at}})T_R$, ending up in the state $(|0\rangle + ie^{i\phi}|1\rangle)/\sqrt{2}$. This phase is converted into a

> population imbalance by a second pulse. The final state is $\sin(\phi/2)|0\rangle+\cos(\phi/2)|1\rangle$. As for the Rabi spectroscopy, the population imbalance is used as a measure of the detuning between the flywheel and the transition. This method presents an advantage over the Rabi spectroscopy, since the sample can be isolated from most external perturbations during the period of free evolution. In particular, this greatly simplifies the interrogation of moving atoms, since the antennas or cavities transfering the flywheel signal are not required to extend over all the range of the atomic motion.

Independent of the way they work, atomic clocks can serve two major purposes: *Primary standards* are built to “realize” the SI second. They produce a signal which matches as closely as possible the frequency of the hyperfine transition of ^{133}Cs, which is the reference of the SI second [42]. *Secondary standards* are not neccessarily based on the mentioned Cs transition. They are built to generate a highly stable signal. This signal can only be linked to the SI second by calibrating the secondary standard against a primary one.

1.1 Theory of atomic clocks

1.1.1 The Ramsey pulse sequence

Since it is this type of interrogation which we will use in our clock, we will describe it in more detail here. We will use the notation of the previous paragraphs. We will not assume a particular type of atomic transition, since the interrogation scheme is used for a whole whealth of transitions. Examples are the microwave interrogation of a hyperfine transition or the optical interrogation of an electric multipole transition.

The Bloch sphere picture To illustrate the following considerations, we will use the Bloch sphere picture. This is a map from the space of pure states of an effective spin 1/2 system to the 3–dimensional unit sphere. Each pure state can be written in the form

$$\psi = \cos\left(\frac{\alpha}{2}\right)|0\rangle + \sin\left(\frac{\alpha}{2}\right)e^{i\beta}|1\rangle.$$

The corresponding point on the Bloch sphere is the point on the unit sphere in $\mathbb{R}^3$, which has the same polar angles.

$$\begin{aligned} x &= \sin(\alpha)\cos(\beta) \\ y &= \sin(\alpha)\sin(\beta) \\ z &= \cos(\alpha) \end{aligned}$$

Some examples of this map are presented in Fig. 1.

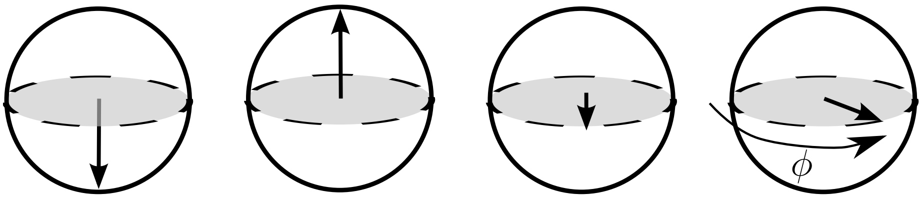

$|0\rangle$ $|1\rangle$ $1/\sqrt{2}(|0\rangle + i|1\rangle)$ $1/\sqrt{2}(|0\rangle + e^{i\phi}|1\rangle)$

Figure 1: Examples of state vectors and their corresponding images on the Bloch sphere.

Interaction between the atom and the flywheel signal An atom interacting with the flywheel signal can be described by an interaction Hamiltonian:

$$\begin{aligned}\widehat{H} &= \widehat{H}_0 + \widehat{H}_I \qquad (1)\\ &= \hbar\omega_{\mathrm{at}}|1\rangle\langle 1| + \hbar\Omega_I f(t)\cos(\omega_{\mathrm{fw}}t + \theta)(|1\rangle\langle 0| + |0\rangle\langle 1|) \qquad (2)\\ &= \hbar\omega_{\mathrm{at}}|1\rangle\langle 1| + \left(\frac{\hbar\Omega_I}{2} f(t)(e^{i\omega_{\mathrm{fw}}t+\theta} + e^{-i\omega_{\mathrm{fw}}t-\theta})|1\rangle\langle 0| + h.c.\right) \qquad (3)\end{aligned}$$

Here, Ω_I quantifies the coupling between the atom and the flywheel signal. $f(t)$ is an envelope function, describing the interrogation pulses. It takes values in the interval $[0;1]$.

This Hamiltonian is best viewed in an interaction–picture–like description, by transforming the states and operators into a "co–rotating frame" by the unitary operator $\widehat{U}_0(t) = \exp(i\omega_{\mathrm{fw}}t|1\rangle\langle 1|)$ according to

$$\begin{aligned}|\psi\rangle &\rightarrow |\psi\rangle_{\mathrm{int}} = \widehat{U}_0|\psi\rangle\\ \widehat{A} &\rightarrow \widehat{A}_{\mathrm{int}} = \widehat{U}_0\widehat{A}\widehat{U}_0^\dagger\end{aligned}$$

In particular, the interaction part of the Hamiltonian transforms to

$$\begin{aligned}\widehat{H_I}_{\mathrm{int}} &= \widehat{U}_0\widehat{H}_I\widehat{U}_0^\dagger\\ &= \left(\frac{\hbar\Omega f(t)}{2}(e^{i\theta} + e^{i(2\omega_{\mathrm{fw}}t+\theta)})|1\rangle_{\mathrm{int}}\langle 0|_{\mathrm{int}} + h.c.\right)\end{aligned}$$

In all the following, we will neglect the term $e^{i(2\omega_{\mathrm{fw}}t+\theta)}$. This is the widely used rotating wave approximation (RWA), which can be justified for $\Omega_I, \Delta \ll \omega_{\mathrm{at}}$, with $\Delta = \omega_{\mathrm{at}} - \omega_{\mathrm{fw}}$. Also, we will drop the labels $|\cdot\rangle_{\mathrm{int}}$ and refer by $|0\rangle$ and $|1\rangle$ to the transformed atomic states. With these assumptions, the full Hamiltonian in the co–rotating picture becomes

$$\widehat{H} = \hbar\Delta|1\rangle\langle 1| + \frac{\hbar\Omega_I}{2} f(t)\left(e^{i\theta}|1\rangle\langle 0| + h.c.\right). \tag{4}$$

This is an effective spin-1/2 Hamiltonian. Adding a total energy of $-\hbar\Delta/2$, it can be

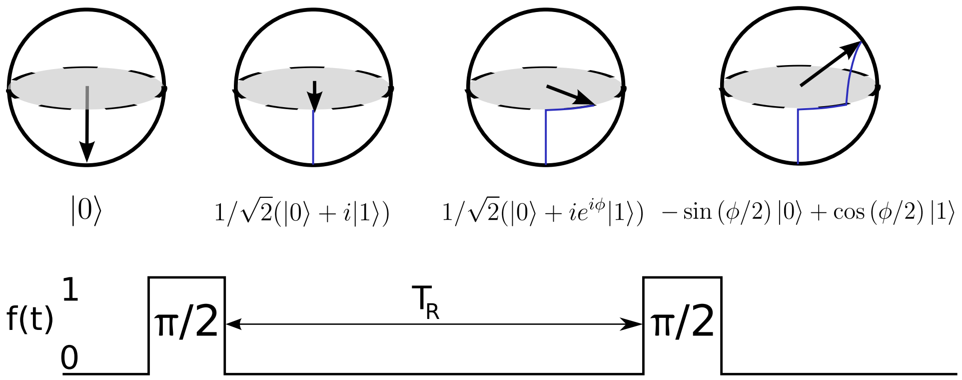

Figure 2: Evolution of the atomic state during an interrogation. In this example, the interrogation is performed near resonance: $\Delta \ll \Omega$

rewritten using the Pauli matrices $\hat{\vec{\sigma}}$

$$H = \frac{\hbar}{2}\vec{\Omega} \cdot \hat{\vec{\sigma}} \tag{5}$$

$$\vec{\Omega} = \begin{pmatrix} \Omega_I f(t)\cos(\theta) \\ \Omega_I f(t)\sin(\theta) \\ \Delta \end{pmatrix} \tag{6}$$

In the special case that f is constant $f(t) = f$, $\vec{\Omega}$ is constant, too, and the solution of this Schrödinger equation takes the simple form

$$|\psi(t)\rangle = \exp\left[-i\vec{\Omega} \cdot \hat{\vec{\sigma}}\; t/2\right] |\psi(0)\rangle \tag{7}$$

In the Bloch sphere picture, this corresponds to a rotation of the state $|\psi(0)\rangle$ by an angle $|\Omega|t$ around the axis $\vec{\Omega}$.

State evolution during the Ramsey interrogation The evolution of the atomic state during the Ramsey interrogation can be understood from equation 7. Assuming $\theta = 0$, the action of the Ramsey sequence on the atoms is expressed by the following operator

$$\begin{aligned} \widehat{R} &= \exp\left[-i\frac{\pi}{2}\frac{\hat{\sigma}_x}{2} - i\Delta t_P \frac{\hat{\sigma}_z}{2}\right] \exp\left[i\phi\frac{\hat{\sigma}_z}{2}\right] \exp\left[-i\frac{\pi}{2}\frac{\hat{\sigma}_x}{2} - i\Delta t_P \frac{\hat{\sigma}_z}{2}\right] \\ &\overset{\Delta \ll \Omega}{=} \exp\left[-i\frac{\pi}{2}\frac{\hat{\sigma}_x}{2}\right] \exp\left[i\phi\frac{\hat{\sigma}_z}{2}\right] \exp\left[-i\frac{\pi}{2}\frac{\hat{\sigma}_x}{2}\right] \end{aligned}$$

where $t_P = \pi/(2\Omega_I)$ is the duration of a Ramsey pulse and $\phi = -\Delta T_R$.
Near resonance, where the interrogation is usually performed, the pulse sequence rotates the atomic state in the following way:
In the limit of $\Delta t_P \ll \pi/2$, the first pulse is adjusted such as to satisfy $|\Omega|t_P = \pi/2$. and $\vec{\Omega} \| \vec{e}_x$. This pulse places the system in the superposition $1/\sqrt{2}(|0\rangle + i|1\rangle)$.

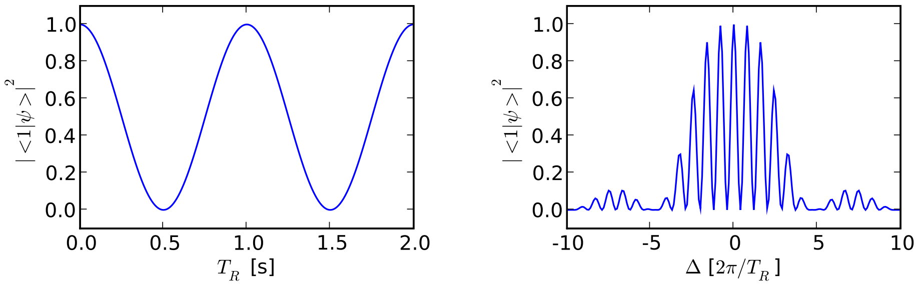

Figure 3: Ramsey fringes in the time domain (left, for $\Delta = 2\pi/[1\mathrm{s}]$) and the frequency domain (right). In the frequency domain, the fringes have a period of $2\pi/T_R$ and are modulated by an envelope function (the "Rabi pedestal" [45]) stemming from the finite Rabi frequency Ω_I of the $\pi/2$ pulses: For large detunings $\Delta \gg \Omega_I$, the excitation pulses are not resonant any more, so $|\langle 1||\psi\rangle|^2 \to 0$.

During the period of free evolution T_R, the system rotates around the z–axis with the angular velocity Δ. The superposition thus picks up a phase $\phi = -\Delta T_R$, ending up in the state $1/\sqrt{2}(|0\rangle + ie^{i\phi}|1\rangle)$.
The second pulse rotates rotates the system by $\pi/2$ around the x–axis. The resulting final state is

$$-\sin(\phi/2)|0\rangle + \cos(\phi/2)|1\rangle. \tag{8}$$

Ramsey fringes The measurable result of a Ramsey sequence is an excitation probability of the excited atomic state – i.e, experimentally, a population imbalance of the atomic states. According to equation 8, this imbalance is an oscillating function of $\phi = -\Delta T_R$. For a fixed Δ, it is a measure of T_R, for a fixed T_R it is a measure of Δ. Experimentally, either version can be realized and the result is refered to as Ramsey fringes in the time and frequency domain, respectively. Plots of both situations are presented in Fig. 3. In an atomic clock, T_R is always kept fixed, so that the Ramsey interrogation yields a measure of the detuning Δ (Ramsey fringes in the frequency domain). To maximize the sensitivity to Δ, the clock is operated on the slope of the central Ramsey fringe (figure 4). The maximum slope that can be obtained is

$$\frac{dp}{d\Delta}\Big|_{\max} = \frac{T_R}{2} = \frac{\pi}{2} \cdot \frac{Q_{\mathrm{at}}}{\omega_{\mathrm{at}}} \tag{9}$$

where Q_{at} is the quality factor of the clock, the frequency of the clock divided by the half width of the central Ramsey fringe.

At this point, two apparent paradoxa merit further comments:

To measure Δ, we have to keep T_R fixed. Since ϕ varies linearly with both T_R and Δ, an error on T_R will translate into an equally large error on Δ. At first sight, this seems impossible: How can we fix a time without having a precise clock, which to build is the very goal of this endeavour? The paradox is resolved by considering that the error of one interrogation is $\sigma_{\omega_{\mathrm{at}}}/\omega_{\mathrm{at}} = \sigma_\Delta/\Delta \cdot \Delta/\omega_{\mathrm{at}}$ with $\sigma_{\omega_{\mathrm{at}}}$ denoting the error bar

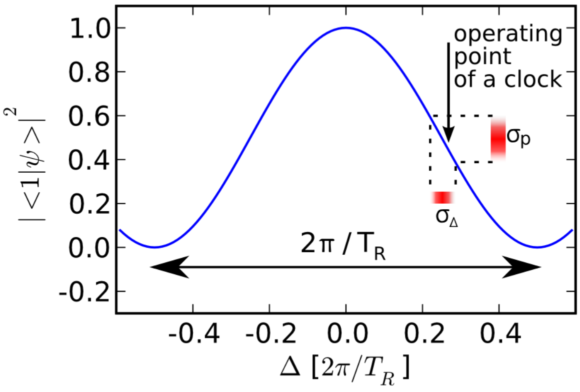

Figure 4: The central frequency–domain Ramsey fringe. Clocks are operated at the point of highest slope, where the transisition probability is the most sensitive to Δ. Here, a given error σ_p on the measurement of the transition probability translates into a minimal error σ_Δ on the frequency measurement.

on the clock interrogation. σ_Δ is therefore suppressed by the factor $\Delta/\omega_{\text{at}}$, typically of the order of 10^{-10}. Therefore it is possible to reach a relative error bar $\sigma_{\omega_{\text{at}}}/\omega_{\text{at}} = 10^{-13}$ with a moderate timing precision of $\sigma_{T_R}/T_R = 10^{-3}$. T_R can therefore be controlled from a clock having a performance largely inferior to the atomic clock.

Naively, one might argue by the time–frequency uncertainty principle that the error bar on a frequency measurement taking a measurement time T_R cannot be lower than $1/T_R$. For typical values ($T_R = 1\text{s}$, $f_{\text{at}} = 10^{10}\text{Hz}$), this would correspond to a relative error bar of $\sigma_{\omega_{\text{at}}}/\omega_{\text{at}} = 10^{-10}$. However, the relative error bar of today's benchmark atomic clocks after a $T_R = 1\text{s}$ integration time is only $\sigma_{\omega_{\text{at}}}/\omega_{\text{at}} = 10^{-14}$! To solve this paradox, we refer to figure 4. Indeed, the width of the central Ramsey fringe is $2\pi/T_R$, as predicted by the uncertainty argument. Clocks can beat this limit, since they measure synchronously on multiple atoms.

1.1.2 Clock stability

Figures of merit of a clock The general idea behind all measures of the performance of an atomic clock is to indicate how close its output signal matches the underlying atomic transition. To quantify this performance, we recall that a passive atomic clock repeatedly measures the frequency of a flywheel against the atomic transition and corrects it accordingly. For a real clock, each of these measurements will be precise only within a certain error bar, which includes the noise on the atomic transition, emerging from the manipulation and detection of the atomic sample, as well as the noise of the flywheel, which the atomic clock is about to measure and correct. Evidently, the corrected flywheel signal matches the atomic transition only within the error bar of these repeated clock measurements. Therefore, the performance of an atomic clock is quantified by stating the error bar which the clock can put onto the frequency of the flywheel after a certain period τ of operation, the “integration time”.

In practice, there is a wealth of different figures of merit measuring different aspects of this performance. For this work, three of them are particularly important:

1. **Short–term stability**: the error bar on the frequency measurement after a given, short, integration time (typically $\tau = 1$s). For short integration times, the error bar is typically limited by white noise contributions, which average out during further integration. Short–term stability therefore is only the starting point of the error bar, which diminishes during further integration (typically as $1/\sqrt{\tau}$) up to a certain limit.
2. The ultimate error bar a given clock can put onto the frequency measurement after an arbitrary long integration time.
3. **Accuracy**: The systematic error bar estimating the deviation of the measurement 2) from the frequency of the atomic transition of a single atom, isolated from all external perturbations. In the case of primary standards, this quantity estimates the possible deviation of the clock from the SI second, since here the frequency of the unperturbed atomic transition is known by definition.

In the following, we will define these three quantities in more detail. For a more in–depth overview, the reader is refered to [48, 40].

The Allan variance There exists a widespread procedure to estimate the error of the frequency measurement after an integration time τ: The clock is run N times subsequently for a time τ. This yields a set of frequency measurements $\bar{f}_i, i \in \{1, \ldots, N\}$. It is convenient to express them as normalized deviations from the atomic frequency by the relation $\bar{y}_i = \bar{f}_i / f_{\mathrm{at}} - 1$. The error of one of these measurements is estimated by computing the **Allan variance**

$$\sigma_y^2(\tau) = \frac{1}{2}\frac{1}{N}\sum_{i=2}^{N}(\bar{y}_i - \bar{y}_{i-1})^2. \tag{10}$$

Note that this variance is in general different from the usual statistical variance $1/N \sum_{i=1}^{N}(\bar{y}_i - \bar{y})^2$. They are equal for the special case that $\bar{y}_n$ is a white noise. The Allan variance is prefered against the statistical variance, since it converges in the limit $N \rightarrow \infty$ for some common types of noise, whose statistical variances do not converge. An instructive example is a monotonous drift of the clock, which has a finite Allan variance, whereas its statistical variance diverges.
An Allan standard deviation can be defined as the square root of the Allan variance.

Stability of a Ramsey interrogation To give a concrete example, we will now compute the error of a Ramsey–type clock. We will assume the clock to perform one interrogation in a cycle time T_C, which includes the time to prepare the atomic sample as well as the time to perform the actual clock measurement. Each single interrogation of this kind is a measurement of the flywheel frequency in units of the atomic transition frequency, with an error bar which stems from two sources of noise (see figure 4):

- Noise on the measurement of the transition probability $|\langle 1|\psi\rangle|^2$, typically noise on the detection of the atomic populations.
- Noise on the detuning Δ. Part of this noise is the noise of the flywheel, which the atomic clock is about to measure and correct. The other contribution is noise on the atomic transition due to the manipulation of the atomic sample (e.g. varying Zeeman shifts from nearby coils).

We will assume both sources to contribute white noise of standard deviation σ_p and σ_Δ. We convert σ_p into a frequency noise $\sigma_p \cdot d\Delta/dp$ using equation 9. From eq. 10 and the law of Gaussian error propagation, we obtain the Allan standard deviation after an integration time τ

$$\sigma_y(\tau) = \sqrt{\frac{\sigma_\Delta^2}{\omega_{\text{at}}^2} + \frac{4\sigma_p^2}{\pi^2 Q_{\text{at}}^2}}\sqrt{\frac{T_C}{\tau}} \tag{11}$$

The term under the first square root can be interpreted as the error of one clock interrogation. Arising from white noise, this error decreases after $N = \tau/T_C$ interrogations by a factor $1/\sqrt{N}$.

In the best of today's atomic clocks, the dominating source of noise is the quantum projection noise [49]. This noise reflects the fact that the interrogation projects each atom into either $|0\rangle$ or $|1\rangle$ even though the interrogation is performed at an intermediate p with $0 < p < 1$. For a clock interrogating N_{at} atoms, this creates a detection noise of $\sigma_p = 1/(2\sqrt{N_{\text{at}}})$, so that the Allan variance of such an "ideal" clock becomes

$$\sigma_y(\tau) = \frac{1}{\pi Q_{\text{at}}\sqrt{N_{\text{at}}}}\sqrt{\frac{T_C}{\tau}} \tag{12}$$

This noise is not a fundamental limit, though. It is surmountable by preparing the atomic sample in an entangled "spin–squeezed state" [50, 51].

Allan variance as a filter It is helpful to formulate a continuum limit of equation 10. Therefore, one describes the relative frequency noise of the atomic clock as a time dependent function $y(t)$, including again the noise of the flywheel as well as noise on the atomic transition. Equation 10 then becomes

$$\sigma_y^2(\tau) = \frac{1}{2}\lim_{T\to\infty}\frac{1}{T}\int_{-T/2}^{T/2} dt\,\left((y * h_\tau)(t)\right)^2 \tag{13}$$

where $*$ denotes the convolution. $h_\tau(t)$ is the impulse response of the Allan variance. It encodes the process of "taking averages of y over the intervals $[t-\tau : t]$ and $[t : t+\tau]$ and

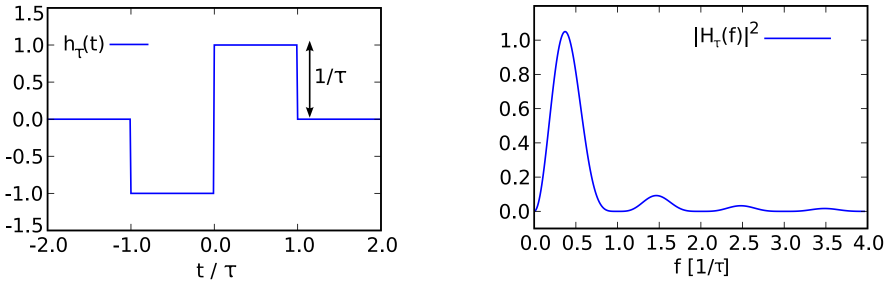

Figure 5: Impulse response $h_\tau(t)$ of the Allan variance (left) and the square modulus of its Fourier transform $|H_\tau(f)|^2$ (right). In this example, we assume a clock without dead time.

substracting them", whose discrete equivalent is the term $y_i - y_{i-1}$ of equation 10. This function is a full description of the clock cycle, including dead times (with $h_t(t) = 0$) or periods of reduced sensitivity of the clock. The restriction of this function to one clock cycle (the interval $[0 : T_C]$) is known as the "sensitivity function" of the clock. A simple example for a clock without dead time is depicted in figure 5.

Applying Parseval's theorem, the average in equation 13 can be taken in the frequency rather than the time domain:

$$\sigma_y^2(\tau) = \frac{1}{2} \int_0^\infty df \, S_y(f) \cdot |H_\tau(f)|^2 \tag{14}$$

Here, $H_\tau(f)$ is the Fourier transform of the impulse response and $S_y(f)$ is the one–sided spectral density of the frequency noise. The Allan variance can be seen as the total frequency noise transmitted by the filter $H_\tau(f)$.

Allan variance of different types of noise Noise is usually classified by its spectral density. To this end, the spectral density $S_y(f)$ is expanded into a power series

$$S_y(f) = \sum_{\alpha=-\infty}^{\infty} h_\alpha f^\alpha \tag{15}$$

We note that each of these components can be equally described by a relative phase noise $S_x(f) = 4\pi^2 h_\alpha f^\beta$ with $\beta = \alpha - 2$, since frequency is the derivative of phase. In practice, one encounters only terms with low α:

α	type of noise
-2	random walk frequency noise
-1	flicker frequency noise
0	white frequency noise
1	flicker phase noise
2	white phase noise

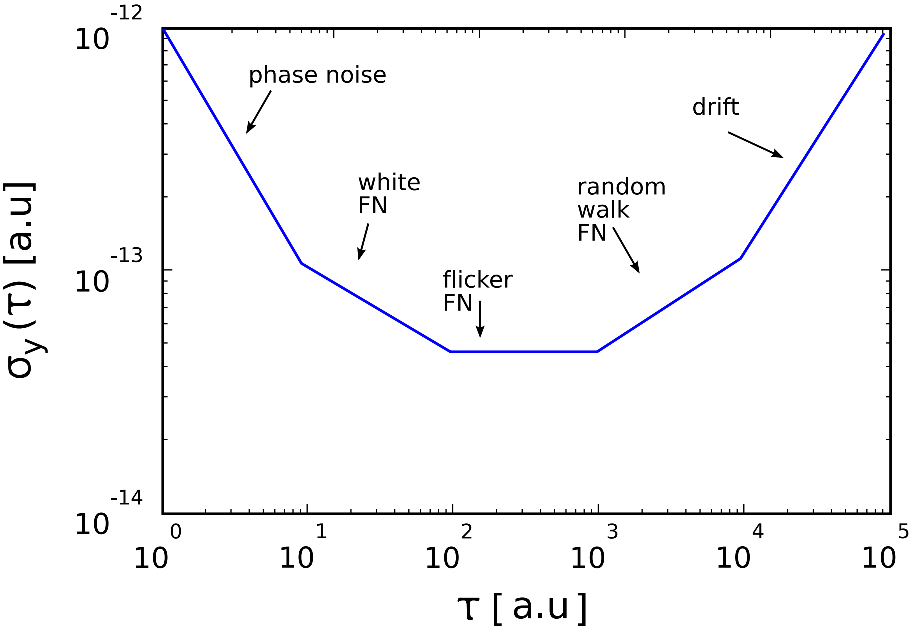

Figure 6: Log–log plot of the Allan variance of an ideal clock (conceptual). Each contribution to $S_y(f)$ dominates in a different region of τ, where it imprints a characteristic slope μ on the Allan variance.

For each of these idealized types of noise, its contribution to the Allan variance can be calculated from equation 14. For an ideal clock (without dead time), it turns out that each of these component contributes exactly one term to the power expansion of the Allan variance 14.

$$\sigma_y^2(\tau) = \sum_{\mu=-\infty}^{\infty} a_\mu \tau^\mu. \tag{16}$$

In particular, $\alpha = -2$ maps to $\mu = 1$; $\alpha = -1 \rightarrow \mu = 0$; $\alpha = 0 \rightarrow \mu = -1$; $\alpha = 1, 2$ both map to $\mu = -2$. A linear drift $y(t) = y_0 + Dt$, which is strictly speaking not a noise, can also be told from the Allan variance: It gives rise to a component of power $\mu = 2$. The important conclusion is that the components of the frequency noise $S_y(f)$ can be immediately read of from a log–log plot of the Allan variance, as is demonstrated in figure 6.

Conclusion The Allan variance makes it possible to give an exact definition for the figures of merit of paragraph 1.1.2.
Short–term stability is identified with a_{-1}, which we have seen to arise from white frequency noise. This contribution limits the clock stability at short timescales. It averages out for longer integration times according to a $1/\sqrt{\tau}$ law.
The ultimate error bar the clock can provide on a frequency measurement is a_0, the level of the $\mu = 0$ floor, which stems from frequency flicker noise. Strictly, this can be considered an ultimate limit only if the random walk frequency noise and drifts are

negligible. However, this is often the case for atomic clocks, and in particular for primary standards.
Accuracy, the systematic error bar on the SI second, cannot be read off from figure 6. It has to be estimated from complementary measurements, often by varying external parameters like e.g. the electric background field or the temperature of the clock.

1.2 Today's benchmark atomic clocks

Atomic fountain clocks Atomic fountain clocks use a hyperfine transition as their frequency reference. The atomic sample consists of a freely falling cloud, which is laser–cooled and then launched such that it passes twice through a microwave cavity, which excites the transition. This clock has been proposed in the 1950s and been realized in the early 1990s [52]. Today, it is this kind of clock, running on Cesium atoms, which realizes the SI second. It has achieved a short–term stability of $1.6 \cdot 10^{-14}\sqrt{\mathrm{s}}$ and has been integrated down to $2 \cdot 10^{-16}$ [53], [54], [55].

Optical atomic clocks The frequency reference of these clocks is an optical transition. The flywheel is a laser, which is locked to the resonance of an ultrastable cavity or – via the frequency comb technology [56] – to a microwave frequency standard, to be stable at short timescales. Basically, three species of this kind have been developed (see [47] for a more in–depth overview):

- **Untrapped atom clocks** interrogate a sample of freely falling atoms. They use a Ramsey–Bordé interrogation [57], a modified version of the Ramsey technique, which eliminates the first–order Doppler shift. These clocks have achieved a short–term stability of $3 \cdot 10^{-15}\sqrt{\mathrm{s}}$ which has been integrated down to as low as $1 \cdot 10^{-16}$ [34].
- **Ion clocks** use a trapped ion as their atomic sample. They operate in the Lamb–Dicke regime, where the recoil of an absorbed or emitted photon is transfered to the whole trap instead of the motional degrees of freedom of the atom. Recently, a short–term stability of $4 \cdot 10^{-15}\sqrt{\mathrm{s}}$ has been reported, which integrates down to $5.2 \cdot 10^{-17}$ [33].
- **Optical lattice clocks** use an atomic sample, which is confined to an optical lattice. In this way, they also reach the Lamb–Dicke regime, albeit for a larger sample than ion clocks. Care has to be taken to choose a "magic wavelength" of the lattice where the trapping light does not shift the atomic transition [58]. These clocks have reached a short–term stability of $3 \cdot 10^{-15}\sqrt{\mathrm{s}}$, integrating down to $1 \cdot 10^{-16}$ [34].

All these devices, fountain clocks as well as most optical clocks, are stationary setups, filling a whole laboratory. As the next section will show, there exist interesting applications, which need clocks of a comparable performance, but of a smaller size.

Source	positioning error [m]
Selective availability	24.0
Ionosphere delay	7.0
Troposphere delay	0.7
Clock and ephemeris error	3.6
Receiver noise	1.5
Multipath	1.2

Table 1: Error sources of the GPS signal, after [59], [60]. Selective availability was an artificial error, introduced into the civilian C/A signal. It has been removed since 2000. Multipath refers to stray signals, which are reflected on the ground before hitting the reciever.

1.3 Global navigation satellite systems (GNSS)

Satellite navigation systems are arguably the most prominent application of today's atomic clocks, the most important one to date being no doubt the american global positioning system (GPS). Its "space segment" consists of a set of satellites, which are placed in medium–earth orbit. The essential payload of each satellite is a set of atomic clocks, Cesium beam or Rubidium vapor–cell clocks . Their time is continuously broadcast to earth. This transmission is performed on different frequencies and with different encodings. Only one encoding, the coarse/acquisition (C/A) code, is publicly documented. This is transmitted on only one frequency. Another encoding, the precision/encrypted (P/Y) code is transmitted on two different frequencies. The key for this code is distributed by the U.S. Air Force.
To determine a position, a user measures the delay of the clock signal of several satellites, which is directly proportional to his distance to the satellites. The position is then computed from these distance constraints by triangulation. Basically, the signal of three satellites is sufficient to determine a three–dimensional position. This however implies that time is known, more precisely that the user has a clock of a performance comparable to the GPS clocks, which is furthermore synchronized to GPS time. This problem can be surmounted by receiving the signal of at least four satellites and performing a triangulation for the four variables position and time.

It is evident that the error on the clock signal of a satellite will contribute to the error on the position measurement. However, an analysis of the error budget of the single–frequency signal shows that this error is dwarfed by other sources, most notably the delay in the Ionosphere (see table 1). However, this error varies with the frequency of the signal. Therefore, it can be largely removed when the user has access to more than one frequency. Using the two frequencies of the P(Y) code, the GPS signal has been integrated down to a positioning error of the centimetre–level and the GPS time has been transfered by this method with an uncertainty of 10^{-15} after one day of integration [61][62].

It is for this reason that GPS could indeed benefit from better clocks. Therefore, defence and space agencies all over the world fund a number of developments in the field

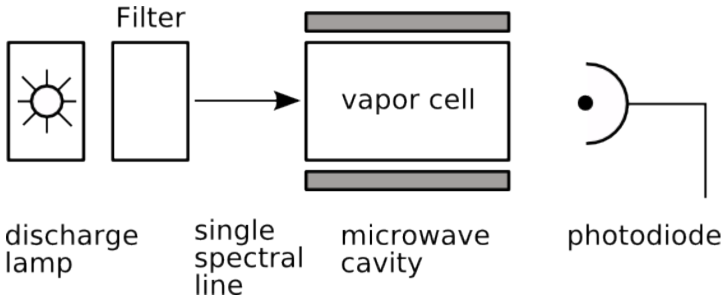

Figure 7: An atomic vapor cell clock as it is used in nowaday's navigation satellites. Light of one spectral line pumps an Alkali vapor into a dark state. A microwave repumps the atoms, giving rise to an absorption peak of the probe light if it is resonant.

improved compact clocks. This will be the subject of the next section.

1.4 Compact atomic clocks

Vapor cell clocks A whole family of clocks is based on hyperfine transitions of Alkali metal atoms, typically Rubidium or Cesium. These transitions can be excited and detected in a room–temperature atomic vapor cell in several ways:

Optical–microwave double resonance This clock performs a spectroscopy on a hyperfine transition by means of an optical–microwave double resonance (see figure 7 for an illustration). A vapor cell containing the atomic sample is illuminated by a spectral line, which drives an optical transition from only one of the two clock states $|1\rangle$ or $|0\rangle$ (for the following, we will assume from $|1\rangle$). It pumps the atomic vapor into the state $|0\rangle$, which is dark. The vapor cell is placed into the field of a microwave cavity. This microwave will repump the atoms into the state $|1\rangle$, if it is resonant with the atomic transition. In this case, the atomic vapor will continuously scatter light from the probe beam, which is detected as an absorption maximum by a photodiode. The probe light is not required to be coherent, so that it can be produced by a filtered discharge lamp. These lamps are more reliable than lasers and have favorable noise properties, which renders them attractive for space applications. See [63] and [64] for an overview of these clocks.

This type of clock is running on the GPS satellites [65]. Its current [66] and near–future versions [67] specify a stability of $\sigma_y(\tau) = 3 \cdot 10^{-12}\sqrt{\text{s}}$, which integrates down to $5 \cdot 10^{-14}$.

The first generation of GALILEO will carry Rubidium clocks of comparable performance ($4 \cdot 10^{-12}\sqrt{\text{s}}$ stability and $3 \cdot 10^{-14}\sqrt{\text{s}}$ flicker floor)[68], the goal for future development of these clocks is slightly higher, ($1 \cdot 10^{-12}\sqrt{\text{s}}$ stability and $1 \cdot 10^{-14}\sqrt{\text{s}}$ flicker floor) [69].

Pulsed optically pumped (POP) clocks This clock can be understood as an improved version of the double–resonance clock. They are based on the same hardware and differ only in the interrogation scheme. Instead of performing a continuous spectroscopy, the POP clock follows a pulsed scheme: It prepares the sample in the state $|0\rangle$ by optical pumping and then performs a Ramsey interrogation driven from the microwave cavity. The resulting population imbalance is detected either optically or by extracting the free–induction–decay signal with the microwave cavity [70, 71]. Performing a Ramsey interrogation on an atomic vapor is possible, since atoms in a vapor cell have a short but non–zero coherence time of the order of 10ms [72]. With respect to double–resonance clocks, the pulsed interrogation significantly reduces the sensitivity to lightshifts as well as AM and FM noise of the interrogation light. For this reason, POP clocks have improved the short–term stability to $1.2 \times 10^{-12}\sqrt{\mathrm{s}}$. They have been integrated down to 3×10^{-14} [70]. The latter value is limited by a continuous drift due to the cell, which is a major concern for all kinds of vapor cell clocks.

Coherent population trapping (CPT) clocks These clocks, too, interrogate a hyperfine transition in an atomic vapor. However, they can perform the interrogation using only optical photons, eliminating the need for a microwave cavity. To this end, the vapor cell is illuminated by two phase–coherent laser beams, near–resonant with the transition from an excited state $|e\rangle$ to the states $|0\rangle$ and $|1\rangle$ respectively. It can be shown that, if the laser frequencies differ exactly by the transition frequency $\omega_{|0\rangle\to|1\rangle}$, the atoms are pumped into a dark state $(|0\rangle + e^{i\phi}|1\rangle)/\sqrt{2}$, which does not couple to the beams. This phenomenon, known as coherent population trapping (CPT), is used in clocks in several ways:

In CPT masers [73], the sample is placed in a microwave cavity and illuminated continuously. The dark state has an oscillating magnetic dipole moment and, therefore, emits radiation, which is extracted by the microwave cavity as in a conventional maser.

In continuous CPT clocks, the absorption of the beams across the cell is monitored [74]. The signature of CPT is a minimum of this absorption, occuring on resonance, where the sample is pumped into the dark state. By locking the detuning between the lasers to this minimum, the difference frequency of the lasers is locked to the frequency of the atomic transition. It can therefore be used as a continuous clock signal.

Pulsed CPT clocks [75] employ a pulsed scheme, which is reminiscent of the Ramsey scheme. A pulse of both lasers pumps the atoms into the dark state. This is equivalent to the first $\pi/2$–pulse of the Ramsey scheme, since the dark state is a coherent superposition of $|0\rangle$ and $|1\rangle$. The lasers are then switched off during a period of free evolution. As for the Ramsey scheme, the superposition picks up a phase during this period, proportional to the detuning of the difference frequency of the lasers from the atomic resonance. In the picture of the dressed CPT states, this transfers the atom into a mix of the dark and the bright state. The population of the bright state is detected by a second pulse of both lasers, which at the same time repumps the atoms into the dark state. With this technique, a short–term stability of $7 \times 10^{-13}\sqrt{\mathrm{s}}$ has been achieved, which integrates down to a few 10^{-14}, if a constant drift is removed [72].

Figure 8: The HORACE clock: the cooling and the interrogation take place in the microwave cavity (copper block on top), which is part of a UHV chamber. The laser light is coupled by multimode glass fibers (green cables), the microwave is coupled by waveguides (rods connected to the cavity). Image courtesy of F.X. Esnault.

Requiring only lasers, electronics and a vapor cell, CPT is an extremely promising candidate for chip–scale atomic clocks. Such clocks would be yet another order of magnitude smaller than the liter–scale space clocks and might find an application in advanced ground–based applications like the synchronisation of data transmission networks. At the NIST, a clock has been built, whose "physics package" occupies less than a cm^3. Stabilities of $4 \times 10^{-11}\sqrt{\mathrm{s}}$ have been reported and integrated down to 6×10^{-12} [30, 76].

Hydrogen Masers In addition to a Rubdium vapor cell clock, the first generation of GALILEO staellites will also use a passive hydrogen maser. Its performance is superior to the Rubdium vapor cell clocks, with a stability of $< 10^{-12}\sqrt{\mathrm{s}}$ at short term and a flicker floor at $7 \cdot 10^{-15}$ [68]. However, it is considerably bigger and heavier than a vapor cell clock and consumes more power [68, 77].

Cold atom clocks (HORACE) A natural improvement on the previous clocks is to use laser–cooled atoms. This is the key idea behind the HORACE project (figure 8), which can be thought of as a simplified version of an atomic fountain clock. This clock performs a Ramsey interrogation on an untrapped, laser–cooled atomic vapor, which is placed under UHV inside a microwave cavity. The role of this cavity is twofold: It creates the microwave excitation field as well as the optical molasses to perform the laser–cooling. To perform the latter task, its inner faces are highly reflective in the optical domain. When the interior of the cavity is illuminated with laser light, random reflections on these faces create a random light field. This light field contains a sufficient component of optical molasses to laser–cool the atomic vapor. This clock has reached a short–term stability of $2.2 \times 10^{-13}\sqrt{\mathrm{s}}$ and has been integrated down to 4×10^{-15} [32]. This performance has been measured in a ground–based clock. Here, interrogation times are limited to the 10ms timescale, since the atoms fall freely during the interrogation and hit the walls after this time. A better performance is expected in microgravity.

Compact ion clocks (LITE) This kind of clock is based on a hyperfine transition in the electronic ground state of the $^{199}\mathrm{Hg}^{+}$ ion. A cloud of these ions is captured in a linear multipole trap, where a microwave is coupled to the ions to perform a Ramsey or Rabi interrogation. The resulting population inversion can be detected by flourescence imaging driven from a Hg discharge lamp. This clock has two essential advantages: Using trapped ions, it can achieve long interrogation times. Furthermore, the hyperfine transition has a frequency of 40.507GHz, higher than the hyperfine transitions used in atomic clocks. Typical shifts (e.g., the Zeeman–shift or the collisional shift) are of the same absolute size than in other clocks, but the fractional frequency shofts are smaller. A liter–size prototype of such a clock has been built at the NASA jet propulsion laboratory (JPL). It has achieved a short–term stability of $1 - 2 \times 10^{-13}\sqrt{\mathrm{s}}$ and has been integrated down to 1×10^{-15} [78, 79]. Laboratory–size clocks of this technology have been integrated down to 3×10^{-16}.

Compact optical clocks Optical clocks have revolutionized the field of primary standards, so it is a natural idea to introduce their technology into the field of compact clocks. Indeed, the NIST Ca clock has been advertised as a compact clock [80]. In a compact setup, this clock has achieved a short–term stability of $3\times10^{-15}/\sqrt{\mathrm{s}}$, integrating down to several 10^{-16}.

Atomic clocks for scientific space missions There are several clocks which have been developed to be operated on the International Space Station, with the goal to test fundamental physics by precision measurements. These clocks differ significantly from the compact clocks of the previous paragraphs: Each of them is a prototype, with an intended work life of at most a few years. The most prominent example in our laboratory is the PHARAO space clock [81]. It is best understood as an atomic fountain clock in space: Atoms are captured and cooled in optical molasses and launched by the moving–molasses technique. The moving atoms then undergo a Ramsey interrogation by crossing two microwave cavities (a single one does not suffice in zero-g, since the atoms do not fall back). At the end of their trajectory, they are detected by flourescence. In space, this clock is predicted to reach a stability of $1.1 \cdot 10^{-13}\sqrt{\mathrm{s}}$, integrating down to less than 10^{-16}. At the moment, PHARAO is scheduled to fly on the ISS in 2010, as part of the ACES mission. This mission will also contain a hydrogen maser and a bidirectional microwave link to earth. In this way, it can be used as a time transfer tool to compare distant clocks with a precision of 10^{-17} after one week of integration.
Two similar projects are PARCS and RACE [82]. PARCS is an atomic Cs clock, similar

to PHARAO, aiming at a stability of $7 \cdot 10^{-14}\sqrt{s}$, integrating down to better than 10^{-16}. To our best knowledge, PARCS has been cancelled to make way for the NASA moon landing program.

RACE is a fountain clock operating on Rubidium. It is a "juggling" design, in which a new atomic sample is launched while the previous one is still flying through the spectroscopy zone. It features two independent spectroscopy zones (i.e, four Ramsey cavities) and a double-MOT, one MOT to load the sample and another one to launch it into one of the spectroscopy zones. Its goal is a stability of $3 \cdot 10^{-15}\sqrt{s}$, integrating down to 10^{-17}. Its main objective – besides the demonstration of these impressive figures – are time distribution at the 10^{-17} level and precision tests of general relativity.

Outlook We cannot cite publications about the clocks of tomorrow, but we can get a glimpse of their performance from the calls for proposals of space agencies and from the specifications researchers are willing to commit.

ESA call for proposals Foreseeing the demands on compact clocks of tomorrow, the European Space Agency (ESA) has opened, or is about to open, several tenders: For the next Galileo generation, new technologies like POP, CPT or cold atoms will be considered. A tender for the development of an optically pumped Cesium clock is already open ("EBB Development of Caesium clock for space", AO5579) and a more generic tender, targeting several "innovative clock concepts" is likely to follow ("Development of innovative atomic clock for satellite", 07.1ET.12). The goal here is a factor of two improvement in stability over the existing clocks.

In the long term, ESA seems to bet onto optical standards. In this field, two tenders are intended: "Development of key optical clock technologies" (07.129.18) aims at the construction of breadboard prototypes of the basic components of a space–proof optical clock. "Demonstration of optical clocks based on cryogenic resonators" (08.129.15) demands the development of an optical clock, ready for ground applications and with the potential for space applications. This clock shall be based on a cryogenic optical resonator, which can be used either as a stand–alone clock or as a flywheel for other clocks. It shall reach a stability of $7 \times 10^{-14}\sqrt{s}$, integrating down to 7×10^{-16} at $\tau = 10^4$s.

Search for anomalous gravitation using atomic sensors (SAGAS) This project is a candidate for a deep space mission between 2015–2025 [83] and has been proposed to the European Space Agency in 2007. Its goal is to create a gravity map of the outer solar system and to search for anomalous gravitation. Its payload would contain two atomic clocks, an optical ion clock, optimized for long–term performance, and an atomic accelerometer, based on a hyperfine transition, which can also be run as a clock. The latter would use a molasses–cooled sample (similar to HORACE) and perform an interferometric measurement based on Raman transitions. The mission proposal predicts a performance of 10^{-12} both for one–shot stability and accuracy.

The optical ion clock is predicted to deliver a $1 \times 10^{-14}\sqrt{s}$ stability averaging down to 1×10^{-17} at 10 days of integration. The accuracy is predicted to be below the latter

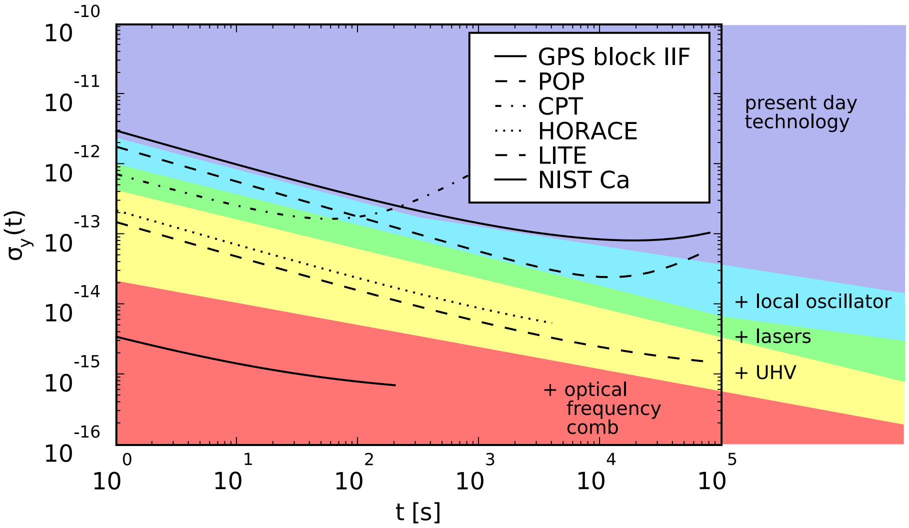

Figure 9: The performance of today's prototypes of compact clocks. All data is taken from the references cited in the text.

level. This confirms that optical clocks are promising candidates for future compact clocks. We note, however, that the cited mission proposal relies on an **optical** link to earth. This is partly due to scientific reasons, but also because it is not sure whether space–proof frequency combs will be available before the proposed launch date.

Conclusion A comparison of today's compact clocks is presented in Fig. 9. As can be seen, performances several orders of magnitude better than the current GNSS clocks have already been achieved in the laboratory. With several satellite navigation systems being built around the world, it is likely that clocks of this performance will fly in GNSS applications in a few years.

Another conclusion is evident: Moving to better performance, compact atomic clocks rely on more and more advanced technologies, like lasers or ultrahigh vacuum. It even seems like some barriers (like, e.g. the notorious drift caused by vapor cells) can only be broken by the use of more complicated technologies (ultrahigh vacuum in this case). Making these technologies compact and reliable enough for space applications is a major part of the work. In the field of primary standards, breaking a world record with a laboratory–scale setup can be considered an accomplished mission. In contrast, it is at most half of the work in the field of compact clocks. Therefore, we cannot yet tell from figure 9, which of the cited laboratory setups will first make the race to a spaceborne application. But we are looking forward to see it.

Coming back to this thesis, the conclusion we draw from figure 9 is the following: There is considerable interest in building clocks with a stability in the low $10^{-13}\sqrt{\mathrm{s}}$ range. And to get there, local oscillators, lasers and ultrahigh vacuum are completely admissible tools. We will show in the following section, that, using these tools, a clock based on the atom chip technology can play in this league. It is this insight which has motivated the present work.

2 Atom chips

In this thesis, we present a novel type of compact clock, similar to the clocks described in the previous section 1.4. It is based on an atom chip, an experimental tool which has been developed over the last ten years. In this chapter, we will discuss the underlying concept of atom chips, without refering to the specific application of our clock. We start by an overview of the brief history of atom chips and an outline of the many possible ways to create microtraps on a chip. We then focus on the most widespread type of traps, magnetic traps created by microfabricated conductor structures and describe, which conductor structures can create such traps. Here, we take the point of view of [84] by describing a microtrap as being composed of elementary 2–dimensional traps. We consider some practical limitations, most notably the trap depth and the adiabaticity of the loading procedure, before we conclude by giving typical orders of magnitude for these traps.

2.1 The History of atom chips

Traps for neutral particles have a long history. Magnetic traps for neutrons have been proposed as early as 1961 [85] and have been realized in the late 70s [86]. It was only with the advent of laser cooling in the 1980s that magnetic trapping of neutral atoms was achieved [87]. This technique became the standard tool of the work towards Bose–Einstein condensation and indeed the first BECs have been achieved in magnetic traps [1, 2].

The magnetic field of these early traps was produced by macroscopic current–carrying coils, mounted at a distance of at least several centimeters from the trap. Such a configuration is a natural choice, since it allows to mount the coils outside the ultrahigh vacuum system. A simple scaling relation shows, however, that it is not the optimal choice: The magnetic field at the distance r of a wire with dimensions $w \ll r$ and carrying a current I scales like I/r. Moreover, the steepness of a trap is characterized by the magnetic gradient $\partial B/\partial r$, which scales as I/r^2. It is therefore highly desirable to place the conductors as close as possible to the trap they generate. This argument was pointed out in 1995 [3], along with a proposal to drastically reduce r: The magnetic trapping field could be produced by a microfabricated structure. On such an "atom chip" the distance between the wire and the trap would be reduced by several orders of magnitude from centimeter to micron distances. Of course, microstructures also support less current than macroscopic coils. In practice, however, heat dissipation is more efficient for smaller structures. It is therefore safe to assume that when scaling a conductor structure down by a factor of $k < 1$, the maximum current will decrease by less than a factor of k^2, such that the gradient $B' \sim I/r^2$ will increase.

It turns out that this idea greatly enhances the flexibility of magnetic traps. To produce a trap with a given stiffness, a microfabricated conductor layout requires much less current than a macroscopic coil. Since this current flows typically through Ohmic conductors, microtraps require less power than macroscopic setups. In this way, atom chips make it possible to achieve Bose–Einstein condensation in a setup that is portable

and autonomous [88, 89].
For a given current, in turn, a microtrap will produce a far tighter confinement than a macroscopic coil. This is beneficial in several ways: The density of a trapped quantum gas increases for increasing confinement. And a high density allows for a highly efficient evaporative cooling. Indeed, a laser–cooled cloud can be cooled into a BEC in ~ 1s in a microtrap, one order of magnitude faster than in a macroscopic trap [8]. Furthermore, the higher confinement renders new trapping regimes accessible. An example for this application are one–dimensional quantum gases. Here, a strong confinement is applied along two directions of the trap, strong in the sense that a sufficiently cold quantum gas in this trap only populates the fundamental level of the trap along these directions ($\mu < \hbar\omega_\perp$). For the remaining direction, the confinement is deliberately chosen weak. The gas then exhibits quasi–one–dimensional dynamics along this weak direction. Atom chips have been used for a number of studies in this regime [10, 11, 12].
High field gradients and curvatures, created by small structures, also imply that the trapping field falls off rapidly around the trap center. This allows to place multiple traps close to each other, with a separation on the scale of r. This, together with the fact that the microfabricated conductor layouts are easily scalable, allows to create highly complex trap layouts, a true “quantum lab on a chip” [90, 91, 92]. In spite of their complexity, such traps can be constructed from elementary building blocks. This high degree of integration is reminiscent of modern microelectronics.
Furthermore, a magnetic trap on an atom chip is inherently close to a surface. This allows to study the interaction between a quantum gas and solid state systems, such as room–temperature surfaces [18, 15, 16, 19, 20], superconducting surfaces [93, 94, 95] or mechanical nanoresonators [13, 14].

This idea has been realized in the late 1990s, when atoms were for the first time guided [4, 5] and trapped [6] in surface traps. The term “atom chip” finally was coined in [7]. In such traps, atoms have been cooled into BEC [8, 9] and Fermi degeneracy [96]. The electromagnetic microtrap just described is without doubt the most widespread approach to trap atoms on a chip. It is worth noting, however, that a number of complementary methods have emerged over time:

Permanent magnetic potentials can be fabricated by writing microscale patterns onto a ferromagnetic film. These patterns can be designed to form traps, which are tunable by an external bias field. BEC has been achieved in these traps [97], [98].

Electrostatic potentials In spite of being neutral objects, atoms still have a non–zero electric polarizability. Therefore, electric fields can be used to create potentials. Microfabricated electrodes have been used to this end [99]. However, atoms are high-field-seekers for electric fields, so a purely electrostatic trap is forbidden by Earnshaw's theorem.

TOP potentials In this technique, the atoms are subjected to a time-dependent potential. At each instant in time, the potential is made such as to provide a confinement of frequency ω_{t}. However, this potential is varied with a frequency $\omega_{\mathrm{TOP}} \gg \omega_{\mathrm{t}}$. It can be shown that this “time–orbiting potential” (TOP) creates an effective potential which is the time average of the varying potential. This concept originally emerged to prevent Majorana losses in quadrupole traps [100]. However, it has recently been successfully exploited in electromagnetic chip traps [101] and makes trap layouts like ring traps accessible [102], [103], [104].

Dressed-state potentials Magnetic transitions in the atomic ground state – with a frequency in the microwave or RF range – can be used to create or modify traps. There are two variations of this technique: One approach is similar to optical dipole traps: The atoms are subjected to a driving field with a position-dependent Rabi frequency $\Omega(\vec{r})$ which is detuned by Δ from the atomic transition. This induces on the atoms a lightshift $V(\vec{r}) = \frac{\hbar\Omega(\vec{r})^2}{4\Delta}$ [105], which acts as a potential.

The other approach involves two components: A near-resonant driving field acting on a transition between two states $|g\rangle$ and $|e\rangle$ and a static (typically magnetic) trapping field. The static trapping field shifts the states $|e\rangle$ and $|g\rangle$ in a different manner and creates thus a position-dependent detuning $\Delta(\vec{r})$. The resulting dressed states are a position-dependent mixture of $|g\rangle$ and $|e\rangle$. Since both states couple differently to the static field, this mixture modifies the trap. A typical application consists in creating a barrier inside a trap by mixing in an antitrapped state $|e\rangle$ at its center [106]. Two variants of dressed state traps have been investigated on microchips:

- RF dressing Radio-frequency (RF) fields can be used to address transitions between adjacent m_F sublevels of the atomic ground state. This has been used to create dressed-state potentials [106] [107].
- MW dressing Microwave (MW) fields can be used to address transitions between different F sublevels of the atomic ground state. Using the near-field of microfabricated microwave guides, state-dependent potentials can be created. [22], [108].

Optical fields Finally, microfabricated **optical** structures, such as microlenses or microfabricated holograms, allow for the manipulation of optical fields. These fields can be used to create optical microtraps [109] or other miniaturized optical elements like micro-MOTs [110].

In the following, we will concentrate on the most widespread type of surface trap, the electromagnetic atom chip, which confines atoms in the magnetic field of a current, which circulates in a microfabricated wire.

2.2 Electromagnetic Atom Chips

2.2.1 Overview: How to trap an atom with a wire

Trapping principle To create the trapping potential, a magnetic trap exploits the fact that atoms have a non–zero magnetic dipole moment. We will discuss this property in more detail in section 3. For the moment, we simply note that, at small magnetic fields, this dipole moment depends only on the total atomic angular momentum, which, in the electronic ground state, is labeled by the two quantum numbers F, m_F. If an atom in the $|F, m_F\rangle$ state is immersed into a magnetic field of magnitude B, it experiences an energy shift

$$\Delta E_B(B) = g_F m_F \mu_B \,|B| \tag{17}$$

where g_F is the Landé g-factor. This formula is valid for magnetic fields much weaker than the hyperfine splitting $\Delta E_B \ll \Delta E_{\mathrm{HFS}}$. The Landé g-factor for ^{87}Rb takes the values $g_1 \approx -1/2$, $g_2 \approx 1/2$, which implies that there exist three low-field-seeking states $|2,2\rangle, |2,1\rangle$ and $|1,-1\rangle$.

The important consequence of equation 17 is that a position–dependent magnetic field $\vec{B}(\vec{x})$ translates into a position–dependent potential $V(\vec{x})$ seen by the atoms. In particular, a trap corresponds to a local minimum of the magnetic field.

We will now discuss, which wire layouts can create magnetic traps. First, we discuss how traps can be created in two dimensions. Subsequently, we show, how these 2D traps can be assembled to form various traps in three dimensions.

Example: a trap created by a single wire The simplest surface trap is constructed from a single wire and a homogeneous bias field as shown in figure 10. For a wire along x and a bias field along y, the resulting field is independent of x. In each y–z–plane the bias field cancels the field of the wire at a position $\vec{x}_0 = (y = 0, z = z_0)$ with

$$z_0 = \frac{\mu_0 I}{2\pi B_0} = 2\mathrm{mm} \cdot \frac{I/\mathrm{A}}{B_0/\mathrm{G}}$$

Since the bias field is homogeneous, it does not affect higher–order derivatives of the wire field. In particular, the gradient of the resulting field is equal to the gradient of the wire field, which, at $\vec{x}_0$, has the value

$$B'_{\mathrm{wr}} = \frac{\partial B_y}{\partial z}\Big|_{\vec{x}_0} = \frac{\partial B_z}{\partial y}\Big|_{\vec{x}_0} = \frac{2\pi B_0^2}{\mu_0 I} = 5\frac{\mathrm{G}}{\mathrm{cm}} \cdot \frac{(B_0/\mathrm{G})^2}{I/\mathrm{A}}$$

Therefore, the magnetic field can be expanded around $\vec{x}_0$ as

$$\vec{B}(\vec{x}) = B'_{\mathrm{wr}} \begin{pmatrix} 0 & 1 \\ 1 & 0 \end{pmatrix} (\vec{x} - \vec{x}_0) = B'_{\mathrm{wr}} \begin{pmatrix} z - z_0 \\ y \end{pmatrix}$$

In the y–z plane the modulus of this field grows in every direction around $\vec{x}_0$. Consequently, the line $(0, 0, z_0) + \lambda \vec{e}_x, \lambda \in \mathbb{R}$ is a minimum of the magnetic field. A sample of low–field seeking atoms can be held in this minimum above the wire.

The 2D quadrupole minimum The type of minimum encountered in the previous paragraph is the most basic building block of chip traps. Since we will frequently refer to it in the following paragraphs, it is useful to introduce some symbols and definitions:

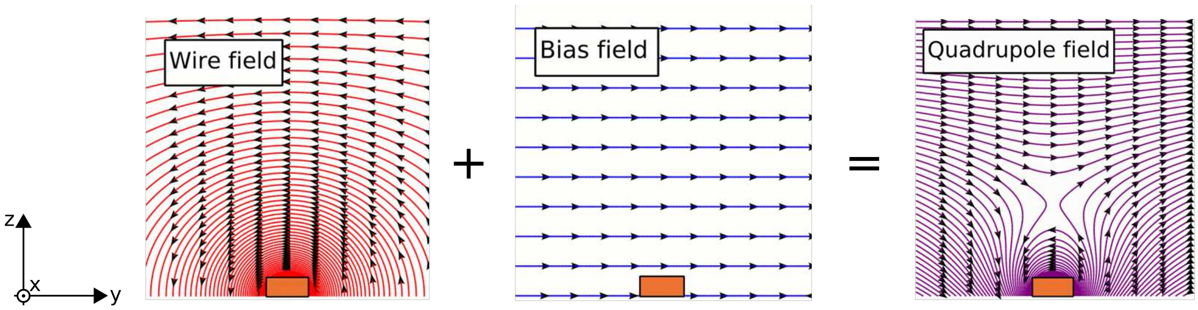

Figure 10: The simplest possible chip trap: The field of a wire (left, current flowing out of the paper plane) is superposed with a homogeneous field (middle) to form a quadrupole minimum (right). A sample of low–field seeking atoms would accumulate at the quadrupole minimum and float above the wire.

A 2D quadrupole minimum is a field configuration, where the magnetic field vanishes at a point $\vec{x}_0$ and and grows linearly around this point with the Jacobian matrix $\mathbf{dB}$.

$$\vec{B}(\vec{x}) = \mathbf{dB} \cdot (\vec{x} - \vec{x}_0) = \begin{pmatrix} \frac{dB_y}{dy} & \frac{dB_y}{dz} \\ \frac{dB_z}{dy} & \frac{dB_z}{dz} \end{pmatrix} (\vec{x} - \vec{x}_0) \tag{18}$$

The Maxwell equation $\mathsf{rot}\vec{B} = 0$ implies that the Jacobian matrix $\mathbf{dB}$ is symmetric and can therefore be diagonalized. We will refer to the two resulting orthogonal eigenvectors $\vec{e}_+$ and $\vec{e}_-$ as the "quadrupole axes" and to the corresponding eigenvalues B'_+ and B'_- as "quadrupole gradients". The quadrupole gradients must satisfy the condition $B'_+ + B'_- = 0$, in order to fulfill the Maxwell equation $\mathsf{div}\vec{B} = 0$.
To give a concrete example, let us apply these definitions to the example of the previous paragraph (figure 10). The two quadrupole axes of this 2D quadrupole are $\vec{e}_\pm = \vec{e}_y \pm \vec{e}_z$, rotated by 45° with respect to the z–axis. The quadrupole gradients are $B'_\pm = \pm B'_{\mathrm{wr}}$
In 3D–space, a 2D quadrupole field has a third distinguished axis: The axis of the resulting trap ($\vec{e}_x$ in the example of the previous paragraph). We will refer to this axis as the "zero line" of the quadrupole.
In a way, the 2D quadrupole field can be seen as the most basic building block of chip traps. Since we will frequently refer to it below, we will introduce the symbols depicted in fig. 11.

Grouping wires to elementary trapping fields Generally, a chip design is more complex than the wire trap presented above and contains multiple current–carrying wires and a bias field of arbitrary magnitude and direction. However, to analyze the resulting trap, it is helpful to split the complex layout and the bias field into multiple simple components, each of which creates an elementary trap like the one above.

Mathematically, let us assume the atom chip to have N wires with wire i carrying

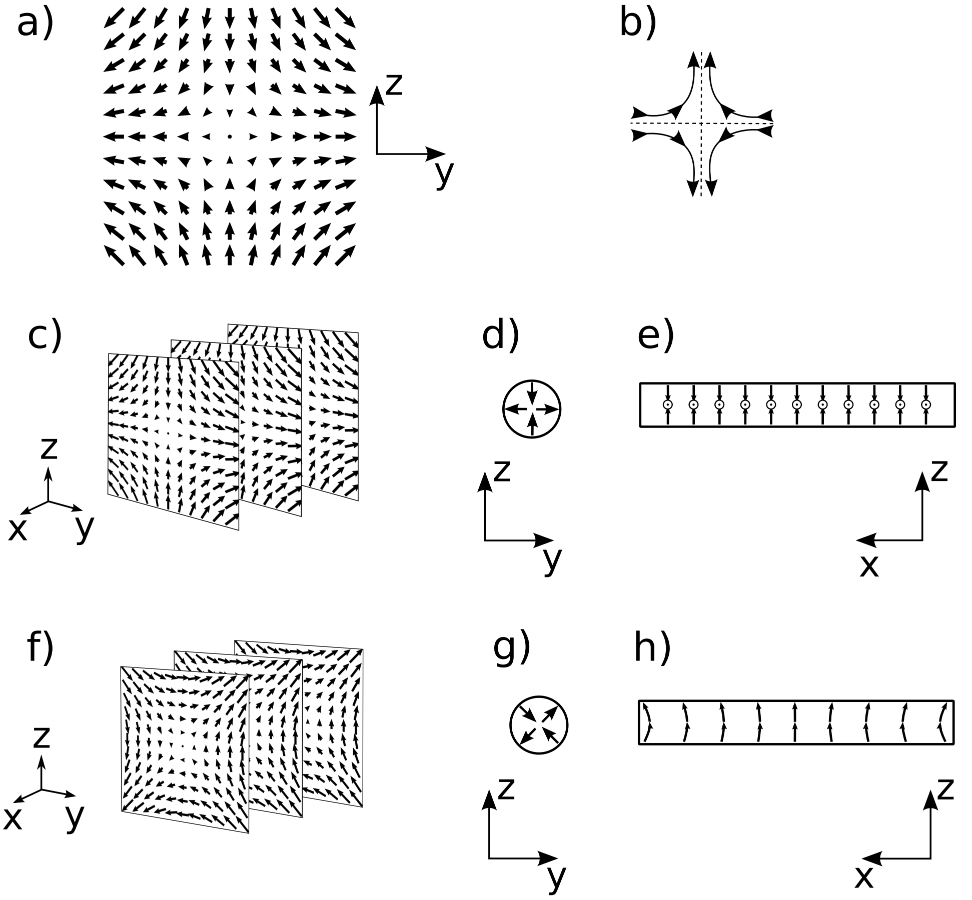

Figure 11: A 2D quadrupole field (a). The quadrupole axes are directed along y and z, the quadrupole gradients are of equal size. A quadrupole minimum (b): We will denote by this symbol a point, where a complex field locally looks like (a). A 2D quadrupole field in a 3D space (c): The field depends only on y and z. In each plane x =const, it looks like (a). As an abbreviation for this field, we introduce the symbols (d) and (e). The arrows in (d) and (e) are intended to visualize the fieldlines of (c), as seen from the side when looking down either the negative x–axis (d) or the negative y–axis (e). We introduce the same symbols for a 2D quadrupole field with 45°–rotated axes (f–h). Note that symbols (d,e,g,h) denote a field which extends over the entire 3D space.

current I_i. It creates the field

$$\vec{B}(\vec{x}) = \sum_{i=1}^{N} \vec{B}_{\text{wire i}}(I_i, \vec{x}) + \vec{B}_0 \tag{19}$$

To find and analyze the resulting traps, it is extremely convenient to choose M subsets of the wires $W_j = \{i_1, i_2, ...\}$ and to split the bias field $\vec{B}_0 = \sum_{j=1}^{M} \vec{B}_{0,j}$ such that each subset of wires together with its bias field $\vec{B}_{0,j}$ creates a basic trap, typically a two–dimensional quadrupole trap. Eq. 19 can then be written in the form

$$\vec{B}(\vec{x}) = \sum_{j=1}^{M} \left(\sum_{i \in W_j} \vec{B}_{\text{wire i}}(\vec{x}) + \vec{B}_{0,j} \right) \tag{20}$$

which is a sum over traps instead of a sum over wires. The basic building blocks of atom chips are elementary traps, rather than wires and currents. This idea was developed along with the first magnetic surface trap [84]. In the following paragraphs, we will first present a number of such elementary traps and then demonstrate this technique by dissecting today's most common trap layouts into their elementary trapping fields.

2.2.2 Elementary Circuits to create 2D quadrupole fields

Two–dimensional traps can be produced by different trap layouts as depicted in Fig. 12. A similar overview can be found in [111].

We have already introduced the layout 12a), which is the simplest trap. It is formed by adding a homogeneous bias field B_0 along $-y$ to the field created by a wire carrying a current along x. The axes of the resulting 2D quadrupole field form an angle of 45° with the z–axis.

A more complex layout is 12 b) [112]. Here, two wires carry parallel currents (which we will assume to be equal and denote by I). A bias field B_0 along y digs a trap into their magnetic field in much the same way as for the single–wire trap of fig. 12 a). The configuration can be operated in two regimes: $B_0 < B_{\text{crit}}$ and $B_0 > B_{\text{crit}}$, separated by a critical field $B_{\text{crit}} = \mu_0 I/(2\pi d)$.

For $B_0 = 0$, a quadrupole forms in the middle between the two wires. For increasing bias field, the quadrupole shifts up along z. At the same a second quadrupole forms far from the wires, where the field asymptotically looks like layout 12 a). At the critical field $B_0 = B_{\text{crit}}$, both quadrupoles coalesce, forming a hexapole minimum. For $B_0 > B_{\text{crit}}$, two quadrupoles form, which move towards the wires on the left and right half of a demicircle.

We note that this situation is symmetric. Applying a B_0 of opposite sign would create a rotation-symmetric version of the trap below the plane of the wires.

The layout of 12 c) allows to create a quadrupole field with axes parallel to the axes of the coordinate system. Applying a bias field B_0 along the z–axis creates two quadrupole traps on the z–axis. As in the layout 12 b), they approach each other when the bias

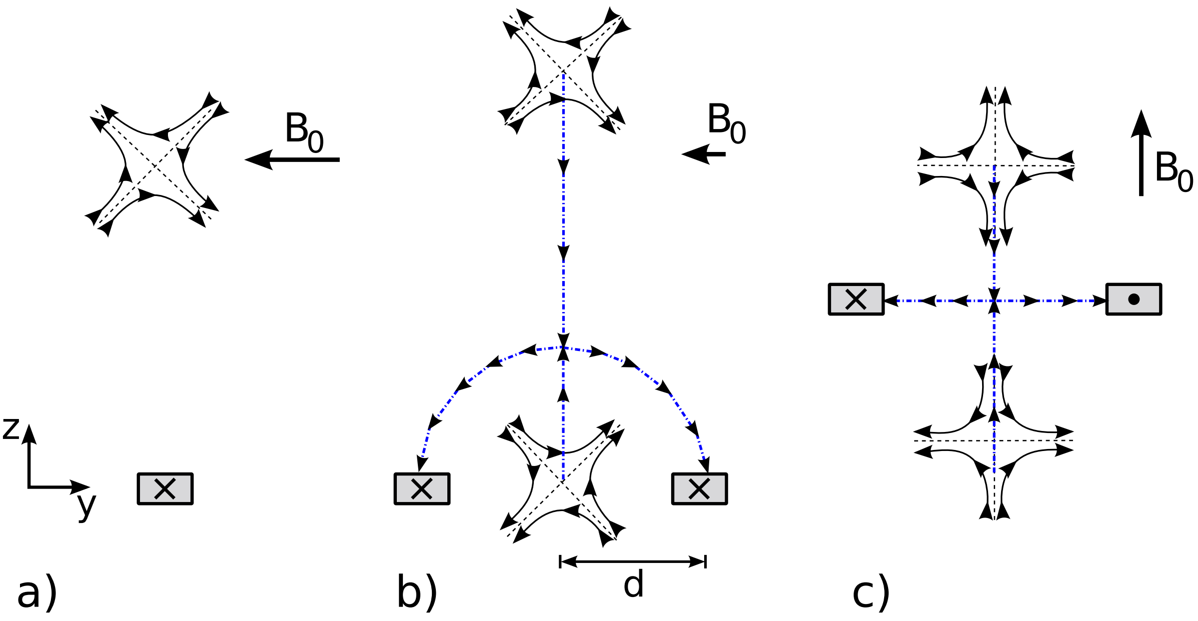

Figure 12: 2D trap layouts. Traps can be created by a single wire (a) or double–wire configurations carrying parallel (b) or antiparallel currents (c). The blue dash–dotted lines indicate the paths along which the quadrupole minima move for increasing bias field.

field is increased until they coalesce for a critical field B_{crit}. For fields $B_0 > B_{\mathrm{crit}}$, two quadrupoles form, approaching the two wires in the $z = 0$ plane.

As a rule of thumb, it is helpful to summarize figure 12 in the following way: A trap can be created over any wire of a chip [12 a)] and between any pair of wires [12b) and c)].

The configurations of fig. 12 create two essential building blocks, which we will frequently refer to in the following: (1) 2D quadrupole fields with axes aligned along the y and z–axes of the coordinate system (as in configuration 12 (c)). We will refer to them as an “upright quadrupole”. (2) 2D quadrupole fields, whose axes form an angle of 45° with the z–axis (such as 12 (a) or 12 (b) for $B_0 < B_{\mathrm{crit}}$). We will refer to them as “45°–rotated quadrupoles”.
This angle is somewhat arbitrary, since it depends on the orientation of the bias field. It turns out, however, that in most common trap layouts, the bias fields are chosen as in fig. 12, such that the configurations 12 (a) and (b) create indeed 45°–rotated quadrupoles. In the following, we will assume that these configuration always create this kind of field.

2.2.3 Crossing 2D quadrupole fields in 3D

So far, we have considered only 2D traps. Of course, a real–world trap must be three–dimensional. There is a straightforward way to achieve confinement in all three dimensions in chip traps: To cross orthogonal 2D traps.

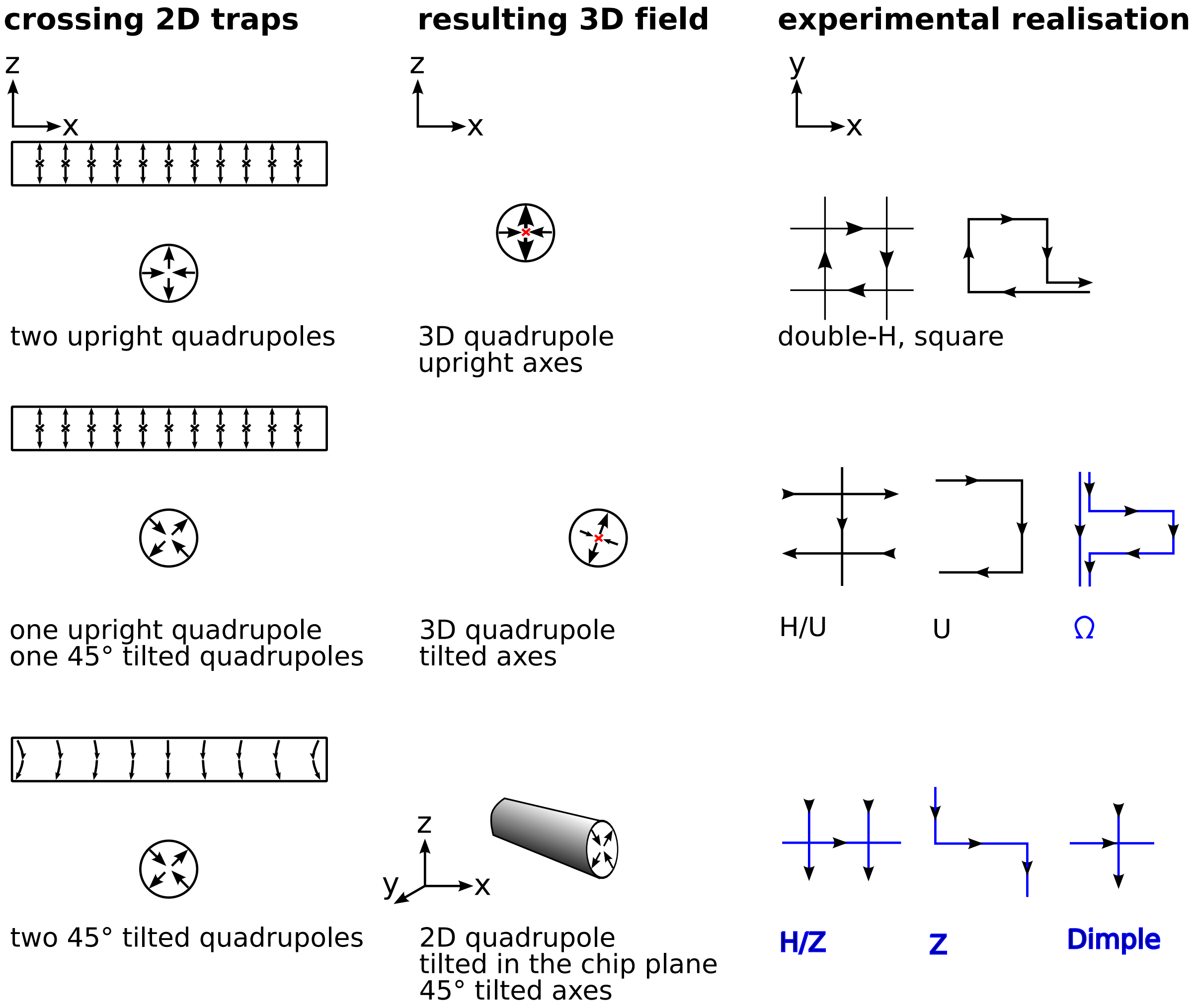

Figure 13: The common chip trap layouts (column "experimental realization") implement different layouts of figure 12. The resulting 2D quadrupole traps cross and give rise to various 3D fields. The layouts drawn in blue rely additionally on the hexapole component of the wire field to realize 3D confinement (see below).

In the previous paragraph, we have discussed several wire configurations to create two types of traps: 2D quadrupoles with upright axes and 2D quadrupoles with 45° rotated axes. Crossing these two types of traps gives rise to three elementary scenarios depicted in Figure 13. In two of these scenarios, the resulting field provides confinement in all three directions. In one scenario, the result is merely a tilted quadrupole. To close this trap, additional higher–order field components are needed, which we will discuss below (paragraph "hexapole contributions").

In terms of chip layout, six possible orthogonal crossings can be assembled from the three structures of fig. 12. We are aware of five of these structures being actually used in experiments. By far the most widespread ones are the "dimple" (a×a with the definitions of fig. 12), the "Z" (a × b) and the "U" (a× c). Some experiments also use the Ω (b× c) and the square (c×c).

In the following three paragraphs, we will discuss the field which arises from these quadrupole crossings. This is rather technical and provides no deeper insight than figure 13. If the idea is clear from this figure, we recommend to skip this part and proceed immediately to the paragraph "hexapole contributions"

For all the following considerations, we will assume that the zero line of the lower quadrupole lies in the $z = 0$–plane and the upper one in the $z = z_0$–plane. We will denote the gradients of the lower/upper quadrupole by B'_l and B'_u respectively and 3D–vectors by $\vec{x} = (x, y, z)$.

We emphasize the fact that all the following calculations deal with the crossing of **ideal** quadrupoles. They neglect higher-order multipole components, which are present in the 2D traps of Fig 12. The results are only valid in a region where both 2D trapping fields are predominantly quadrupolar.

Upright x Upright The theoretically simplest scenario consists in crossing two 2D quadrupoles with upright axes (first row in Fig. 13). The resulting field is

$$\begin{aligned}\vec{B}(\vec{x}) &= B'_l \begin{pmatrix} -x \\ 0 \\ z \end{pmatrix} + B'_u \begin{pmatrix} 0 \\ -y \\ z - z_0 \end{pmatrix} \\ &= B'_x \begin{pmatrix} x \\ 0 \\ 0 \end{pmatrix} + B'_y \begin{pmatrix} 0 \\ y \\ 0 \end{pmatrix} + B'_z \begin{pmatrix} 0 \\ 0 \\ (z - z'_0) \end{pmatrix}\end{aligned}$$

with

$$\begin{aligned} B'_x &= -B'_l; \qquad B'_y = -B'_u; \qquad B'_z = B'_u + B'_l \\ z'_0 &= z_0 \frac{B'_u}{B'_l + B'_u}. \end{aligned}$$

This field is a 3D quadrupole, whose axes are oriented along the axes of the coordinate system. This technique is used to create the 3D quadrupole field for micro-MOTs [113].

Upright x 45° **rotated** The second scenario consists in crossing two 2D quadrupoles, one of which has 45° rotated axes in the x–z–plane, the other one having upright axes in the y–z–plane (second row in Fig. 13). In this case, the exact expression of the resulting field is not particularly instructive. It can be shown that a 3D quadrupole field forms at the position

$$x = z_0 \frac{B'_u}{B'_l}; \qquad y = z = 0$$

with gradients

$$B'_1 = \frac{1}{2}(B'_u + \sqrt{B'^2_u + 4B'^2_l}); \qquad B'_2 = B'_u; \qquad B'_3 = \frac{1}{2}(B'_u - \sqrt{B'^2_u + 4B'^2_l})$$

The "2"-axis is the y–axis, the other axes lie in the x–z–plane, tilted against the z–axis by an angle

$$\alpha = \arctan\left(\frac{B'_3}{B'_l}\right)$$

This technique is widely used to create magnetic quadrupole traps and the quadrupole fields for mirror–MOTs.

At first sight, one might be tempted to classify also the Ω–trap as this type, which is used in another experiment of our group [14]. However, this trap operates in a regime of strong contribution of the hexapole component (see below), so that it creates a quadratic minimum rather than a quadrupole.

45° **rotated x** 45° **rotated** The third scenario consists in crossing two 2D quadrupoles, both of which have axes being 45° rotated with respect to the z–axis (as sketched in the lowest row of fig. 13). The sum of their fields is

$$\vec{B}(\vec{x}) = B'_l \begin{pmatrix} z \\ 0 \\ x \end{pmatrix} + B'_u \begin{pmatrix} 0 \\ z - z_0 \\ y \end{pmatrix}$$

It is clear that this field is nonzero everywhere. It forms a 2D quadrupole with a constant non–zero field perpendicular to the quadrupole axes. The quadrupole forms along the line

$$B'_l x + B'_u y = 0; \qquad z = \frac{B'^2_u}{B'^2_u + B'^2_l} z_0$$

The quadrupole axes are orthogonal to this line and rotated to the z–axis by 45°. Their gradients are

$$B'_{+/-} = \pm\sqrt{B'^2_l + B'^2_u}$$

This situation is found in the famous Z and dimple layouts. We note as a conclusion from the above reasoning that both the Z and dimple traps tilt in the x–y–plane. However, to create confinement in all three directions, these layouts rely on higher-order multipole contributions of the wire field. This mechanism will be the subject of the next paragraph.

2.2.4 Hexapole contributions

It is not clear, how the layouts of the lowest row of figure 13 can provide confinement in all three directions. The above reasoning cannot explain this, since we have only discussed quadrupole contributions so far. We have not yet used the degree of freedom of higher order field components. Indeed, it is these that are used to close the quadrupole tube in the last row of figure 13 and the following paragraphs will discuss, how this is done:

The 2D hexapole field To discuss higher-order multipole moments in chip traps we will start again by considering the 2D situation. The lowest-order magnetic minimum with vanishing first derivative is the 2D hexapole field [84]. In a coordinate system with vectors $\vec{x} = (x, z)$ it can be written as

$$\vec{B}_{\text{hex}}(\vec{x}) = B'' \begin{pmatrix} x^2 - z^2 \\ -2xz \end{pmatrix} \tag{21}$$

The only free parameters are the field curvature B'' and the orientation of the hexapole axis. For all further reasoning, we will assume the latter to be oriented along the x–axis. If a homogeneous field $B_x \vec{e}_x$ is added, the hexapole field remains a minimum, centered at the origin.

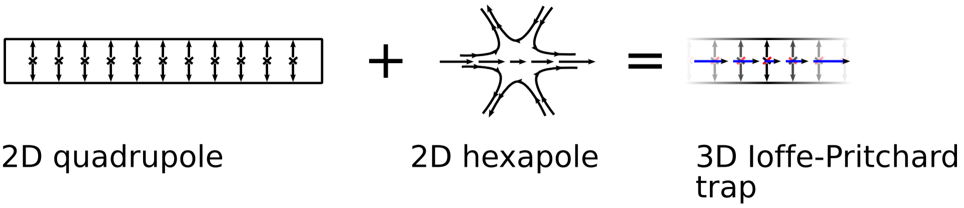

Figure 14: Superposing a 2D quadrupole field with an orthogonal 2D hexapole field creates a maximally asymmetric 3D Ioffe-Pritchard trap.

Superposing a 2D quadrupole with the hexapole field We will now discuss, how 3D confinement is obtained by adding this 2D hexapole field to another 2D trap in the orthogonal directions. Let us consider the situation of figure 14, where the field 21 is crossed with a 2D quadrupole with upright axes (along z and y, gradient B', its axis coinciding with the x–axis). The resulting field reads as follows (B_x being an arbitrary homogeneous field along the quadrupole tube):

$$\vec{B}(\vec{x}) = \begin{pmatrix} B_x & & +B''(x^2 - z^2) \\ & -B'y & \\ & +B'z & -2B''xz \end{pmatrix} \tag{22}$$

Expanding the magnitude of the resulting field around the origin yields

$$B(\vec{x}) = B_x + B''(x^2 - z^2) + \frac{B'^2}{2B_x}(y^2 + z^2) \tag{23}$$

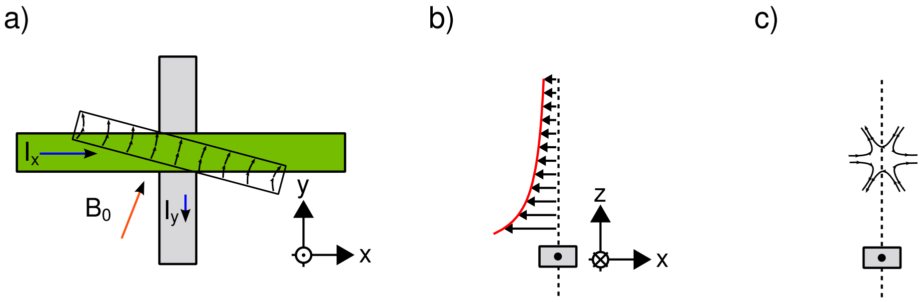

Figure 15: The dimple trap layout (a). Basically, each of the wires implements the single–wire trap (figure 12 a), The two resulting 2D quadrupoles cross (last line of figure 13) such that a tilted quadrupole tube forms above the wire crossing. For small I_y, its tilt is negligible and the tube is closed by the curvature of the field of the gray wire (b and c) in very much the same way as is shown in figure 14.

This field has a minimum of nonzero field at the origin and, provided that $B'' < B'^2/(2B_x)$, provides confinement in three directions. In every direction, the confinement is harmonic. By equation 17, a harmonic magnetic field $B = B''x^2/2$ with curvature B'' will create an equally harmonic potential $V(x) = m\omega^2x^2/2$ with trap frequency

$$\omega = \sqrt{\frac{g_F\, m_F\, \mu_B}{m} B''} \mathrel{\widehat{=}} 2\pi \cdot 9\text{Hz}\sqrt{B''/\left[10^6\text{G/m}^2\right]} \tag{24}$$

The numeric value is valid for ^{87}Rb in the trapped $m_F = \pm 1$ states.

The trap just discussed is a special case of the commonly used Ioffe–Pritchard trap. This trap crosses a 2D quadrupole with a 3D hexapole field, which allows to tune the field at the center and all three curvatures [84]. This is in contrast to the IP trap on a chip, which crosses the quadrupole with a **2D** hexapole field and where eq. 23 implies that only two curvatures and the field at the center can be chosen freely.

Experimental realization of the 2D hexapole field Experimentally, hexapole components are exploited in the Ω, H, Z and dimple layouts. They are present in the field of the longitudinally confining wires and can be used to close a quadrupole trap.

To see how this is done precisely, let us first consider the dimple trap as it is shown in figure 15. It consists of two crossed wires along x and $-y$ carrying currents I_x and I_y and two bias field $B_{0,x}$ and $B_{0,y}$ along x and y. To first order, this layout creates two crossing 2D quadrupoles (as in the last row of figure 13). The resulting field is thus a 2–dimensional quadrupole above the wire crossing, which is tilted in the x–y–plane Let us assume that the currents are chosen such that the quadrupole field of I_y is much weaker than the quadrupole created by I_x. The transverse confinement then arises basically from I_x and the quadrupole contribution of I_y merely tilts the resulting 2D quadrupole slightly in the x–y–plane.

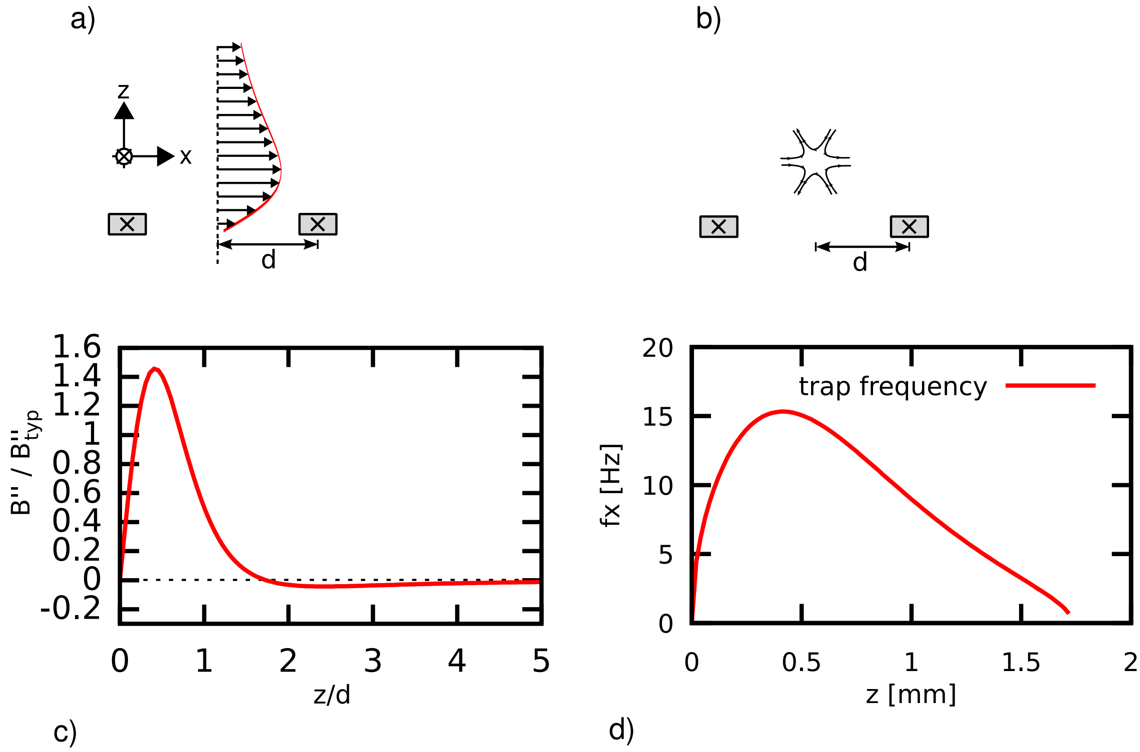

Figure 16: On the z–axis, the field of two parallel wires has a nonzero curvature $B'' = d^2B_x/dz^2$ (a). This is tantamount to saying that it has a nonzero hexapole component on the z–axis (b). (d) shows the curvature B'' on the z–axis between the parallel wires, normalized to $B''_{\text{typ}} = \frac{I\mu_0}{\pi d^3}$. (e) shows the resulting trap frequency $f_x = \omega_x/(2\pi)$ for ^{87}Rb in the trapped $m_F = \pm 1$ states, assuming $d = 1\text{mm}$ and $I = 1\text{A}$.

This quadrupole is converted into a Ioffe-Pritchard trap by exploiting the hexapole contribution of I_y. The field of I_y on the z–axis is directed along x and of magnitude

$$B_x(z) = -\frac{\mu_0 I_y}{2\pi z}.$$

It therefore has a curvature (i.e., a hexapole component) of strength

$$B''(z) = \frac{d^2B_x}{dx^2} = -\frac{d^2B_x}{dz^2} = \frac{\mu_0 I}{4\pi z^3} = 4\cdot 10^6 \frac{\text{G}}{\text{m}^2}\cdot\frac{I/\text{A}}{(z/\text{mm})^3} \tag{25}$$

and this hexapole component closes the quadrupole as has been demonstrated in figure 14.

The same mechanism is used in the Z and the H trap layouts. Here, the hexapole contribution is created by two wires along y, carrying parallel currents (figure 16). On the z–axis between the wires, their field has a nonzero curvature (i.e. a hexapole component) of strength

$$B''(z) = \frac{I\mu_0}{\pi}\frac{2z\,(z^2-3d^2)}{(d^2+z^2)^3} \tag{26}$$

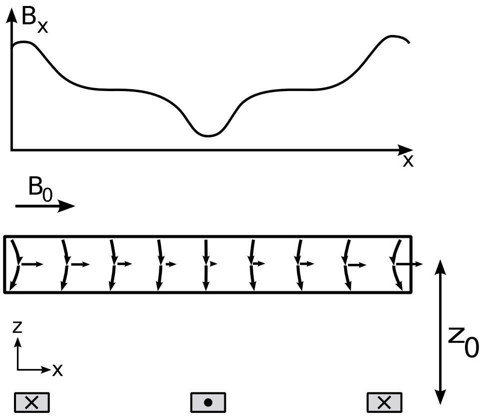

Figure 17: Limiting case of strong transverse confinement. The wires along y imprint a potential $V(x) = g_F m_F \mu_B |B_x(x)|$ on the axis of the 2D quadrupole.

A plot of this field curvature, along with the resulting trap frequency, is presented in figure 16 (c) and (d). The curvature has a maximum at $z/d = \sqrt{2} - 1$. It crosses zero at $z/d = \sqrt{3}$ and becomes negative for $z/d > \sqrt{3}$. To form a stable trap in this latter regime, a bias field along $-x$ has to be applied. This reverses the sign of the curvature, so that a stable trap can form. In this regime, the trap is effectively a dimple trap (see below), since, for $z \gg d$, the two wires asymptotically look like a single wire carrying a current $2I$.

Limit of strong transverse confinement A useful intuition for all traps of the lowest row of figure 13 can be obtained by considering the case of a 2D quadrupole along x, floating at a height z_0 above several wires, all of which run along y and which create a field $\vec{B}_w$. (Fig. 17). We will consider the limit that, at $z = z_0$, the gradient of the 2D quadrupole B'_u is much stronger than all gradients of $\vec{B}_w$. In particular, we assume $B'_u \gg dB_{w,z}/dx\big|_{(x,0,z_0)} \forall x$. In this case, the resulting field minimum will form on the line $(x, -B_{w,z}/B', z_0)$, but, because of the above condition, the tilt of the quadrupole is negligible. The magnetic field at its center is thus the x–component of the field of the crossing wires, creating a potential $V(x) = g_F m_F \mu_B |B_0 + B_{w,x}(x)|$. From an engineering perspective, the wires are a useful tool to “dig dimples” and “place endcaps” on the potential along x.

Nonperturbative situations The above reasoning relies on the expansion of the magnetic field into multipole contributions around the trap center. In regions far from the trap, especially near conductors, the field can deviate significantly from this approximation. The most important example of such a situation is a dimple trap, with both currents and bias fields being of the same size. In this case, the resulting trap is tilted by 45° and higher-order contributions bend it towards the chip in a ring-like manner [84].
During chip design, we numerically simulate the field generated by our chip.

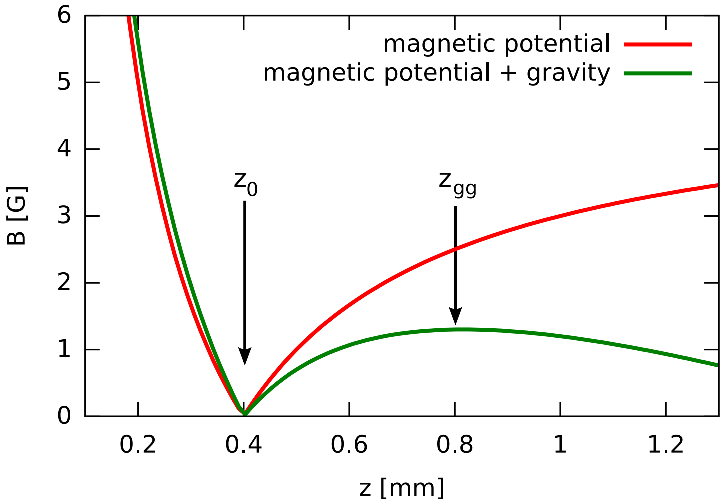

Figure 18: Trapping potential for the configuration of Fig 12 a), A current of $I = 3$A is placed at $z = 0$ and the trap is created by a bias field of $B_0 = 8$G. Gravity acts like an additional gradient, which severely alters the shape of the trap and reduces its depth.

2.2.5 Trap depth

The depth of a chip trap is the potential difference between the center of the trap and the highest barrier of the total trapping potential. This total potential includes not only the magnetic potential but also gravity. The latter significantly influences the trap depth, as we will now illustrate for the single–wire trap of Fig. 12 a). The potential energy landscape of this configuration is illustrated in fig. 18. In absence of gravity, the "highest barrier" is at infinity and the trap depth ΔE is defined by the bias field

$$\Delta E = g_F m_F \mu_B B_0 \overset{^{87}\text{Rb clock states}}{=} 33\mu\text{K} \cdot B_0/\text{G}$$

Gravity adds a potential gradient $dV/dz = -mgz$ which counteracts the magnetic confinement, since the chip is typically mounted upside–down. In this case, the highest barrier lies at a finite height z_{gg}, where the gravitational gradient is just canceled by the magnetic potential:

$$z_{gg} = \sqrt{\frac{m_F g_F \mu_B \mu_0 I}{4\pi m g}} \overset{^{87}\text{Rb clock states}}{=} 800\mu\text{m}\sqrt{\frac{\text{I}}{\text{A}}} \tag{27}$$

$$\frac{dB}{dz}\Big|_{z_{gg}} = \frac{mg}{g_F m_F \mu_B} \overset{^{87}\text{Rb clock states}}{=} 30\frac{\text{G}}{\text{cm}} \tag{28}$$

$$\Delta E = g_F m_F \mu_B B(z_{gg}) - mg(z_{gg} - z_0) \tag{29}$$

A quadrupole chip trap in presence of gravity is asymmetric, with gradients towards / away from the chip of $dV/dz = g_F m_F \mu_B |z - z_{gg}|\, dB/dz \pm mgz$.

The trap depth for a trap of given gradient grows with the current in the conductor. This becomes clear from considering the scaling transformation $I \to \lambda^2 I$, $B_0 \to \lambda B_0$.

Under this transformation $z_0 \to \lambda z_0$, but the gradient $dB/dz|_{z_0}$ is kept constant. The distance to the barrier grows linearly $z_{gg} - z_0 \to \lambda(z_{gg} - z_0)$, as does the magnetic field at the barrier $B(z_{gg}) \to \lambda B(z_{gg})$. Due to equation 28 this amounts to a higher trap depth.

Experimentally, trap depth is a concern mostly for weak traps with gradients of the order of the gravitational gradient. For these traps, a high–current conductor on the backside of the chip can create a deeper trap than a conductor on the chip.

2.3 Optimal loading of chip traps

In chip traps, nearly all the experimental cycle can be performed by adiabatic ramps between different traps. The only exception is the loading of the initial magnetic trap. Typically, this trap is charged from a cloud coming from a compressed MOT (cMOT), which has been further cooled by polarization gradient cooling ("optical molasses"). This cloud, which is not in thermal equilibrium, is captured by "building around" the initial chip trap. The cloud then thermalizes in the trap. The parameters of this initial chip trap must be chosen such as to make this transfer as adiabatic as possible. In this section, we will derive the optimal trap parameters for this task.

We will quantify adiabaticity by the increase of entropy of the cloud, between its value S_1 before the transfer and its value S_2 in the initial trap. With this definition, the optimal parameters for the initial chip trap are such that $\Delta S = S_2 - S_1$ is minimized.

This criterion merits a comment: Strictly speaking, the relevant figure of merit would be the phase space density $n\Lambda^3$ in the magnetic trap (with n being the number density and Λ the thermal deBroglie–wavelength). This, however, is directly related to the entropy per particle [114] by the relation

$$n\Lambda^3 = \exp\left[\frac{5}{2} + \gamma - \frac{S}{N}\right]$$

where γ is a constant characterizing the trap potential ($\gamma = 3/2$ for a harmonic trap, $\gamma = 3$ for a spherical quadrupole trap). For reasons to be discussed in section 2.3, the trap will always be adiabatically transformed to a final trap which is harmonic. The initial trap's γ therefore does not influence the peak density of this final trap and the adiabaticity of the loading process is fully characterized by the entropy $\frac{S}{N}$ in the initial magnetic trap.

1D case We will first study the 1D case of this problem for a harmonic trap and a quadrupole trap.

Let the trap have a potential $V(x, \lambda)$ with some adjustable parameter λ. Precisely, we will parametrize the harmonic trap by $V(x) = m(2\pi\lambda)^2 x^2/2$, λ being the trap frequency. The quadrupole trap will be parametrized by $V(x) = \lambda|x|$.

We will assume the initial cloud to be normally distributed, with a width σ in position space and a temperature T_1 in momentum space.

$$\rho_1(x, p) = \frac{1}{\sqrt{2\pi}\sigma} e^{-\frac{x^2}{2\sigma^2}} \cdot \frac{1}{\sqrt{2\pi m k_B T_1}} e^{-\frac{p^2}{2mk_B T_1}}$$

The validity of this assumption is not completely clear. At the center of a MOT, light pressure is so high that the core of the cloud has a constant rather than normally distributed density [115][116]. In the last phase of the compressed MOT, however, we attenuate the repumper laser to reduce the light pressure, so that this effect should not play a role and we will assume a normally distributed density, as has been done by previous authors [105]. A cloud with this distribution has a total energy and entropy

$$E_1 = \frac{k_B T_1}{2} \qquad S_1 = \frac{k}{2}\left(2 + \log\left(2\pi m k_B T_1\right) + \log\left(2\pi\sigma^2\right)\right)$$

Building up the initial trapping potential $V(x)$ transfers to the cloud an energy

$$\Delta E = \int_{-\infty}^{\infty} dp \int_{-\infty}^{\infty} dx \rho_1(x,p) V(x) \tag{30}$$

After the transfer, the cloud thermalizes in the trap at a new temperature T_2. In spite of $\Delta E > 0$, this temperature is not neccessarily higher than T_1. The reason is that the trapped gas has a different heat capacity than an untrapped gas.

This temperature is obtained by solving for T_2 the equation of energy conservation:

$$E_1 + \Delta E \overset{!}{=} E_2 = -\frac{d\log(Z_2)}{d(1/k_B T_2)}$$

where Z_2 is the partition function

$$Z_2(\lambda, T_2) = \int_\Gamma e^{-\frac{V(x,\lambda)}{k_B T_2} - \frac{p^2}{2mk_B T_2}} dx dp$$

The entropy can be calculated by

$$S_2(\lambda) = \frac{E_2}{T_2} + k_B \log(Z_2(\lambda, T_2))$$

and, subsequently, ΔS can be computed and minimized. The exact calculation is lengthy and we will not present it in detail. We find that for a transfer into an optimum harmonic trap

$$T_1 = T_2; \qquad \Delta S = 0; \qquad \lambda = \frac{1}{2\pi}\sqrt{\frac{k_B T_1}{m}}\frac{1}{\sigma}$$

a result, which has also been obtained in [105]. For the transfer into an optimal quadrupole trap, we find

$$T_1 = T_2; \qquad \Delta S > 0; \qquad \lambda = \sqrt{\frac{\pi}{2}}\frac{k_B T_1}{\sigma} \tag{31}$$

The salient conclusion is that the initial magnetic trap should be harmonic.

3D case It is straightforward to extend this calculation to a 3D trap for the special case that it is the linear sum of 1D traps and a density that factorizes into the different axes

$$V(\vec{x}) = V_x(x) + V_y(y) + V_z(z) \qquad \rho_1(\vec{x}) = \rho_{1x}(x)\rho_{1y}(y)\rho_{1z}(z)$$

In this case, the transfer is mode–matched, if it is mode–matched for each of the axes. The general 3D case is more difficult and best optimized experimentally.

Experimental values Expressing the above criteria in experimental units, mode–matching is achieved for a harmonic trap of

$$\omega = 50\text{Hz}\frac{\sqrt{T_1/10\mu\text{K}}}{\sigma/100\mu\text{m}}$$

and, for a quadrupole trap, an optimal (though not mode–matched) transfer is achieved for

$$\frac{dB}{dz} \overset{^{87}\text{Rb clock states}}{=} 38\frac{\text{G}}{\text{cm}} \cdot \frac{T_1/10\mu\text{K}}{\sigma/100\mu\text{m}}$$

Coming from the molasses, our atoms typically have a temperature of 10μK and are distributed in a cloud of $\sigma = 200\mu$m in all three directions. Using the above criteria, the transfer would be perfectly mode–matched for a harmonic trap of $\omega = 25$Hz and optimal (though not mode–matched) for a quadrupole trap of $dB/dz = 19$G/cm.

The latter is experimentally not achievable, since it is lower than the gravitational gradient (equation 28).

2.4 Orders of magnitude

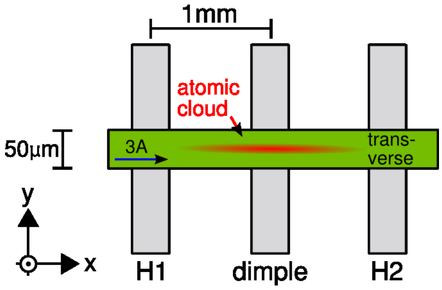

Figure 19: The canonical trap layouts of an atom chip. Transverse confinement (along y and z is created by a single–wire trap (green)). The resulting 2D quadrupole tube is closed by the curvature of a dimple wire (middle) or an H/Z configuration (H1 and H2). The numbers are order–of–magnitude values of our chip design.

To conclude and to prepare the following chapter, we will give some orders of magnitude for the traps which can be realistically realized on atom chips.

As we have shown, chip traps can produce two types of magnetic trap: quadrupole and

Ioffe–Pritchard traps. The usefulness of the former type is severely limited by an effect known as Majorana transitions: At the center of a quadrupole trap, the magnetic field vanishes and its orientation changes sign on an infinitsimally small length scale. An atom coming close to this center cannot adiabatically follow the orientation of the magnetic field and can undergo a nonadiabatic transition to an untrapped state.
The same process is also possible in Ioffe–Pritchard traps. Here, however, the magnetic field at the trap bottom B_0 has a nonzero and adjustable value, which can be chosen sufficiently high to suppress these transitions. $B_0 > 1G$ is a typical condition to lower these losses below the rate of background collisions [117]. Therefore, all traps in our experiment will be Ioffe–Pritchard traps satisfying this criterion.

To give orders of magnitude for this type of trap, we recall that the canonical way to produce a Ioffe–Pritchard trap on a chip is the one shown in figure 19: Transverse confinement is created by a simple wire trap and the resulting 2D quadrupole is closed to a Ioffe–Pritchard trap by the curvature of either a dimple wire or the H/Z layout. Typically, the longitudinal confinement (along x in fig. 19) is chosen much weaker than the transverse confinement (along y and z in fig. 19) $\omega_x \ll \omega_y, \omega_z$. In this situation, eq. 23 implies that the transverse frequencies are nearly equal

$$\omega_y \approx \omega_z = \frac{B'^2}{2B_0} \leq 10\text{kHz} = \omega_{\max}$$

where the inequality uses our typical experimental values ($B_0 = 1\text{G}$, $I = 3\text{A}$ in a wire of width $w = 50\mu\text{m}$). The longitudinal confinement is created by the curvature B'' of the field of the dimple or H/Z wires. An order of magnitude for the maximum confinement can be obtained from eqs. 25, 24. They state that the longitudinal confinement of a dimple trap can reach up to $\omega_x = 1\text{kHz}$ (assuming that the trap can approach the wire up to $50\mu\text{m}$).
The lowest possible trap frequencies are not limited by the layouts. To see this, we refer to fig. 16 (d) and note that even lower frequencies can be reached by lowering the current or increasing the spacing between the H/Z conductors. The lower limit of the trap frequency rather arises from the physical size of the cloud. As a rule of thumb, we do not want our clouds to exceed 5mm of length, which a cloud at 500nK would reach for trap frequencies below

$$\omega_{\min} = 0.5\text{Hz}$$

This limit is also useful to avoid two other difficulties, which become exceedingly critical in traps with sub-Hz frequencies: The time to adiabatically expand a cloud into a shallow trap grows quickly for decreasing trap frequencies. Furthermore, a cloud in a sub-Hz trap becomes exceedingly sensitive to vibrations, since the vibrational background is typically larger at low frequencies.

3 Theory of the atomic clock on a chip

This chapter can be seen as the synthesis of the two preceding ones: We discuss how a competitive compact atomic clock can be constructed using the atom chip technology and how its parameters must be chosen to achieve the best possible performance.

Naturally, atom chips have been considered as candidates for future compact atomic clocks immediately after they had come into existence (see, for example [118], the "News and Views" comment of R. Folman and J. Schmiedmayer on [8]). The implementation of such a chip clock, however, is not straightforward, since a magnetic trap is an inherently difficult environment for a clock medium. The magnetic trapping field and the mean–field potential of the atomic cloud both shift the clock transition of an atom, when it is immersed into the trap. If these shifts were constant, they would not be critical, at least not for a clock which serves as a secondary standard. *Variations* of these shifts, however, are critical. Variations in time directly transform into noise on the clock's frequency. Variations in space, in turn, lead to dephasing of the atomic sample, which limits the possible interrogation time.

Luckily, there exists a pair of hyperfine states, for which both states are magnetically trappable and all the mentioned shifts are sufficiently small [39]. This state pair is formed by the hyperfine states $|0\rangle = |F = 1, m_F = -1\rangle$ and $|1\rangle = |2, 1\rangle$ of ^{87}Rb. The magnetic moments of these states are equal to first order, so that they experience the same magnetic trapping potential. Moreover, their *transition frequency*, which is proportional to the *energy difference* between both states, is shifted by a magnetic field only to second–order. The mean–field shift, which arises from collisions in the atomic cloud, is also small for this state pair, since the inter– and intra–species scattering properties for both states are nearly equal. The immediate consequence is that a superposition of these states remains coherent for a long time, even in a magnetic trap. Indeed, coherence times up to 2.5s have been measured for this system [39].

The first atom chip experiment using this state pair, [29], used it as a probe for external sources of decoherence. In this experiment, the coherence between the states was found not to be compromised by the nearby surface of the atom chip, with coherence times of the order 2–3s even at micron distances from the chip. Running as a clock, the setup immediately reached a stability of $1.7 \times 10^{-11}\sqrt{\text{s}}$, allthough it had not been custom–built for this application.

The clock which we describe in this thesis is an extension of this work, intended to push this result into the commercially interesting $10^{-13}\sqrt{\text{s}}$ range. A conceptual view is presented in figure 20. It is proposed to work in the following way:
The interrogation is performed on a cloud of ^{87}Rb, either a cold thermal cloud or a condensate, which is held in a magnetic microtrap above an "atom chip". Initially, the sample will be prepared in the state $|0\rangle$. The clock transition is a two–photon transition between this state and the state $|1\rangle$. To coherently control this transition, we will couple a microwave and an RF signal to the chip, providing the two photons needed to excite the transition. By exposing the atoms to two subsequent $\pi/2$–pulses of this two–photon drive, we can perform a Ramsey interrogation of the mentioned transition in the magnetic trap. To read out the resulting population imbalance, we will perform a

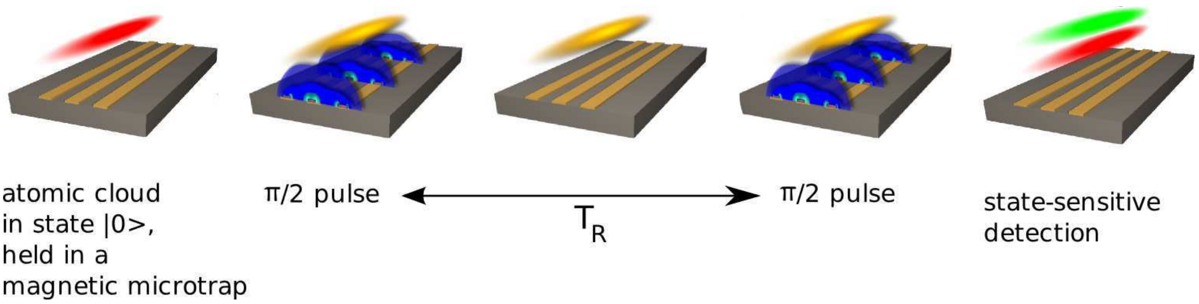

Figure 20: Atomic clock on a chip (conceptual): Atoms are held in a magnetic microtrap. A hyperfine transition between two trapped states is interrogated by a Ramsey scheme.

state–selective detection of the atomic clouds by absorption imaging on a CCD camera.

In this chapter, we will lay out in detail the theory of this atomic clock on a chip. We start in section 3.1 by discussing the laws which govern the evolution of the atomic cloud, for the case of a Bose–Einstein condensate and a thermal cloud. We then discuss the details of the interaction of the atoms with the static magnetic trapping field, the coupling to the excitation pulses and the collisions between atoms.
We subsequently make use of this theory in an analysis of the coherence time of an atom in our trap (section 3.2). Here, we propose a simple model of decoherence, which leads to a prediction of an optimum parameter set for a trap with a maximum coherence time. Finally, we develop another major result of this thesis in section 3.3 by predicting the stability budget of the proposed clock. Previous estimates [119][108] have taken into account noise of the magnetic field and of the number of atoms. We extend them by including phase and amplitude noise of the interrogation microwave as well as losses in the cloud.

3.1 Description of the system

3.1.1 Overview: global Hamiltonian, description of a BEC and a thermal cloud

As the previous paragraph, this subsection will describe the clock cycle, but in a quantitative way. We first introduce a global Hamiltonian of the system, describing the trap, interactions in the cloud and the excitation pulses. Afterwards, we discuss how the atomic cloud, either a BEC or a thermal cloud, evolves under this Hamiltonian during a clock cycle.

The global Hamiltonian Our system is most conviently described in the formalism of second quantisation: Let $\psi^\dagger_\alpha(\vec{x})$ and $\psi_\alpha(\vec{x})$ be creation and annihilation operators creating or annihilating an atom in the internal state $|\alpha\rangle$ (with $\alpha \in \{0,1\}$) at the position $\vec{x}$. They shall satisfy the bosonic commutation rule

$$[\psi_\alpha(\vec{x}), \psi^\dagger_\beta(\vec{x}')] = \delta^\beta_\alpha \delta(\vec{x} - \vec{x}'). \tag{32}$$

In this formalism, our system can be described by a global Hamiltonian [120, 121], which describes the magnetic trap, the interactions in the atomic cloud and the excitation pulses.

$$\begin{aligned}\hat{H} =&\hat{H}_0 + \hat{H}_{\text{int}} + \hat{H}_{\text{ex}} = \\ &\int_V d^3\vec{x} \sum_\alpha \psi^\dagger_\alpha(\vec{x}) \left(-\frac{\hbar^2\nabla^2}{2m} + V_\alpha(\vec{x}) + \alpha\hbar\Delta_{01}\right)\psi_\alpha(\vec{x})+ \\ \frac{2\pi\hbar^2}{m}&\int_V d^3\vec{x} \sum_{\alpha,\beta} a_{\alpha\beta}\psi^\dagger_\alpha(\vec{x})\psi^\dagger_\beta(\vec{x})\psi_\alpha(\vec{x})\psi_\beta(\vec{x})+ \\ &\int_V d^3\vec{x} \sum_{\alpha\neq\beta} \frac{\hbar\Omega_{\alpha\beta}(\vec{x})}{2} f(t)\psi^\dagger_\alpha(\vec{x})\psi_\beta(\vec{x})\end{aligned} \tag{33}$$

Each of the terms of this Hamiltonian will be discussed in a subsection of its own in the following. For the present discussion, we only make the most essential comments:

$\hat{H}_0$ is a single–particle Hamiltonian describing the motion of each atom in the trapping potential $V_\alpha(\vec{x})$. This trapping potential is state–dependent (index α) and slightly different for both clock states, due to the second–order Zeeman shift. We operate the clock at parameters where the difference is small ($V_1 - V_0 \ll V_\alpha$). Neglecting this difference, the potential for both clock states in our experiment is a three–dimensional harmonic trap of the form

$$V_\alpha(\vec{x}) = \frac{m}{2}(\omega_x^2 x^2 + \omega_y^2 y^2 + \omega_z z^2) - mgz. \tag{34}$$

characterized by the three trap frequencies $\omega_x, \omega_y, \omega_z$.
The term $\alpha\hbar\Delta_{01}$ accounts for the hyperfine splitting between the states $|0\rangle$ and $|1\rangle$. We have adopted the convention that $\psi_\alpha(\vec{x}), \psi^\dagger_\alpha(\vec{x})$ annihilate and create atoms in the rotating frame of the interrogation microwave (see chapter 1, eqs. (1) ff.). In this frame, the hyperfine splitting is reduced to $\hbar\Delta_{01} = \hbar(\omega_{\text{at}} - \omega_{\text{fw}})$, the detuning between the flywheel signal and the atomic resonance.

$\hat{H}_{\text{int}}$ describes the elastic collisions of atoms in the trapped cloud. Elastic collisions of cold bosonic atoms are commonly described by a contact potential $V_{\text{int}}(\vec{x} - \vec{x}') = \frac{4\pi\hbar^2}{m} a_S \delta(\vec{x} - \vec{x}')$ where the strength of the interaction is characterized by the s–wave scattering length a_S [122, 123, 124]. H_{int} is the second–quantized version of this potential. For our system, there are three possible types of elastic collisions, between pairs of atoms in the respective internal states ($|0\rangle$, $|0\rangle$), ($|0\rangle$, $|1\rangle$) and ($|1\rangle$, $|1\rangle$). This leads to three contributions to $\hat{H}_{\text{int}}$, characterized by three scattering lengths $a_{00}, a_{01} = a_{10}$ and a_{11}.

$\hat{H}_{\text{ex}}$, finally, describes the interaction of the atoms with the excitation pulses driven from the flywheel. The excitation signal coherently transfers atoms between the states $|0\rangle$ to $|1\rangle$ with a Rabi frequency $\Omega_{01} = \Omega^*_{10}$ and this transfer is switched on in pulses, which we describe by an envelope function $f(t)$.

Bose–Einstein condensate Let us now turn to the question how the atomic cloud evolves under the Hamiltonian (33). This is most transparent for the case that the cloud forms a Bose–Einstein condensate, which happens for sufficiently low temperatures

$k_B T \ll \hbar\bar{\omega}N^{1/3}$, with $\bar{\omega} = (\omega_x\omega_y\omega_z)^{1/3}$ being the harmonic mean of the trap frequencies. In this paragraph, we assume this condition to be fulfilled and discuss the evolution of a condensate over a cycle of our clock.

Generally, a BEC of our clock states is a two–component condensate, with each of the clock states $|0\rangle, |1\rangle$ being described by a position– and time–dependent macroscopic wavefunction ψ_0, ψ_1, which is related to the density of the cloud by $n_\alpha(\vec{x}) = |\psi_\alpha(\vec{x})|^2$. It is instructive to express the wavefunctions in polar coordinates $\psi_\alpha = |\psi_\alpha|e^{i\phi_\alpha}$. This is the hydrodynamic picture ([125], chapter 7.1.1) where the wavefunctions are interpreted as two superfluid quantum liquids with amplitudes $|\psi_\alpha|$ and phases ϕ_α. This picture is particularly suited for the study of our clock, since, as we shall see, the clock signal is precisely the differential phase $\phi_1 - \phi_0$.

The time evolution of these wavefunctions is goverened by the Hamiltonian (33), which in this description turns into the coupled Gross–Pitaevski equations [122, 126]

$$i\hbar\partial_t\psi_0 = \left[\frac{\hbar^2\nabla^2}{2m} + V_0 + \frac{4\pi\hbar^2}{m}\left(a_{00}|\psi_0|^2 + a_{01}|\psi_1|^2\right)\right]\psi_0 + \frac{\hbar\Omega_{01}}{2}f(t)\psi_1 \tag{35}$$

$$i\hbar\partial_t\psi_1 = \left[\frac{\hbar^2\nabla^2}{2m} + V_1 + \hbar\Delta_{01} + \frac{4\pi\hbar^2}{m}\left(a_{01}|\psi_0|^2 + a_{11}|\psi_1|^2\right)\right]\psi_1 + \frac{\hbar\Omega_{01}^*}{2}f(t)\psi_0.$$

Before the first $\pi/2$ pulse all atoms are prepared internally in the state $|0\rangle$ and externally in some condensate wavefunction ψ so that $\psi_0 = \psi, \psi_1 = 0$. Typically, ψ is a Thomas–Fermi distribution [105]

$$\psi(\vec{x}) = \max[(\mu - V(\vec{x}))/U_0, 0]^{1/2}. \tag{36}$$

with $U_0 = 4\pi\hbar^2 a_{00}/m$ and μ being the chemical potential. This distribution is only an approximation, which requires that $U_0 n \gg \hbar\omega_{x,y,z}$. Our typical traps have densities in the range $\langle n\rangle \approx 10^{14} - 10^{15}\text{cm}^{-3}$. This implies that the approximation is fulfilled for trap frequencies $\omega \ll 2\pi \cdot 750\text{Hz}$.

The first $\pi/2$ pulse transfers this density coherently to the state $|1\rangle$. For a real and spatially homogeneous Rabi frequency Ω_{10} the resulting wavefunctions read

$$\psi_0 = -i\psi_1 = \psi/\sqrt{2} \tag{37}$$

with ψ being the wavefunction of the condensate before the $\pi/2$ pulse.

Between the $\pi/2$ pulses both wavefunctions evolve freely. We will postpone the discussion of this evolution and first complete the review of the clock cycle by discussing the effect of the second $\pi/2$ pulse. This second pulse closes the interferometer and maps the differential phase $\phi_1 - \phi_0$ to a measurable signal, the population inversion between both clock states. To see this quantitatively, let us assume it to take place on a much faster timescale than the evolution of ψ_α and denote by t_- an instant just before and by t_+ an instant just after this pulse. The pulse remixes both spin components, leading to new wave functions

$$\begin{pmatrix}\psi_0\\ \psi_1\end{pmatrix}(t_+) = \frac{1}{\sqrt{2}}\begin{pmatrix}1 & i\\ i & 1\end{pmatrix}\cdot\begin{pmatrix}\psi_0\\ \psi_1\end{pmatrix}(t_-).$$

These new wavefunctions can be seen as an interference between the wavefunctions before the pulse. Consequently, their amplitude contains information about the differential phase $(\phi_1 - \phi_0)$ before the pulse.

$$|\psi_0|^2(t_+) = \left[(|\psi_0|^2 + |\psi_1|^2)/2 + |\psi_0||\psi_1|\sin(\phi_1 - \phi_0)\right](t_-)$$

This differential phase $\phi_1 - \phi_0$ is the most essential result of a clock measurement. We will now study, how this phase evolves between the two $\pi/2$ pulses. Basically, its evolution is governed by eq. (35), which can be rephrased in the hydrodynamic picture as ([125], eqs. 7.18,7.19)

$$\begin{aligned}
\frac{\partial(|\psi_\alpha|^2)}{\partial t} &= -\frac{\hbar}{m}\nabla\cdot(|\psi_\alpha|^2\nabla\phi_\alpha) \\
-\hbar\frac{\partial\phi_0}{\partial t} &= -\frac{\hbar^2}{2m|\psi_0|}\nabla^2|\psi_0| + \frac{\hbar^2}{2m}(\nabla\phi_0)^2 + V_0 + \frac{4\pi\hbar^2}{m}(a_{00}|\psi_0|^2 + a_{01}|\psi_1|^2) \qquad (38) \\
-\hbar\frac{\partial\phi_1}{\partial t} &= -\frac{\hbar^2}{2m|\psi_1|}\nabla^2|\psi_1| + \frac{\hbar^2}{2m}(\nabla\phi_1)^2 + V_1 + \hbar\Delta_{01} + \frac{4\pi\hbar^2}{m}(a_{01}|\psi_0|^2 + a_{11}|\psi_1|^2)
\end{aligned}$$

Immediately after the first $\pi/2$ pulse, both wavefunctions are equal (eq. 37). We can therefore assume $|\psi_1|^{-1}\nabla^2|\psi_1| \approx |\psi_0|^{-1}\nabla^2|\psi_0|$ and $(\nabla\phi_1)^2 \approx (\nabla\phi_0)^2$, so that the differential phase $\phi_1 - \phi_0$ evolves at a rate

$$\begin{aligned}
\omega_{01} &= \partial_t(\phi_0 - \phi_1) \\
&= \Delta_{01} + (V_1 - V_0)/\hbar + \frac{4\pi\hbar}{m}(a_{11}|\psi_1|^2 - a_{00}|\psi_0|^2 + a_{01}(|\psi_0|^2 - |\psi_1|^2)) \\
&= \Delta_{01} + (V_1 - V_0)/\hbar + \frac{2\pi\hbar}{m}n((a_{11} - a_{00}) + f(2a_{01} - a_{11} - a_{00})) \qquad (39) \\
&= \Delta_{01} + (V_1 - V_0)/\hbar + \delta\omega_{\mathrm{mf}} \\
&= \Delta_{01} + \delta\omega.
\end{aligned}$$

Here, we have introduced the density $n = |\psi_0|^2 + |\psi_1|^2$, the population inversion $f = (|\psi_0|^2 - |\psi_1|^2)/n$ and $\delta\omega_{\mathrm{mf}}$ as an identifier for the mean–field shift.
Let us interpret this result: In the limit of equal wavefunctions considered here, the cloud can be considered as being composed of stationary atoms, with a locally different phase difference $\phi_1 - \phi_0$, which precesses at a locally different rate ω_{01}. This rate contains the clock signal Δ_{01}, but also a position–dependent clock shift $\delta\omega$, which arises from the differential Zeeman shift $(V_1 - V_0)/\hbar$ and the mean–field shift $\delta\omega_{\mathrm{mf}}$

Of course, we have to question the validity of the approximation made above. Stated more precisely, it must read $\hbar/(2m)||\psi_1|^{-1}\nabla^2|\psi_1| - |\psi_0|^{-1}\nabla^2|\psi_0|| \ll \delta\omega$ and $\hbar/(2m)|(\nabla\phi_1)^2 - (\nabla\phi_0)^2| \ll \delta\omega$. As stated above, it is well fulfilled immediately after the first Ramsey pulse of our clock. It breaks down after some time, however, if the clock shift $\delta\omega$ is position–dependent. Then, the phase variation $\phi_1 - \phi_0$ grows locally different according to eq. (39) and develops a gradient $\nabla(\phi_1 - \phi_0)$. This gradient drives a separation of the atomic species, a process known as "demixing". This can be understood from an energy perspective: A non–vanishing clock shift $\delta\omega$ means that the effective trapping potential, including the mean–field shift, is different for both states, so it is energetically favourable to separate them.

In previous studies on mixed condensates of our clock states [36, 126], the system demixed on a timescale of < 100ms after the first $\pi/2$ pulse. These studies, however, have been conducted in a parameter region with a large clock shift $\delta\omega$. We will take care to run our clock at parameters which lead to a minimum $\delta\omega$, in order to suppress dephasing due to a varying clock shift. We estimate that demixing appears on a similar or slightly longer timescale as dephasing, since the emergence of a spatially varying phase is the precursor of a spatially varying density. By this argument, demixing should not appear in a clock, since the interrogation time is neccessarily lower than the dephasing–limited coherence time.

Thermal cloud of classical particles Let us now consider the case that the clock is operated on a thermal cloud, whose temperature T is sufficiently high that $\lambda_{\mathrm{db}} = \sqrt{2\pi\hbar^2/(mk_BT)} \ll a_{\mathrm{ho}} = \sqrt{\hbar/(m\omega)}$, but sufficiently low that $k_BT \ll \hbar\omega_{\mathrm{at}}$. In this situation, an atom can be treated semiclassically, by describing its external degrees of freedom as a classical particle with well–defined position and momentum $(\vec{x}, \vec{p})$ and treating the internal degrees of freedom as a quantum–mechanical two–level system. The Hamiltonian (33) then has the following meaning: The term H_0 describes the oscillation of this classical particle in the harmonic trapping potential $V_\alpha(\vec{x})$. H_{ex} allows to prepare the internal degree of freedom in an arbitrary coherent superposition of $|0\rangle$ and $|1\rangle$ and we will show later (sec. 3.1.3) that this manipulation can be assumed not to affect the classical motion. As for the condensate, the terms $V_1 - V_0$ and H_{int} lead to a position–dependent "clock shift", which renders the transition frequency position–dependent

$$\begin{aligned}\omega_{01}(\vec{x}) &= \Delta_{01} + \delta\omega \\ &= \Delta_{01} + (V_1 - V_0)/\hbar + \delta\omega_{\mathrm{mf}}(n(\vec{x}), f(\vec{x}))\end{aligned} \tag{40}$$

Here, $\delta\omega_{\mathrm{mf}}$ is the mean–field shift, arising from collisions of the atom with the surrounding cloud. It depends on the local density of the cloud n and the population inversion $f = (n_0 - n_1)/n$ by a relation, which we will derive in section 3.1.4

$$\delta\omega_{\mathrm{mf}} = \frac{4\pi\hbar}{m} n((a_{11} - a_{00}) + f(2a_{01} - a_{11} - a_{00})) \tag{41}$$

The study of the phase accumulated by one atom is complicated by two facts: An atom oscillates classically in the potential and therefore explores different regions with different local clock shifts (41). Furthermore, the combined external and internal dynamics of the atoms leads to an evolution in time of n and f. A number of models have been proposed to quantitatively describe the effect of these dynamics on the atomic density, population inversion and coherence [127, 121]. Here, we only summarize the evolution of n and f for the case of our clock.

Immediately after the first $\pi/2$ pulse, the atoms thermally populate the potential (34), which results in a density

$$n(\vec{x}) = n_0 e^{-\frac{V(\vec{x})}{k_BT}}.$$

Internally, all atoms are prepared in a coherent superposition $(|0\rangle + e^{i\phi}|1\rangle)/\sqrt{2}$, so f=0. As for the condensate, a spatially inhomogeneous clock shift $\delta\omega$ can separate the two hyperfine species. This can happen even for $\hbar\delta\omega \ll k_B T$, in a process known as "spin waves" [119, 38, 127]. In such a spin wave, the populations n_0 and n_1 separate in an oscillatory manner, leading to a position–dependent and oscillating f. This process is only present when both the inhomogeneity of the clock shift and the density exceed a critical amount [37]. For this reason, this effect will not play a role in our clock: As we will discuss in the following sections, we will take care to operate the atomic clock at parameters where $\delta\omega$ is minimal, in order to minimize the dephasing caused by a varying frequency shift. We will also operate it at lower densities than in [37], in order to reduce noise produced by a fluctuating mean–field shift. Both choices should also suppress spin waves.

3.1.2 Interaction with the trapping field

We now turn to a detailed discussion of each contribution to the Hamiltonian (33). We start by the single–particle Hamiltonian

$$\hat{H}_0 = \int_V d^3\vec{x} \sum_\alpha \psi^\dagger_\alpha(\vec{x}) \left(-\frac{\hbar^2\nabla^2}{2m} + V_\alpha(\vec{x}) + \alpha\hbar\Delta_{01} \right) \psi_\alpha(\vec{x}).$$

Here, we will neither discuss the kinetic energy term $-\hbar^2\nabla^2/[2m]$, nor the hyperfine splitting Δ_{01}, but focus instead on the origin of the trapping potential $V_\alpha(\vec{x})$. The origin of this potential is the interaction of the atoms with the magnetic trapping field $B(\vec{x})$, which we will now discuss in detail.

Eigenstates and –energies of an atom in a magnetic field A magnetic field couples to an atom by the spins of the valence electron and the nucleus and the angular momentum of the valence electron. This coupling competes with the mutual interactions between these spins, which are independent of the magnetic field. Therefore, both the atomic eigenstates and –energies are a function of the magnetic field, which we will discuss in the following.

Both of our clock states belong to the $5S_{1/2}$ ground state of ^{87}Rb. This state is characterized by $L = 0, J = S = 1/2, I = 3/2$, where S is the spin of the valence electron, L is its angular momentum and I is the spin of the nucleus. The Hamiltonian of this ground state is a sum of the hyperfine coupling (magnetic coupling between J and I) and the interaction with the magnetic field:

$$\hat{H} = \hat{H}_{\text{hfs}} + \hat{H}_B = A_{\text{hfs}} \hat{\vec{J}} \cdot \hat{\vec{I}} + \frac{\mu_B}{\hbar} \left(g_J \hat{J}_z + g_I \hat{I}_z \right) \cdot B \tag{42}$$

Here, A_{hfs} is the hyperfine coupling parameter, g_I is the coupling constant of the nucleus and g_J the coupling constant of the valence electron. All of them are constants of the ^{87}Rb atom. We have assumed the magnetic field to be oriented along the z–direction, $\vec{B} = B\vec{e}_z$.

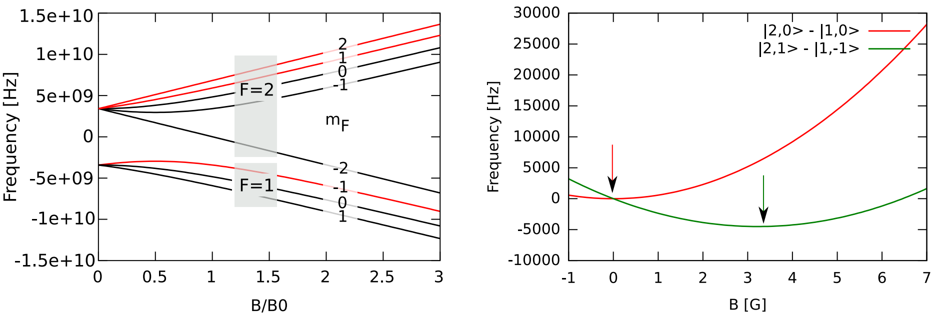

Figure 21: Left: Eigenenergies of the ^{87}Rb atom, calculated as a function of the magnetic field with the Breit–Rabi formula (eq. (43)). Red lines indicate the magnetically trappable states. The numeric values for all coupling constants have been taken from [129]. Right: frequency shifts of the $|2,0\rangle - |1,0\rangle$ and $|2,1\rangle - |1,-1\rangle$ transitions as a function of the magnetic field. The arrows indicate the "sweet spots", where the frequency is to first order insensitive to fluctuations of the magnetic field.

The eigenstates and eigenenergies of the Hamiltonian (42) are best understood by considering the limiting regimes of dominating H_{hfs} or dominating H_B, which are characterized by B and separated by a critical $B_0 = 2A_{\text{hfs}}/(g_J \mu_B) \approx 2\text{kG}$.
If the magnetic coupling is small against the hyperfine splitting, $B \ll B_0$, the dominating term in equation (42) is $\hat{H}_{\text{hfs}}$, whose eigenstates are the eigenstates $|F, m_F\rangle$ of the total angular momentum $\hat{\vec{F}} = \hat{\vec{J}} + \hat{\vec{I}}$, which can take the quantum numbers $F = 1, 2$, $m_F = F, F-1, \ldots, -F$.
For increasing fields, these states adiabatically transform into the eigenstates of H_B, which are the eigenstates $|J, m_J, I, m_I\rangle$ of the angular momenta of the electron and the nucleus. Consequently, these states are the eigenstates of the system for $B \gg B_0$.

To determine the crossover between these regimes, the Hamiltonian (42) can be analytically diagonalized, resulting in the Breit–Rabi–formula [128], which describes the atomic eigenenergies as a function of the magnetic field. For the case of ^{87}Rb, it reads

$$E_{F,m_F}(B) = g_I \mu_B m_F B \pm A_{\text{hfs}} \left(1 + m_F x + x^2\right)^{1/2} \tag{43}$$

where $x = (g_J - g_I)\mu_B B/(2A_{\text{hfs}})$. The "+" sign applies to the $F = 2$ manifold and the "−" sign to $F = 1$ and the special case ($m_F = 2$ and $x > 1$). We have labeled the eigenenergies by the quantum numbers F, m_F, even though the $|F, m_F\rangle$ states are eigenstates of the atom only for small magnetic fields.

A plot of the resulting eigenenergies is presented in figure 21. In a typical atom chip experiment, only the region of low fields is attainable. Here, four states are low–field–seekers, which can be magnetically trapped: $|2,2\rangle, |2,1\rangle, |1,-1\rangle$ and $|2,0\rangle$. The last one, however, depends too weakly on the magnetic field to be of any practical use. These field–dependent eigenenergies are precisely the potential of our clock states $V_0(B) = E_{|1,-1\rangle}(B), V_1(B) = E_{|2,1\rangle}(B)$.

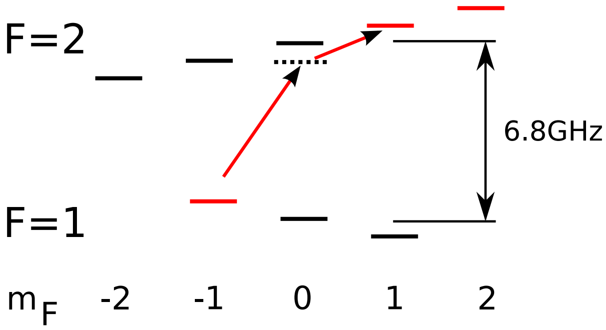

Figure 22: Hyperfine states in presence of a low magnetic field. Magnetically trapped states are drawn in red. The red arrows indicate the two–photon transition addressing our clock state pair.

Zeeman shift of the transition frequency between different states The choice of our state pair $|0\rangle = |1, -1\rangle$ and $|1\rangle = |2, 1\rangle$ is motivated by the fact that there exists a "sweet spot" at the "magic field" $B_m = 3.23\text{G}$, where the transition frequency between the states is to first order insensitive to magnetic field fluctuations (see figure 22). In the vicinity of this value, it varies quadratically,

$$\Delta f_{|1\rangle - |0\rangle} = \frac{V_1(B) - V_0(B)}{2\pi\hbar} = \Delta f_0 + \beta(B - B_m)^2. \tag{44}$$

with $B_m = 3.22892\text{G}$, $\Delta f_0 = -4497.3\text{Hz}$, $\beta = 431.3596\text{Hz/G}^2$ [39, 37]. Notice, however, that only the **difference frequency** varies quadratically. Each individual state shifts linearly by $\Delta E \approx B\mu_B/2$, rendering it magnetically trappable.

At low magnetic fields, the hyperfine structure contains one more sweet spot, for the state pair $|2, 0\rangle$–$|1, 0\rangle$ at $B_{m,0-0} = 0$. Conventional microwave atomic clocks, such as Rb fountain clocks, use this state pair and operate near this field. The 2nd–order Zeeman shift for this state pair $\beta_{0-0} = 575\text{Hz/G}^2$ is slightly stronger than for our state pair. This inconvenient is outweighed by the fact that the states are linked by a one–photon transition and that a low magnetic field is experimentally easier to control.

3.1.3 Interaction with the excitation pulses

We will now discuss in detail the last term $\hat{H}_{\text{ex}}$ of the Hamiltonian (33), which we will express for the following discussion in first quantization

$$\hat{H}_{\text{ex}} = \int_V d^3\vec{x} \sum_{\alpha \neq \beta} \frac{\hbar\Omega_{\alpha\beta}(\vec{x})}{2} f(t)\psi^\dagger_\alpha(\vec{x})\psi_\beta(\vec{x}) = \frac{\hbar\Omega_{10}(\hat{\vec{x}})}{2} f(t)|1\rangle\langle 0| + h.c. \tag{45}$$

This subsection discusses two major topics: Firstly, the coherent coupling Ω_{10} between our clock states $|0\rangle = |1, -1\rangle, |1\rangle = |2, 1\rangle$ actually arises from a two–photon transition. We couple a microwave and a RF photon to the atoms, which together link the two clock states, resonantly enhanced by either the $|2, 0\rangle$ or the $|1, 0\rangle$ state. We review the

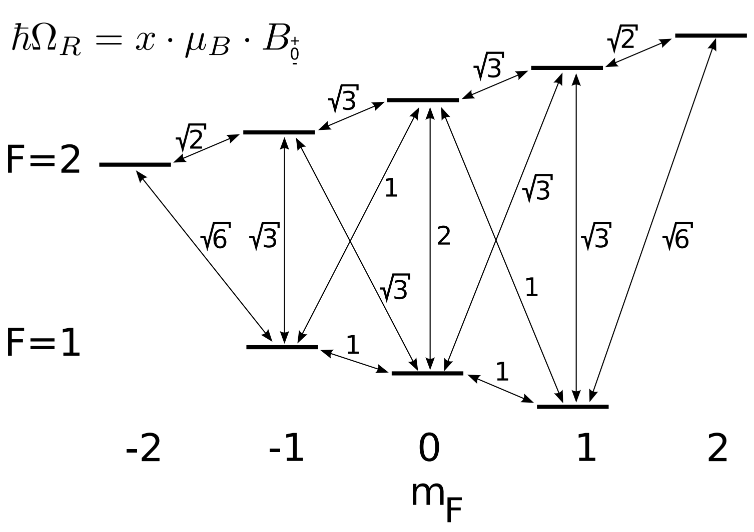

Figure 23: Strengths of the magnetic dipole transitions in the ^{87}Rb ground state manifold. $B_{+,0,-}$ refers to the amplitude of the co–rotating $+, 0, -$–component of the B–field: $\vec{B}(t) = \sum_{q=(+,0,-)} B_q \vec{e}_q e^{i\omega t} + h.c$, where $\vec{e}_q$ are the unit vectors of the spherical basis $\vec{e}_\pm = (\vec{e}_x \pm i\vec{e}_y)/\sqrt{2}$, $\vec{e}_0 = \vec{e}_z$.

theory of two–photon transitions and compute the effective two–level coupling Ω_{10}. Secondly, the coupling Ω_{10} is in general complex and position–dependent in both amplitude and phase, since the size of atomic cloud is comparable to the wavelength and dimensions of the excitation field. We discuss the effect of such an inhomogeneous excitation on the motional state of the atoms and the coherence of the atomic cloud.

Dipole matrix moments in the ground state manifold The hyperfine states of the $5S_{1/2}$ ground state manifold are linked by magnetic dipole transitions, as can be seen from the fact that the coupling Hamiltonian $\hat{H}_B$ of eq. (42)

$$\hat{H}_B = \frac{\mu_B}{\hbar}\left(g_I \hat{\vec{I}} + g_J \hat{\vec{J}}\right)\vec{B} \approx \frac{g_J \mu_B}{\hbar}\vec{B} \cdot \hat{\vec{J}} \tag{46}$$

has non–vanishing matrix elements $\langle F', m_F'|\hat{H}_B|F, m_F\rangle$ between the low–field atomic eigenstates $|F, m_F\rangle$. To describe transitions between these states, we employ the theory of section 1.1.1. To this end, we assume $\vec{B}(t)$ in eq. (46) to be time–harmonic $\vec{B}(t) = \vec{B}_0 e^{i\omega t} + h.c.$. Writing out eq. (46) in the $|F, m_F\rangle$ basis and identifying the result with equation (1), we obtain the Rabi frequency

$$\hbar\Omega_I = \frac{2 g_J \mu_B}{\hbar}\vec{B}_0 \cdot \langle F', m_F'|\hat{\vec{J}}|F, m_F\rangle \tag{47}$$

The matrix element $\langle F', m_F'|\hat{\vec{J}}|F, m_F\rangle$ can be calculated analytically analogous to the calculation of the electric dipole matrix moment for optical transitions [129]. Alterna-

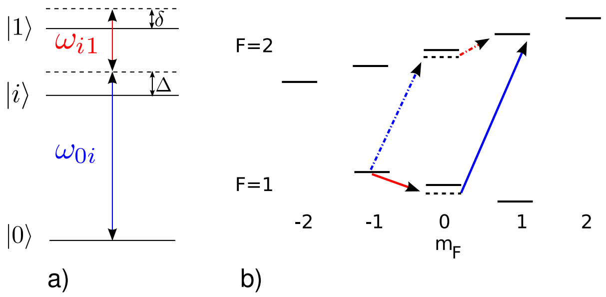

Figure 24: Two photon–transition. Principle (a) and two possible implementations for our state pair (b, dashed and full lines respectively). The intermediate state can be chosen to be $|2,0\rangle$ or $|1,0\rangle$. For either case, the detuning Δ can be chosen negative or positive, resulting in four different configurations.

tively, one can transform the the $|F, m_F\rangle$ states to the basis $|J, m_J, I, m_I\rangle$, where the relevant matrix elements are known. The resulting values are presented in figure 23.

Two–photon transitions in a three–level system The theory of two–photon transitions in a three–level system is discussed in [130] and we will quote only the result which is relevant for this work: Consider a three–level system $|0\rangle, |i\rangle, |1\rangle$ with energies $E_0 = 0, E_i, E_1$, with one–photon transitions linking the state pairs $(|0\rangle, |i\rangle)$ and $(|i\rangle, |1\rangle)$. In this system, Rabi oscillations can be driven between the states $(|0\rangle, |1\rangle)$, which do not significantly populate the intermediate state $|i\rangle$. To this end, both one–photon transitions are driven simultaneously by two fields with (Rabi) frequencies $(\Omega_{i0}, \Omega_{1i}), \omega_{0i}, \omega_{i1}$, detuned from the intermediate state $|i\rangle$ by Δ and the final state $|1\rangle$ by δ. See figure 24a) for an illustration. The resulting time evolution is that of a two–level system formed by the states $|0\rangle, |1\rangle$ (eqs. 22,23 of [130], all Rabi frequencies are assumed to be real)

$$|\langle 1|\psi(t)\rangle|^2 = \frac{\Omega_{R10}^2}{\Omega_{10}^2}\sin^2(\Omega_{10}t/2); \quad |\langle 0|\psi(t)\rangle|^2 = 1 - \frac{\Omega_{R10}^2}{\Omega_{10}^2}\sin^2(\Omega_{10}t/2); \quad |\langle i|\psi(t)\rangle|^2 \approx 0 \tag{48}$$

with

$$\Omega_{R10} = \frac{\Omega_{i0}\Omega_{1i}}{2\Delta}; \quad \Omega_{10}^2 = \Omega_{R10}^2 + (\delta - \delta'_{10})^2; \quad \delta'_{10} = \frac{\Omega_{1i}^2 - \Omega_{i0}^2}{4\Delta} \tag{49}$$

The shift δ'_{10} can be identified with the AC Zeeman shift, induced on the state pair $|0\rangle, |1\rangle$ by the driving fields.

To derive this result, a number of approximations are made: First, the rotating–wave approximation is used, amounting to $\hbar\Delta, \hbar\delta, \hbar\Omega_{i0}, \hbar\Omega_{1i} \ll (E_1 - E_i), E_i$. The population of state $|i\rangle$ is negligible only for $\Omega_{i0}^2, \Omega_{1i}^2 \ll \Delta^2$. Furthermore, it is assumed that $\delta \ll \Delta$. The deduction in [130] is made for the case $\omega_{0i} = \omega_{i1}$. The extension to the general case requires that each driving field addresses only one transition. With the above approximations, this is fulfilled as far as $\omega_{0i} \gg \omega_{i1}$ or $\omega_{0i} \ll \omega_{i1}$.

For our state pair, there are four different implementations of this scheme. We can choose either $|1,0\rangle$ or $|2,0\rangle$ as the intermediate state and freely choose the sign of Δ. The

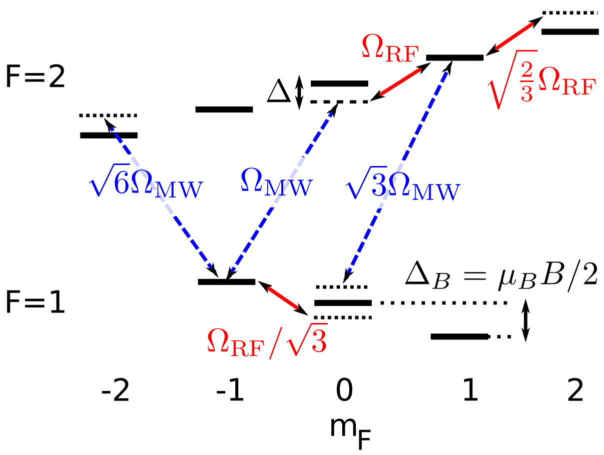

Figure 25: Couplings of the RF and microwave photons in the full manifold.

criteria for this choice are discussed in [131]: One has to avoid scattering into untrapped states and interfering paths between the clock states. All experiments to date [131], [119], [29] passed through the state $|2,0\rangle$ and used a detuning of $-0.7\text{MHz} < \Delta < 1.24\text{MHz}$.

Lightshifts in the ^{87}Rb hyperfine manifold In the ^{87}Rb ground state manifold, the RF and microwave radiation couple to several transitions other than the intended transitions $|1,-1\rangle \rightarrow |2,0\rangle$ and $|2,0\rangle \rightarrow |2,1\rangle$, as shown in fig. 25. All these couplings are off–resonant as one–photon transitions. Also, they can be linked to only one resonant two–photon transition involving the clock states. Therefore, the theory of the previous paragraph remains valid for the levels $|1,-1\rangle, |2,0\rangle, |2,1\rangle$ and the remaining couplings can be taken into account by perturbation theory. Each coupling from a clock state to a non–clock state $|m\rangle$ then leads to a lightshift, which is derived in [130]. Quantitatively, the lightshift on the clock transition caused by radiation of frequency ω is given by ([130], rewritten in the approximation $\omega - \omega_{i0} \ll \omega_{i0}, \omega - \omega_{i1} \ll \omega_{1i} \forall i$)

$$\delta_{01} = \sum_s \frac{\Omega_{s0}^2}{4(\omega_{s0} - \omega)} - \sum_s \frac{\Omega_{1s}^2}{4(\omega_{1s} - \omega)} \tag{50}$$

where s runs over all non–clock levels of the hyperfine manifold. This sum can be interpreted as the sum of all shifts induced on the level 0 (first term) minus all shifts induced on the level 1 (second term). Interestingly, the lightshift δ'_{01} of eq. 49 can be identified as the $i = |2,0\rangle$ term of this series. In our case, the full coupling Hamiltonian can also be diagonlized exactly. See A for a derivation.

To obtain the relevant couplings for our experiment, we note that our excitation pulses are σ–polarized, containing an equal amount of σ_+ and σ_- polarization. This, with the appropriate Clebsch–Gordan coefficients, leads to the couplings shown in Fig. 23. From these, we obtain the following lightshift of the two–photon transition

$$\delta_{01} = \Omega_{\mathrm{MW}}^2 \left(\frac{1}{4\Delta} + 6\frac{1}{4(\Delta - 2\Delta_B)} + 3\frac{1}{4(2\Delta_B + \Delta)} \right) + \Omega_{\mathrm{RF}}^2 \left(\frac{1}{4\Delta} - \frac{2}{3\cdot 4\Delta} - \frac{1}{3\cdot 4\Delta} \right) \tag{51}$$

$$\overset{\Delta \ll \Delta_B}{\approx} \frac{\Omega_{\mathrm{MW}}^2}{4\Delta}$$

The salient conclusions are twofold: The RF photon is "lightshift neutral" and does not shift the transition. The lightshift of the microwave photon mainly arises from the coupling to the intermediate state. Eq. 51 assumes this state to be $|2,0\rangle$, but an analogous calculation extends this result to the intermediate state $|1,0\rangle$.

To minimize the lightshift, the optimum choice consists in choosing Ω_{RF} as high as possible. The limit here is the condition $\Omega_{\mathrm{RF}} \ll \Delta$, to ensure a negligible population of the intermediate state. Δ must be chosen as high as possible. Here, there is no physical limit, but for the above theory to be valid, the rotating wave condition $\Delta \ll \Delta_B$ must be fulfilled.

Effect of the excitation on the motional atomic state The time evolution (48) is that of an effective two–level system of the states $|0\rangle, |1\rangle$. It is possible to summarize the RF and microwave coupling to one single coupling Hamiltonian (45) which leads to the same time evolution:

$$\hat{H}_{\mathrm{ex}} = \frac{\hbar\Omega_{10}(\hat{\vec{x}})}{2}|1\rangle\langle 0| + h.c.; \qquad \Omega_{10} = \frac{\Omega_{i0}\Omega_{1i}}{2\Delta}.$$

Here, we have allowed for a position–dependent coupling $\Omega_{10}(\hat{\vec{x}})$, with $\hat{\vec{x}}$ being the position operator. Also, we allow for a complex Ω_{i0}, Ω_{1i} to include the phase of the RF and microwave fields. The detuning from the two–photon resonance is summarized to the term $\Delta_{01} = \delta - \delta_{01}'$ of (33).

In general, the excitation field $\Omega_{10}(\vec{x})$ can be position dependent in both amplitude and phase. Exciting an atom with such a position–dependent field can modify its external state of along with its internal state. It is this side effect which we will study in the following paragraph. We will show that a magnetic trap on a chip can be made sufficiently strong to confine the atoms in the Lamb–Dicke regime, where the absorption of the microwave and RF photons does not change the motional atomic state.

Position–dependent phase Let us first consider the case that the microwave radiation is delivered to the atoms by a propagating wave along the x–direction. In this case

$$\Omega_{10}(\hat{x}) = \Omega_0 e^{ik\hat{x}}$$

with k being the wave number of the microwave. The phase gradient of the RF radiation can be neglected even if the RF photon is coupled from a propagating wave, since $k_{RF} \ll k_{MW}$. The only contribution to the position–dependency of Ω_{10} then is the

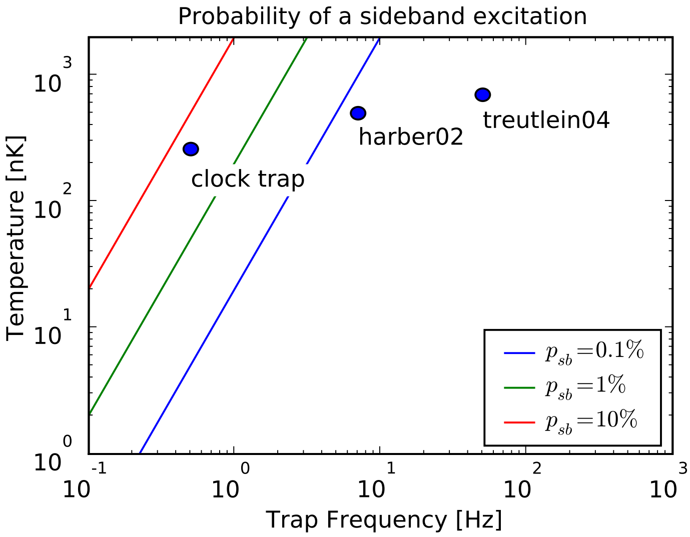

Figure 26: Probability of a sideband excitation in a thermal cloud. The data points "harber02" and "treutlein04" represent the parameters of [39] and [29], assuming the worst–case scenario that the microwave is a propagating wave, propagating along the weakest trap axis. The precise amplitude and phase profile of the freely propagating microwave is not known in these experiments. The data point "clock trap" represents the ideal clock trap which we will derive in section 3.2, with the interrogation being equally performed by a wave propagating along the weakest trap axis.

phase gradient of the microwave. Typically, the atoms are confined in the x–direction to a trap with frequency ω_x, so it is convienient to expressing $\hat{x}$ in terms of the ladder operators $\hat{a}, \hat{a}^\dagger$ of a harmonic oscillator with trap frequency ω_x:

$$\Omega_{10}(\hat{x}) = \Omega_0 e^{i\sqrt{\frac{\hbar k^2}{2m\omega_x}}(\hat{a}^\dagger+\hat{a})} \overset{\eta \ll 1}{\approx} \Omega_0 \left(1 + i\eta(\hat{a}^\dagger + \hat{a})\right).$$

Here, we have introduced the Lamb–Dicke parameter $\eta = \sqrt{\hbar k^2/(2m\omega_x)} = E_{\text{recoil}}/(\hbar\omega_x)$. In this configuration, sideband transitions (between different trap levels $|m+1\rangle, |m\rangle$) will be suppressed against carrier transitions by a ratio

$$\frac{|\langle m+1|\langle 1|\hat{H}_I|m\rangle|0\rangle|^2}{|\langle m|\langle 1|\hat{H}_I|m\rangle|0\rangle|^2} = (m+1)\eta^2.$$

where $|\alpha\rangle|\beta\rangle$ denotes an atom in the external quantum state $|\alpha\rangle$ and the internal quantum state $|\beta\rangle$. During a π–pulse, the total probability for a sideband transition to the adjacent states $|m \pm 1\rangle$ is $p_{\text{sb}} = (2m+1)\eta^2$. For a condensate ($m = 0$), the probability of such an excitation is clearly negligible ($\eta^2 < 10^{-4}$ even for a trap of $\omega = 2\pi \cdot 0.1$ Hz). For a thermal cloud ($\bar{m} = k_B T/(\hbar\omega_x)$), a plot of the excitation probability for our relevant parameter space is presented in figure 26.

Position–dependent amplitude We now turn to the discussion of a position–dependent amplitude of the Rabi frequency. A variation of the amplitude, too, can transfer recoil to the atom, as has been pointed out in [132]. In our experiment, the amplitude of the Rabi frequency varies most, when the microwave photon is delivered from a standing wave along the x–axis. Assuming the cloud to be placed at $x = 0$ in an antinode of such a standing wave, the Rabi frequency reads

$$\Omega_{10}(\hat{x}) = \Omega_0 \left(1 - \frac{1}{2}k^2\hat{x}^2\right) = \Omega_0 \left(1 - \frac{1}{2}\eta^2(\hat{a}^{\dagger 2} + \hat{a}^2 + \hat{a}^\dagger\hat{a} + \hat{a}\hat{a}^\dagger)\right)$$

The probability of a sideband excitation is thus of the order $m^2\eta^4$, suppressed for $\eta < 1$ to one higher power than for a phase gradient.

Effect of a non–negligible Lamb–Dicke parameter If the Lamb–Dicke parameter is negligible, the $\pi/2$ pulses do not change the motional quantum state of the atoms, leading to a Doppler–free interrogation. A non–negligible Lamb–Dicke parameter compromises this in two ways:
If p_{sb} is non–negligible, but $p_{\mathrm{sb}}^2 \ll 1$, a fraction $2p_{\mathrm{sb}}$ of the contrast of the Ramsey fringes is lost. This is due to the fact that a fraction $2p_{\mathrm{sb}}$ of the atoms changes their motional state during one of the Ramsey pulses. For these atoms the two arms of the Ramsey interferometer are not closed, so they do not contribute to the signal.
If even p_{sb}^2 is non–negligible, the Ramsey interferometer can be closed by a second–order process, in which the atom changes its motional quantum number by ±1 during the first and ∓1 during the second $\pi/2$ pulse. Such an atom contributes to the signal, but has effectively interrogated a transition of frequency $\omega_{01} + \omega_x$. In the worst case (when this "wrong" transition leads the atom to the top of a Ramsey fringe), this process induces an error $\Delta_f = p_{\mathrm{sb}}^2$ on the population inversion $f = (N_0 - N_1)/(N_1 + N_0)$.

In our experiment, we have to limit the latter process to contribute a smaller error than the shot–noise–limit $\sigma_f = 1/\sqrt{N} \approx 1\%$. This amounts to $p_{\mathrm{sb}} = 10\%$, which is also an acceptable limit for the loss of fringe contrast by first–order sideband processes. If the interrogation is performed with a propagating wave, it corresponds to the red line in figure 26. For interrogation with a standing wave, even lower trapping frequencies and/or higher temperatures can be used. In summary, the Lamb–Dicke regime for the microwave photon can be easily reached in a chip trap, so we will assume the clock to operate in this limit in all the following.

Semi–classical interpretation of the loss of fringe contrast As discussed, a phase or amplitude gradient during the excitation can reduce the contrast of the Ramsey fringes. This can be understood semi–classicaly by assuming that each atom of the cloud is excited by the first $\pi/2$ pulse into a coherent superposition $\cos(\theta/2)|0\rangle + e^{i\phi}\sin(\theta/2)|1\rangle$, with a position–dependent $\theta(x)$ for a position–dependent amplitude or a position–dependent $\phi(x)$ in the case of a position–dependent phase of the excitation field. On the Bloch sphere, the cloud is smeared out on either the equator, in the case of a position–dependent phase, or a longitude, in the case of a position–dependent amplitude. Aver-

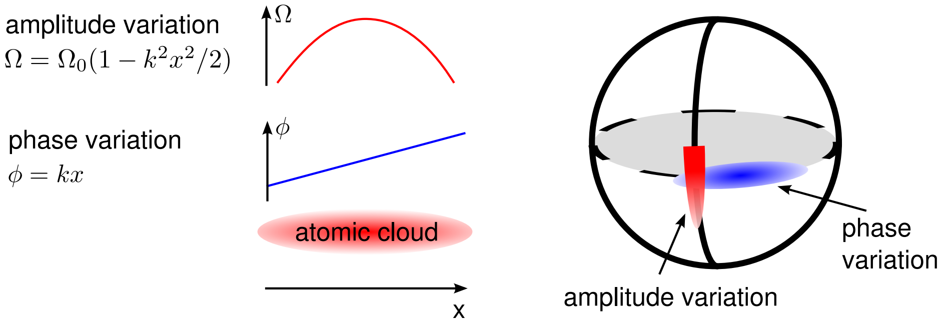

Figure 27: Decoherence induced by a variation of the driving field in amplitude or phase. The atomic state, averaged over the whole cloud, is in a partly classical mixture, which reduces the contrast of the Ramsey fringes.

aged over the whole cloud, this reduces the length of the Bloch vector, which corresponds to the contrast of the measurement. See figure 27 for an illustration.

Doppler effect, comparison with fountain cavities Performing a clock interrogation on trapped atoms has one essential advantage: The interrogation is Doppler–free, if it is performed at a negligible Lamb–Dicke parameter $\eta \ll 1$. To see this, one uses the fact that in quantum mechanics, the Doppler effect can be interpreted as a consequence of the recoil of the absorbed photon [133]. This is best seen for a two–level atom (with levels $|0\rangle$, $|1\rangle$, separated by $\hbar\omega_{\text{at}}$) which propagates as a plane wave and absorbs a photon. This atom undergoes a transition between the two plane–wave states $|\vec{k}\rangle|0\rangle$ and $|\vec{k}+\vec{k}_r\rangle|1\rangle$, where $k_r = \omega_{\text{ph}}/c$ is the recoil transmitted by the absorbed photon. To excite this transition, the photon must have a frequency

$$\omega_{\text{ph}} = \omega_{\text{at}} + \frac{1}{\hbar}\left[\frac{(\vec{k}+\vec{k}_r)^2}{2m} - \frac{k^2}{2m}\right] = \omega_{\text{at}}\left(1 + \frac{v}{c}\cos\theta + O(k_r^2)\right)$$

where v is the velocity of the atom and θ is the angle between this velocity and the incident light wave. This relation corresponds exactly to the classical formula of the Doppler effect. In a trap, this recoil is quantized, since the atom can change its external state only between different trap levels. If, moreover, the trap is so stiff that $\eta \ll 1$, the atom cannot change its motional state at all during the excitation. The recoil of the photon is then transmitted to the trap as a whole and the interrogation becomes Doppler–free [134].

This presents a huge advantage compared to clocks which operate on untrapped atoms. In these clocks, a finite propagating wave ratio in the excitation zone immediately causes a Doppler shift in the interrogation. As a consequence of this effect, the cavities of atomic fountain clocks are carefully optimized to produce a maximally pure standing wave [135]. In this respect, the use of trapped atoms significantly simplifies the design. The details of the excitation field are irrelevant, with the only constraint that the resulting Lamb–Dicke parameter must not exceed the limits discussed in the previous paragraphs.

3.1.4 Collisions in the atomic cloud

The atoms in the cloud interact. These interactions compromise the clock operation in two ways: Elastic collisions give rise to a mean–field potential, the term $\hat{H}_{\text{int}}$ of the Hamiltonian (33). As we have seen, this term leads to a position–dependent shift of the clock frequency. Inelastic collisions lead to losses, which cause fluctuations, since they render the mean–field shift time–dependent. In this subsection, we will discuss both of these effects, but describe only the details which are relevant for our experiment. For a more detailed discussion, the reader is refered to [125].

Inelastic collisions Phenomenologically, inelastic collisions are categorized by the way they scale with the atomic density n. Precisely, the decay rate of the atomic density n_α is expanded into a power series in density

$$\frac{\dot{n}_\alpha}{n_\alpha} = -\gamma_\alpha - \sum_\beta \gamma_{\alpha\beta} n_\beta - \sum_{\beta\gamma} \gamma_{\alpha\beta\gamma} n_\beta n_\gamma + \ldots .$$

The terms of this expansion can be interpreted as follows:

One–body losses, which are independent of the atomic density, are described by γ_α. They limit the lifetime of each atom to the timescale γ_α^{-1}. Experimentally, such losses arise mostly from collisions with the background gas of the vacuum.

Two–body losses arise from inelastic collisions between two atoms. Consequently, they scale linearly with n_β, which is proportional to the probability for an atom in state α to hit an atom in state β. These losses are the dominant loss process for our clock states. Their rates have recently been measured in a condensate of these states [126] to be

$$\gamma_{01} = 0.780(19) \times 10^{-13} \text{cm}^3/\text{s}; \qquad \gamma_{11} = 1.194(19) \times 10^{-13} \text{cm}^3/\text{s} \tag{52}$$

γ_{00} is negligible against these rates. Physically, these losses arise from two different processes:

- **Spin–exchange collisions:** These losses have the same physical origin as the elastic collisions described by $\hat{H}_{\text{int}}$: The repulsive core felt by two overlapping atoms. The strength of this core depends on the spin of the valence electrons of the colliding atoms (electrons with parallel spins will experience a stronger Fermi repulsion). Such a collision can induce transitions between different $|F, m_F\rangle$ states, since the $|F, m_F\rangle$ states are not eigenstates of the electron spin. It does, however, conserve the total internal angular momentum $\vec{F} = \vec{F}_1 + \vec{F}_2$ of the colliding atoms 1 and 2. Mostly, these transitions scatter atoms into untrapped states, so that they amount to losses from the trap. For our clock states, there are several possible reactions of this kind

$$\begin{aligned} |2,1\rangle + |2,1\rangle &\to |2,2\rangle + |2,0\rangle \qquad (53) \\ |2,1\rangle + |1,-1\rangle &\to |2,0\rangle + |1,0\rangle \end{aligned}$$

- **Dipolar relaxation:** These losses arise from the magnetic dipole interaction between the spins of the colliding atoms. This interaction does not conserve $\vec{F}$, it only conserves the total angular momentum $\vec{L}+\vec{F}$, where $\vec{L}$ is the orbital angular momentum of the colliding atoms (classically speaking: Their impact parameter). In this way, two colliding atoms in an s–wave state (with orbital angular momentum L=0) can be scattered into a d–wave state (L=2) and the angular momentum for this process is taken from the internal angular momentum.

We are not aware of a measurement which would distinguish between these two mechanisms. The loss rates (52) include both.

Three–body losses arise from inelastic collisions, where two atoms collide to form a molecular bound state. These collisions involve a third atom taking up the excess momentum and energy. Therefore, the rate of these collisions is proportional to n^2, the probability of atomic three–body–encounters. The rate constant for this process in the $|1,-1\rangle$ state of ^{87}Rb has been measured to be $\gamma_{111} = 4.3 \times 10^{-29}\text{cm}^6/\text{s}$ for a thermal cloud and $\gamma_{111} = 5.8 \times 10^{-30}\text{cm}^6/\text{s}$ for a condensate, differing by a factor of 3! because of the bunching of the bosonic atoms in the thermal cloud [136].

Elastic collisions Elastic collisions arise from the isotropic interatomic potential created by the van–der–Waals–interaction at long distance and the repulsive core of the overlapping electron shells for short distances. For collisions of cold bosonic atoms, however, these details are irrelevant and the potential can be replaced by a contact interaction, the term $\hat{H}_{\text{int}}$ of the Hamiltonian (33).

$$\hat{H}_I = \frac{2\pi\hbar^2}{m}\int_V d^3\vec{x} \sum_{\alpha,\beta=0,1} a_{\alpha\beta}\, \psi^\dagger_\alpha(\vec{x})\psi^\dagger_\beta(\vec{x})\,\psi_\beta(\vec{x})\psi_\alpha(\vec{x}) \tag{54}$$

where the strength of the contact potential is characterized by the s–wave scattering lengths a_{ij}.

To compute the clock shifts arising from this potential, we will outline an analysis of Kurt Gibble [137]. The basic idea is to consider a cloud of only two atoms, where all shifts from the potential 54 can be computed explicitly.

Let us consider two identical bosonic atoms. Let $|0\rangle, |1\rangle$ be two accessible orthonormal internal states and $|\phi\rangle, |\chi\rangle$ two accessible orthonormal external states (with $\langle\vec{x}|\phi\rangle = \phi(\vec{x})$ for some wavefunction ϕ). Let $|\phi\chi\rangle$ denote a distinguishable two–particle state $|\phi\rangle_1|\chi\rangle_2$.

With these conventions we can derive the possible two–particle states of the two–atom system: In a thermal cloud, the atoms of a colliding pair are in different external states and arbitrary internal states. Their two–particle state must therefore be a linear combination of the symmetric states

$$|d\rangle = (|\phi\chi\rangle + |\chi\phi\rangle)|00\rangle \ / \ \sqrt{2} \tag{55}$$

$$|t\rangle = (|\phi\chi\rangle + |\chi\phi\rangle)(|01\rangle + |10\rangle) \ / \ 2 \tag{56}$$

$$|u\rangle = (|\phi\chi\rangle + |\chi\phi\rangle)|11\rangle \ / \ \sqrt{2} \tag{57}$$

$$|s\rangle = (|\phi\chi\rangle - |\chi\phi\rangle)(|01\rangle - |10\rangle) \ / \ 2 \tag{58}$$

We will refer to $|t\rangle$ as the "triplet state" and to $|s\rangle$ as the "singlet state" and denote the total state vector by the linear combination $\psi = d|d\rangle + t|t\rangle + u|u\rangle + s|s\rangle$, obeying the normalization condition $|d|^2 + |t|^2 + |u|^2 + |s|^2 = 1$.
To compute the clock shift of the mean–field interaction, one has to compute the time evolution of these states over one clock cycle. For the evolution stemming from the Hamiltonian 54, one notes that all the states are eigenstates of the collision Hamiltonian 54. This is easily proven by expanding $|\phi\rangle|\alpha\rangle$ and $|\chi\rangle|\alpha\rangle$ in the form $|\chi\rangle|\alpha\rangle = \int d^3\vec{x}\chi(\vec{x})\psi_\alpha^\dagger(\vec{x})$ and using the commutation relations (32) several times. For the time evolution stemming from the excitation pulses, one assumes a generic coupling Hamiltonian $H_I = \hbar\Omega_\phi/2|\phi\rangle|1\rangle\langle\phi|\langle 0| + \hbar\Omega_\chi/2|\chi\rangle|1\rangle\langle\chi|\langle 0| + H.C.$ with Rabi frequencies Ω_χ, Ω_ϕ, which are in general different for different external states. The resulting time evolution reads

$$\begin{aligned}
i\partial_t d &= \frac{\bar{\Omega}}{\sqrt{2}}t - \frac{\Delta\Omega}{\sqrt{2}}s - \Delta g d \\
i\partial_t t &= \frac{\bar{\Omega}}{\sqrt{2}}u + \frac{\bar{\Omega}^*}{\sqrt{2}}d + \delta g t \\
i\partial_t s &= \frac{\Delta\Omega}{\sqrt{2}}u - \frac{\Delta\Omega^*}{\sqrt{2}}d - 2\bar{g}s \\
i\partial_t u &= \frac{\bar{\Omega}^*}{\sqrt{2}}t + \frac{\Delta\Omega^*}{\sqrt{2}}s + \Delta g u
\end{aligned}$$

with

$$\begin{aligned}
\Delta g &= (g_{11} - g_{00}); \;\; \delta g = (2g_{01} - g_{00} - g_{11}); \;\; \bar{g} = (g_{11} + g_{00})/2 \\
g_{\alpha\beta} &= \frac{4\pi\hbar}{m}a_{\alpha\beta}\int d^3\vec{x}|\phi(\vec{x})|^2|\chi(\vec{x})|^2 \\
\bar{\Omega} &= (\Omega_\phi + \Omega_\chi)/2; \qquad \Delta\Omega = (\Omega_\phi - \Omega_\chi)/2
\end{aligned}$$

By calculating the time evolution over a full Ramsey cycle, it can be shown that the different terms lead to a clock shift of ([137], eq. 5)

$$\Delta\nu = \frac{\Delta g}{2\pi} + \frac{\delta g}{A\pi}\cos(\bar{\theta}_1)\cos(\Delta\theta_2)\sin(\bar{\theta}_1)\sin(\bar{\theta}_2) - \frac{\bar{g}}{A\pi}\sin(2\Delta\theta_1)\sin(\Delta\theta_2)\cos(\bar{\theta}_2) \quad (59)$$

where $\bar{\theta}_\alpha = \bar{\Omega}t_{\pi/2}, \Delta\theta_\alpha = \Delta\Omega t_{\pi/2}$ are the pulse surfaces of the αth $\pi/2$ pulse, $t_{\pi/2}$ is the duration of a $\pi/2$ pulse and A is the amplitude of the Ramsey fringes ($A = 2$ if there is no decoherence).

Let us now apply this theory to our experiment: Let us first assume that the Rabi frequency is independent of the external state, $\Delta\Omega = 0$. In this case, the first two terms of eq. (59) give a nonzero contribution. Assuming perfect fringes ($A = 2$) and expanding to lowest order in $\bar{\theta}_1, \bar{\theta}_2$, one obtains

$$\Delta\nu = \frac{\Delta g}{2\pi} + \frac{\delta g}{2\pi}\frac{n_0 - n_1}{n_1 + n_0}. \quad (60)$$

with n_1, n_0 being the densities of the $|0\rangle$ and $|1\rangle$ populations. In a cloud of N atoms, the shift of one atom arises from the collisions with the other $N-1$ atoms. Neglecting collisions of more than two atoms, this shift is calculated by summing $N-1$ contributions of eq. 60. The result is the frequency shift of one atom, immersed into a cloud of density n, with a population inversion $f = (n_0 - n_1)/n$

$$\Delta\nu = \frac{2\hbar}{m} n[(a_{11} - a_{00}) + f \cdot (2a_{01} - a_{11} - a_{00})] \qquad \text{for a thermal cloud.} \tag{61}$$

This result has been experimentally verified on our clock transition [39]. Note, however, that this same reference [39] errourneously states that the prefactor $2a_{01} - a_{11} - a_{00}$ of the term proportional to f depends on the coherence between the $|0\rangle$ and $|1\rangle$ parts of the atomic wavefunction. This issue has been the subject of the "factor of 2 controversy". Meanwhile eq. 61 has been proven to be valid for coherent superpositions as well as classical mixtures of $|0\rangle$ and $|1\rangle$, both experimentally [138] and theoretically [137].

The frequency shift for an atom in a condensate can be derived analogously by assuming both atoms to be in the same external state ϕ. In contrast to the thermal case, the singlet state then does exist, and the collisional shift of the states $|d\rangle, |t\rangle, |u\rangle$ is a factor of two smaller. The final result is

$$\Delta\nu = \frac{\hbar}{m} n[(a_{11} - a_{00}) + f \cdot (2a_{01} - a_{11} - a_{00})] \qquad \text{for a condensate.} \tag{62}$$

The results (61, 62) have been derived with the approximation that the Rabi frequency does not depend on the external state ($\Delta\Omega = 0$). The validity of this assumption remains to be checked: We recall from section 3.1.3 that the Rabi frequency is homogeneous along the y– and z–directions, where the atoms are confined in a strong trap, but varies in phase or amplitude along the x– direction, where the trap is weak. Again, two cases arise in this direction, depending on whether the microwave is coupled from a standing or a propagating wave. In the case of a standing wave with wavevector k, the Rabi frequency varies along x as

$$\Omega(x) = \Omega_0 \left(1 - \frac{1}{2}k^2 x^2\right)$$

An atom in the lth motional quantum state of the trap $|l\rangle$ will experience an average Rabi frequency $\Omega_l = \langle l|\Omega(\hat{x})|l\rangle$. The difference $\Delta\Omega$ of the Rabi frequency of two random atoms will be of the order of $\Delta\Omega = (\Omega_{l=0} - \Omega_{l_{\text{th}}})/2$ with $l_{\text{th}} = k_B T/[\hbar\omega]$. $\Omega_{l_{\text{th}}}$ can be computed from the virial theorem $m\omega^2 x^2/2 = k_B T/2$, yielding

$$\langle l_{\text{th}}|\Omega(\hat{x})|l_{\text{th}}\rangle = \Omega_0 \left(1 - \frac{k^2 k_B T}{2m\omega^2}\right)$$

With our numerical values $k \approx 20\text{mm}$, $T = 500\text{nK}$, $\omega_x = 2\pi \cdot 0.5\text{Hz}$, we obtain

$$\Delta\Omega = 0.1 \cdot \Omega_0$$

The shift due to this variation should therefore be observable. It arises from the second and third term of eq. 59. To see it, one would either have to operate the clock with a

population imbalance, so that $\cos(\bar{\theta}_1) \neq 0$ and the 2nd term is nonzero, or with a 2nd Ramsey pulse, which is not a perfect $\pi/2$ pulse. In this case, $\cos(\bar{\theta}_2) \neq 0$, and the 3rd term would be nonzero. In usual clock operation, where $f = 0$ and $\bar{\theta}_2 = \pi/2$, the shift will not be visible.
Let us finally turn to the case that the microwave is coupled as a propagating wave. In this case $\Delta\Omega = 0$, yielding no shift.

3.2 Coherence

We will now derive a first result from the above theory and estimate the coherence time of a superposition of our clock states in a magnetically trapped cloud. This coherence time is limited by dephasing, arising from the fact that the frequency shifts in a magnetically trapped cloud are position–dependent. We will show in subsection 3.2.1 how this limits the coherence time of the cloud. We will then study how the trap parameters must be chosen to minimize this effect, treating first a trap in zero–g (subsection 3.2.2), then a trap in presence of gravity (subsection 3.2.3).

3.2.1 Decoherence by dephasing

The dominant source of decoherence in our system is dephasing: As discussed above, the transition frequency of an atom is shifted in the trap, mainly by the second–order Zeeman shift and the mean–field shift induced by the surrounding atoms. Seen as a clock, each atom advances or lags slightly against the average atom in the cloud. The detection, however, does not measure with atomic resolution, and, averaged over the cloud, this dephasing leads to a loss of contrast.

Decoherence in the density matrix and Bloch vector descriptions This is best quantified in the density matrix formalism. Immediately after the first $\pi/2$ pulse, each atom is prepared in the state $|\psi_0\rangle = (|0\rangle + i|1\rangle)/\sqrt{2}$, corresponding to the following density matrix of its internal states:

$$\hat{\rho} = \frac{1}{2}\begin{pmatrix} 1 & i \\ -i & 1 \end{pmatrix}$$

As a simple model, let us assume that the varying frequency shifts are normally distributed over the cloud, so that the detuning $\Delta = \omega_{\text{at}} - \omega_{\text{fw}}$ of each atom is described by the distribution

$$p(\Delta) = p_0 e^{-\frac{(\Delta-\Delta_0)^2}{2\sigma_\Delta^2}}$$

During the Ramsey time, each atom accumulates a phase, evolving into the state $|\psi_1(\Delta)\rangle = (|0\rangle + ie^{i\Delta t}|1\rangle)/\sqrt{2}$, with a statistically varying Δ for each atom. The density matrix is thus given by

$$\begin{aligned}\hat{\rho} &= \frac{1}{2}\int d\Delta\ p(\Delta)\ |\psi_1(\Delta)\rangle\langle\psi_1(\Delta)| \\ &= \frac{1}{2}\int d\Delta\ p(\Delta)\begin{pmatrix} 1 & ie^{i\Delta t} \\ -ie^{-i\Delta t} & 1 \end{pmatrix} \qquad (63) \\ &= \frac{1}{2}\begin{pmatrix} 1 & ie^{i\Delta_0 t}e^{-\sigma_\Delta^2 t^2/2} \\ -ie^{-i\Delta_0 t}e^{-\sigma_\Delta^2 t^2/2} & 1 \end{pmatrix} \qquad (64)\end{aligned}$$

In the Bloch sphere picture, this can be seen as a Bloch vector of length $e^{-\sigma_\Delta^2 t^2/2}$, i.e., shorter than the radius of the unit sphere, which turns around the z–axis of the sphere with the angular velocity Δ_0.

Effect on the Ramsey fringes When the Ramsey cycle is closed at time t by the second $\pi/2$ pulse, the resulting excitation probability reads

$$|\langle 1|\psi\rangle|^2 = \frac{1}{2}(1 + e^{-\sigma_\Delta^2 t^2/2}\cos(\Delta t))$$

In presence of decoherence, the Ramsey fringes decay with a time constant of $1/\sigma_\Delta$. As in section 3.3.1, one can find an optimum Ramsey time T_R, maximizing the slope of the central fringe. This results in the optimum quality factor

$$Q_{\text{opt}} = \frac{e^{-1/2}}{\sigma_\Delta \pi}\omega_{\text{at}}$$

achieved at a Ramsey time of

$$T_R = \sigma_\Delta^{-1}$$

Computation of σ_Δ The frequency spread σ_Δ of a given trap can be easily calculated, if the atoms are assumed to be static. In this case, the spread of the Zeeman and mean–field shift over the equilibrium distribution of the atoms can be evaluated analytically or numerically.

We will use this method extensively in the following, in spite of two concerns: A minor concern is that the frequency shift might not be distributed normally as assumed above. A major concern, however, is the assumption of static atoms. For a condensate, it can be justified by eq. (39). Indeed, in a condensate, the phase evolves only locally, as long as the spatial dynamics of the wavefunctions is negligible. This will be the case in our clock, since the interrogation time must end before external dynamics ("demixing") sets in.

The situation is less clear for a thermal cloud, where the atoms move and collide during the interrogation time. Here however, experiments show that motion and collisions tend to improve the coherence time [39]. The spread calculated from static atoms can thus be used as a worst–case estimate. Furthermore, we will show below, that the optimized trap parameters calculated in this way agree fairly well with experimental data.

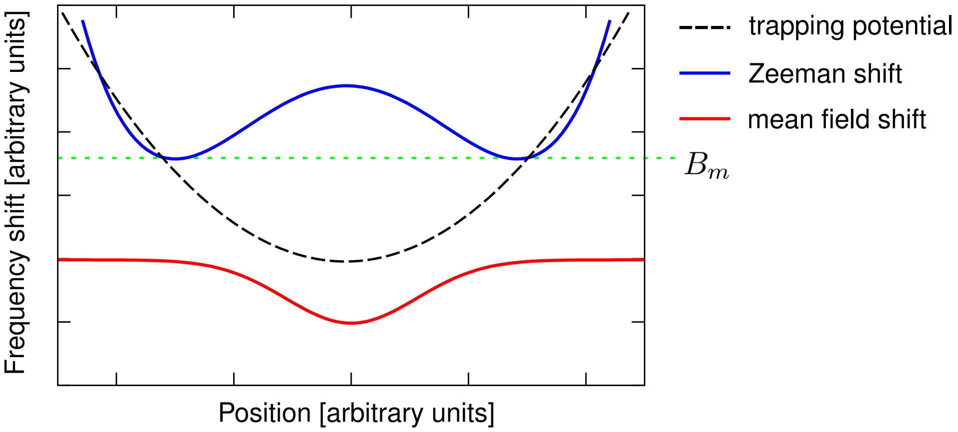

Figure 28: Clock shifts in a magnetic trap (conceptual): The trapping potential as well as the atomic density are position–dependent. Consequently, the Zeeman as well as the mean–field shift vary with position. The curvature of the Zeeman shift can be tuned by choosing the offset of the trap bottom from the magic field B_m. By a proper choice of this offset, it can compensate the mean–field shift.

3.2.2 Magnetically trapped cloud in zero–g

We will now estimate the frequency spread σ_Δ for a magnetically trapped thermal cloud in absence of gravity. Basically, this presents a situation as in fig. 28. In this special case, however, the calculation can be simplified using an idea sketched in figure 29: We will express all relevant quantities – the Zeeman shift, the atomic density and the mean–field shift – as functions of B, so that the spread can be computed analytically as a one–dimensional integral. For the sake of convenience, we will shift the origin of B, such that $B = 0$ corresponds to the bottom of the trap.

Definitions As discussed above, the frequency spread is caused by the position–dependent Zeeman shift (eq. (44))

$$\delta\Delta_B = \beta(B - (B_m - B_0))^2 = \beta(B - \Delta B)^2 \tag{65}$$

and the position–dependent mean–field shift (assuming a symmetric population $n_0 = n_1$)

$$\delta\Delta_n = \frac{4\pi\hbar}{m}(a_{11} - a_{00})n = \bar{\alpha}_{\text{th}}\, n_0 e^{-\frac{\mu_B}{2k_BT}B}. \tag{66}$$

Our goal is to calculate the spread of the sum of these shifts $\delta\Delta = \delta\Delta_B + \delta\Delta_n$

$$\sigma_\Delta^2 = \left\langle \delta\Delta^2 \right\rangle - \left\langle \delta\Delta \right\rangle^2 \tag{67}$$

where $\langle\cdot\rangle$ denotes the average over the equilibrium single–particle density. This density, too, depends only on B and can therefore be rewritten as a density over the variable B.

$$n_B(B) = n_0 g(B) e^{-\mu_B B/(2k_BT)} \tag{68}$$

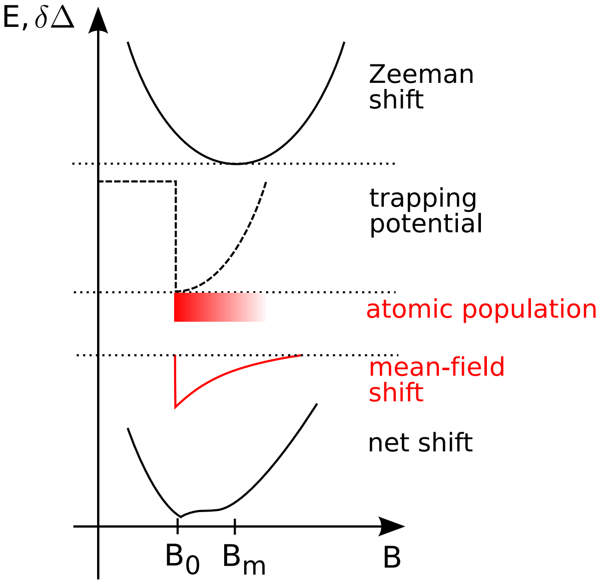

Figure 29: Calculation of the frequency spread in absence of gravity: The Zeeman shift varies quadratically with B. The mean–field shift in the trap is a pure function of magnetic field, too, so the spread can be computed from a one–dimensional integral. The compensation described in figure 28 reappears in this picture in the following way: By choosing the background field of the trap, the cloud can be placed in a well–defined region of the Zeeman parabola, such that the sum of Zeeman and mean–field shift yields a modified (and, ideally, flattened) profile of the net shift $\delta\Delta(B)$.

where $g(B)dB$ is the infinitesimal space available at a magnetic field B: $g(B) = dV/dB$ with $V(B) = \int_V d^3\vec{x}\Theta(B - B(\vec{x}))$, Θ denoting the Heaviside step function. With these definitions, the expectation value reads

$$\langle f \rangle = \int_0^\infty dB\, n_B(B) f(B)/N.$$

Scale invariance of the harmonic trap For a harmonic trap, we obtain

$$g(B) = \frac{2\pi}{\bar{\omega}^3} \sqrt{\frac{\mu_B}{m}}^3 \sqrt{B}$$

It follows, that the single–particle density

$$n_B/N = \frac{2\pi}{\bar{\omega}^3} \sqrt{\frac{\mu_B}{m}}^3 n_0 \sqrt{B} e^{-\frac{\mu_B B}{2k_B T}} \overset{n_0 \text{ from eq. (84)}}{=} \frac{1}{\sqrt{2\pi}} \sqrt{\frac{\mu_B}{k_B T}}^3 e^{-\frac{\mu_B}{2k_B T} B} \sqrt{B} \tag{69}$$

is independent of $\bar{\omega}$ and N. It only depends on the temperature and the magnetic field and is universal for all harmonic traps. From inspection of eqs. (67), (65), (66), it follows immediately that σ_Δ depends only on the parameters T, n_0 and ΔB. It does not depend explicitly on the choice of the trap frequencies, they only enter implicitly via n_0.

The same conclusion can be drawn from a different argument: Consider a scaling transformation of space along one direction by a factor λ, $x_i \to x'_i = \lambda x_i$. Evidently, such a scaling transformation will leave all shifts and averages invariant, if n and B are rescaled such that $n'(\vec{x}') = n(\vec{x})$, $B'(\vec{x}') = B(\vec{x})$. Such a scaling transformation of space can be implemented by transforming the trap parameters in the following way:

$$N \to \lambda N \qquad \omega \to \omega/\lambda$$

In other words: Once we have found a trap with minimum frequency spread, we can generate a continuum of equally “optimal” traps by applying transformations of this kind. Experimentally, this transformation can be thought of as stretching or squeezing the trap and then filling or emptying the new trap (changing N), such as to keep n_0 invariant.

We note that this argument is equally valid for the multiplication of traps. Using M identical traps increases the available volume $g(B)$ by a factor of M. Rescaling N by $1/M$, one recovers the same expectation values and shifts as for a single trap.

There exists another, less evident, scaling relation: If the trap parameters are scaled according to

$$T \to \lambda T \qquad \Delta B \to \lambda \Delta B \qquad n_0 \to \lambda^2 n_0$$

the frequency spread in the trap scales according to

$$\sigma_\Delta \to \lambda^2 \sigma_\Delta.$$

It is therefore sufficient to calculate the spread for one specific T and one specific set of ωs. The solution can be scaled to other values of T and ω using the scaling relations.

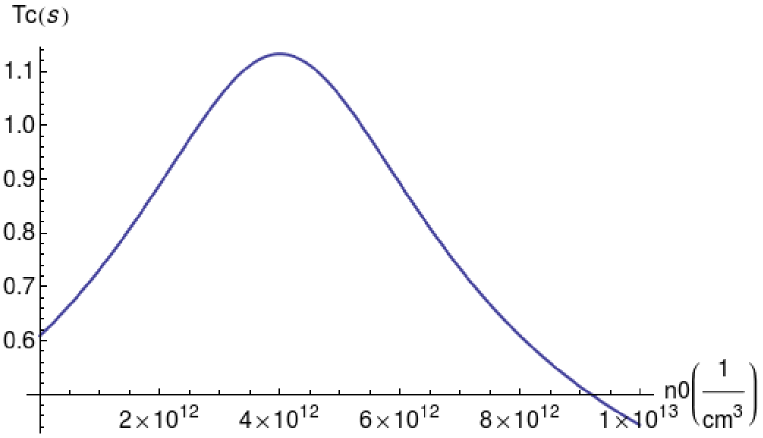

Figure 30: Coherence time in a harmonic trap in zero–g as a function of the peak density. The temperature is $T = 500\text{nK}$. For each $n0$, ΔB is set to its optimum value, where the Zeeman shift optimally compensates the mean–field shift for a particular $n0$. (as discussed in figure 28)

Evaluation The resulting frequency spread is presented in figure 30. The data shown has been calculated at $T = 500\text{nK}$, choosing the optimum ΔB for each $n0$. With these assumptions, the linewidth becomes a pure function of $n0$. Interestingly, there is an optimum peak density, where the compensation works best. This optimum lies at

$$n_{0,\text{opt}} = 4 \cdot 10^{12}\text{cm}^{-3} \qquad \Delta B_{\text{opt}} = 0.06\text{G}.$$

and produces a coherence time of $> 1\text{s}$. These parameters are well in the reach of chip traps.

3.2.3 Magnetically trapped cloud in presence of gravity

The above reasoning does not include gravity. Including it severely changes the situation. For a harmonic trap, gravity shifts the center of the trap away from the minimum of the magnetic field by the "gravitational sag"

$$\Delta z = \frac{g}{\omega_z^2}.$$

It has, however, no effect on the frequencies of the trap.

Analysis by a 3D Monte–Carlo model To estimate σ_Δ in presence of gravity, we have developed a Monte–Carlo model. It reads the parameters $(\omega_x, \omega_y, \omega_z), \Delta B, T, n_0$ and calculates the spread σ_Δ. To this end, it generates a cloud of N test atoms, which is distributed according to the density of a thermal cloud in a harmonic trap in presence of gravity. All shifts are then evaluated numerically for each atom and the spread σ_Δ is calculated by averging over the ensemble of the N test atoms. As the previous model,

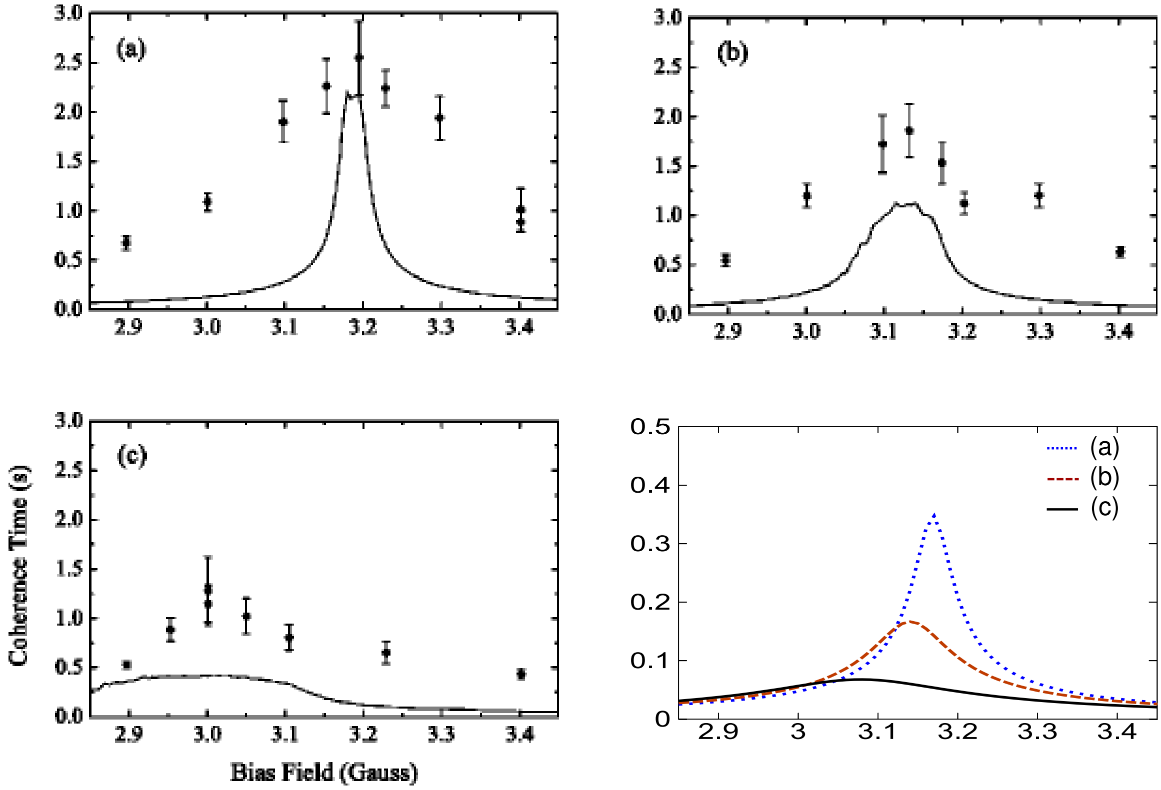

Figure 31: Comparison of our Monte–Carlo model (lower right graph) with the results of [39]. The black data points of these graphs are experimental data, the black line is a Monte–Carlo model similar to ours, but including motional averaging. All data has been taken on thermal clouds of $T = 480\text{nK}$ in a trap of $(\omega_x, \omega_y, \omega_z) = 2\pi(7, 230, 230)$, with peak densities of $n_0 = 4 \cdot 10^{12}\text{cm}^{-3}$ (a), $n_0 = 1.3 \cdot 10^{13}\text{cm}^{-3}$ (b) and $n_0 = 3.2 \cdot 10^{13}\text{cm}^{-3}$ (c). Note the difference of the vertical scales between (a–c) and the data of our model (lower right graph).

it neglects motional and collisional averaging, resulting in a worst–case estimate of the coherence time.

The choice of a Monte–Carlo model is rather a question of convenience. An analytic treatment is possible even in presence of gravity and has actually been performed in parallel with the Monte Carlo simulation [139] .

Comparison with experimental data To validate the model, we compared its result to experimental results. In [39], coherence times of a magnetically trapped thermal cloud of our clock states have been measured for several parameter sets and we reproduce this data in figure 31. At a fixed temperature and peak density, the coherence time attains a maximum at a specific value of the bias field. This is exactly the compensation effect shown in figure 28. By tuning ΔB, the Zeeman shift can be tuned such as to partly cancel the mean–field shift. The maximum coherence time attained decreases with increasing peak density.

Comparing our model to this data, the most evident observation is that, for all cases, our model significantly underestimates the coherence time. This stems from the fact that the model does not include motional and collisional averaging. However, it succeeds to correctly capture all qualitative features, like the decrease of the maximum coherence time for increasing densities and the shift of the optimal bias field to lower fields for increasing densities. Quantitatively, this shift is slightly underestimated. Nevertheless, we are confident that the model can at least give an indication of where in the parameter space optimal parameters might hide.

Estimation of the optimal trap parameters We will now use the model to estimate the optimal trap parameters and the resulting minimal linewidth. In presence of gravity, the magnetic field and the density are given by

$$B = \frac{m}{\mu_B}(\omega_x^2 x^2 + \omega_y^2 y^2 + \omega_z^2 z^2)) \tag{70}$$

$$n = n_0 e^{-\frac{m}{2k_B T}(\omega_x^2 x^2 + \omega_y^2 y^2 + \omega_z^2 z^2) - 2gz)} \tag{71}$$

As for the zero–g case, the analysis can be simplified by exploiting scaling relations of the system. For the x– and y–directions, the scaling argument of the zero–g case can be applied: The frequency spread is invariant under the transformation (transformed variables being denoted by a prime)

$$\omega_x' = \lambda \omega_x \qquad n_0' = n_0 \qquad T' = T \qquad \Delta B' = \Delta B. \tag{72}$$

This transformation can be understood as "stretching the trap by a factor λ^{-1}", since it follows from eqs. (70),(71) that $n'(\lambda^{-1}x, y, z) = n(x, y, z), B'(\lambda^{-1}x, y, z) = B(x, y, z)$. Evidently, such a scaled version of the trap has the same frequency spread σ_Δ. The scaling relation for the y–direction is completely analogous: $\omega_y' = \lambda \omega_y$.

For ω_z, this argument does not apply any more, because of the gravity term linear in z. There is, however, a more complicated scaling relation. A scaling of

$$\omega_z' = \omega_z/\sqrt{\lambda} \qquad T' = \lambda T \qquad n_0' = \lambda^2 n_0 \qquad \Delta B' = \lambda \Delta B \tag{73}$$

creates a λ bigger trap with a λ^2 bigger spread

$$n'(x, y, \lambda z) = \lambda^2 n(x, y, z); \qquad B'(x, y, \lambda z) = \lambda B(x, y, z)$$

$$\sigma_\Delta' = \lambda^2 \sigma_\Delta.$$

The only relevant parameters are therefore n_0, T and ΔB. Consequently, it is sufficient to calculate the spread as a function of these variables for one specific choice of $\omega_x, \omega_y, \omega_z$. The result can be extrapolated to all other traps using the scaling relations. A result of such a calculation is presented in figure 32 The best coherence times are found in the region of both low densities and temperatures. This region, however, is experimentally unaccessible, since, for a given N, it corresponds to unrealistically low values of ω_x. The best realistic coherence time is found at the lowest possible value for ω_x. To compute the

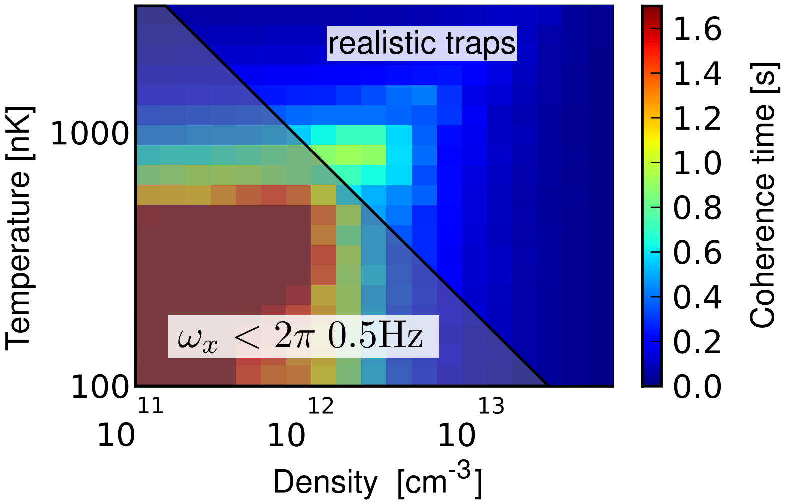

Figure 32: Coherence times calculated by the Monte–Carlo algorithm for a trap of $\omega_y = \omega_z = 1\text{kHz}$. As for the zero–g case, ΔB in each pixel is set to the value which maximizes the coherence time. The region to the left of the black line, for an atom number of $N = 10^5$, corresponds to an unrealistically low trapping frequency $\omega_x < 2\pi \cdot 0.5\text{Hz}$.

optimum trap parameters, we therefore assume $\omega_x = \omega_{\text{min}} = 2\pi \cdot 0.5\text{Hz}$. Furthermore, we assume $\omega_y = \omega_z$, as it is the case for a typical atom chip trap. Fixing the atom number (in our case to $N = 10^5$) then restricts the optimization to one line in the n_0–T–plane for a given ω_z. We have carried out such an optimization, ranging from $\omega_z = 2\pi \cdot 100\text{Hz}$ to $\omega_z = 2\pi \cdot 2\text{kHz}$ and from $n_0 = 10^{11}\text{cm}^{-3}$ to $n_0 = 3.2 \cdot 10^{13}\text{cm}^{-3}$. We find the parameters of the optimum trap

$$\omega_z = 2\pi \cdot 450\text{Hz} \qquad T = 260\text{nK} \qquad n_0 = 1.3 \cdot 10^{12}\text{cm}^{-3} \qquad \Delta B = 0.03\text{G} \tag{74}$$

yielding a coherence time of

$$T_C = 1.7\text{s} \tag{75}$$

3.2.4 Conclusion, Outlook

In summary, the coherence time is limited by dephasing due to the varying frequency shifts over the cloud. This effect can be partly cancelled by mutually compensating its two components, the second–order Zeeman shift and the mean–field shift. This compensation, however, is hampered by the gravitational sag, which shifts the atomic cloud away from the magnetic minimum and thus precludes an efficient compensation. Consequently, coherence times in microgravity should be considerably better than in presence of gravity.

In the following, we will discuss a number of aspects that could further influence the coherence time.

Spin echo techniques In nuclear magnetic resonance, inhomogeneities of the transition frequency can lead to dephasing of the spins and loss of coherence. Here, a large portion of the signal can be recovered by “refocusing” the dephased spins with “spin–echo” techniques. The simplest of these techniques consists of a $\pi/2$–π–$\pi/2$ sequence [140]. Its sensitivity to shifts changes sign after the intermediate π pulse. A constant shift of a spin is thus cancelled over the whole sequence. In this way, all constant inhomogeneous shifts are cancelled and cannot lead to dephasing any more.

In the case of our system, the application of this technique seems difficult, if not impossible: Most importantly, a straightforward application of a spin–echo sequence would also cancel the clock signal, which is a constant shift. One might argue that spin–echo could nevertheless be useful for other potential applications of our system, like e.g. a quantum memory, but even then the shift experienced by an atom is not constant over time, due to its motion and collisions in the trap. Indeed, it has been shown in [108] that spin–echo in our system is not observable for interrogation times of the order of seconds.

Anharmonic traps The above reasoning has been carried out for a harmonic trap, since this kind of trap is the most straightforward to implement. Better coherence properties, however, could be obtained with other types of trap. The ideal trap would be a box–like trap, with a constant magnetic field and density at its interior, In such a trap, the clock frequency would not vary over the cloud at all.

Interestingly, such “box traps” can be realized on atom chips [141]. Their trapping potential rises with a higher than harmonic power (typically x^4) along the weak trapping direction. Along the strong directions, their potential remains harmonic. In these directions, however, motional averaging could potentially suppress the shifts.

3.3 Stability budget

We will now turn the results of the previous sections into an estimation of the most important figure of merit of our clock: Its stability. The goal we have in mind is to estimate the potential of an “ideal” atom chip clock. Therefore, we will assume for each parameter the best value that can be obtained with current technology, rather than the value we estimate to reach in our first–generation experiment.

3.3.1 Contrast of the Ramsey fringes

The central idea of what limits the stability of a clock has already been shown in fig. 4. We reprint it here as figure 33, since all calculations in this section will refer to it.

We recall from section 1 that a Ramsey–type atomic clock is limited by noise on the excitation probability p as well as noise on the detuning Δ. Modeling both terms by

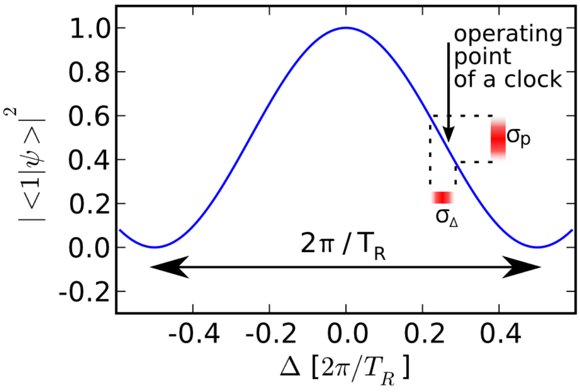

Figure 33: The central frequency–domain Ramsey fringe. Clocks are operated at the point of highest slope, where the transisition probability is the most sensitive to Δ. Here, a given error σ_p on the measurement of the transition probability translates into a minimal error σ_Δ on the frequency measurement.

white noise of standard deviation σ_p and σ_Δ, the clock stability reads (eq. (11))

$$\sigma_y(\tau) = \frac{\sigma_{\omega_{\text{at}}}}{\omega_{\text{at}}}\sqrt{\frac{T_C}{\tau}} = \sqrt{\frac{\sigma_\Delta^2}{\omega_{\text{at}}^2} + \frac{4\sigma_p^2}{\pi^2 Q_{\text{at}}^2}}\sqrt{\frac{T_C}{\tau}}$$

Here, $\Delta = \omega_{\text{at}} - \omega_{\text{fw}}$ refers to the detuning, T_C is the cycle time. Q_{at} is the quality factor of the atomic clock, related to the slope of the central Ramsey fringe by (eq. (9))

$$Q_{\text{at}} = \frac{2\omega_{\text{at}}}{\pi}\frac{dp}{d\Delta}\Big|_{\max}$$

To obtain $dp/d\Delta|_{\max}$, we use a model describing the Ramsey fringes in presence of particle losses and decoherence ([108], eqs. 4.8, 4.5)

$$p(T_R) = |\langle 1|\psi\rangle|^2 = \frac{1}{4}\left[(e^{-T_R/\tau_0} + e^{-T_R/\tau_1}) + 2e^{-T_R/\tau_c}\cos(\Delta T_R)\right] \tag{76}$$

$$\tau_c = \frac{1}{2}\left(\frac{1}{\tau_0} + \frac{1}{\tau_1}\right) + \frac{1}{\tau_\phi} \tag{77}$$

Here, τ_ϕ is the timescale of dephasing, which we have discussed in detail in the previous subsection (3.2): the superposition $(|0\rangle + e^{i\phi}|1\rangle)/\sqrt{2}$ decoheres into a classical mixture on a timescale τ_ϕ, resulting in a loss of fringe contrast. In a real experiment, the fringe contrast is further reduced by particle losses, described in (76) by attributing a lifetime of τ_i to the state $|i\rangle, i \in \{0, 1\}$. Losses contribute to decoherence, since an atom in the coherent superposition $(|0\rangle + e^{i\phi}|1\rangle)/\sqrt{2}$ can lose its $|0\rangle$– or $|1\rangle$–part in a loss. In this case, it is lost from the trap with a classical probability of $p = 0.5$, but with an equal probability the other part remains in the trap as an incoherent atom.

For the following considerations, we will assume $\tau_0, \tau_1 \gg \tau_\phi$. In our experiment, the lifetimes τ_0, τ_1 are limited by two–body losses in the atomic cloud, and in an "ideal" atom chip clock, the density could always be chosen so low that the above condition would be fulfilled.

With this assumption, we obtain from eq. (76) the optimum Q–factor

$$Q_{\text{opt}} = \frac{2\omega_{\text{at}}\tau_\phi}{e\pi} \tag{78}$$

achieved at an optimum Ramsey time of

$$T_{R,\text{opt}} = \tau_\phi$$

In the following, we will assume $\tau_c = 2.5\text{s}$, a value measured by several authors in a typical magnetic trap [39, 29]. Note that this value is greater than the optimum coherence time (75) predicted by our analysis of section 3.2. This analysis only presents a worst–case estimate and needs to be calibrated against experimental data. We therefore prefer to use the experimental value cited above. In this way, we obtain the optimal values for the quality factor and the Ramsey time

$$Q = 2.5 \cdot 10^{10}; \qquad T_R = 2.5\text{s} \tag{79}$$

Using these values, we will now estimate the contributions σ_p and σ_Δ to the single–shot error bar $\sigma_{y,\text{one shot}}$ of the frequency measurement.

3.3.2 Detection noise σ_p

Shot noise The excitation probability p is measured at the end of a clock cycle by measuring N_1 and N_0 and computing $p = N_1/(N_1 + N_0)$. Consequently, the error σ_p is dominated by noise of the detection. It has been shown [49] that a proper design of the detection system can achieve an error bar $\sigma_{N_\alpha} \ll 1/\sqrt{N_\alpha}$, so that the noise σ_p is dominated by the atomic shot noise, which contributes a white–noise of amplitude.

$$\sigma_p = \frac{1}{2\sqrt{N}}$$

Its contribution to the clock stability is therefore

$$\sigma_{y,\text{sn}} = \frac{1}{\pi Q \sqrt{N}} = 1.3 \cdot 10^{-13} \cdot \frac{1}{\sqrt{N/(10^4\text{atoms})}} \tag{80}$$

Technical noise Following our philosophy of estimating the performance of an "ideal" clock, we will not include technical detection noise in the stability budget. Nevertheless, it will be helpful for the following analysis to quote a figure–of–merit of a typical detection system used in an atom chip experiment. Such data is presented in sec. 3.6 of [108], stating that

$$\sigma_N = 0.6\sqrt{N} \tag{81}$$

can be achieved in a setup comparable to ours. Strictly, this has been measured only for one specific $N = 2.5 \cdot 10^3$. However, the quoted noise is dominated by photonic shot noise. In a straightforward extension (using a factor of k more photons to detect a factor of k more atoms), this noise scales such that the above formula will remain valid for higher values of N. We will therefore use it as a rule of thumb. However, we emphasize the fact that this noise does not arise from any fundamental limit whatsoever. It merely is the best figure of a "typical" carefully constructed imaging system we are aware of. With more advanced schemes, e.g. optical cavities, atoms can be counted with an error $\sigma_N \ll 1$.

3.3.3 Frequency noise σ_Δ

Magnetic field noise σ_B We recall from section 3.1.2 that a magnetic field B shifts the clock frequency by (eq. (44))

$$\Delta f_{|1\rangle-|0\rangle} = \Delta f_0 + \beta(B - B_m)^2$$

In the clock, the atomic cloud will be sufficiently cold to fulfill $k_B T/(g_F m_F \mu_B) \ll B_0$ with $B_0 \vec{e}_x$ being the magnetic field at the trap bottom. We can therefore assume that all atoms experience approximately the field B_0, which we will expand into $\vec{B}_0 = (B_m + \Delta B + \sigma_B)\vec{e}_x$. Here, ΔB is a deliberately introduced offset from the magic field B_m and σ_B is a white noise term, modelling fluctuations of the background field. To minimize the sensitivity to fluctuations, a natural choice is to operate the trap at the magic field ($\Delta B = 0$). In this case, magnetic field noise shifts the atomic transition only to second order. However, we will show in section 3.2, that a nonzero detuning $\Delta B = 0.03\text{G}$ may be favorable to increase the coherence time of the cloud. For both scenarios, we estimate the field noise to contribute to the single–shot error a term

$$\sigma_y = \frac{2\sqrt{2}\pi\beta\sigma_B^2}{\omega_{\text{at}}} = 9.0 \cdot 10^{-14}\,(\sigma_B/\text{mG})^2 \qquad \text{for a clock operating at } \Delta B = 0$$

$$\sigma_y = \frac{4\pi\beta\Delta B\sigma_B}{\omega_{\text{at}}} = 3.8 \cdot 10^{-12}(\sigma_B/\text{mG}) \qquad \text{for a clock operating at } \Delta B = 0.03\text{G}$$

To keep these fluctuations below the shot noise level (eq. (80)), we have to control the x–component of the magnetic field with a precision of

$$\sigma_B < 1.2\text{mG} \qquad \text{for a clock operating at } \Delta B = 0$$

$$\sigma_B < 35\mu\text{G} \qquad \text{for a clock operating at } \Delta B = 0.03\text{G}$$

As we will discuss in section 4, our experiment is designed such as to reach the latter target.

Fluctuation of the atomic number density We recall from section 3.1.4 that the mean–field of the atomic cloud shifts the clock transition by (eq. 61, 62)

$$\begin{aligned}\omega_{01}-\omega_{01,\mathrm{free}} &= \frac{4\pi\hbar}{m}a_0 n\left((a_{11}-a_{00})+f(2a_{01}-a_{00}-a_{11})\right) && (82)\\ &= \frac{4\pi\hbar}{m}a_0 n(-4.97-0.27f) && \text{for a thermal cloud}\\ \omega_{01}-\omega_{01,\mathrm{free}} &= \frac{1}{2}(\omega_{01}-\omega_{01,\mathrm{free}})_{\mathrm{thermal}} && (83)\\ &= \frac{4\pi\hbar}{m}a_0 n(-2.49-0.14f) && \text{for a condensate}\end{aligned}$$

Fluctuations in both the atomic density n and the population inversion f translate directly into a fluctuation of the clock frequency. In this paragraph, we will focus on the former effect, a shift caused by fluctuations of n. Fluctuations of f will be treated in following paragraphs. The dominant contribution to this shift are fluctuations of the total atom number N. These fluctuations, however, can be largely corrected for *ex post*. To this end, one computes the atomic density from the detection data of a clock measurement, N_1, N_0, and corrects the frequency measurement to compensate eq. (59). $\langle n\rangle$ is computed from the relations

$$\langle n\rangle_{\mathrm{th}} = \frac{n_0}{\sqrt{8}} = (N_0+N_1)\left(\frac{m}{4\pi k_B T}\right)^{3/2}\bar{\omega}^3 \quad \text{for a thermal cloud}$$

(84)

$$\langle n\rangle_{\mathrm{BEC}} = \frac{4}{7}n_0 = \frac{4}{7}\frac{m}{4\pi\hbar^2 a}\frac{15^{2/5}}{2}\left(\frac{Na\sqrt{m\bar{\omega}}}{\sqrt{\hbar}}\right)^{2/5}\hbar\bar{\omega} \quad \text{for a BEC in the Thomas–Fermi limit}$$

Here, $\bar{\omega} = (\omega_x\omega_y\omega_z)^{1/3}$ is the harmonic mean of the trap frequencies and a is the scattering length, which we will approximate by $a \approx a_{00}$. Using such an ex post correction, fluctuations of n are corrected up to the uncertainty $\sigma_{\langle n\rangle}$. We will now discuss which errors limit the extrapolation of these values.

Contribution to $\sigma_{\langle n\rangle}$ from the detection noise For a "typical" detection, a contribution to $\sigma_{\langle n\rangle}$ arises from the detection noise σ_N as given by eq. (81). Its contribution to the stability is computed using eqs. (81), (59) and (84):

$$\begin{aligned}\sigma_y &= \frac{4\pi\hbar a_0}{m\omega_{01}}(a_{11}-a_{00})\langle n\rangle_{\mathrm{th}}\frac{\sigma_N}{N} && (85)\\ &= 5.7\cdot 10^{-14}\left(\frac{\bar{\omega}}{2\pi\,100\mathrm{Hz}}\right)^3\left(\frac{T}{500\mathrm{nK}}\right)^{-3/2}\sqrt{\frac{N}{10^4\mathrm{atoms}}} && \text{thermal}\\ \sigma_y &= \frac{2\pi\hbar a_0}{m\omega_{01}}(a_{11}-a_{00})\langle n\rangle_{\mathrm{BEC}}\frac{\sigma_N}{N} && (86)\\ &= 8.8\cdot 10^{-12}\left(\frac{\bar{\omega}}{2\pi 100\mathrm{Hz}}\right)^{6/5}\left(\frac{N}{10^4\mathrm{atoms}}\right)^{-1/10} && \text{BEC}\end{aligned}$$

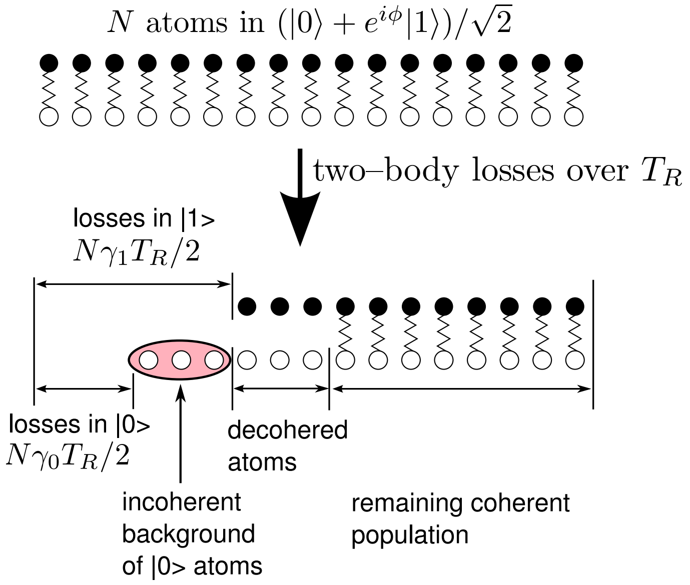

Figure 34: Two–body losses in our system: Losses appear in both clock states $|0\rangle$ and $|1\rangle$, with the loss rate in state $|1\rangle$ being larger. Consequently, an incoherent background population builds up in state $|0\rangle$. The coherent population is further reduced by loss–induced decoherence, which is already included in the coherence time assumed above.

Fluctuations due to particle loss Atoms can be lost in our system due to the unavoidable two–body losses. These losses can cause a fluctuating mean–field shift in two ways:
Firstly, they limit the ex post correction described above. Even if the atom number is perfectly measured at the end of the clock cycle, this measured N is the result of a Poissonian process and consequently, the extrapolation of its past must contain a statistical error. The uncertainty $\sigma_{\langle n\rangle}$ is then limited by this unknown evolution of N over the clock cycle.
Secondly, the losses in our system are asymmetric: Atoms in state $|1\rangle$ are more likely to decay than atoms in state $|0\rangle$. This leads to the emergence of an incoherent background population in state $|0\rangle$, which causes a fluctuating shift on the remaining coherent population.

An illustration of these losses is presented in figure 34. Precisely, we will describe them as in [108] by an exponential decay: $\dot{N}_i = -\gamma_i N_i, i \in \{0,1\}$. Assuming a balanced population of the clock states $N_0 = N_1$, the loss rates γ_i are given by

$$\begin{aligned} \gamma_0 &= \gamma_{01} g^{(2)}_{01}(0) \langle n\rangle /2 \\ \gamma_1 &= \gamma_{01} g^{(2)}_{01}(0) \langle n\rangle /2 + \gamma_{11} g^{(2)}_{11}(0) \langle n\rangle /2 \end{aligned} \quad (87)$$

Fluctuations due to symmetric particle loss Let us assume losses to be small ($\gamma_0, \gamma_1 \ll T_R^{-1}$). Then, during the interrogation, a total number of

$$N_{\text{sym}} = N(\gamma_0 + \gamma_1)T_R/2$$

atoms is lost from the trap and this number fluctuates from shot to shot by $\sqrt{N_{\text{sym}}}$. This fluctuation cannot be corrected for ex post, since N is measured only at the end of the clock cycle. Using the loss rates from [126], this fluctuation degrades the stability by

$$\begin{aligned}
\sigma_y &= \frac{4\pi\hbar a_0}{m\omega_{01}}(a_{11} - a_{00}) \langle n \rangle_{\text{th}} \left(\frac{T_R(2\gamma_{01} + \gamma_{11}) \langle n \rangle_{\text{th}}}{2N} \right)^{1/2} && (88) \\
&= 2.3 \cdot 10^{-14} \frac{N}{10^4 \text{atoms}} \left(\frac{\bar{\omega}}{2\pi 100\text{Hz}} \right)^{9/2} \left(\frac{T}{500\text{nK}} \right)^{-9/4} \left(\frac{T_R}{2.5\text{s}} \right)^{1/2} && \text{thermal} \\
\sigma_y &= \frac{2\pi\hbar a_0}{m\omega_{01}}(a_{11} - a_{00}) \langle n \rangle_{\text{BEC}} \left(\frac{T_R(2\gamma_{01} + \gamma_{11}) \langle n \rangle_{\text{BEC}}}{4N} \right)^{1/2} && (89) \\
&= 4.3 \cdot 10^{-11} \left(\frac{\bar{\omega}}{2\pi 100\text{Hz}} \right)^{9/5} \left(\frac{N}{10^4 \text{atoms}} \right)^{1/10} \left(\frac{T_R}{2.5\text{s}} \right)^{1/2} && \text{BEC}
\end{aligned}$$

We have normalized this number to the parameters of the norm trap ($\bar{\omega} = 2\pi \cdot 100\text{Hz}$, $N = 10^4$), even though the above approximation $\gamma_0, \gamma_1 \ll T_R^{-1}$ is not fulfilled for this trap. Consequently, the result is valid only for condensates with a much lower density than in our norm trap. A clock would have to operate at such a much lower density, in order to supress this huge shift.

Fluctuations due to asymmetric particle loss Two colliding atoms in state $|1\rangle$ can be lost by spin–exchange processes or dipolar relaxation. In this way, atoms in the interrogation state $(|0\rangle + e^{i\phi}|1\rangle)/\sqrt{2}$ can lose their $|1\rangle$ part by collisions, which leads to the emergence of an incoherent population in state $|0\rangle$. We note that spin–exchange scattering (but not dipolar relaxation) also leads to the emergence of a population in $|2, 2\rangle$, but we will neglect this latter effect for two reasons: We are not aware of loss rate measurements for state $|1\rangle$, which would include the ratio of spin–exchange to dipolar relaxation. Furthermore, the population in $|2, 2\rangle$ could be removed by repumping it to an untrapped state, e.g. by a weak, continuous microwave radiation.

In contrast, this is not possible for the incoherent population in state $|0\rangle$. Also, this population cannot be detected ex post, since it is indistinguishable from the clock signal. To estimate the shift which this population induces on the remaining coherent atoms, we will assume the losses to be small $(\gamma_1 - \gamma_0)T_R \ll 1$. During the interrogation time, the incoherent $|0\rangle$ population then grows to a mean number of $N_{\text{asym}} = \gamma_{11} T_R g_{11}^{(2)}(0) \langle n \rangle N/4$ atoms, with a shot–noise–limited fluctuation of $\sigma_{N_{\text{asym}}} = \sqrt{N_{\text{asym}}}$. The shift contributed by these atoms is described by eqs. 61, 62, with $f = 1$. With these assumptions, they degrade the clock stability by

$$\begin{aligned}
\sigma_y &= \frac{4\pi\hbar a_0}{m\omega_{01}}(-2a_{00}+2a_{01})\left\langle n\right\rangle_{\mathrm{th}}\left(\frac{T_R\gamma_{11}\left\langle n\right\rangle_{\mathrm{th}}}{2N}\right)^{1/2} && (90)\\
&= 1.5\cdot 10^{-14}\frac{N}{10^4\text{atoms}}\left(\frac{\bar\omega}{2\pi 100\text{Hz}}\right)^{9/2}\left(\frac{T}{500\text{nK}}\right)^{-9/4}\left(\frac{T_R}{2.5\text{s}}\right)^{1/2} && \text{for a thermal cloud}\\
\sigma_y &= \frac{2\pi\hbar a_0}{m\omega_{01}}(-2a_{00}+2a_{01})\left\langle n\right\rangle_{\mathrm{bec}}\left(\frac{T_R\gamma_{11}\left\langle n\right\rangle_{\mathrm{bec}}}{4N}\right)^{1/2} && (91)\\
&= 2.7\cdot 10^{-11}\left(\frac{\bar\omega}{2\pi 100\text{Hz}}\right)^{9/5}\left(\frac{N}{10^4\text{atoms}}\right)^{1/10}\left(\frac{T_R}{2.5\text{s}}\right)^{1/2} && \text{for a BEC}
\end{aligned}$$

Amplitude noise of the excitation pulses Noise on the amplitude of the $\pi/2$ pulses will affect the clock in two ways: A fluctuating pulse surface $\Omega_I t_p$ will lead to shot–to–shot fluctuations of the population inversion (f in eqs. 61, 62), leading to shot–to–shot fluctuations of the mean–field shift. Furthermore, fluctuations on the Rabi frequencies $\Omega_{\mathrm{RF}}, \Omega_{\mathrm{MW}}$ of the RF and microwave excitation fields lead to a fluctuating lightshift (δ_{01} of eq. (51)).

To estimate the influence of the former effect, we calculate the effect of an error σ_f on eqs. 61, 62. To this end, we expand $f = \cos(\Omega_I t)$ around its intended value $f = 0, \Omega_I t = \pi/2$ to obtain

$$\sigma_f = \frac{\pi}{2}\frac{\sigma_{\Omega_I}}{\Omega_I}$$

Ω_{RF} and Ω_{MW} enter symmetrically into eq. (49). We will therefore consider only the error on Ω_{MW}, assuming that $\sigma_{\Omega_{\mathrm{RF}}} = 0$. The influence of $\sigma_{\Omega_{\mathrm{RF}}}$ can be estimated by exchanging Ω_{RF} and Ω_{MW}. The detuning of the microwave is precisely controlled, so the main contribution to $\sigma_{\Omega_{\mathrm{MW}}}$ comes from fluctuations of the microwave power P_{MW}. Using the relation $\sigma_{\Omega_{\mathrm{MW}}}/\Omega_{\mathrm{MW}} = \sigma_{\mathrm{P_{MW}}}/[2P_{\mathrm{MW}}]$ we obtain

$$\begin{aligned}
\sigma_y &= \frac{4\pi\hbar a_0}{m\omega_{01}}(a_{11}+a_{00}-2a_{01})\left\langle n\right\rangle_{\mathrm{th}}\frac{\pi}{4}\frac{\sigma_{P_{\mathrm{MW}}}}{P_{\mathrm{MW}}} && (92)\\
&= 4.1\cdot 10^{-15}\left(\frac{N}{10^4\text{atoms}}\right)\left(\frac{T}{500\text{nK}}\right)^{-3/2}\left(\frac{\bar\omega}{2\pi 100\text{Hz}}\right)^{3}\left(\frac{\sigma_{P_{\mathrm{MW}}}/P_{\mathrm{MW}}}{10^{-2}}\right) && \text{thermal}\\
\sigma_y &= \frac{2\pi\hbar a_0}{m\omega_{01}}(a_{11}+a_{00}-2a_{01})\left\langle n\right\rangle_{\mathrm{BEC}}\frac{\pi}{4}\frac{\sigma_{P_{\mathrm{MW}}}}{P_{\mathrm{MW}}} && (93)\\
&= 6.5\cdot 10^{-13}\left(\frac{\bar\omega}{2\pi 100\text{Hz}}\right)^{6/5}\left(\frac{N}{10^4}\right)^{2/5}\left(\frac{\sigma_{P_{\mathrm{MW}}}/P_{\mathrm{MW}}}{10^{-2}}\right) && \text{BEC}
\end{aligned}$$

Let us now turn to an estimate of the influence of the latter effect, shot–to–shot fluctuations of the lightshifts created by the $\pi/2$ pulses. We recall from section 3.1.3 that only the microwave photon creates a lightshift, of magnitude (eq: 51)

$$\delta_{01} = \frac{\Omega_{\mathrm{MW}}^2}{4\Delta}$$

To minimize the absolute value of this lightshift, we will place as much power as possible into the RF photon. As discussed in section 3.1.3, this is limited by the conditions $\Omega_{\mathrm{RF}} \ll \Delta, \Delta \ll \Delta_B$ and for the following reasoning we will assume the values $\Delta = \Delta_B/10 = 2\pi \cdot 200\mathrm{kHz}$, $\Omega_{\mathrm{RF}} = \Delta/10 = 2\pi 20\mathrm{kHz}$, which, with the assumption $\Omega_I = 2\pi \cdot 1\mathrm{kHz}$, implies $\Omega_{\mathrm{MW}} = 20\mathrm{kHz}$.
Even though this choice minimizes the absolute value of the lightshift, shot–to–shot fluctuations of the shift can still degrade the clock stability. To compute this shot–to–shot fluctuation, we note that the lightshift is present only during the $\pi/2$ pulses and we will discuss its effect only for the first one (the result being equally valid for the second one). During this pulse, the coherence is gradually built up and the phase of the superposition $(\cos\theta|0\rangle + e^{i\phi}\sin\theta|1\rangle)$ is sensitive to a shift δ'_{01} according to $d\phi/dt = g(t)\delta'_{01}$ with the sensitivity function g, which, during the first $\pi/2$ pulse varies as $g(t) = \sin(\Omega_I t)$ [44]. The fluctuating lightshift then causes a phase uncertainty

$$\sigma_\phi = \frac{2}{\pi}\sigma_{\delta_{01}} t_P = \frac{\sigma_{\delta_{01}}}{\Omega_I}$$

Each $\pi/2$ pulse contributes this uncertainty, and both pulses are uncorrelated. Quadratically summing up both contributions and using eq. (49), we obtain their contribution to the clock stability:

$$\sigma_y = \frac{\sqrt{2}\sigma_{\Omega_{\mathrm{MW}}}}{\Omega_{\mathrm{MW}} T_R \omega_{\mathrm{at}}} = 1.4 \cdot 10^{-13} \left(\frac{\sigma_{\Omega_{\mathrm{MW}}}/\Omega_{\mathrm{MW}}}{10^{-2}} \right).$$

Noise of the local oscillator, Dick effect We recall from section 1 that an atomic clock measures $\Delta = \omega_{\mathrm{at}} - \omega_{\mathrm{fw}}$. Noise on the atomic transition is indistinguishable from noise on the flywheel, and consequently, the latter also contributes to the stability budget. This effect is particularly pronounced for clocks with a pulsed mode of operation, which take repeated measurements separated by a cycle time T_C. Due to an aliasing effect, they are particularly sensitive to flywheel noise at integer multiples of the cycle frequency $f_n = n/T_c, n \in \mathbf{N}$, a phenomenon known as the “Dick effect”.

To estimate the influence of this effect on our clock stability, we will follow the treatment in [44]. We will assume that our clock takes a cycle time T_C for one measurement, composed of a loading time T_L and a measurement time T_R such that $T_L + T_R = T_C$. We will neglect the time t_P spent with the excitation pulses, assuming that $t_P \ll T_R$. Evidently, noise of the flywheel will not affect the clock during the loading time. However, it has maximum impact during the Ramsey time. Again, this is best expressed by the sensitivity function g, defined stepwise by

$$g(t) = \begin{cases} 0 & 0 < t < T_C - T_R \\ 1 & T_C - T_R < t < T_C \end{cases} \tag{94}$$

so that the evolution of the atomic phase can be written as $d\phi/dt = g(t)\Delta(t)$. It can then be shown [142, 44] that the flywheel noise contributes to the clock stability by

$$\sigma_y(\tau) = \tau^{-1/2} \times \left[\sum_{n=1}^{\infty} \left| \frac{g_n}{g_0} \right|^2 S_y^{\mathrm{fw}}(n f_C) \right]^{1/2} \tag{95}$$

$$g_n = \frac{1}{T_C} \int_0^{T_C} dt\, g(t)\, e^{-i2\pi n f_C t} \tag{96}$$

Here, $f_C = 1/T_C$ is the cycle frequency and S_y^{fw} is the spectral density of the flywheel's frequency noise. A pulsed clock picks up noise at all integer multiples $n f_C$ of the cycle frequency and converts it to a white frequency noise with an efficiency $|g_n/g_0|^2$.

In our prototype experiment, the flywheel signal will be generated by a cryogenic oscillator. Ultimately, the reference oscillator will be a highly–stable quartz. Let us first consider the former case, that the interrogation signal is provided by a cryogenic oscillator and upconverted to our clock frequency by a synthesis chain (see section 6). In comparable setups [44], the dominant source of flywheel noise has been found to be the noise of the synthesis chain, with the dominant contribution being flicker phase noise. We will model it by the data of ([44], p.139),

$$S_y^{\mathrm{fw}}(f) = 4.5 \cdot 10^{-28} \mathrm{Hz}^{-2} f \tag{97}$$

Inserting this into eqs. (94), (96), (95), and summing over the first 400000 terms, we obtain the contributions

$$\sigma_y(\tau) = 3.4 \cdot 10^{-14} \cdot \sqrt{\mathrm{s}} \qquad \text{for } T_R = 2.5\mathrm{s}, T_C = 23\mathrm{s}$$
$$\sigma_y(\tau) = 1.6 \cdot 10^{-14} \cdot \sqrt{\mathrm{s}} \qquad \text{for } T_R = 2.5\mathrm{s}, T_C = 5\mathrm{s}$$

Ultimately, the interrogation signal will be driven from an ultra–stable, but non–cryogenic, quartz oscillator. To estimate the Dick effect in this case, we will use the data of the reference oscillator of the PHARAO space clock ([81], data converted according to [48])

$$S_y(f) < 2.4 \cdot 10^{-27} \mathrm{Hz} f^{-1} + 1.2 \cdot 10^{-26} + 3 \cdot 10^{-27} \frac{1}{\mathrm{Hz}} f + 1.9 \cdot 10^{-28} \frac{1}{\mathrm{Hz}^2} f^2$$

Using the same procedure as for the cryogenic oscillator, we obtain the contributions

$$\sigma_y(\tau) = 4.1 \cdot 10^{-13} \cdot \sqrt{\mathrm{s}} \qquad \text{for } T_R = 2.5\mathrm{s}, T_C = 23\mathrm{s}$$
$$\sigma_y(\tau) = 1.2 \cdot 10^{-13} \cdot \sqrt{\mathrm{s}} \qquad \text{for } T_R = 2.5\mathrm{s}, T_C = 5\mathrm{s}$$

3.3.4 Stability budget

We will now assemble the results of the previous paragraphs to a stability budget for our clock. To this end, we suppose that all of the above errors are uncorrelated contributions of white frequency noise, which add quadratically and scale with the integration time τ as

$$\sigma_y(\tau) = \sigma_{y,\text{one shot}}\sqrt{\frac{T_C}{\tau}}.$$

We will consider two scenarios of the stability budget:

1. The prototype experiment of [29, 108], with $\langle n\rangle = 4\cdot 10^{11}\text{cm}^{-3}$, $N = 10^4$ atoms.
2. An improved version, similar to the proposal in [108], with the parameters
    - $(\omega_x, \omega_y, \omega_z) = 2\pi(5, 70, 70)\text{Hz}$
    - $T = 500\text{nK}$
    - $N = 10^4$ atoms
    - $T_R = 2.5\text{s}$
    - $T_C = 23\text{s}$

    and featuring the following technical improvements:
    - an optimized detection – shot–noise limited for measurements of N_0, N_1, and better than the loss limit for measurements of $N_0 + N_1$
    - ex post correction of the fluctuating mean–field shift
    - control of the magnetic field to $\sigma_B = 35\mu\text{G}$

    We plan to reach these specifications in the first generation of the dedicated clock experiment described in this thesis.
3. The improved version as above, with the following technical improvements
    - an atom number of 10^5
    - a cycle time of $T_C = 5\text{s}$, while keeping a Ramsey time of $T_R = 2.5\text{s}$.

In all improved scenarios, we assume a control of the power of the excitation fields to the relative 10^{-3} level. The resulting budgets are presented in table 2. With respect to the proof–of–principle experiment, one order of magnitude can be gained with straightforward improvements. The commercially interesting target of $10^{-13}\sqrt{\text{s}}$ could be reached with substantial improvements on the loading procedure, which seem realistic in the long term.

3.3.5 Outlook

Scaling behaviour It is interesting to ask whether there exist ideal parameters for clock operation and the above formulae seem to give a clear answer: The key to a good clock performance is a high number of atoms, in order to suppress the atomic shot noise. A high atom number also increases all uncertainties related to the mean–field shift and

	proof of principle [29, 108]	**improved version** + mag. shield + shot–noise lim. det. + shallow trap	**long–term perspective** +more atoms +faster loading
detection noise	$1.02 \cdot 10^{-12}$	$1.3 \cdot 10^{-13}$	$4.1 \cdot 10^{-14}$
magnetic field noise	$3.2 \cdot 10^{-12}$	$1.2 \cdot 10^{-16}$	$1.2 \cdot 10^{-16}$
fluctuating mean–field shift			
• uncorrected σ_N	$8.8 \cdot 10^{-13}$	–	–
• sym. + asym. losses	–	$1.1 \cdot 10^{-16}$	$1.1 \cdot 10^{-15}$
$\pi/2$ pulses, mf shift	–	$1.5 \cdot 10^{-17}$	$1.5 \cdot 10^{-16}$
$\pi/2$ pulses, lightshift	–	$1.4 \cdot 10^{-14}$	$1.4 \cdot 10^{-14}$
Dick effect	–	$7.1 \cdot 10^{-15}$	$3.4 \cdot 10^{-15}$
total single–shot noise	$3.4 \cdot 10^{-12}$	$1.4 \cdot 10^{-13}$	$4.4 \cdot 10^{-14}$
cycle time	23s	23s	5s
stability	$1.7 \cdot 10^{-11}\sqrt{\mathrm{s}}\tau^{-1/2}$	$6.8 \cdot 10^{-13}\sqrt{\mathrm{s}}\tau^{-1/2}$	$1.0 \cdot 10^{-13}\sqrt{\mathrm{s}}\tau^{-1/2}$

Table 2: Stability budgets for three scenarios of the clock

losses, but these errors can easily be reduced by choosing a higher temperature (which makes it even easier to achieve high atom numbers).
This idea looks appealing, but must be stated with a clear caveat: It is not clear how the coherence time scales with temperature and, as we have shown in the last subsection 3.2, there are good reasons why it could diminish for increasing temperature.

Thermal cloud vs. BEC Our setup is able to produce a BEC and one might well ask whether a BEC could be a better clock medium than a thermal cloud. The above formulae suggest that this is not the case, because of the huge two–body loss rate. Even a BEC with only $N = 10^4$ in the "improved" trap of table 2 would have a mean density of $\langle n\rangle = 1.2 \cdot 10^{-13}\text{cm}^{-3}$, resulting in a loss rate for the state $|1\rangle$ of $\gamma = 1.4\text{s}^{-1}$. Apart from limiting the interrogation time, such huge losses would give rise to equally huge fluctuations of all mean–field induced shifts. Nonetheless, the ability to perform Ramsey spectroscopy on a BEC will be an interesting tool, e.g. to precisely measure the dependence of the mean–field shift on a population imbalance (the constant ξ in a mean–field shift of the kind $\delta\omega = \kappa n(\zeta + f\xi)$).

Caveats and uncertainties in this budget A number of assumptions in the above budget are subject to care: Firstly, there is the issue of a possible population of the state $|2, 2\rangle$. This state can be populated by atoms of state $|2, 1\rangle$ undergoing a spin–exchange collision. The state $|2, 2\rangle$ is equally trapped, so these atoms would accumulate in the trap and lead to fluctuating shifts of an unknwon order of magnitude. We are optimistic that this problem can be circumvented, e.g. by applying a continuous shield of microwave radiation which pumps these atoms into an untrapped state. Secondly, we have neglected background losses in the above budget, arguing that they could be made negligible in an "ideal" clock by a careful construction of the vacuum system. In a first–generation experiment, however, the vacuum lifetime can well be limited to the order of seconds. This could reduce the possible interrogation time below the projected 2.5s. The stability, however, should remain of the same order of magnitude.

The most crucial unknown clearly is the coherence time of the system. This depends strongly on the parameters of the trap [39] and is difficult to predict. Strictly speaking, we cannot even be sure whether the projected 2.5s of coherence time can be reached in the "improved" trap of table 2. On the other hand, there might exist parameter sets leading to a greatly enhanced coherence time. This would potentially lead to an even better stability, since, according to eqs. (11),(78), stability scales with $1/T_R$. Clearly, an experimentally validated model of the coherence in different traps is the missing link to estimate the ultimate potential of a chip clock.

Scalability of the clock Being built on an atom chip, our clock is inherently scalable: It would be easily possible to run several clocks in parallel, either by duplicating the whole setup or by implementing multiple clocks on the same chip, and it is interesting to ask whether such an approach could improve the performance of the clock.
The most evident way to parallelize the clock would be to operate multiple identical

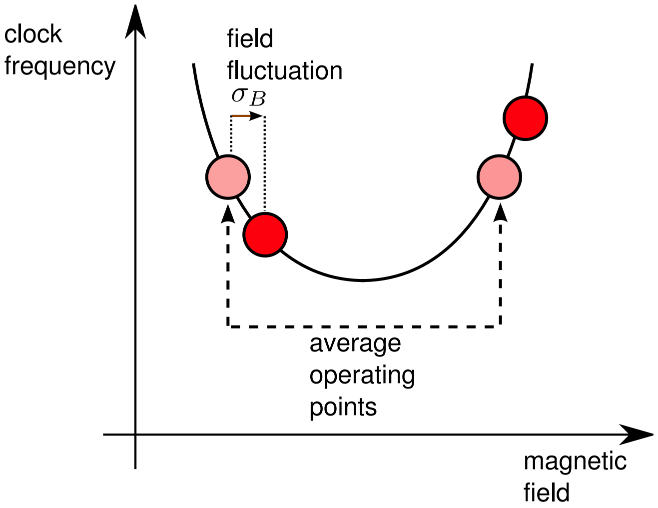

Figure 35: Technical shifts can be largely reduced by operating multiple clocks in parallel. Here, two clocks (red circles) operate at slightly different values of the magnetic field. Each of them is first–order sensitive to fluctuations of the magnetic field, albeit with different sign. A stable clock signal can be generated by taking the average of both clocks. At the same time, the difference of their signals can be used to measure the magnetic field.

copies of the whole clock in parallel, each of them including all technical features to produce and interrogate an atomic cloud on its own. Such an array of clocks would have one significant advantage: It would not suffer from the dead time which occurs in our clock during the preparation of a new atomic cloud. In an array of clocks, the dead time of one clock could be bridged by another clock taking data at this same time. In this way, the array as a whole could measure continuously, even if every single clock had a nonzero dead time.

On a lower level, one could implement multiple clocks on one chip. In contrast to the upper scenario, these micro–clocks would probably have to load and measure synchronously, since otherwise the magnetic fields and light fields of a charging clock would create shifts on a measuring clock nearby. Even with this constraint of synchronous operation, however, parallelization could be beneficial in several ways. In the best case it would be possible to charge each micro–clock from a magneto–optical trap of its own, by creating multiple quadrupole minima in the same optical molasses field [143]. In this way, M micro–clocks could provide a factor of M more atoms than a single clock, which would reduce the atomic shot–noise by $1/\sqrt{M}$.

Furthermore, an array of micro–clocks could be used to reduce technical noise, in a way that is illustrated in figure 35 for the case of two parallel clocks. Each of the micro–clocks could be run at slightly different parameters, for instance at magnetic field values slightly higher or lower than the magic field. At these operating points, both micro–clocks are first–order sensitive to shot–to–shot fluctuations of the magnetic field, albeit with different sign. If the average of both micro–clocks is taken as the overall clock signal, this first–order dependence cancels. The resulting clock would be as stable as one single clock operating at the magic field.

At the same time, however, the *difference* of both clock signals is a measure of the magnetic background field. In this way, fluctuations of the background field could be measured along with the clock signal without additional overhead and these measurements could be used to correct shifts of even higher order. Similar configurations can be conceived that are sensitive to other technical fluctuations like e.g. noise of the microwave pulses. Such an approach might significantly alleviate the demands on shielding and the stability of the DC and RF current supplies.

Interestingly, this approach would be beneficial even if the micro–clocks were loaded from a fixed number of atoms N, produced, e.g., by a single MOT. This becomes clear by considering the performance of a shot–noise–limited clock (eq. (12))

$$\sigma_y(\tau) = \frac{1}{\pi Q_{\mathrm{at}}\sqrt{N}}\sqrt{\frac{T_C}{\tau}}$$

Splitting this clock into M micro–clocks with atom number N/M each, and defining the overall clock signal as the average of all M clock signals, one recovers the same stability as for a single clock with N atoms. In this way, M micro–clocks could deliver the same stability as a single clock, but their individual clock signals would add $M-1$ new observables, which could be used to sense external noise.

4 Experimental setup

To transform the ideal clock of the last section into reality, some technical preparations are necessary: To fill an atom chip trap with atoms, the chip has to be mounted in an ultrahigh vacuum chamber and the atoms must be pre–cooled by laser cooling techniques. The requires an experimental setup comprising a laser system, an UHV chamber and magnetic field coils, which has been devised in a similar fashion for multiple atom chip experiments all over the world [84, 117, 144, 145]. Basically, our implementation resembles closely these previous ones, and we sketch it in the subsections 4.2 to 4.4.2 of this chapter. More place is devoted, however, to the technical features which we have designed and constructed specifically for this particular setup. This is most notably the magnetic shielding (subsection 4.5) and a study of the homogeneity of the magnetic fields (subsection 4.6).

The design of the chip and the electronics are so crucial components that they will be the subjects of dedicated later chapters (5, 6).

4.1 The components of our setup

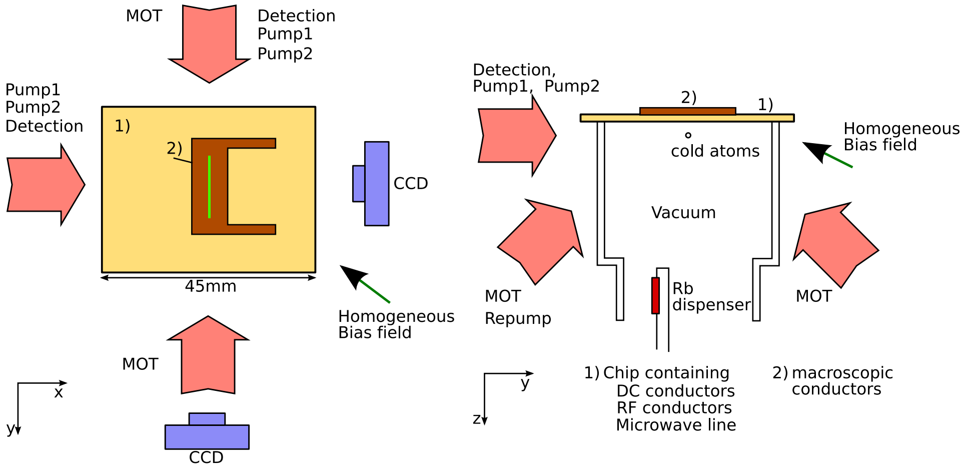

Figure 36: The components of our setup

The components of our experimental setup are depicted in Figure 36. From a physical perspective, we have only few and well–controlled tools to produce, manipulate and detect our atoms:

1. A dispenser to prepare a Rb vapor, and an ultrahigh vacuum (UHV) chamber to isolate it from collisions with other gases
2. Laser beams to cool the atoms, pump them into certain internal states and detect them
3. Static magnetic fields,

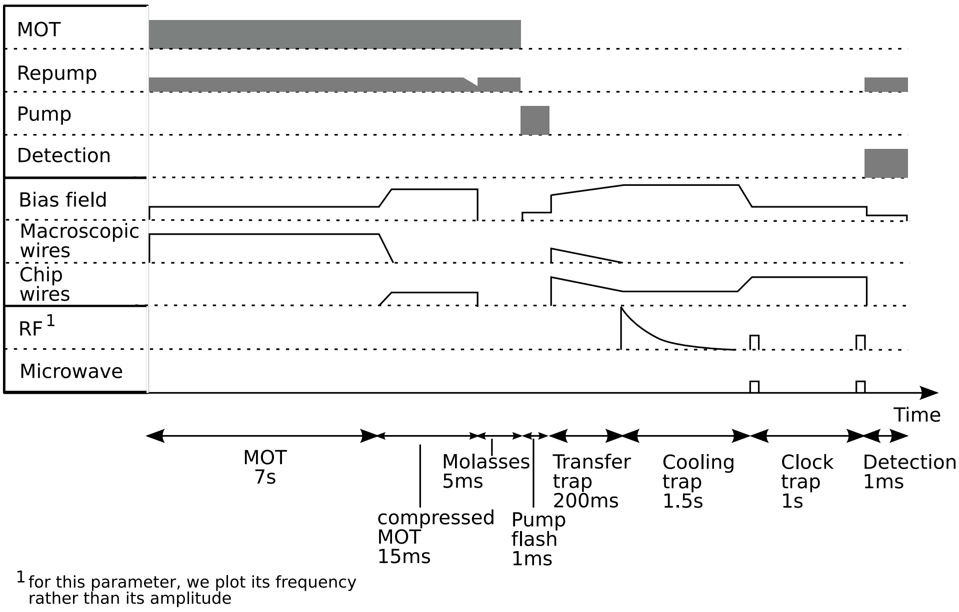

Figure 37: An experimental cycle

   a) a homogeneous bias field of arbitrary magnitude and direction produced by three pairs of coils
   b) the near–fields produced by the chip
   c) the near–fields produced by the macroscopic conductors on the back side

4. A radio–frequency field, coupled to the atoms from one conductor on the chip

5. A microwave field, coupled to the atoms from an integrated transmission line on the chip

6. CCD cameras, to destructively image the atoms with one of the detection beams

During an experimental cycle we use all these tools, as is shown in Figure 37. This cycle is the standard one used in our group [117]. We start by collecting a large (10^7) number of atoms from the ambient vapor in a mirror–MOT. This MOT is subsequently compressed by increasing the gradients of the magnetic quadrupole field. After a short phase of molasses cooling, the cloud is cold enough to be captured by a magnetic trap. The following magnetic trapping phase lasts ≈ 3s, in which we compress the atoms, perform evaporative cooling and finally the clock interrogation. At the end of the cycle, the atoms are destructively imaged.

4.2 The vacuum system

4.2.1 The chamber

The chip is mounted on an ultrahigh (UHV) vacuum chamber‘ (Fig. 38). We use a patented technology [146] to mount it. The chip itself is glued with Epotek 353ND glue

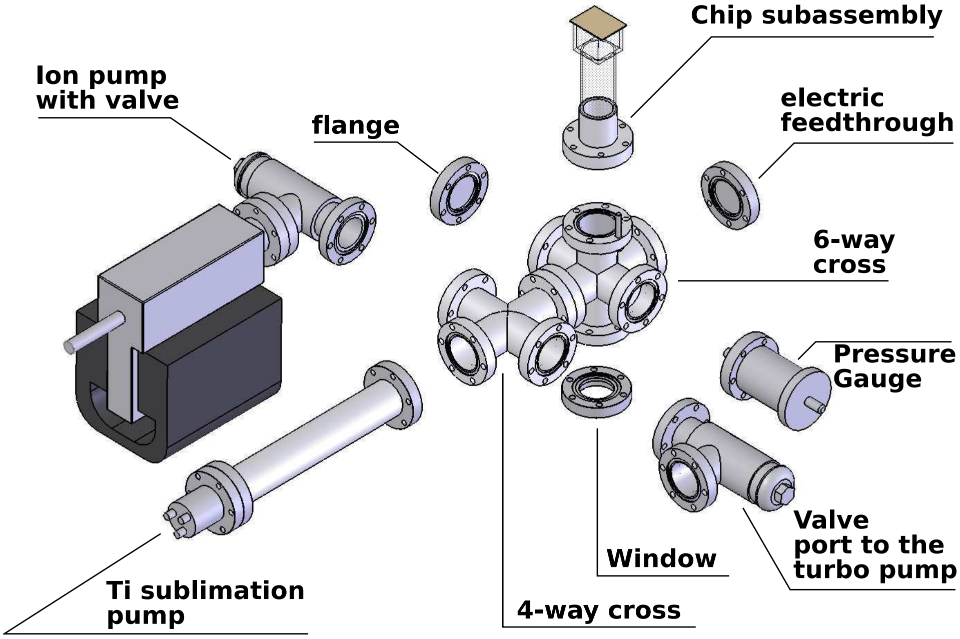

Figure 38: The vacuum chamber

to a commercial Pyrex spectroscopy cell (Hellma), whose outer faces are antireflection-coated for 780nm. This cell is glued to a glass-metal transition (Allectra 120S-CP-137-F2). In our case this part is custom-made to be completely non–magnetic. It consists of a Pyrex tube on the glass side and on the metal side of a Copper tube mounted on a CF40 flange of 316LN steel. This whole subassembly is pre-mounted and installed on the vacuum chamber as a whole.

All other parts of the vacuum chamber are standard CF40 parts. We extend the chip assembly by a 6-way and a 4-way cross (Allectra 413-CFX6-040 and 413-CFX4-040 respectively), providing us with seven CF40 ports to the chamber. We use them to install an ion pump (Meca2000 PID 25, connected via a Meca2000 VUV40 valve), a Titanium sublimation pump (Meca2000 PFT.3 mounted in an Allectra 413-CFX2-040-250 tube), a valve to connect a turbomolecular pump. (Meca2000 VUV40), a Bayard-Alpert pressure gauge (Leybold IE514), a window under the chip (Allectra 120-VPG-C40) and a 9-pin SUB-D electric feedthrough (Allectra 210S-D09-CF40T). One remaining port is closed by a flange. All components were joined using Allectra soft-type 411-CG40-W gaskets.

We mounted two Rubidium dispensers (SAES RB/NF/3.4/12 FT10+10) by spot-welding them to a $\varnothing$1mm insulated copper wire and connecting the wires with crimp sockets to the SUB-D feedthrough. The stiffness of the wire suffices to keep the dispenser in place, so no further mechanical support is neccessary.

In addition, we mounted a carbon ring in the port of the 4–way cross which connects to the valve connecting the ion pump to the chamber. This should protect the pump against the Rubidium vapor.

4.2.2 Cleaning procedure

We cleaned all steel parts, including the valves and the electric feedthrough, by passing them through two ultrasound baths, one “clean bath” in 99% quality acetone, preceeded by one “used clean bath” in the remaining acetone of the last clean bath. We cleaned the gaskets in a 9:1 mixture of Ethanol and HCl and thoroughly rinsed them in water to remove the detergent.

4.2.3 Bakeout

We ran the system through two successive bakeouts, the first at a higher temperature without the chip subassembly, the second at a lower temperature with the chip in place. During both bakeouts, the system was pumped by a turbomolecular pump, which was backed by a roughing pump.

The first bakeout was performed at a temperature of 200°C, lasted for seven weeks and resulted in a pressure of $2.7 \cdot 10^{-10}$mbar. During this bakeout, we replaced the chip subassembly by a flange. In this configuration, the chamber's maximum temperature is 200°C, limited by the magnet of the ion pump. By temporarly removing it, the maximum temperature can be raised to 220°C, limited by the electric feedthrough. We raised the temperature to around 200°C. The exact temperature is slightly different for different parts of the chamber, so we monitored the temperature at several points with K-type thermocouples, taking care not to exceed the temperature limits of the different parts. We switched on the ion pump after four weeks.

During the bakeout, we degassed the pressure gauge, the dispensers and the titanium filaments of the Ti sublimation pump. We degassed the dispensers by progressively raising their current. Each time the current is raised, the vacuum pressure rises rapidly and passes a peak. At high currents, this peak transforms into a continous increase of pressure as the dispenser is activated and Rubidium is released. The highest current during our degassing procedure was 5A, applied for several minutes. In total, this degassing procedure lasted several hours. It turned out later on, however, that the dispensers had not been activated. We suggest for future bakeouts to add a degassing phase in which they are subjected over several hours to a current of $4 - 4.5$A.

The titanium filaments are degassed in an analogous manner, incrementing the current in steps of 5A from 15A to 30A and waiting for the dirt peak to pass. We also performed two steps at 35A and 38A. At these high currents, we apply repeated pulses of one minute until the dirt peak has passed. During the first bakeout, we accidentally exceeded these values, resulting in the filaments being burnt. We replaced them when we installed the cell.

Generally, one should perform all degassing operations as early as possible and close the valve to the ion pump during this time. After cooling down, we open the chamber under an excess pressure of nitrogen and mount the cell subassembly.

The second bakeout was performed with the chip cell in place. It lasted five weeks at a temperature of 110°C and resulted in a vacuum pressure of $2.3 \cdot 10^{-10}$mbar.

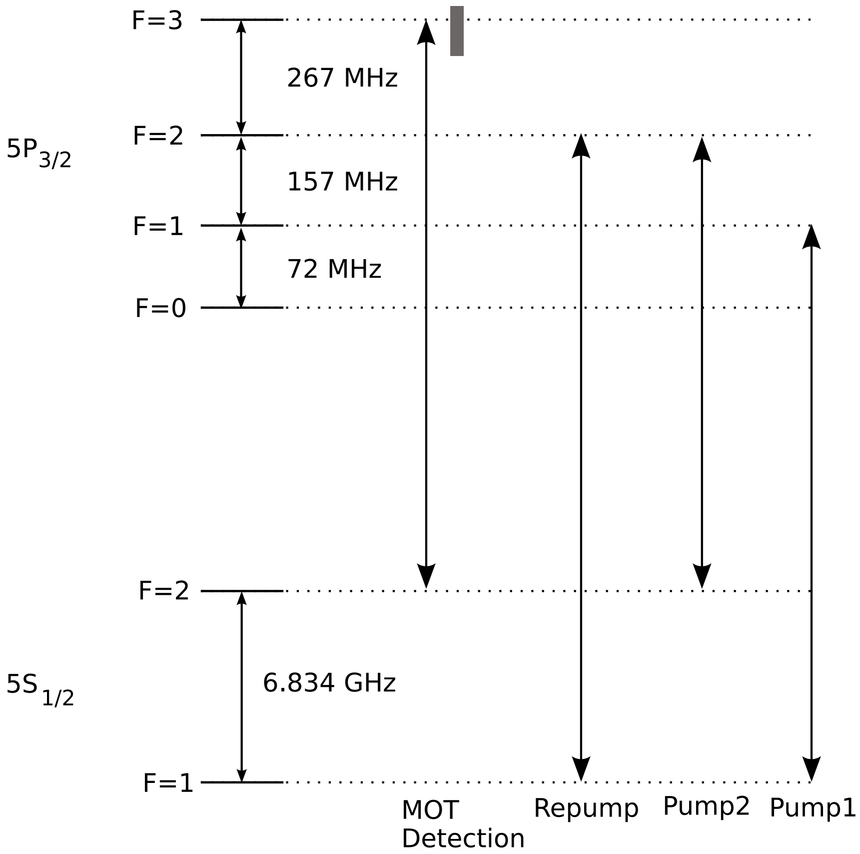

Figure 39: The laser beams. All beams address the ^{87}Rb D_2 transition between the states $5S_{1/2}$ and $6P_{3/2}$. Three diode lasers are used to create all beams. The shaded bar for the laser MOT/detection indicates the tuning range of this laser.

With the chip in place, the temperature is limited by the ribbon cables connecting the chip. To avoid temperature gradients, we constructed an oven around it by wrapping oil-free aluminum foil and glass fiber wool around a scaffolding of laboratory posts.
The ion pump was switched on from the first day. We redegassed all elements except the gauge during this bakeout following the same procedure as described above. After the bakeout, we performed a leak check with a Helium leak tester and deteced no leak higher than the 10^{-11}mbar l/s level.

4.3 The laser system

This section will be a brief one, since the laser system will be described in more detail in the thesis of Clément Lacroûte. The laser system is similar in concept to previous work in our group [147], but uses the SYRTE design for each laser, to achieve an improved compactness and stability.

In total, our laser system consists of two extended–cavity diode lasers (ECDL) and a slave diode, which is injection–locked to one of the ECDLs. This setup produces the laser frequencies of Fig. 39. Some of these frequencies can be reached by the same physical laser, by tuning the laser or by using an acoustooptic modulator. In the following, we will refer to a “laser” as a beam addressing one of the transitions of Fig. 39, even though this does not strictly correspond to one physical laser.

The orientation of the laser beams are given in Fig. 36. All lasers are expanded into a Gaussian beam with diameter $2\sigma = 13mm$. Each laser can be shut quickly by an acoustooptic modulator and slowly, but with a higher rejection, by a mechanical shutter. The beam expanders along x and y can be shut seperately so that the Detection and the pumping pulses are performed with light coming from either the x or the y direction. In detail, the lasers perform the following tasks:

Cooling laser (MOT) This laser drives the cooling transition in the MOT, the compressed MOT (cMOT) and the molasses. It is coupled to the atoms by four beam expanders, in the classic “mirror–MOT” configuration ([84]). It is detuned from the 2–3 transition by $\Delta_{\mathrm{MOT}} = -2.5\Gamma$ during the MOT, where $\Gamma = 6\mathrm{MHz}$ is the natural linewidth of the transition. We increase the detuning to $\Delta_{\mathrm{cMOT}} = -4\Gamma$ during the last 4.5ms of the compressed MOT and the beginning of the molasses. During the molasses, we gradually lower it to up to $\Delta_{\mathrm{molasses}} = -11\Gamma$.

All cooling beams are circularly polarized. The sign of the polarization (σ_+ or σ_-) is chosen such that counterpropagating beams always have the same helicity. Since the quantisation axis of the atoms is defined by the magnetic field, they have opposite polarizations with respect to the atoms. During the MOT, the magnetic quadrupole field tunes the atoms towards resonance with the σ_+–beam and away from resonance with the σ_-–beam, so that they are pumped towards and driven on the $|5S_{1/2}, 2, 2\rangle \rightarrow |6P_{3/2}, 3, 3\rangle$ cycling transition. During the molasses, the magnetic field is shut down. The beams create a field, which is linearly polarized everywhere, with a strong polarization gradient [115].

The balance of the cooling beams’ intensities is optimized experimentally. Their overall power is optimized to be as intense as possible. We reached peak intensities of $1\mathrm{mW/cm}^2$ for the horizontal and $3.5\mathrm{mW/cm}^2$ for the 45° beams, enough to saturate the atoms.

Detection The detection beam is generated by tuning the cooling laser into resonance with the 2–3 transition. By changing the sign of the magnetic field, its polarization can be chosen to be either σ_+ or σ_- with respect to the atomic quantization axis. We use σ_+ radiation to image atoms in the $|2, 1\rangle$ or $|2, 2\rangle$ states, exciting the atoms on the $|5S_{1/2}, 2, 2\rangle \rightarrow |6P_{3/2}, 3, 3\rangle$ cycling transition. To image atoms in the $|1, -1\rangle$ state, we first repump them into the $F = 2$ manifold. We then choose the σ_- configuration to image them on the $|5S_{1/2}, 2, -2\rangle \rightarrow |6P_{3/2}, 3, -3\rangle$ cycling transition. To avoid losses into dark states, we systematically apply the repumper laser (see below) during the detection pulses. We always use absorption imaging as described in [105], [108]. We adjust the laser power to be $I \approx I_{\mathrm{sat}}/10$, so that the atomic absorption is described by the Lambert–Beer law [148]. The detection pulses have a typical duration of 300μs.

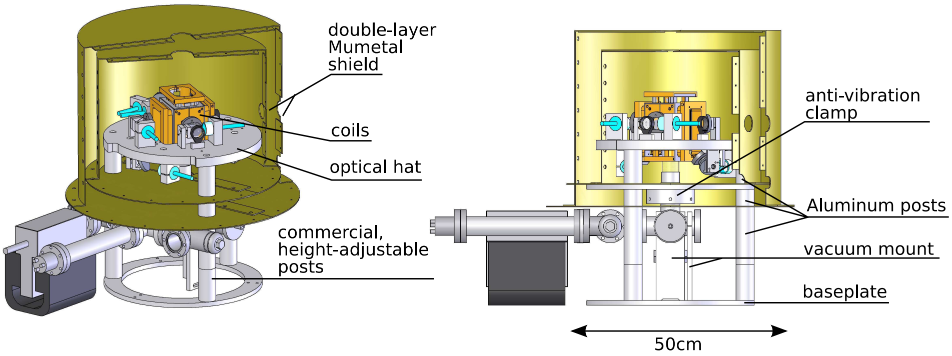

Figure 40: The mechanical structure

Repumper laser The cooling and detection light can off–resonantly excite the atoms into the $|6P_{3/2}, F = 2\rangle$–state, from which they can decay into the “dark” $F = 1$ manifold, which does not couple to the cooling beams [115] any more. The repumper laser excites these atoms on the 1–2 transition and pumps them back into the $F = 2$ manifold. This laser always runs at a fixed frequency. It is coupled into a 45° MOT beam, so that its polarization with respect to the atoms is not well defined. The intensity of this laser is about $100\mu\text{W/cm}^2$.

Pump2 This laser runs on the 2–2 transition and is used to pump the atoms into a well–defined internal state. We select its polarization to be either σ_+ or σ_- by applying a magnetic field along or opposite to its propagation direction. We use the σ_+–configuration to pump the atoms into the state $|2, 2\rangle$, which is magnetically trapped. In this configuration, we avoid losses into dark states by applying the repumper laser along with the pump laser. Using the laser in the σ_-–configuration pumps the atoms into the magnetically untrapped state $|2, -2\rangle$. In practice, this state is not completely dark, due to inevitable impurities of the polarization. Without a repump laser, this will lead to the atoms eventually being pumped into the dark $F = 1$ manifold. We use this configuration to pump into the clock state $|1, -1\rangle$ In this case, the Pump2 laser depopulates the $F = 2$ manifold and the Pump1 laser pumps the resulting $F = 1$ atoms into $|1, -1\rangle$. The intensity of both beams is optimized experimentally.

Pump1 This laser runs on the $1 - 1$ transition and is used to pump atoms inside the $F = 1$ manifold into the state $|1, -1\rangle$ as described above. Its polarization is the same as for the Pump2 laser, such that both can be chosen to be σ_-–polarized with respect to the atomic quantization axis at the same time.

4.4 The mechanics

The central part of the experiment is the vacuum chamber. It is mounted independently from all other components. After the bakeout, the MOT beams, the shielding and the coils are installed around the cell. All these peripheric components are mounted on a custom–made structure. The coils and the MOT beams are pre-aligned on a custom-made platform which is transfered to the mounting structure as a whole. We refer to this platform as "the optical hat", since it fits around the cell like a hat. After having mounted this assembly, the Mumetal shielding is assembled around the whole setup in place. Even after the shield has been closed, the vacuum system is mechanically decoupled from the periphery (coils, optics and shield), so that the former can be aligned inside the latter at any time.

4.4.1 The structure

The vacuum mount The vacuum chamber is supported by the ion pump on one side and by custom-made vacuum mounts on the other side. These custom-made mounts fit around the arms of the vacuum crosses and are attached to the optical table with a standard clamp. Three of them sit under the 6-way cross, a fourth one supports the Ti sublimation pump.

The peripheric structure The mounting structure is based on a ring-shaped baseplate which is fixed to the optical table with standard clamps. Three pillars emerge from this plate. They are made from several Aluminum posts which are joined to each other by M6 headless screws. Each pillar is joined to the baseplate by a height-adjustable commercial post (Edmund Optics 20mm Dia. adjustable post holder, NT54-933). This allows us to fine-tune the height and the inclination of the peripheric elements once they are in place.

Both Mumetal shields are fixed to the mounting structure on their bottom plate, by locking them between two Aluminum posts making up the pillars. The optical hat is mounted on top of the pillars and fixed to them by screws.

To avoid vibrations of the cell with respect to the detection optics, we added an anti-vibration clamp locking the cell to the mounting structure. This clamp consists of a ring which fits around the flanges connecting the chip assembly to the 6-way cross. This ring is screwed onto a circular plate which is locked between two Aluminum posts together with the bottom plate of the inner Mumetal shield. Six M6 threads are tapped into the clamp, arranged in a starlike layout. The clamp is fixed to the vacuum flange by screws passing through these threads. Notice that this fixation can be performed once the structure is aligned and that it is totally reversible.

Assembly and alignment of the peripheric structure The assembly starts by laying out the baseplate and mounting the pillars. The bottom plates of the shields as well as the anti-vibration clamp have to be inserted right from the start. At this moment, we also feed some wires through the center hole of the shields, to be able to demagnetize them in place.

Once the whole mounting structure is in place, the optical hat is installed around the cell from above. To guide it during its descent, we screwed long (>50cm) M6 threaded rods into the uppermost Aluminum rod, which fit through the corresponding holes of the optical hat. We screwed wingnuts to these rods and placed the optical hat on them. It is then carefully lowered by rotating the wingnuts. To remove the wingnuts, we lower the optical hat as much as possible and then support it by three laboratory lifting platforms. In this state we remove the threaded rods and wingnuts and lower the hat for the last centimeters using the platforms. Once it sits on the Aluminum rods, we screw it to them. During this procedure, the position and orientation of the hat with respect to the (fixed) chip cell is continuously observed. If neccessary, we correct it by displacing or rotating the whole mounting structure on the optical table. To this end, we pull or push the circular baseplate using improvised screw-and-clamp constructions on the optical table.

After this critical step, the circular baseplate is fixed to the table using standard clamps. The height and inclination of the optical table can still be fine-tuned using the Edmund posts. Typically, these parameters are adjusted such as to have a re-injection of the 45° beams from one fiber to the other (see below). Once a satisfying alignment is achieved, the hat can optionally be locked to the vacuum chamber using the anti-vibration clamp.

We install the imaging optics in their lens tube and fix them in their mounts. We leave them fixed in their place when we close the shielding. The shields can be closed around the lens tubes. The cameras are connected to the lens tubes on the outside of the shields using Thorlabs SM1 series zoom housings.

4.4.2 The optical hat

As stated above, the optical hat is a subassembly which is pre-aligned separately and fits around the chip cell as a whole. It contains all the optics required to shape the MOT-beams, i.e., the beam expanders as well as the polarization optics. It also houses the coils. Both faces of the hat are used to mount optical components, much in the same way as in the space clock PHARAO [81]. This allows for a compact and mechanically highly stable setup.

Layout Basically, the optical hat is a 20mm thick circular plate made of Fortal. Its diameter is 350mm, leaving a 12mm space between the hat and the inner shield. On one side of the shield, there is an additional 20mm deep slit to comfortably feed through the optical fibers from the upper side to the lower side.

The coils reside in a rectangular 122mm by 102mm hole in the center of the hat. They are attached to the hat by eight angle brackets, fixed to the y–coils on one side and to the optical hat on the other side. Each y–coil is attached to two pairs of brackets, one on the upper face and one on the lower face of the hat. The brackets are fabricated from Armodur, a machineable plastic. This material was chosen to electrically isolate the coils from the hat in order to avoid Eddy currents.

The optical components are mounted on both faces of the optical hat. The position of each optical element is predefined and fixed by the layout of the drillings and threads in the hat. The lower face holds the optics generating the 45° beams, whereas the upper face holds the optics for the horizontal MOT beams, the pump and the detection beams. Each beam emerges from a purpose defined beam expander fixed by a homebuilt mount.

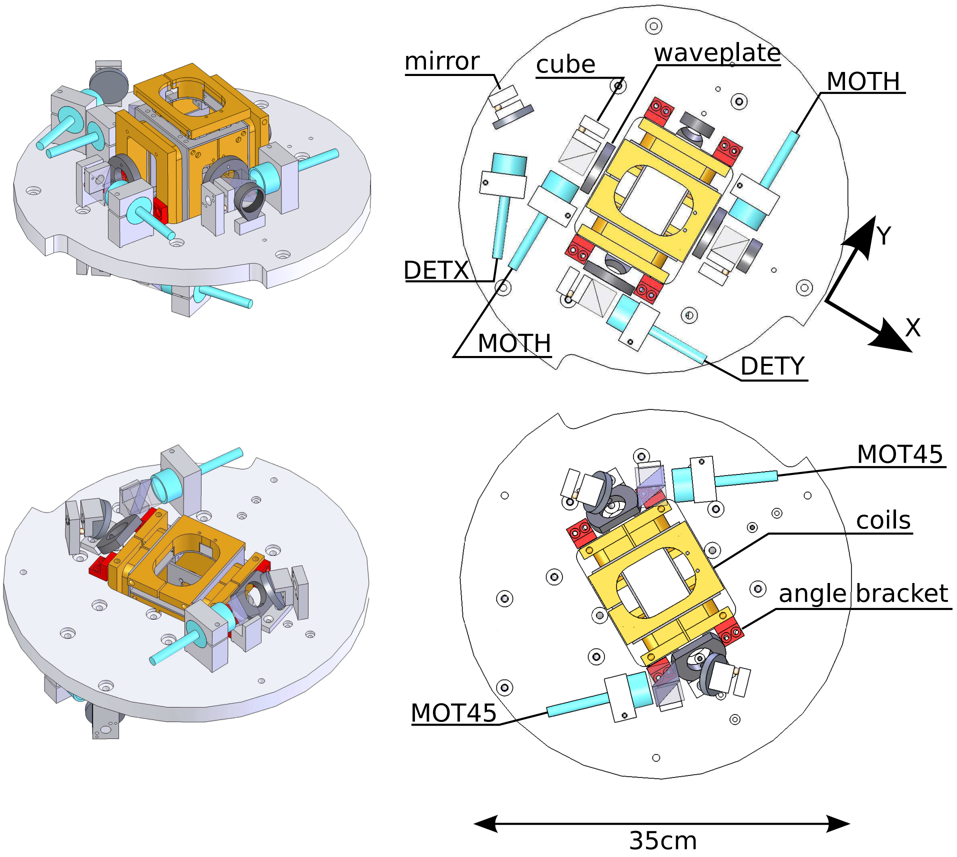

Figure 41: The optical hat. Both faces carry optical elements. All uppercase labels designate beams.

Its polarisation is then cleaned by a polarizing beamsplitter cube and finally converted into circular polarization by a $\lambda/4$ waveplate. All beams on the upper face are parallel to the hat surface and point to a virtual point 3mm under the chip surface. The 45° beams emerge parallel to the hat face and are tilted to their 45° angle by a mirror. They point to the center of the chip. Their collimators and polarization-cleaning cubes are mounted such as to make sure that the electric field vector of the light lies in the plane of the mirror. This should minimize depolarization due to the mirror.

Nearly all mounts are custom-made in order to be completely amagnetic. The only exceptions are the mounts of the λ-waveplates and the mounts of the imaging optics. The λ-mounts have been taken from a stock of old mounts of unknown origin, but have been tested to be amagnetic. For the imaging optics, we use standard Thorlabs 1″ lens tubes and their respective mounts. They are made from Aluminum, causing no magnetic concerns.

Alignment When assembling the optical hat, we first mount and align the optics and then insert the coils. For the alignment, we start with the lower face. We first align the beams geometrically and then optimize the polarisations. The geometric alignment is done by installing a “chip simulator” on the upper face. This is a mirror in the plane of the chip. It allows us to validate the alignment of the beams by performing a re-injection, i.e. coupling the light from one beam into the fiber of the opposite one. To optimize the polarisation, we place a mirror behind the $\lambda/4$–waveplate. We then optimize the angle of the $\lambda/4$–waveplate such that a maximum of power is reflected from the polarisation–cleaning cube. We also fine-tune the orientation of the collimator by turning it around its axis such as to optimally match the polarisation axis of the outgoing beam to the axis of the cube. To verify this, we mecanically stress the fiber and turn the collimator such that the resulting power fluctuations behind the cube are minimized.

The upper face is aligned in a similar way. To geometrically align the beams, we replace the waveplates by circular apertures. The polarizations are optimized as described for the lower face.

4.5 The Mumetal shield

4.5.1 Overview

The core of the experiment is shielded from magnetic stray fields by a two-layer Mumetal enclosure (Fig. 42). It is composed of two shells of 2mm thick Mumetal. They are cylindrically shaped with a (height, diameter) of (27.7, 37.8)cm and (36.7, 46.2)cm respectively. Each shell is made of four pieces, a two-piece hull sitting on a two-piece bottom plate. The shields are assembled around the vacuum chamber and fixed to each other by M4 screws. The inner shell encloses the whole optical hat, which is made of strictly non-magnetic components. The (potentially magnetic) vacuum flange between the glass-metal transition and the 6-way cross sits between the inner and the outer shell. All the shield has been manufactured by Mecamagnetic.

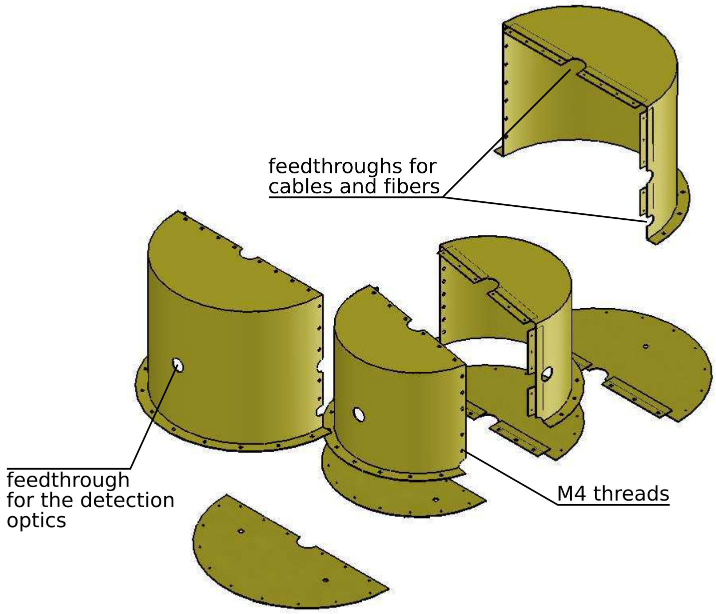

Figure 42: The Mumetal shield.

The main goal when designing the Mumetal shield is to reach sufficient attenuation of external fields. Constraints for the design are imposed by several parasitic effects: The shielding must not be permanently magnetized, either by an external field or by the coils, since this would create a remnant background magnetic field. The switching behavior of the coils might be compromised by the shield in several ways: By its high permeability it could increase the inductance of the coils, acting as an effective iron core. Also, it creates a path for Eddy currents.

4.5.2 Attenuation factors

Specification Our requirements in terms of attenuation factors stem from the stability analysis of the clock as it has been stated in section 3.3. We recall from this analysis that for a stability of $\sigma_y(\tau) = 1 \cdot 10^{-13}\sqrt{\mathrm{s}}$ we require the rms fluctuation σ_B to be

$$\sigma_B < 0.6\mathrm{mG} \quad \text{for a clock working at the magic field} \tag{98}$$

$$\sigma_B < 35\mu\mathrm{G} \quad \text{for a clock working at a detuning of } \Delta B = 0.03G \tag{99}$$

The fluctuations of the background magnetic field are of the order of $\sigma_B = 10\mathrm{mG}$. This translates into the follwing requirements for the shielding factors:

$$A > 17 \quad \text{for a clock working at the magic field}$$

$$A > 300 \quad \text{for a clock working at a detuning of } \Delta B = 0.03G$$

Strictly speaking, this requirement applies only to the direction along the trap axis, which is the transverse direction of the shielding cylinder.

	inner shield	outer shield	double–layer shield
A_a	140	115	3948
A_t	159	130	6833

Table 3: Calculated shielding factors

We also emphasize that shielding the background fields is a neccessary, but not sufficient condition to reach control of the magnetic fields at the required level. Additional care must be taken to control all fields produced inside the shield, most notably the fields produced by the coils and chip wires.

Analytical estimation There are analytical formulae to calculate the shielding factors of a cylindrical shield [149, 150]. Let us consider a cylindrical shield of radius R and length L, whose walls are made from Mumetal walls of thickness d with a relative permeability of μ_r. Its transverse shielding factor is [149]

$$A_t = \frac{\mu_R d}{2R}. \tag{100}$$

For the axial shielding factors, both references only give formulae for $L/R > 2$. Approximating our geometry by $L/R = 2$, one obtains [150]

$$A_t = 1.13 A_a.$$

The shielding factors $A_t, A_a$of a multilayer shield are products of the shielding factors of each layer (A_{t_i}, A_{a_i} denoting the transverse and axial shielding factors of the ith of n shields respectively)

$$\begin{aligned} A_t &= A_{t_n} \prod_{i=1}^{n-1} A_{t_i} \left[1 - \left(\frac{R_i}{R_{i+1}}\right)^2\right] && (101) \\ A_a &= A_{a_n} \prod_{i=1}^{n-1} A_{a_i} \left[1 - \left(\frac{L_i}{L_{i+1}}\right)\right] && (102) \end{aligned}$$

If $R_i \ll R_{i+1}$, the shielding factor of a multi–layer shield is simply the product of the shielding factors of the single shields. Formula 100 suggests to build the shield as small as possible. In our case, the size of the inner shield is limited by the size of the optical hat. The optimum radius of the outer shield follows from equations 100 and 101 to be $R_o = \sqrt{3} R_i$ with R_o and R_i being the radius of the outer and inner shield, respectively. Similarly, the optimum length would be $L_0 = 2L_i$. This choice would conflict with the flanges of the vacuum chamber in the axial direction and pose severe constraints on the detection optics in the transverse direction. Therefore, we opted for the more reasonable diameter cited above. For our geometry, assuming $\mu_R = 3 \cdot 10^4$, the analytic formulae predict the shielding factors quoted in Table 3. This calculation justifies the investment into a two-layer shield. One single layer would not be sufficient to reach the target stated above.

	inner shield	outer shield	double–layer shield
A_a	107 ± 7	117 ± 6	3400 ± 300
A_t	220 ± 30	170 ± 20	10800 ± 1400

Table 4: Measured shielding factors

Measurement We have measured the shielding factors of our shield. To measure the transverse shielding factor, we placed the shield at the center of a Helmholtz setup of two coils of dimensions $1.5 \times 1.5\text{m}^2$. The field was measured with a fluxgate magnetometer. The axial shielding factor was measured in the same way, except that the shield was placed at the center of only one coil.

These measurements yield the shielding factors quoted in Table 4.5.2 The transverse shielding factors are systematically higher than predicted. Most probably, our Mumetal has a higher permeability than assumed above. In contrast, the axial shielding factors are systematically lower than predicted. We speculate that this may be due to the existence of two opposite feedthroughs on this axis.

4.5.3 Parasitic effects

Saturation effects Mumetal is a soft ferromagnetic material. It will be permanently magnetized when it carries a flux density comparable or larger than its saturation flux density B_S. For Mumetal, this parameter has the value $B_R = 0.8\text{T} = 8\text{kG}$. [151]. Hysteresis may play a role at smaller field strengths, too, however there is no corresponding specification and full hysteresis loops for several fields are not available. This effect poses a constraint for our design. We have to avoid that the shield is magnetized by either an ambient field or by the field of the coils.

Saturation by external fields There exist analytical formulae to estimate the flux density inside a Mumetal shield, when it is subjected to a homogeneous external field [149]. The flux density in the walls of a long cylindrical shield ($L \gg R$), when it is exposed to a homogeneous transverse field B_0 is given by

$$B_w = 2B_0 \frac{R}{d}. \tag{103}$$

This formula has an instructive interpretation: The shield picks up the magnetic flux on twice its transverse cross section, $\Phi = 4B_0RL$, and funnels it completely into its walls of cross section $A = 2dL$. The literature cited above also gives an estimate for the axial direction. As for the axial shielding factor, this formula is not applicable to our geometry ($L < 2R$). Approximating $L \approx 2R$, it predicts a peak flux density of the same order of magnitude as for the transverse case.

Applied to our outer shield, the above formula predicts that the shield will be saturated by a homogeneous external field of

$$B_0 = 35\text{G}.$$

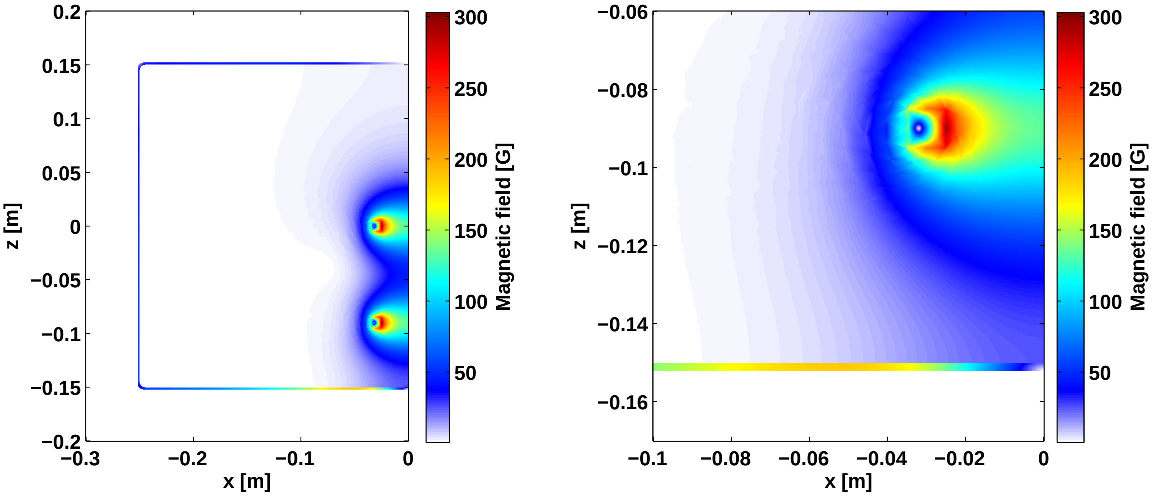

Figure 43: Finite-Element simulation of the field distribution inside the Mumetal shield. Shown is only the half cross section of the shield and the coils, since the simulation is axially symmetric. The coils are supposed to have 61 windings and to carry its maximum current of 10A. The right image is a zoom into the most critical region of the shield, right under the lower z coil.

Realistic external fields are much smaller, of the order of magnitude of the terrestric field, $B_0 = 0.5$G. Saturation by external fields is thus uncritical.

Saturation by the coils The flux generated by our coils is partly carried by the shield and might thus magnetize it. Presumably, this problem is most critical for the coils along the z–axis, since they are mounted closer to the wall of the shield than any other pair. We carried out a finite–element simulation for this pair to check whether its flux might magnetize the shield. The simulation was based on a numerical model developed by Tobias Schneider to design the shielding of the ENS double well experiment. It is based on the magnetostatics model of COMSOL Multiphysics. It treats the shield and the coil as axially symmetric objects, thus reducing the problem to a 2D simulation. The geometry of the model was slightly modified to correspond to our coil. The permeability of the Mumetal was assumed to be $\mu_R = 30000$. The coils were simulated assuming the parameters of our experiment, i.e. to have 61 windings and to carry their maximum current, which is 10A.

The result of this simulation is shown in Fig. 43. As expected, the shield region carrying the highest field lies right under the lower coil. However, even the highest value of the magnetic field inside the shield is only ≈ 200G, much smaller than the saturation field $B_S = 8$kG of the Mumetal.

We have measured the hysteresis of the fabricated shield. Therefore, we installed the inner shield with the coils inside. We then applied a magnetization cycle by ramping the current of one pair of coils to its maximum value and back to zero. We performed

	x	y	z
Remanence field	0.4 mG	0.8 mG	0.7mG

Table 5: Measured remanence fields after a magnetization pulse of the coils. The field at the center of the coils reaches typically 60G at the peak of a pulse.

this cycle several times, varying the sign of the current. We find that the background magnetization inside the shield after one of these cycles changes by the values of table 5.

It is not completely clear to which extent this effect will limit our experiment. If this hysteresis is reproducible over a large number of runs it should not disturb the clock measurement, which applies the same sequence of magnetic fields for each interrogation. Also, one might think about applying a demagnetization pulse before each experimental cycle.

Inductivity of the coils The Mumetal shield might compromise the switching speed of our coils by increasing their inductance. The order of magnitude of this effect can be estimated by computing the inductance from the above finite–element simulation. Integrating the magnetic energy density over the region enclosed by the shield, one obtains an inductance of $L_{\text{inner}} = 500\mu\text{H}$. Integrating the magnetic energy density over the walls of the shield yields $L_{\text{wall}} = 18n\text{H}$, which is much smaller. This effect should thus be negligible

We also measured the inductance of the coils inside and outside the shield using a Philips PM6304 RCL meter. We found no increase of the inductance within the error of the measurement, which was $\approx 10\mu\text{H}$, compared to a typical coil inductance of $\approx 1\text{mH}$.

Eddy currents The Mumetal shield might also reduce the switching speed of the coils by creating a path for Eddy currents. We experimentally checked for this effect by mounting the coils inside the shield and placing a pickup coil at their center to measure the change of the magnetic field when we switch them on or off. We find that the signal on the pickup coil drops to less than 10% of its peak value in less than 3ms. This is the same time as it takes the field to settle outside the shield, limited by the switching speed of the power supply (Delta Elektronika SM030-10).

With the benefit of hindsight, we propose to measure this effect more precisely with a vector analyzer, for instance with the Philips PM6304 RCL meter mentioned above. An inductive coupling to the shield should change the complex impedance of the coils at high frequencies, as becomes clear from the equivalent circuit of such a situation (Fig. 44). This change in impedance could be used to measure R_S, which would in turn quantitatively predict the bandwidth of the coils in the shield.

4.5.4 Conclusion

In summary, our shield exceeds our expectations in terms of shielding factors while it does not significantly compromise the switching times of our coils. The only minor concern is

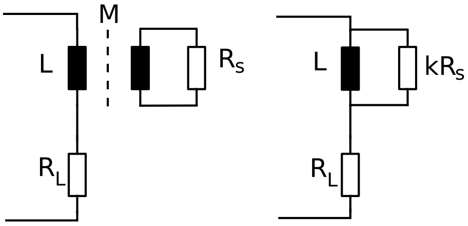

Figure 44: Equivalent circuit of a coil driving Eddy currents in a shield. The coil inductance is inductively coupled to the nonzero resistance R_S of the shield walls by a mutual inductance M. In the equivalent circuit, this corresponds to a virtual resistance short circuiting the coil at high frequencies

the hysteresis induced by operating the coils. With the benefit of hindsight, one might have considered fabricating it from a less permeable material which is less susceptible to saturation, e.g. PERMENORM [152]. However, to make a sound statement, one would have to consider the full hysteresis loops of the respective material for several amplitudes of the driving field, which is not readily available.

4.6 The coils

The chip cell is mounted between three orthogonal pairs of coils, which are wired in Helmholtz configuration to produce a homogeneous field of arbitrary direction and magnitude at the position of the atoms. Each coil is made from ⌀1mm copper wire, which is wound to a custom-made copper mount (Fig. 45). The mount is a copy with minor modifications of a design by Tilo Steinmetz, which is widely used in the LKB and LMU/MPQ atom chip groups. It is designed such that all coils can be pre-assembled and fit around the chip cell as a whole.

The design of the mount being fixed, the main design decision is the number of windings of coil. Additional constraints arise from two requirements of our experiment: We require the bias field to be highly homogeneous, since inhomogenities might preclude us from working with highly elongated clouds. In addition, we need a high temporal stability of the coils' positions and dimensions in order to avoid clock shifts from a drifting magnetic field. We assessed the performance of the design with respect to both of these constraints.

4.6.1 Winding numbers of the coils

	x	x gradient	y	y gradient	z	z gradient
winding number	88	7	60	9	61	8
field (@I=10A) [G]	126	12	59	9	36	5

Table 6: Winding numbers of our coils and the resulting maximum fields. The two coils of each pair have identical winding numbers.

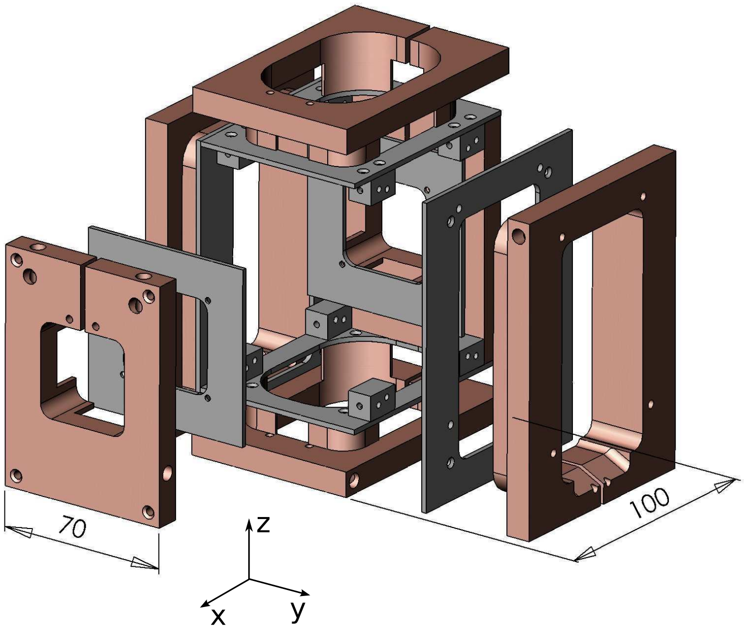

Figure 45: The mount of the coils producing the bias fields.

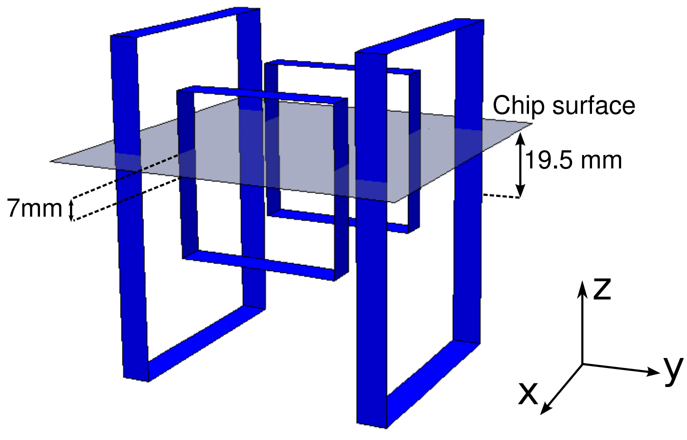

Figure 46: Numerical model of the coils. The picture is taken along the same axis as figure 45. Two imperfections create inhomogeneities: The coils deviate from the Helmholtz shape and they are displaced against the chip plane

The number of turns wound to each coil is chosen as low as possible, in order to minimize the inductance of the coil. For the y and z coils, we chose them such that we can produce the maximum required field with a reasonable current of 10A (see table 6). For the x coils we chose a winding number higher than required, so that we can produce the background field of the clock interrogation with a low current and thus use a more stable current supply. Inductance is not that critical for this pair, since it is never switched on rapidly.

We wound two separate coils onto each support. This allows us to add fields which may be driven from different power supplies. The smaller coil may also be used to add a gradient to the field. Therefore, it is refered to as the "gradient coil".

4.6.2 Spatial homogeneity of the coil field

The field of the coils contains inhomogeneities for several reasons: Firstly, the coils are square and their typical width $2R$ and separation d deviate significantly from the Helmholtz geometry $R = d$. Secondly, the coils are vertically displaced against the chip plane (see fig. 46). Additional inhomogeneities can arise, when the coils are not aligned perfectly. We will now study each of these effects.

Deviation from the Helmholtz shape Let us first estimate the inhomogeneity caused by the fact that the coils deviate from the Helmholtz shape. This effect is most critical for the clock trap, which might be distorted by inhomogeneities of the bias field. Keeping in mind the trap frequencies $(f_x, f_y, f_z) = (0.5, 450, 450)$Hz it is clear that this problem will be most severe along the x-direction, where the trap is weakest.
The primary source of inhomogeneity in this direction is the curvature $\frac{d^2B_x}{dx^2}$ produced by the x–coils. The z–coils do not contribute, since they are switched off during the clock trap and the field of the y–coils is directed purely along y in the $y = 0$ plane for symmetry reasons.
$\frac{\partial^2 B_x}{\partial x^2}$ can be estimated by an analytic calculation. To this end, we model the x–coils by two coaxial circular coils of radius R, separated by a distance d. Calculating their field from the Biot-Savart law yields for the magnetic field at the center of the coil pair

$$B\Big|_{x=0} = \frac{\mu_0 I R^2}{\left(R^2 + \left(\frac{d}{2}\right)^2\right)^{3/2}}. \tag{104}$$

We calculated this field for our experimental values $R = 56/2\text{mm}, d = 58\text{mm}$, $I = N \cdot 0.24\text{A}$. This yields the following values for the curvature and the resulting trap frequency

$$\begin{aligned} B_x(x=0) &= 3.2\text{G} \\ \frac{d^2B_x}{dx^2} &= 9.4\frac{\text{kG}}{\text{m}^2} \\ f_x &= 0.87\text{Hz} \end{aligned}$$

As a complementary approach, we conducted a numerical simulation. We modeled each of our coils by a rectangle of wires which were assumed to be infinitely flat in one direction and reproduced the width of our coils in the other one. All coils were simulated using their physical dimensions. The simulation also models the chip wires at their physical location. The simulation was carried out using a Mathematica toolbox developed in our group.

Simulating all coils with the current values of the clock trap, we observe a harmonic confinement in the longitudinal direction of frequency $f_x = 0.8$Hz coming from the coils. This agrees well with the analytic calculation, indicating that the non-Helmholtzian geometry of the x–coils is indeed the primary source of inhomogeneity. We checked that this inhomogeneity remains harmonic over the whole trap length of several millimeters.

In summary, the curvature of the coil field creates a small harmonic confinement of ≈ 0.8 Hz. To reach frequencies below this value, one would have to compensate this curvature by an opposite curvature from the chip wires. However, this may prove difficult, since the coil might not be perfectly aligned to the chip and compensation can only be achieved if the curvatures of the chip and the coils are centered around the same point on the x axis.

Displacement of the coils The coils are not perfectly aligned with respect to the chip. There is a systematic misalignment, since in our design of the coils, the chip surface is shifted by 7mm along the z-direction from the axis of the x–coils, which is in turn shifted along the z-direction from the axis of the y–coils.

We checked for the influence of the systematic misalignment using the simulation mentioned above. We observe in this simulation that a cloud in a typical trap of $(0.5, 1\mathrm{k}, 1\mathrm{k})$Hz tilts by $\approx 6°$ in the x-y-plane. We attribute this to the displacement of the chip, which creates a nonzero gradient dB_z/dx along the trap.

Misalignment Stochastic misalignments can cause additional inhomogeneities. Again, this effect is most severe along the x–direction. In this direction, additional inhomogeneties can arise mainly in two ways:

If the chip is displaced from the center of the coils in the y–direction by Δy, the y–coils will create a nonzero gradient $\partial B_x/\partial x$. From our numerical simulation, we estimate that, when the coils generate a typical bias field of $B_y = 20$G, a displacement of $\Delta y = 0.1$mm will create a gradient of $\partial B_x/\partial x = 1$G/m, which shifts the trap by $\Delta x = 0.3$mm.

If the chip is tilted in the x-y-plane by an angle α, the curvature of the y–coils d^2B_y/dy^2 is converted into a curvature $d^2B_x/dx^2 = d^2B_y/dy^2 \sin(\alpha)^2$. However, from our simulation, we measure the curvature of the y–coils for typical bias fields to be $d^2B_y/dy^2 = 10\mathrm{kG/m^2}$, of the same order of magnitude as the curvature of the x–coils, so this effect should not play a role.

4.6.3 Temporal stability of the coil field

Even more critical for our experiment is the **temporal** stability of the coils. We recall from Eq. 98 that changes in the magnetic field B_x translate directly into frequency shifts of our clock and that we require this field to be stable to at least 35μG (rel. 10^{-5}). Changes in the coil dimensions will create fluctuations of the magnetic field, even if the current in the coils is perfectly controlled. The resulting requirement on the stability of the coils' dimensions can be estimated from Eq. 104 by taking the partial derivatives $\partial B/\partial d$ and $\partial B/\partial R$. Again, the effect is most critical for the x-coils, since the background field of the clock trap is created by them. Inserting their actual dimensions and currents, our required field stability translates into the following requirements

$$\begin{aligned}\frac{\sigma_R}{R} &= 6.7 \cdot 10^{-6} \\ \frac{\sigma_d}{d} &= 4.1 \cdot 10^{-6}\end{aligned}$$

This corresponds to a $\sigma_{d,r}$ of the order of only hundred nanometers. The main contribution to changes of the dimensions will presumably be the thermal expansion of the support and the coil windings. Both are made from copper, which has a coefficient of thermal expansion of $1.6 \cdot 10^{-5}$. To reach the above stability, we would have to stabilize the temperature of our coils to within $0.2°$, which seems feasible.

5 The chip

5.1 The atomic clock chip

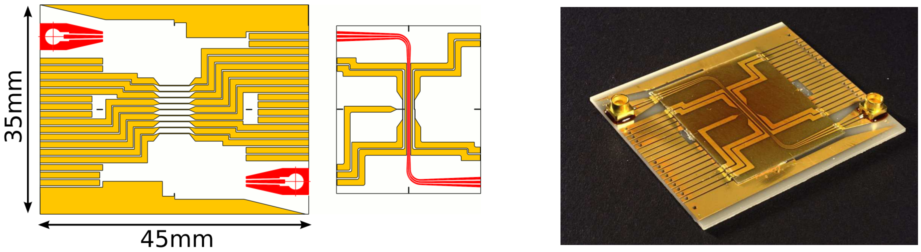

Figure 47: The chip used in the experiment: It consists of two chips, the lower "base chip" and the upper "science chip", both of which contain conductors (left). The base chip is fabricated from 0.8mm thick Aluminum Nitride (AlN), while the science chip is fabricated from 0.25mm thick AlN. The chip is hybrid, containing DC conductors (yellow) as well as a microwave guide (red). Both chips are glued onto each other (right). Connections between the chips are performed by bond wires. The Connection to the supplies is performed by feeding ribbon cables through the holes visible on the photo, which are connected with an electrically conductive epoxy to the gold conductors. The microwave is connected by the Mini–SMP connectors visible on the corners of the chip.

We will now describe in detail the chip, which is used in our experiment. It is depicted in Figs. 47 and 48. It is a hybrid chip, containing DC conductors as well as a microwave transmission line. All the experimental cycle takes place at the center of the chip. The chip is able to prepare a cold cloud, a thermal cloud or a BEC, and to place it into the near–field of the transmission line, where the magnetic field of the microwave can induce hyperfine transitions. The philosophy of our chip design was the following: We first designed the microwave transmission line, assuming our atoms could be held at any place above the chip in the optimum clock trap. Afterwards, we designed the DC wires around the transmission line. The following paragraphs will describe both components in more detail.

5.1.1 The microwave transmission line

Our clock states $|1,-1\rangle$ and $|2,1\rangle$ are linked by a two–photon transition with a transition frequency close to the hyperfine splitting $f = 6.835\text{GHz}$ [129]. To excite this transition, we have to couple two photons to the atoms, one in the RF domain ($f = 1\text{–}2\text{MHz}$) and another one in the microwave domain. Technically, the coupling of the former is easy, since it can be coupled into any wire of the chip. This is not true for the latter. Coupling the microwave photon to the chip requires a dedicated coupling structure, the transmission line visible in fig. 47. It is this structure which we will describe in detail in this section.

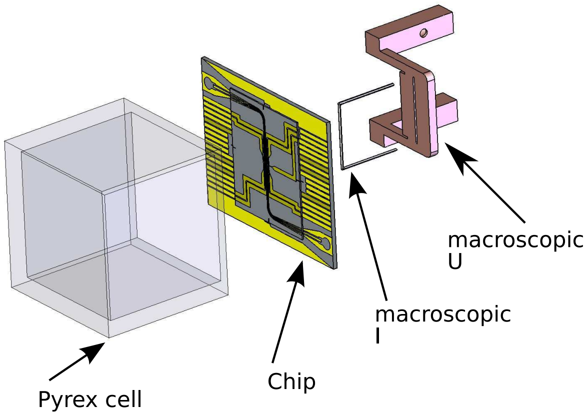

Figure 48: The chip assembly. The chip as shown in Fig. 47 is glued onto a spectroscopy cell. On the backside, we mount additional macroscopic conductors: A macroscopic U wire to create the quadrupole field for the MOT and a macroscopic I wire to create the field for the compressed MOT and to support the initial magnetic trap. The macroscopic U is custom made from copper and has a thickness of 2mm. The macroscopic I is bent from $\varnothing = 0.5$mm enamelled copper wire.

As a preparing remark, we recall from section 3.1.3 that the trap confines the atoms in the Lamb–Dicke regime for the RF and microwave photon. Consequently, the details of the excitation field are much less critical than they would be e.g. for a fountain clock. In particular, we do not have to take care to provide the excitation field as a maximally pure standing wave. All former experiments on our clock transition have exploited this observation to the fullest and used a freely propagating microwave to create the excitation field [39],[29]. However, as we will discuss, this approach has several drawbacks, so we decided to couple the microwave to the atoms by immersing them into the near-field of a microwave transmission line integrated on the chip. Before describing the details of this transmission line, we will spend the following paragraph to sketch the theory of microwave guides. For a more in–depth overview, see [153]

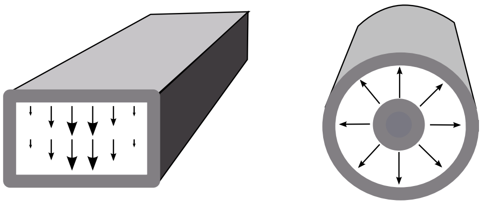

Figure 49: Two typical waveguide structures. A hollow-core waveguide (left) supports various TE and TM modes, but no TEM mode. In the coaxial cable (right), the signal is carried by a TEM mode.

Microwave guides It is known that the solution of Maxwell's equations in isotropic media are plane electromagnetic waves

$$\vec{E}(\vec{x},t) = \vec{E}_0 \mathrm{Re}\left[\exp[i\omega t - i\vec{k}\vec{x}]\right] \tag{105a}$$

$$\vec{B}(\vec{x},t) = \vec{B}_0 \mathrm{Re}\left[\exp[i\omega t - i\vec{k}\vec{x}]\right] \tag{105b}$$

satisfying

$$\frac{\omega}{k} = c = \frac{1}{\sqrt{\epsilon\mu}} \qquad \frac{E_0}{B_0} = c.$$

A waveguide is a metallic or dielectric structure, of dimensions $L \gg \lambda = 2\pi c/\omega$ in one direction (we assume direction z) and $a, b \ll \lambda$ or $a, b \approx \lambda$ in the other directions (x, y). We will focus in the following part on metallic waveguides, assumed to be perfect conductors, and assume the waveguide to be embedded into a homogeneous dielectric. Two typical examples can be seen in Fig. 49 The waveguide imposes boundary conditions on the electromagnetic field in the x– and y–directions. The waves will thus be modified to a form

$$\vec{E}(\vec{x},t) = \vec{E}_0(x,y)\,\mathrm{Re}[\exp^{i\omega t - ik_{\mathrm{wg}}z}] \tag{106a}$$

$$\vec{B}(\vec{x},t) = \vec{B}_0(x,y)\,\mathrm{Re}[\exp^{i\omega t - ik_{\mathrm{wg}}z}] \tag{106b}$$

developing a profile $\vec{E}_0(x,y)$ in the transverse direction, which propagates along z with a wave number k_{wg}. In general, a given waveguide can give rise to several solutions of the form 106a, 106b for a given ω. A solution, completely determined by the set $\{\vec{E}_0, \vec{B}_0, k_{\mathrm{wg}}\}$, is refered to as a "mode". We note that k_{wg} can be imaginary, resulting in a damped mode, that cannot propagate. To classify a mode, $\vec{E}_0(x,y)$ and $\vec{B}_0(x,y)$ are decomposed into their components transverse and parallel to the propagation axis $\vec{E}_0 = \vec{E}_T + E_z\vec{e}_z$. Depending on the existence of E_z, B_z or both, the modes can be classified into

- **TE, TM and mixed modes** if $E_z = 0, B_z \neq 0,\ \ B_z = 0, E_z \neq 0$ or $E_z \neq 0, B_z \neq 0$, respectively. These modes are refered to as "transverse electric", "transverse magnetic" and "mixed" modes
- **TEM modes**, for which $E_z = 0, B_z = 0$.

This classification is more than a mere label: The mechanism of propagation is fundamentally different for different types of waves.

TE, TM and mixed modes can be understood as standing waves, which develop between the waveguide boundary conditions in the x–y–plane. If $a \geq \lambda/2$ or $b \geq \lambda/2$, the transverse profile $\vec{E}_0(x,y)$ can be a standing wave, with a nonzero E_z or B_z component. This standing wave is a superposition of waves, which propagate perpendicular to the transmission line with wave vector $\pm\vec{k}_T = n\,2\pi/a\ \vec{e}_x + m2\pi/b\ \vec{e}_y,\ \ n, m \in \mathbb{N} \cup \{0\}$. The

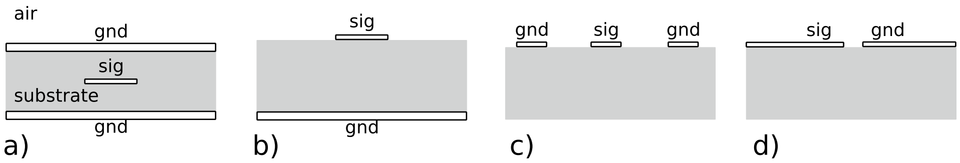

Figure 50: Different layouts of microstructures supporting TEM modes. The stripline (a), the microstrip line (b), the coplanar waveguide (c) and the slotline (d).

modulus of the total wavevector $\vec{k} = \vec{k}_T + k_z \vec{e}_z$ is still fixed by the dispersion relation of the medium $k = \omega/c$. Consequently, the k_z component is reduced with respect to its free-space value.

$$k_{\mathrm{wg}} = k_z = \sqrt{\frac{\omega^2}{c^2} - k_T^2}$$

It follows that a TE or TM mode can only propagate, if the frequency ω exceeds a certain cutoff frequency $\omega > \omega_c = ck_T$.

TEM modes cannot be understood in this way. They exist only in multi–conductor guides and are the quasi–static version of a DC signal applied to the guide. They do not exhibit a cutoff frequency, rather they exist for all ω, even for DC. Their full wave vector is directed along z and they propagate with the speed of light c in the respective medium: $\vec{k} = \omega/c\ \vec{e}_z$. They can develop in a structure with $a, b \ll \lambda$.

Mathematically, they are described by inserting the Ansatz 106a with $k_{\mathrm{wg}} = \omega/c$ into Maxwell's equations and applying the additional constraint $E_z = B_z = 0$. The result are the following equations for the transverse field $\vec{E}_T$:

$$\vec{H}_T = \frac{1}{\eta} \vec{e}_z \times \vec{E}_T \tag{107a}$$

$$0 = \nabla_T \times \vec{E}_T \tag{107b}$$

$$0 = \nabla_T \cdot \vec{E}_T \tag{107c}$$

where $\eta = \sqrt{\mu/\epsilon}$ is the impedance of the medium and the solutions are subject to the boundary conditions imposed by the waveguide. $\vec{H}_T$ is completely determined from knowledge of $\vec{E}_T$. $\vec{E}_T$ in turn is given by the quasi–electrostatic problem 107b,107c.

As stated above, TEM modes can even propagate in guides with dimensions $a, b \ll \lambda$. This renders them an extremely powerful tool to conduct high–frequency signals on microfabricated structures like PCB boards. A whole wealth of microfabricated guiding structures has been developed for this purpose, the most common ones are depicted in figure 50. The transmission line on our chip is of type 50 c)

Imperfections and quasi–TEM modes The above reasoning assumes the waveguide to be immersed into a homogeneous dielectric and the conductors to be perfect. In the real–world implementations of fig. 50, the medium is composed of several regions of

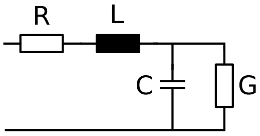

Figure 51: Equivalent circuit of a transmission line. Capacitance, Inductance, series and shunt resistance are modeled by their 1D densities C, L, R and G respectively.

substrate, air, and possibly other media. Furthermore, the conductors and the medium exhibit a nonzero Ohmic resistance.

The former problem is mostly dealt with by modelling the different dielectrics by one dielectric with an effective dielectric constant ([153] p. 401f.). In our case, we solve it by a finite–element simulation of the electric field (see below).

Ohmic losses in the dielectric are usually small and can be calculated as a perturbation. One first finds a solution to equation 107a and calculates the losses from the resulting field $\vec{E}_0$.

Ohmic losses in the conductors give rise to the skin effect. If the transmission line has a conductivity σ and carries a current alternating at a frequency ω, this current will flow only near the surface of the conductors, within a region of skin depth $\delta = \sqrt{2/\omega\mu\sigma}$. In usual applications, the dimensions of the conductors are $\gg \delta$. The losses can then be taken into account as a perturbation. One first calculates a solution to equation 107a, assuming perfect conductors. Perfect conductors are field–free, so the magnetic field is produced by surface currents, which can be calculated from the resulting $\vec{H}_T$. They translate into losses with the surface resistance $R_S = (\sigma\delta)^{-1}$.

We deal with the problem by a finite–element calculation (see below). For practical purposes, we note that the skin depth in gold at the ^{87}Rb frequency $f = 6.8$GHz is $\delta = 0.9\mu$m [108], much smaller than the size of our conductors.

As becomes clear from the definition of the conductivity $\vec{j} = \sigma\vec{E}$, a nonzero conductivity, given a nonzero current density j_z, gives rise to a nonvanishing field E_z. Strictly speaking, the resulting mode is not a pure TEM–mode any more. However, $E_z \ll E_T$ and all important characteristics of TEM–modes remain, so these modes are refered to as “quasi–TEM modes”.

Equivalent circuit model An infinitesimal piece of transmission line of length dz can be described by an equivalent circuit (figure 51). This “distributed parameter circuit” models the capacitance between the conductors Cdz, the inductance of the conductors Ldz, the series resistance of the conductors Rdz and the shunt resistance of the dielectric Gdz. Here, C, L, R and G are 1D densities of capacitance, inductance and resistance. In this model, it can be shown [153], [154] that an infinitely long line of these pieces supports voltage waves

$$V(t,z) = V_0\mathrm{Re}[\exp[i\omega t - \gamma z]]$$

with the propagation constant

$$\gamma = \sqrt{(R + i\omega L)(G + i\omega C)} \tag{108}$$

and corresponding current waves with

$$I(t,z) = \frac{V_o}{Z}\mathrm{Re}[\exp[i\omega t - \gamma z]]$$

where the line impedance is

$$Z = \sqrt{\frac{R + i\omega L}{G + i\omega C}} \tag{109}$$

Design of the transmission line

Transmission line vs. freely propagating beam For our application, a transmission line presents some clear advantages over a freely propagating microwave:

- The microwave power is focussed onto a much smaller cross section, of size $a \cdot b$ instead of at least λ^2 for a freely propagating beam. This results in stronger magnetic fields at the atoms' position and thus a stronger coupling to the atoms.
- The exact profile $B_0(x, y)$ of the excitation field can be controlled by the design. This is not the case for a freely propagating wave, since it is impossible to take into account all possible reflections on the apparatus. In particular, the temporal stability of the near–field of the transmission line will presumably be higher than for a propagating wave, whose reflections on the apparatus might drift over time.

There are in turn a number of challenges, which have to be addressed by the chip design.

- Being confined to the dimensions a, b, the near field of a transmission line is neccessarily inhomogeneous. The transmission line and / or the trap have to be chosen such as to ensure a sufficiently homogeneous Rabi frequency over the cloud.
- The transmission line imposes constraints on the design of the DC conductors. In particular, no DC conductor can cross the transmission line.

High–level design considerations From the various transmission line layouts of figure 50, the coplanar waveguide (CPW) is the most attractive choice to create a suitable near–field to drive atomic transitions. It can be implemented in a geometry like figure 52 a): The CPW is placed on the uppermost layer of the chip, the closest possible to the atomic cloud. Its near–field then extends into the space above the chip surface, where the atomic cloud can be placed in a magnetic trap.
Compared to the stripline and microstrip line layouts of figure 50, the CPW has a number of advantages. Its near–field extends symmetrically into the chip and into the space above the chip surface. In contrast, layouts like the stripline or the microstrip line concentrate the field inside the chip substrate, creating less field at the position of the atoms. For the same reason, the CPW is easy to decouple from the DC wires of the chip. In a CPW design, DC wires can be placed on a lower chip layer, which can be kept free from microwave conductors. For layouts like the microstrip line, microwave

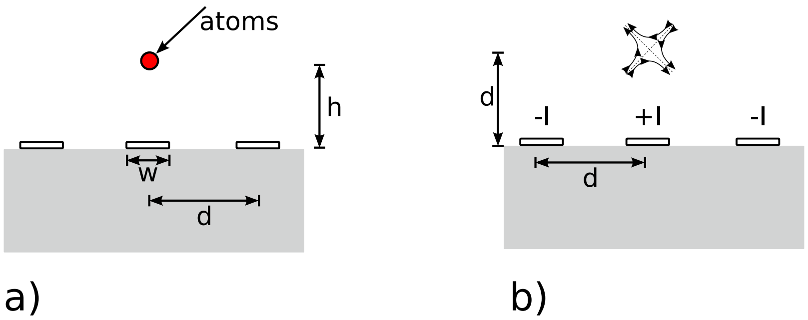

Figure 52: Coupling of the atoms to the magnetic near–field of a coplanar waveguide. The general situation is shown in a). Our design is shown in b). By applying DC currents as shown in the figure, a trap can be created at $h = d$ without using external bias fields [155].

conductors would have to be placed on a lower chip layer, with higher chances to couple into underlying DC wires or structures on the back side of the chip. Basically, all these advantages also hold for the slotline (fig. 50 (d)). This type of line, however, is prone to radiation losses (a voltage across the conductor gap creates dipole radiation). Furthermore, the CPW geometry has the technical advantage that there exist standard connectors terminating in a CPW.

Dimensions of the transmission line With the coarse geometry being fixed by the preceding considerations, the remaining design decision is the choice of the dimensions w, d and h (fig. 52).

An obvious choice would consist in choosing w and d the largest possible. This would create a maximally homogeneous field, since, under a scaling transformation with parameter λ, the gradient of the magnetic field scales with $\sim \frac{1}{\lambda^2}$, whereas the magnetic field scales only with $\frac{1}{\lambda}$. It is clear, however, that d can be at most of the order of the thickness of the chip. The near–field of the structure is also of the order of d and for d larger than the chip thickness, the microwave could couple into structures on a lower chip layer or onto structures on the backside of the chip.

To fix the precise dimension for d, we followed an idea sketched in fig. 52 b) and characterized by $h = d$. In this scenario, a transversally confining trap can be created without using using external bias fields, by passing DC currents of $+I$ and $-I$ through the signal and ground conductors, respectively. These currents could in principle be programmed by connecting all three conductors in series to one current supply. In this configuration, fluctuations of the current supply would affect only the trap frequencies, not the position. We chose the dimensions such that we can create such a trap with transverse trap frequencies up to $f_x = f_y = 1\text{kHz}$ with a reasonable current ($I = 3\text{A}$). This results in choosing $d = 175\mu\text{m}$.

We chose $w = 50\mu\text{m}$ for the width of the center conductor as well as for the ground conductors. This value is the minimum possible value for the conductor to support the maximum DC current ($I = 3\text{A}$) of our current supplies. The choice is motivated by the

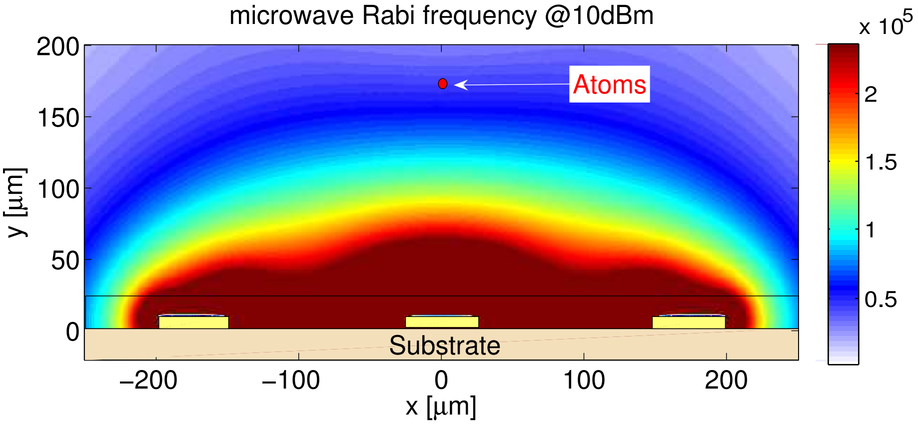

Figure 53: One–photon resonant Rabi–frequency (in units of Hz) of the microwave excitation field for a total microwave power of 10dBm. The static field is assumed to be directed along the transmission line. The translucent box around the conductors indicates the dimensions of the dielectric mirror coating.

fact that we intend to pass a DC current along with the microwave in these conductors to create the trap (see section "The DC conductors" below). Thin wires can create stronger confinement, which is required for the evaporative cooling.

Finite–Element simulation of the resulting excitation field To compute the resulting excitation field, we performed a finite–element simulation of the transmission line. To this end, we used a framework developed by Philipp Treutlein with the software package COMSOL (www.comsol.com). It computes the fields $\vec{E}_T, \vec{H}_T, j_z, E_z$ of a quasi–TEM mode in a plane perpendicular to the transmission line (assumed to be the x–y–plane in the following). This plane may be composed of multiple domains with varying physical properties (see fig. 53 for an example). All fields are assumed to be time–harmonic and the calculation is performed in two steps:

- A magneto–quasistatic model (The "AC power electromagnetics" model) calculates the z–component of the electromagnetic vector potential $A_z(x,y)$, which solves the equation

  $$(i\omega\sigma - \omega^2\epsilon_0\epsilon_r)A_z + \nabla \times (\mu_0^{-1}\mu_r^{-1}\nabla \times A_z) = J_z^e. \tag{110}$$

  The model allows for domains of varying conductivity σ, relative permittivity ϵ_r, permeability μ_r and external current density J_z^e. In particular, the simulation includes the skin effect in domains of nonzero σ. J_z^e allows to select a specific mode and to prevent the simulation from producing a zero solution. The boundary conditions of the simulation box are chosen as $\vec{n} \times \vec{H} = 0$, such as to ensure a zero

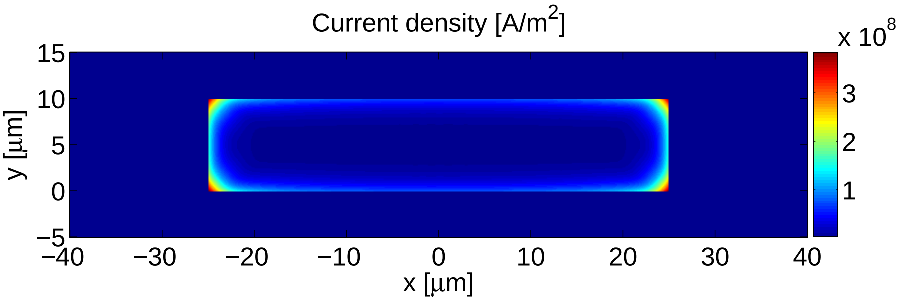

Figure 54: Current density in the central conductor for a microwave power of 10dBm. Due to the skin effect, the current flows mostly on the edges of the conductor.

net current on the CPW. Finally, the resulting A_z is used to calculate $\vec{B}_T$, E_z and j_z.

- A 2D electrostatic simulation computes the electrostatic potential V, which solves the equation
$$-\nabla \cdot (\epsilon_0 \epsilon_r \nabla V) = 0. \tag{111}$$
Again, multiple dielectrics of varying permittivity ϵ_r can be handled. The boundary conditions of the simulation box are chosen as $\vec{n} \cdot \vec{D} = 0$, such as to ensure a zero net charge on the CPW. The boundary condition of the conductors are Dirichlet boundary conditions, such as to guarantee a finite potential V on the surface of the signal line and a zero potential on the ground lines. The result V is subsequently used to generate $\vec{E}_T(x, y)$.

Both solutions are not normalized. To be a valid solution, they must be rescaled such that current and voltage satisfy the line impedance $U/I = Z$. To obtain Z, all the circuit parameters of figure 51 are calculated directly from the simulations, L and R from the magneto–quasi–static model, C and G from the electrostatic model. By means of equations 109 and 108, these values also yield the impedance Z and the propagation constant γ. The resulting Z is then used to correctly rescale the solutions.

Before turning to an analysis of the result of this simulation, we would like to point out some minor caveats to keep in mind: In our simulation we excite the symmetric TEM mode of the waveguide by choosing an appropriate external current density J_z^e and voltage on the central conductor V. However, it is known that CPWs also exhibit an antisymmetric mode, which can also propagate at our frequency. On a long transmission line, only the symmetric mode is present, since the antisymmetric mode decays by radiation losses [156]. For our chip, we cannot exclude that the antisymmetric mode might be excited at perturbations like the connectors or the bond wires. Comparable chips in our group in Munich have produced purely symmetric modes.

In addition, our model cannot simulate TE or TM modes. We can safely neglect them, since the dimensions of our waveguide are much smaller than the wavelength, so these modes would appear at frequencies much higher than the frequencies of our clock excitation.

Another caveat is that the simulation does not take into account DC magnetic fields. Such fields will be present in the experiment, since we will operate the transmission line in presence of the magnetic trap. We cannot exclude that a DC field could modify the distribution of the microwave current, e.g. via the Hall effect.

Characteristic parameters of our transmission line The most immediate result of this simulation are the propagation parameters of the transmission line. We compute the following values for the impedance Z, the wavelength λ and the loss factor l

$$\begin{aligned} Z &= 80\Omega \\ \lambda &= 17.4 \text{ mm} \\ l &= 13\text{dB/m} \end{aligned} \tag{112}$$

λ differs from its value in vacuum $\lambda = c/f = 44\text{mm}$, due to the dielectric properties of the AlN substrate. The propagation losses l are mostly due to Ohmic losses in the conductors. The pronounced skin effect raises the resistance of the transmission line to $R = 586\Omega/\text{m}$ at our clock frequency.

Rabi frequency in the microwave near–field Probably the most important result of the simulation is the strength of the resulting driving field. To characterize it, we compute from the simulation the resonant 1–photon Rabi–frequency of the transition $|1,-1\rangle \to |2,0\rangle$ (see eq. 47 and fig. 23)

$$\hbar\Omega_{\text{MW}} = \frac{2g_J\mu_B}{\hbar}\langle 2,0|g_J J_+|1,-1\rangle B_{\text{MW},+} = \mu_B B_{\text{MW},+} \tag{113}$$

where $B_{\text{MW},+}$ is the modulus of the time–harmonic σ_+–polarised component of the microwave's B field. For the current analysis, we assume the atomic quantisation axis to be directed along the guide, so that $B_{\text{MW},+} = \frac{1}{\sqrt{2}}|\vec{B}_T(x,y)|$. Before applying equation 113, we rescale B and j_z of the magneto–quasistatic simulation such that the total current I corresponds to a given microwave power $P = ZI^2$. A result of such an analysis is shown in Fig. 53.

For realistic microwave powers ($P = 10\text{dBm}$), the one–photon Rabi frequency at the intended position of the atoms is about $2\pi \cdot 50\text{kHz}$. The order of magnitude agrees well with an analytic estimate: The impedance of the line is computed to be 80Ω (see below), so that 10dBm of microwave power correspond to a current of $I = 11\text{mA}$. Replacing the waveguide by a thin conductor, we compute from these values a Rabi frequency of $\Omega = 2\pi \cdot 120\text{kHz}$ at a height $h = 175\mu\text{m}$ over the conductor, which is of the same order of magnitude as the finite element simulation.

We consider it realistic to operate the transmission line at 10dBm of microwave power,

since the current density in the conductors (Fig. 54) remains well below the maximum current density in gold for small conductors, $10^{12}\mathrm{A/m}^2$ [155].
To estimate the duration of the Ramsey pulses at this intensity, we recall that the Ramsey pulses drive a two–photon transition between the levels $|1,-1\rangle$ and $|2,1\rangle$, enhanced by the level $|2,0\rangle$. The microwave drives the transition $|1,-1\rangle \rightarrow |2,0\rangle$, the transition $|2,0\rangle \rightarrow |2,1\rangle$ is driven by a supplementary RF photon. The resonant two–photon Rabi frequency of this transition is given by eq. 49

$$\Omega_{2\Phi}(\vec{x}) = \frac{\Omega_{\mathrm{MW}}(\vec{x})\Omega_{\mathrm{RF}}(\vec{x})}{2\Delta(\vec{x})} \tag{114}$$

We recall from section 3.3 that, in order to avoid lightshifts, we have to choose $\Omega_{\mathrm{MW}} = \Omega_{\mathrm{RF}}$. Assuming $\Delta = 2\pi \cdot 0.7\mathrm{MHz}$, the upper value of $\Omega_{\mathrm{MW}} = 2\pi \cdot 50\mathrm{kHz}$ then leads to

$$\Omega_{2\Phi} = 2\pi \cdot 1.8 \cdot 10^3 \mathrm{s}^{-1}$$

With this frequency, the $\pi/2$ pulses can be performed on a millisecond timescale.

Homogeneity of the excitation field Another requirement of our design is to provide a maximally homogeneous excitation field. To assess the performance of the transmission line in this respect, the relevant quantity is again the two–photon Rabi frequency (eq. 49)

$$\Omega_{2\Phi}(\vec{x}) = \frac{\Omega_{\mathrm{MW}}(\vec{x})\Omega_{\mathrm{RF}}(\vec{x})}{2\Delta(\vec{x})} \tag{115}$$

This quantity should vary as little as possible over the atomic cloud. All its three components, the resonant microwave ($\Omega_{\mathrm{MW}}(\vec{x})$) and RF ($\Omega_{\mathrm{RF}}(\vec{x})$) Rabi frequencies and the intermediate–state detuning $\Delta(\vec{x})$, vary with $\vec{x}$, This variation has a longitudinal component (along the transmission line) as well as a transverse component (in the plane perpendicular to the transmission line). We will now estimate the typical variation of each of these quantities over our atomic cloud.

$\Delta(\vec{x})$ varies over the cloud, since the $|1,-1\rangle$ and $|2,1\rangle$ levels experience a linear Zeeman shift, while the intermediate state $|2,0\rangle$ is insensitive to the magnetic trapping field. The atoms explore a typical field of $B = 2k_BT/\mu_B$, which leads to a typical variation of $\sigma_\Delta \approx \frac{k_BT}{\hbar} = 2\pi \cdot 10\mathrm{kHz}$. where we have assumed a typical temperature of $T = 500\mathrm{nK}$. Assuming the parameters of [39] ($\Delta = 2\pi \cdot 0.7\mathrm{MHz}$), this contributes a variation of the Rabi frequency of

$$\frac{\sigma_{\Omega_{2\Phi}}}{\Omega_{2\Phi}} = \frac{\sigma_\Delta}{\Delta} \approx 1.4 \cdot 10^{-2}$$

To compute the transverse variation of Ω_{MW}, we extract $\vec{B}_{\mathrm{MW}}(x,y)$ from the magneto–quasistatic simulation. To compute the σ_+–polarized component $B_{\mathrm{MW},+}(x,y)$, we compute its component orthogonal of the static trapping field $\vec{B}_S$.

$$B_{\mathrm{MW},+}(x,y) = \frac{1}{\sqrt{2}}\sqrt{B_{\mathrm{MW}}(x,y)^2 - \left(\vec{B}_{\mathrm{MW}}(x,y) \cdot \frac{\vec{B}_S(x,y)}{|\vec{B}_S(x,y)|}\right)^2}$$

The resulting Ω_{MW} is computed from equation 113. We compute its variation over the cloud, weighted by the atomic density in a typical trap of $(\omega_x, \omega_y) = 2\pi \cdot (1\mathrm{k}, 1\mathrm{k})\mathrm{Hz}$ floating at $(x, y) = (0, 175)\mu\mathrm{m}$. This yields a value of

$$\frac{\sigma_{\Omega_{2\Phi}}}{\Omega_{2\Phi}}\Big|_{\mathrm{transverse}} = \frac{\sigma_{\Omega_{\mathrm{MW}}}}{\Omega_{\mathrm{MW}}}\Big|_{\mathrm{transverse}} = 1.6 \cdot 10^{-2}$$

The longitudinal variation of Ω_{MW} depends on the termination of the line (see below). For a matched termination, the microwave is a propagating wave and its variation is limited by losses along the transmission line. They can be computed from the simulation by computing the propagation constant γ. For our case, we compute an attenuation of 13dB/m, leading to a variation over the length of our cloud $\sigma = 2.2\mathrm{mm}$ of

$$\frac{\sigma_{\Omega_{2\Phi}}}{\Omega_{2\Phi}}\Big|_{\mathrm{longitudinal}} = \frac{\sigma_{\Omega_{\mathrm{MW}}}}{\Omega_{\mathrm{MW}}}\Big|_{\mathrm{longitudinal}} = 4 \cdot 10^{-3}.$$

For a maximally unmatched termination (short circuit or open circuit), the microwave forms a standing wave on the chip. Assuming the cloud to be placed in an antinode of the current, we compute a variation of

$$\frac{\sigma_{\Omega_{2\Phi}}}{\Omega_{2\Phi}}\Big|_{\mathrm{longitudinal}} = \frac{\sigma_{\Omega_{\mathrm{MW}}}}{\Omega_{\mathrm{MW}}}\Big|_{\mathrm{longitudinal}} = 2.3 \cdot 10^{-2}$$

The variation of Ω_{RF} is negligible. The RF photon will be coupled from a wire in a distance $d \approx 0.5\mathrm{mm}$ from the atoms. Longitudinally, the current along the wire can be assumed to be constant. Transversally, the variation due to the field gradient of the wire is of the order $\sigma_B/B = \sigma_t/d = 2.2 \cdot 10^{-3}$, where $\sigma_t = 1.1\mu\mathrm{m}$ is the transverse width of our cloud.

In summary, when the interrogation is performed with a propagating wave, all contributions to $\sigma_{\Omega_{2\Phi}}/\Omega_{2\Phi}$ are of the order of σ_Δ/Δ. This latter variation cannot be avoided, but has not been a problem for the previous experiments [39] and [29]. We therefore consider the field of our transmission line sufficiently homogeneous.

If the interrogation is performed by a standing wave, its standing wave profile becomes the dominant source of inhomogeneity, but remains of the order of magnitude of the other variations. According to the analysis of section 3, this interrogation will be preferable when working with highly elongated clouds.

Tapers and connections The above considerations fix the dimensions at the center of the stripline. We gradually change the dimensions over the chip to fit a standard Mini–SMP connector at the end of the line (see fig. 47). Therefore, the impedance varies over the length of this “taper”, from 50Ω at the connector to 80Ω at the center of the transmission line. A third point of definite impedance is the bond connection between the chips, where we took care that enough bond wires could be placed by choosing the layout $d = 300\mu\mathrm{m}$, $w = 350\mu\mathrm{m}$. This results in an intermediate impedance $Z = 63\Omega$ at the bond wires, calculated by the tool txline For simplicity, we vary the **dimensions** of the transmission line linearly between these points. There exist more sophisticated designs, minimizing the reflection from the taper [157], [158].

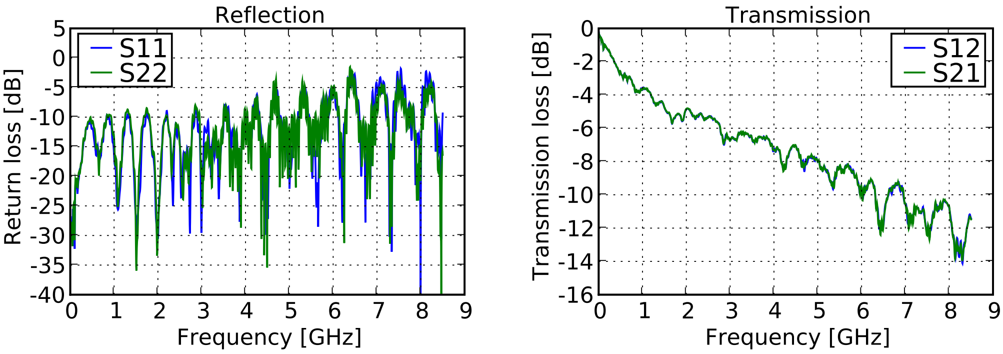

Figure 55: S–parameter measurement of the atomic clock chip. The transmission data (right figure) includes cable losses of −4.5dB at our clock frequency.

We connect the transmission line with a high–curent bias T at each end, so that we can add a DC current to the central conductor (see next paragraph). We have not provided a separate DC access for each of the ground conductors. In the current version of the chip, the ground conductors are connected by the footprint of the Mini-SMP connector. A current programmed between the grounds of the connectors will always flow in parallel through both ground lines. Meanwhile, integrated bias Ts on the chip have been developed in our group at Munich. They could be used in a future chip to provide a separate access to each of the ground lines.

In the microwave domain, the two bias Ts provide us with an access to each end of the transmission line. This allows us to flexibly choose the termination of the transmission line: We can create a propagating wave by injecting the microwave from one side and terminating the transmission line on the other side with a matched load. To perform the interrogation with a standing wave, we could either terminate the transmission line in an unmatched load (open or short circuit) or feed the microwave symmetrically from both ends.

Measurements After fabrication, the chip was characterized by a two–port measurement on a network analyzer. This measurement was performed on the completely glued and bonded chip, but without the glass cell in place. The resulting data is shown in Fig. 55. Resonances are clearly visible in the reflection data. Most probably, they stem from reflections at the bond wires. The transmission loss is −4.75dB over the whole chip, in clear disagreement with the simulation and the design tools, which predicted a loss of < 1dB. We are unable to account for these additional losses. If they were uniform over the whole length of the transmission line, they would create an amplitude variation of less than 2% over the atomic cloud, which would be acceptable.

Numeric values of the S–parameters at our clock frequency are given in table 7 It is worth noting that the measured loss is significantly smaller for the isolated science chip than for the fully assembled chip. One might be tempted to explain the additional losses by losses in the connector or the bond wires. However it might as well be possible that

	S11	S22	S12	S21
CSC1	−24.5	−24.8	−1.92	−1.94
C1	−16.4	−21.2	−4.74	−4.76

Table 7: S–parameters at our clock frequency $f = 6.835$GHz. C1 values are measurements of the fully assembled chip. CSC1 values are measurements of the science chip only. All data shown has been corrected for cable losses.

the microwave couples into structures formed by the combined chip assembly.

The DC resistance of the central conductor of the transmission line was measured to be $R = 1.47\Omega$. The peak DC current in this conductor attains $I = 3$A in an experimental cycle, corresponding to a peak power of 13W. Dissipation of this power is not a problem, since the peak power only lasts for 1–2 seconds, in an experimental cycle of typically 10s. However, with the benefit of hindsight, we would choose a larger width of the conductors in the outer areas of the transmission line. This would come at the expense of shorter tapers and a steeper change of the dimensions inside the taper. However, the return loss of our chip seems not to be limited by the tapers and reducing the resistance of the central conductor would be a prerequisite to prepare for shorter experimental cycles.

Alternative approaches There is one essential shortcoming of our design of our transmission line, the constraints imposed onto the layout of the DC conductors. Since no wire can cross the transmission line, we are forced to move all orthogonal wires onto the base chip. It would be possible, albeit with suppplementary development effort, to surmount this problem:

One approach would consist in switching from the coplanar waveguide to a microstrip line and to connect all crossing conductors with bias–tees. Such a line could be fabricated by microfabricating gold conductors onto the upper face of the science chip and metallizing the bottom face in order to form a groundplane. The bias–tees could be fabricated on the chip, either from lumped circuit elements or from microfabricated structures [159]. To prevent the microwave from propagating into the crossing structures, one would have to terminate the RF ports of the bias–tees by an open load and make sure that no pair of the crossing structures can create a resonator.

Another approach might be to have the DC conductors cross the microstrip line, but to selectively metallize the back side of the chip. In this way, only the microwave conductor would see a groundplane. Due to their high inductance and low capacitance, the DC conductors would create a higher impedance than the line impedance, preventing the microwave from leaking into these ports.

A completely different approach might be to integrate a microwave patch antenna on the chip [153]. Even though such a device would create a propagating wave, its near–field might still be well enough controlled to perform the excitation.

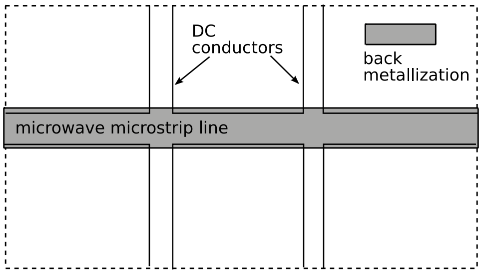

Figure 56: A way of having DC conductors cross a microwave microstrip line. The microwave path is defined by a patterned metallization of the backside of the chip, preventing propagation into the DC conductors.

5.1.2 The DC conductors

By connecting the transmission line with a bias–tee, we can pass a DC current in the central conductor and use it to create confinement in two directions. To create confinement along the direction of the transmission line, we have to add orthogonal conductors. To design these, we have one severe constraint: No conductor can cross the transmission line. Therefore, we placed all orthogonal conductors on the base chip (Fig. 57). To maximize their field strength, gradient and curvature above the chip at the position of the atoms, we chose the thickness of the science chip the thinnest possible. The thinnest commercially available AlN substrate of sufficient planarity had a thickness of 250μm. Basically, all chip traps of an experimental cycle are driven from sc0 (which creates the transverse confinement) and some combination of wires of bc-4 to bc4 (to create the longitudinal confinement). This is a very flexible setup, allowing to create all kinds of H and dimple configurations as shown in Fig. 17.

We will now turn to a detailed description of all traps involved in a cycle – both those driven by the conductors on the chip and those driven by the macroscopic conductors on the back side. We will describe them "in order of appearance", walking through a complete experimental cycle. We will use the same terms as in Figs. 47, 48 and 57.

The MOT The magneto–optical trap is driven by the macroscopic U. We typically apply a current of 55A and a bias field such that 3D quadrupole with gradients (18,15,3) G/cm forms 4mm above the chip surface. This procedure was first described in [160] and has been copied numerous times since then. Our macroscopic U is also based on the layout of this reference. We added the macroscopic I, which is embedded in the macroscopic U. This might change the current distribution of the macroscopic U. However, we never observed any problems suggesting that this might be the case.

The compressed MOT The quadrupole field of the compressed MOT is driven from sc0 and the conductors bc-2 and bc2, carrying currents $(I_{\text{sc0}}, I_{\text{bc-2}}, I_{\text{bc2}}) = (2.4, 3.4, -3.4)$A. We recall that the macroscopic I runs along the x–direction on the backside of the chip. Its leads are far from the center of the chip and oriented along z, so it can create only transverse confinement (in the y–z–plane). We create longitudinal confinement by means

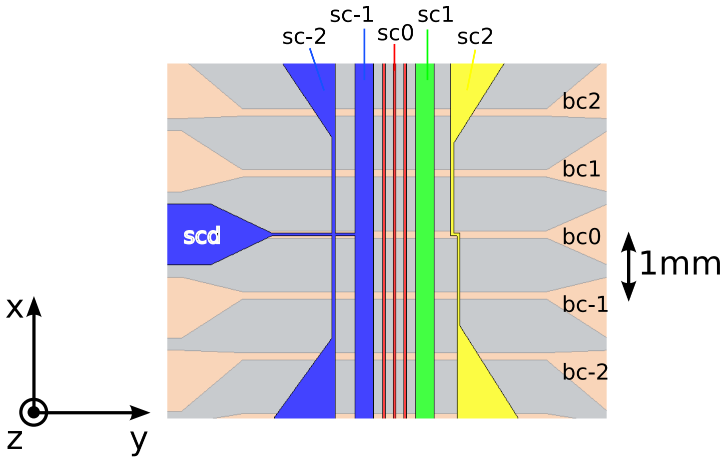

Figure 57: The core of the chip. The transmission line is drawn in red. Its central conductor (sc0) can carry a DC current. All orthogonal structures are placed on the base chip (bc-4 to bc4, not all shown). The RF photon is coupled by sc1 (green), (scd, sc-1 and sc-2) are a backup structure, as is sc2. Not shown are the macroscopic conductors on the back side of the chip (Fig. 48). They are aligned such that the macroscopic I lies parallel to sc0 on the backside of the chip.

of the wires bc-2 and bc2. We choose the bias fields such as to create a 3D quadrupole of gradients $(46, 27, 19)$ G/cm 1.2mm above the chip.

The transfer trap After the compressed MOT, we apply a phase of polarization gradient cooling on the compressed cloud. The goal of the initial magnetic trap – the transfer trap – is to capture this cloud in a way that minimizes the resulting increase in entropy. As we have calculated in section 2.3, this requires a weak confinement (ideally $f = 25$Hz in all directions). There are two further constraints: The trap has to be sufficiently deep to avoid loss of the hottest atoms. Typically, the cloud has a temperature of 10μK, so we require a trap depth of at least ten times this value $h = 100\mu$K. Also, the trap should form as far away from the chip as possible, since losses in the compressed MOT rise, when it approaches the chip. As a rule of thumb, a transfer at a distance of 0.45mm to the chip is feasible [8], but a distance of 1mm is desirable.

In the longitudinal direction, the mentioned targets are easily reached by a dimple trap. It follows from Eqs. 25 and 24 that the mentioned trap frequency is reached by a dimple trap with a dimple current of $I = 3A$ at a height of $d = 0.48$mm over the chip surface. The longitudinal depth of such a trap would be $h = 265\mu$K.

In the transverse directions, the situation is more difficult, since the gravitational gradient reduces the trap depth. As discussed above, the depth of a chip trap of given frequency or gradient can be increased by increasing the current in the conductor. Since currents on the chip are limited, we added the macrocopic I wire on the back side of the chip. Its center lies 1.5mm under the surface of the science chip. The transverse

	haensel01 [8] ($I = 2$A, $B_y = 8$G)	$I_{\mathrm{sc0}} = 3$A	$I_{\mathrm{mcI}} = 20$A	$I_{\mathrm{sc0}} = 3$A, $I_{\mathrm{mcI}} = 20$A
f_z [Hz]	**220**	**130**	**60**	**63**
h [μK]	—	100	100	100
z_0 [μm]	450	525	460	1100
B_x	—	2	2	2

Table 8: Transfer traps in a classic experiment (haensel01) and on our chip (right three columns). The scenarios of our chip have been optimized to provide the lowest possible trapping frequency at $h = 100\mu$K, $B_x = 2$G. We note that the scenario haensel01 was used to trap atoms in the state $|2,2\rangle$, whereas our scenarios are valid for the states $|1,-1\rangle$ and $|2,1\rangle$

confinement of our transfer trap is created by a current in sc0 or the macroscopic I (mcI), or both, with a bias field B_y to form the trap. To create a harmonic confinement, we add a bias field B_x. According to equation 23, this converts the field gradient $B' = dB_y/dz$ to a field curvature $d^2B/dz^2 = B'^2/(2B_x)$ In the limit that B_y can be described by a gradient $B_y = B'_y(z - z_0)$, B_x defines the range in which the trap is harmonic. The trap looks like a harmonic trap near the trap center in a region, where $B_x(z) \ll B_y(z)$. For the region far from the trap center, where $B_y \gg B_x$, the potential becomes linear. The atoms explore a region defined by their temperature. To constrain them to the harmonic region, we require $B_x \gg k_B T/(g_F m_F \mu_B) = 0.3$G.

To estimate the gain provided by the macroscopic I, we numerically optimized several traps, driven either from sc0, from mcI, or both (Table 8). The improvement achieved by the macroscopic I is evident, especially in view of the fact that the energy transfered to the atoms by a mismatched trap (equation 30) rises with the square of the trap frequency.

Another advantage is not not visible from table 8: The potential is only harmonic, if B_y can be described by a gradient $B_y = B'_y(z - z_0)$. Increasing the distance d from the atoms to the trap–creating conductor reduces higher–order components of the wire field $B_y(z)$, which distort the harmonic potential.

Even with the macroscopic I, we cannot reach perfect mode–matching in the z–direction for a transfer in the states $|2,1\rangle$ and $|1,-1\rangle$. We note, however, that we can reach this for the state $|2,2\rangle$, if we relax the condition on h to $h = 50\mu$K.

An intriguing possiblity would be to perform the transfer with the macroscopic U. However, in its actual configuration, it neccessarily creates a quadrupole trap. Transfering into a quadrupole trap would imply another transfer into a Ioffe trap near the chip, so we did not pursue this direction.

The cooling trap To perform the evaporative cooling, we ramp from the initial trap into a trap providing tighter confinement, the cooling trap. This increases the collision rate of the cloud by a factor of $\bar{\omega}^2_{\mathrm{transfer}}/\bar{\omega}^2_{\mathrm{cool}}$, where $\bar{\omega} = (\omega_x\omega_y\omega_z)^{1/3}$ denotes the harmonic average of the trap frequencies. [117]. The requirement for this trap is thus to provide a maximum $\bar{\omega}_{\text{cool}}$. This amounts to maximizing all three trap frequencies.

Confinement in the transverse directions is created by passing a current in sc0 and applying a bias field in the y–direction. Compared to the transfer trap, the trap frequency is increased by lowering the current in the wire, increasing the bias field B_y and lowering the field B_x. In this way, trap frequencies of several kHz are easily achieved.

In the longitudinal direction, confinement can be created either by creating a Ioffe-Pritchard trap from bc-1 and bc1 or by creating a dimple from bc0. For the Ioffe–Pritchard case, the maximum achievable trapping frequency can be read off from Fig. 16. Assuming a maximum current of $I_{bc1} = I_{bc-1} = 3$A and a trap height at the maximum of fig. 16, one could achieve $f_x = 26$Hz. Creating the confinement by a dimple from bc0, the maximum frequency is given by equation 25. Assuming a trap at a height $d = 50\mu$m, i.e., 300μm away from the base chip wires, one could achieve a frequency of $f_x = 190$Hz. Condensates have been achieved in traps with far smaller longitudinal frequencies [8], but a higher frequency would be desirable. Clearly, this limitation is the most severe drawback of our double–layer chipdesign.

The clock trap As calculated above, we aim at performing the clock interrogation in a trap with $(f_x, f_y, f_z) = (0.5, 10^3, 10^3)$Hz. As in the previous traps, transverse confinement is created by sc0 and a bias field along y. We choose $I = 3$A, the maximum current sc0 can support. The bias field is adjusted to $B_y = 34.5$G, in order to reach the mentioned trap frequency. The rationale of this choice is that a high current creates a trap far from the chip, where corrugations of the conductors have little effect. With our parameters, the trap should form at a height $h = 175\mu$m over the chip. Previous studies ([19], [161]) indicate that at this height, the corrugations of the conductors would create potential fluctuations of $\approx 0.4\mu$K, with a correlation length of the order of h. The temperature of our cloud is of this order of magnitude, so the fragmentation of the cloud may limit us to clouds with a length comparable to h. However, the fabrication process of our chips is known to produce smoother wires than the process used in [19]. Therefore, we are optimistic not to be limited by corrugations.

6 The Electronics

Constructing an atom chip experiment is just as much an electronic challenge as it is a physical one and there are multiple reasons for this complexity.

First of all, electromagnetic chip traps rely on currents flowing through conductors on the chip. Evidently, a chip trap can only be as well controlled as is the current that is its source. This current must be well calibrated, to be able to quantitatively adjust the trap parameters. In addition, drifts of the currents must be low on all timescales, in order to reproducibly produce identical traps, between different experimental runs, over hours, days and even months of operation. Finally, the currents must be as noiseless as possible. Noise in a current on the chip translates directly into noise of some trap parameter. For frequencies from Hz to several kHz, this parametrically heats the atoms (imagine a trap filled with atoms hopping up and down at the powerline frequency!). For higher frequencies this leads to losses into untrapped states. Here, a chip experiment is even more challenging than a macroscopic BEC setup. In the latter, the traps are produced from macroscopic coils, which, due to their high inductance, filter noise starting from kHz frequencies. In contrast, the inductance of chip wires is low enough to transmit even RF frequencies. In fact, this is one of their advantages, since it allows to create TOP traps and adiabatic potentials on a chip (section 2). But, as we like to summarize it in the lab, “along with great power come great responsabilities”, in this case to guarantee a low noise level on all currents sent onto the chip.

Secondly, the whole setup is extremely sensitive to all kinds of electromagnetic perturbation. In part, this is a consequence of the problem just sketched. Noise can couple onto the chip wires, either by electromagnetic pickup in the wire and its supply cable, or by electric, magnetic or impedance coupling into the current driver electronics. Even if all this pickup is avoided, e.g. by careful shielding of the cables, the atoms themselves are still sensitive to RF and microwave fields, which can excite them into untrapped states.

A third challenge is specific to our experiment: We need to control several magnetic fields on the 10μG level (rel. 10^{-5}) to prevent fluctuating Zeeman shifts between different clock interrogations. To attenuate external fields, we have designed the Mumetal shield described in the last section. This, however, would be useless, if this performance were spoilt by a less well controlled field produced inside the shield. Consequently, the chip and coil currents driving these fields must also be controlled to the 10^{-5} level.

Finally, we recall from section 1 that a local oscillator (flywheel) signal is needed to perform a clock interrogation. In our case, this signal comes from a cryogenic oscillator and is upconverted to our clock frequency by a homebuilt synthesis chain. This upconversion must not significantly degrade the low phase noise of the original signal.

This chapter will describe the various electronic components, which we have set up to meet the special requirements of this experiment. To adress the issue of current stability and noise of the field–generating currents, we have developed an ultra–stable, feedback–regulated constant current source, which is documented in section 6.1. To generate the local oscillator signal of the interrogation, we have implemented a microwave synthesis chain, which is discussed in section 6.2.

6.1 The current supply

We have developed a homebuilt low–noise, ultrastable unipolar constant current supply to drive the currents in the chip and, possibly, the coils producing the bias field during the clock interrogation. This source accepts an analog programming voltage and regulates its output such that it sources a constant current proportional to this voltage. This section will discuss its design and performance.

6.1.1 Specification

The required performance of our source derives from the calculations of the preceding sections. In summary, we request the following specifications:

Specification		Rationale
max. output current	3A	chip design
Compliance voltage	6V	2Ω charge
modulation bandwidth	100kHz	switching time $< 10\mu$s
relative rms noise in the [10Hz–100kHz] bandwidth	$< 10^{-5}$	avoid parametric heating
Drift over 15 min.	$< 10^{-5}$ rel.	magnetic field stability
Drift over 1s after a step from zero to maximum current.	$< 10^{-5}$ rel.	magnetic field stability

Required feature	Rationale
floating output	drive currents in crossing wires
isolated programming input	protect the control computer, avoid ground loops
display of the output current	visual feedback to detect anomalies
integrated TTL–programmable switch to short–circuit the output	suppresion of quiescent output currents
manual programming input	

The last two specifications (drift over 15min and 1s) merit further comments: As discussed in 3.3, we require the relative shot–to–shot fluctuation of the magnetic field to be $< 10^{-5}$. This fluctuation mainly stems from the thermal drift of the current supply between two cycles. We will be able to insert a calibration cycle measuring the magnetic field every 15min, so we can correct for fluctuations on longer timescales. However, for this calibration to be valid, the magnetic field must converge to better than $< 10^{-5}$ during the 1s long clock interrogation, motivating the last specification.

6.1.2 The circuit

The circuit of our current supply is presented in figures 58 and 59. It is based on the design of the SYRTE laser diode drivers.

The core The core of the current source is presented in figure 59. The output is driven from a high–power constant voltage power supply V+p. The output is connected in series to a measurement resistance (Vishay VFP4Z), which continuously monitors the output current. The voltage over the measurement resistance is buffered by a differential amplifier (LT1128 and connecting 1k resistors) and converted into a current by R_s. This is possible, since the point G is a virtual ground, stabilized by the OP27. The resulting current I_s is proportional to the output current. It is matched against a programming current I_{prog}, provided by the user. The difference of these currents is taken as the error signal and minimized by the OP27. This OpAmp is wired as an integrator and controls the output voltage via the IRF630, realizing an I–regulator for the output current.

Linearized around its operating point, the core implements the well known feedback loop model of control theory, which is sketched in fig. 60. In this model, the output current S_o is split into a sum of two contributions: An unknown "free" current S_f, as it would flow without the feedback loop, and a correction current, injected by the feedback loop such as to compensate the free current and adjust the total output current to a user–defined value. Typically, the unknown "free" current S_f arises from noise coupling into the output. To suppress this noise, the feedback loop, described by the two transfer functions G and H, injects a correction current into the output, such that the total output current S_o is stable. It accomplishes this task by continuously monitoring the output current, matching it against a reference current and correcting it if neccessary. The continuous monitoring is described by the transfer function H. The resulting current $H \cdot S_o$ is then matched against the user reference R, generating the error signal $\epsilon = R - H \cdot S_o$. This signal is amplified by a transfer function G to generate the correction signal. It follows that the closed–loop output current is given by

$$S_o = \frac{1}{1+GH} S_f + \frac{GH}{1+GH} \cdot H^{-1} R \tag{116}$$

For a high loop gain $|GH| \gg 1$, the unknown current S_f is virtually suppressed and replaced by the user–programmed current $H^{-1}R$.

For our core, H comprises the measurement resistance and the LT1128 differential amplifier with its circuitry. We obtain, assuming the LT1128 to be perfect,

$$H(z) = R_m / R_s.$$

The reference current R is the Laplace transform of I_{prog}. G is realized by the OP27 integrator and the output circuitry. We obtain

$$G(z) = \frac{1}{zC(R_M + R_L(z))} \overset{z=i\omega}{=} -\frac{i}{\omega C(R_M + R_L(i\omega))}.$$

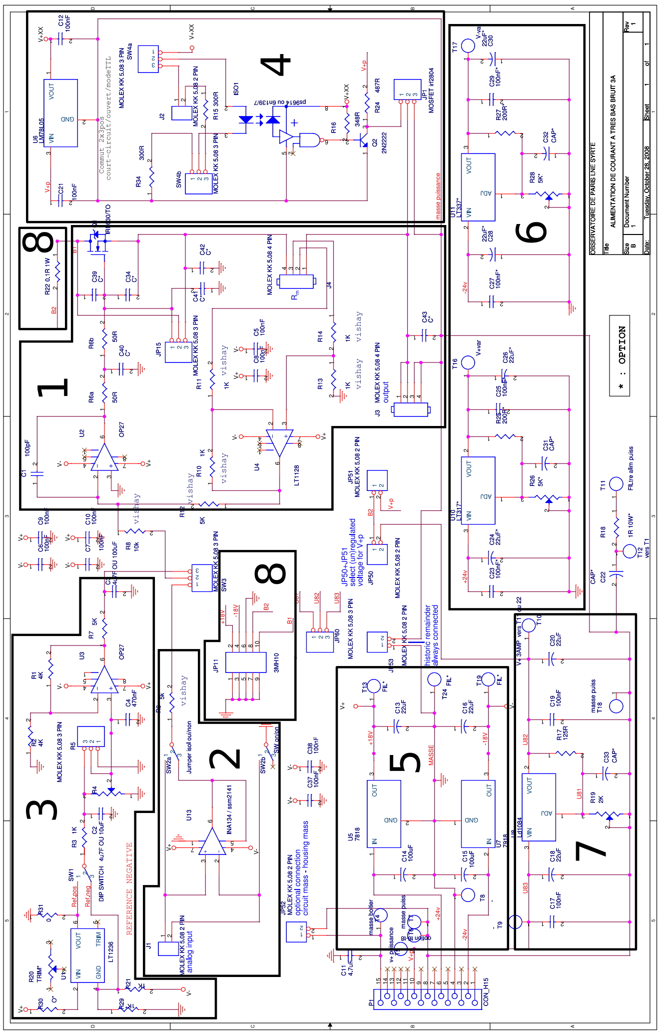

1) Core
2) Analog input
3) Manual input
4) TTL-controlled switch to short-circuit the output
5) 18V regulators for the core supply voltage
6) variable regulators for the core supply voltages (optional)
7) variable regulator for the output supply voltage
8) interface to the display

Figure 58: The circuit of our constant current supply, including all peripheral components.

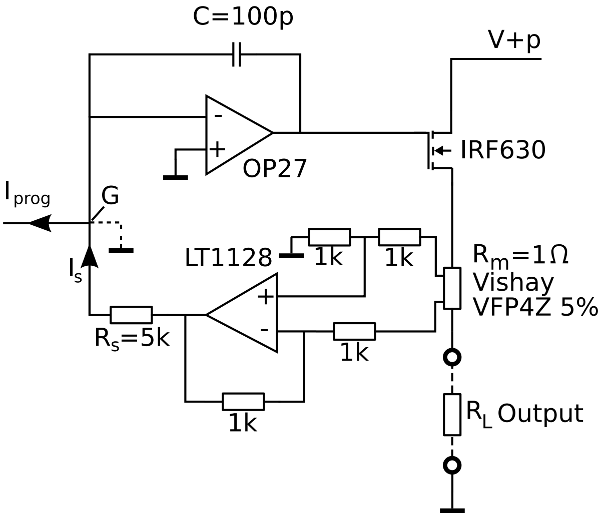

Figure 59: The core of the current source (simplified).

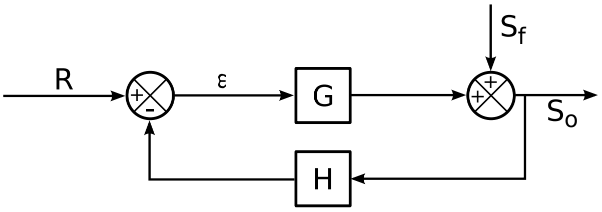

Figure 60: Model of the core. G is formed by the OP27 integrator and the circuitry of the output branch. H is formed by the LT1128 differential amplifier. All letters denote the Laplace–transformed currents at the respective point. They are complex–valued functions of one complex argument.

where we have assumed the OP27 to be perfect and R_M to be real. Furthermore, we have neglected the contribution of the IRF630, since its small–signal resistance $R_{\text{FET}} \approx 0.25\Omega$ is negligible against $R_M + R_L$.

The periphery The current source is driven by two different power supplies. The output branch is driven from a high–power supply V+p, as discussed above. This power supply can optionally be regulated by a LD1084V regulator.
All low–power components, including the core, are driven from a homebuilt ±24V power supply. This supply is regulated to ±18V or, optionally to a variable value. We will refer to this supply voltage as the "core supply voltage".
The grounds of both supplies are connected to each other, but disconnected from the housing, so that they form a single floating ground.

The programming current I_{prog} is generated from a programming voltage by a 15k resistor (Figure 58). The programming voltage in turn is taken either from the analog input voltage provided by the user or from the manual input. The analog input voltage can be either buffered by an INA134 line receiver or be connected directly to the 15k

Figure 61: The housing of the current source. All power–carrying components are mounted on separated heatsinks (right).

resistance. In the latter case, the ground of the current source will be locked to the ground of the analog input voltage.
The manual input is based on an LT1236 voltage reference, which can be adjusted by a potentiometer.

The output of the current source can be short–circuited by an ultra–low–resistance MOSFET (IRF2804, $R_{\text{on}} = 2\text{m}\Omega$). This MOSFET is remote–controlled by a TTL input, which is galvanically isolated by an optocoupler.

Do drive the display, we monitor the current with a second series resistance of $R = 0.1\Omega$, placed between V+p and the drain of the IRF630. The display is connected by a 10–pin ribbon connector and supplied by the core supply voltage.

The housing The current source is integrated into a 3U high and 28TE wide Schroff rack module (reference Schroff 24811-488, see fig. 61). The power carrying components (LD1084V, IRF630 and VFP4Z) are mounted outside the module on heatsinks. We use two separated heatsinks, one for the LD1084V and the IRF630, and another one for the VFP4Z, to isolate the latter from the heat of the former components. All heatsinks are electrically connected to the module wall, to shield the components from electric stray fields. The components are electrically isolated from the heatsinks.

The ground of the housing is connected to the ground of the circuit by a capacitor. As we will discuss below, this greatly improved the electro–magnetic compatibility (EMC) of the source.

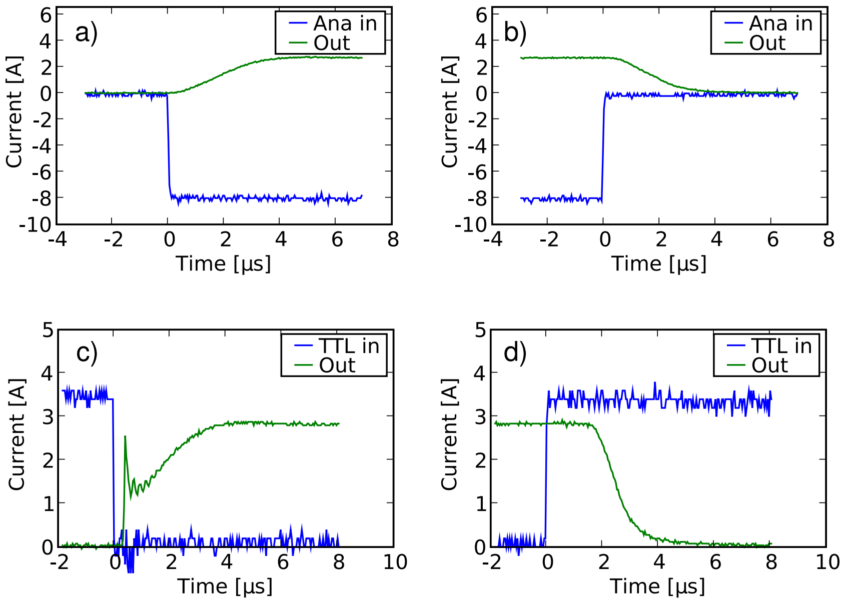

Figure 62: Step response of the current source. A step of the output current is programmed either by the analog input (a and b) or by suddenly opening (c) or closing (d) the TTL-programmed short–circuit in the output. In all cases, the current reacts on a timescale $< 10\mu$s.

6.1.3 Bandwidth and switching times

The bandwidth of the feedback loop is estimated from equation 116. It is given by the condition $|GH| = 1$, resulting in

$$\omega_{\mathrm{bw}} = \frac{R_m}{CR_s(R_m + R_L)} = 2\pi \cdot 160\mathrm{kHz}$$

where we have assumed a 1Ω load in the last step.

We have measured the switching behaviour of the source by running it on a constant load of 1Ω and programming a step of the output current on a timescale much faster than the estimated reaction time of the source. Such a step can be programmed in two ways: Either the current is modulated via the analog input voltage or the current is set to a constant value and the output is suddenly opened or closed using the TTL–controlled short–circuit in the output. Measurements of both cases are presented in figure 62. In both cases, the output current rises or falls on a timescale of $\approx 5\mu$s. This is consistent with a bandwidth of $2\pi \cdot 160$kHz and fast enough for all our experimental purposes.

6.1.4 Stability

Stability of the feedback loop Assuming perfect components, the stability of the feedback loop can be assessed from equation 116. The criterion of stability is the Nyquist criterion. In practice, this criterion is reduced to the rule of thumb that at the bandwidth limit (where $|GH| = 1$), the phase of the open–loop gain GH should keep a phase margin of at least 45° to the point of in–phase coupling: $-\arg(GH) < 180° - 45°$.

In our case $\arg(GH) = \arg(-i/(\omega C R_s)) - \arg(R_M + R_L) = -90° - \arg(R_M + R_L)$. Therefore, our source is stable for

$$\arg(R_M + R_L(i\omega_{\mathrm{bw}})) < 45°.$$

This criterion is most critical for an inductive load $R_L = R_0 + i\omega L$. In this case, the source is stable only if

$$\omega_{\mathrm{bw}} < (R_0 + R_M)/L \tag{117}$$

If the bandwidth is chosen higher than this criterion, the feedback loop will oscillate. When we have to drive inductive loads, we limit the bandwidth by increasing C. The limitation stated by equation 117 is rather severe: To drive our coils (with $R_0 = 2\Omega, L = 1\mathrm{mH}$), the bandwidth would have to be limited to $\omega_{\mathrm{bw}} = 2\pi \cdot 500\mathrm{Hz}$.

Stability of the power transistor In a former prototype the power transistor in the output branch was a BDX53C power Darlington instead of the IRF630. With this prototype, we have observed a second type of instability. This instability showed up as an oscillation of the output current at several MHz, a frequency clearly above the bandwidth of the feedback loop. This oscillation could not be calmed by changing C, confirming that the feedback loop was not involved. It occured mostly for small loads connected by long cables.

The reason for this instability turned out to be the power transistor driving the output. Certain darlington transistors (such as the BDX53C) can be prone to self–excited oscillations. After replacing this transistor by the IRF630, we have not observed this phenomenon any more.

6.1.5 Noise

The residual noise of our current source is presented in figure 63. This data has been taken by passing the current of the source through a 1Ω resistor and measuring the voltage over the resistor with a SRS SR760 FFT spectrum analyzer. The input noise of this analyzer is $< 10\mathrm{nV}/\sqrt{\mathrm{Hz}}$ [162]. The input is floating with a common–mode rejection ratio of 90dB To generate a stable programming current, we used an LM399H precision voltage reference, with an additional low–pass filter. This reference generates a constant voltage of ≈ 7V, programming our source to a 2.2A output current. We verified that the noise of this reference was small against the measured noise of the current source. We took four measurements, with and without using the INA134 buffer for the programming voltage and with and without connecting the circuit ground to the ground of the housing.

Internal noise The white–noise floor of Fig. 63 stems from noise sources in the circuit: Johnson noise of the resistors and voltage and current noise of the OpAmps.
Noise generated in the output branch is not critical, since it is corrected by the feedback loop. For our core, all noise generated between the output of the OP27 and the load

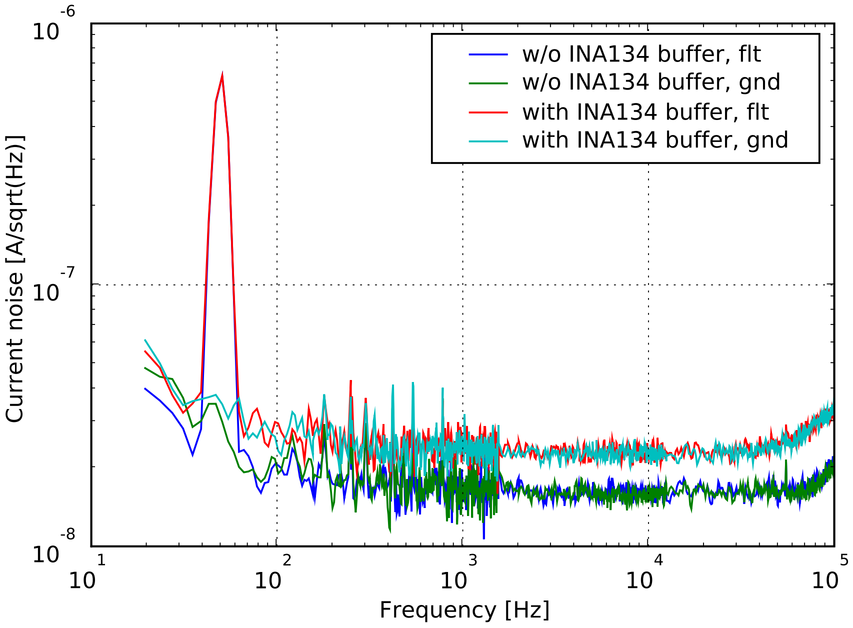

Figure 63: Current noise density of our source. In all measurements, the source is programmed to a constant output current of $I = 2.2$A. For the "gnd" measurements, the ground of the circuit is connected to the ground of the housing, for the "flt" measurements, it is floating and connected to the housing only by the capacitor C11. Two of the measurements were taken without buffering the analog input voltage by the INA134. The relative rms noise in the [20Hz, 100kHz] bandwidth is $I_{\text{rms, gnd}}/I = 2.5 \cdot 10^{-6}$ for the grounded and $I_{\text{rms, flt}}/I = 3.9 \cdot 10^{-6}$ for the floating measurements, respectively. The huge peak at 50Hz is a measurement artefact, due to the finite common–mode rejection of the SR760 (see text).

ground can be neglected.

In contrast, the noise contributions of I_{prog}, the LT1128, the OP27 and their respective circuitry are critical. Every noise generated by these components can be expressed as a noise contribution to the error signal $\epsilon = I_s - I_{\text{prog}}$, which translates into a current noise on the output current by the factor $H^{-1} = R_s/R_M$.

Therefore, an obvious choice is to choose R_M as high and R_s as small as possible. The smallest possible value for R_s is fixed by the capabilities of the LT1128. R_M is limited by power dissipation and the finite supply voltage V+p. Generally, R_M can be chosen larger for a current source with a lower maximum output current. Since the internal noise of the core is practically independent of the output current, the absolute current noise of a current source will be smaller for a smaller (maximum) output current. It is for this reason that current noise is often quoted relative to the output current. However, this does not imply that the relative noise be constant over the whole current range of one given current source.

We will now assess the internal noise of our core:

with the INA134 buffer If the programming voltage is buffered by the INA134, the voltage noise of this buffer is the dominant source of noise. Its output noise floor is specified to be 52nV/$\sqrt{\text{Hz}}$, translating into a current noise density of 17nA/$\sqrt{\text{Hz}}$. We measure a white–noise–floor of 23nA/$\sqrt{\text{Hz}}$. This agrees well, if the additional noise of the core circuit (see below) is taken into account.

without the INA134 buffer In this case, the programming voltage is connected directly to the 15k input resistance of the circuit, bypassing the INA134. Noise contributions then arise from the following sources:

15k input resistance	1 pA/$\sqrt{\text{Hz}}$
R_s (5k)	1.8 pA/$\sqrt{\text{Hz}}$
OP27 current noise	0.4 pA/$\sqrt{\text{Hz}}$
OP27 voltage noise	0.8 pA/$\sqrt{\text{Hz}}$
LT1128 current noise	0.2 pA/$\sqrt{\text{Hz}}$
LT1128 voltage noise	0.4 pA/$\sqrt{\text{Hz}}$
LT1128 1k resistors	1.6 pA/$\sqrt{\text{Hz}}$

Multiplied by the factor $H^{-1} = R_S/R_M$, these contributions sum up to an output current noise density of 14nA/$\sqrt{\text{Hz}}$, which corresponds well to our measurement (16nA/$\sqrt{\text{Hz}}$).

At such a low noise level, the electronic shot noise of the current can become visible. Assuming uncorrelated charge transport, this would predict an output noise level of 70nA/$\sqrt{\text{Hz}}$ [163]. However, the same reference also states that charge transport in metallic conductors usually is not uncorrelated, explaining why we do not observe a noise at this level.

Noise pickup, EMC At frequencies < 1kHz, the noise of the current source is dominated by sharp peaks at multiples of the 50Hz powerline frequency. In the “gnd” spectra of fig. 63, we observe both even and odd harmonics. This can hint towards the source of the noise: Coupling through the power supply contains predominantly the even harmonics (100Hz and multiples), since the supply voltage is rectified. In contrast, pickup is mainly caused by radiation of the transformers in the power supplies. These are placed before the rectifiers and consequently, their radiation contains predominantly the odd harmonics. In our case, both types of harmonics are present, suggesting that the coupling occurs as well by pickup as by coupling through the power supply.

The prominent feature at low frequencies is the huge peak at 50Hz in the “flt” spectra. It is caused by a classic problem of electromagnetic compatibility, a parasitic coupling capacitance between the primary and secondary winding of the power supply’s transformer ([164], illustration fig. 64). This capacitance couples some of the power line signal onto the ground of the current source. From an external perspective, this problem shows

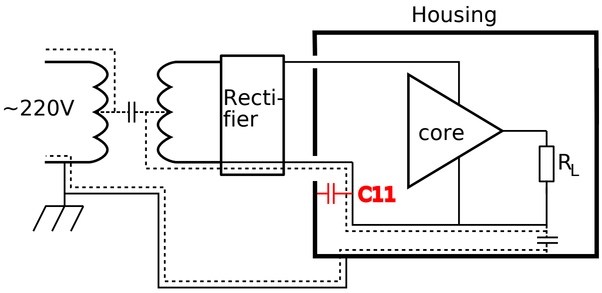

Figure 64: The transformer of the power supply contains a parasitic coupling capacitance between the primary and secondary loop which couples some of the 50Hz line signal onto the ground of the secondary loop. In the current supply, a ground loop (dotted line) can close at AC by a stray capacitance to the housing. The resulting current on the ground network couples into the signal by impedance coupling. We avoid this problem by filtering the ground of the power supply by capacitor C11 or by connecting the ground of the power supply with the ground of the circuit alltogether.

up as a common–mode fluctuation of the output against the lab ground. Basically, our noise measurement is not sensitive to such a fluctuation, since the input of the SR760 spectrum analyzer is floating. There exist two ways, however, how such a common–mode fluctuation can nontheless couple into in the measured signal:
Firstly, the input of the spectrum analyzer has a finite common–mode rejection. It does not completely suppress common–mode fluctuations at its input, but partly converts them to a visible differential signal. The efficiency of this conversion is known as the "common–mode rejection ratio" and is quoted to be −90dB for our SR760 analyzer. This figure agrees well with our measurement: The observed peak has an integrated intensity of 2μVrms, corresponding to a 60mV fluctuation between the circuit and lab grounds. Indeed, we measure an oscillation at 50Hz with this amplitude between both grounds.
Secondly, the common–mode oscillation discussed above could be converted to noise of the output by a mechanism presented in fig. 64. A ground loop can close at AC by a stray capacitance to the housing, such that the common–mode signal sources a current on the ground line of the circuit. This current can then couple into the output via impedance coupling.

Therefore, it is desirable to keep the common–mode fluctuation as low as possible. We have realized this by adding the capacitor C11 between the circuit ground and the housing (figure 64). This capacitor filters the power supply ground. It effectively connects the circuit ground to the lab ground at AC, while it can still float against the lab ground at DC. Without this capacitor, the height of the 50Hz–peak was 10μA/$\sqrt{\text{Hz}}$, more than an order of magnitude larger than in the data of figure 63. Whenever possible, however, we recommend to connect the circuit ground to the lab ground.

6.1.6 Long–term stability

Long–term fluctuations of the output current arise from temperature drifts of the components. As for the noise, all components in the output branch except the measurement resistor are uncritical, since their fluctuations are corrected by the feedback loop. The critical components – R_M, the OP27, the LT1128, the INA134 and their respective circuitry – fluctuate on two different timescales:

On a timescale of minutes to hours, their fluctuation is due to fluctuations of the ambient temperature. The ambient temperature inside the microclimate of the housing fluctuates, as power dissipation in the IRF630 and R_M heats up the interior. We will refer to them as the "temperature drift".

On a timescale of seconds, the components fluctuate because of temperature changes **inside** the components. These changes are due to changes of the power dissipated by the component. A power change heats up the substrate of a component on a timescale $R_C C_C$, where C_C is the component's heat capacity and R_C is the heat resistance of the component's housing. On these timescales, the component's heatsink can be assumed to remain at constant temperature, since it equilibrates on the much longer timescale $R_H C_H$, with R_H, C_H being the heat resistance and capacity of the heatsink. In particular, these drifts cannot be alleviated by choosing a better heatsink. Following the convention of Vishay, we will refer to these fluctuations as the "power drift".

We characterized both kind of fluctuations by driving the output current through a 4–terminal Vishay VFP4Z 1Ω 5% load resistor and measuring the voltage over its sense leads with a Keithley 2000/E 6-1/2 digit voltmeter. We generated the programming current by an LM399H reference (temperature coefficient 1ppm/K). Again, this reference programs our source to a current of 2.2A, precluding us from taking data at the maximum current (3A). The biggest concern of this measurement is the drift of the load resistor. For the analysis of the temperature drift, we neglect it. It is mounted outside a housing on a well–ventilated heatsink, so that its fluctuations will be small against the fluctuations of the components in the housing. For the analysis of the power drift, we can calibrate its influence (see below).

Temperature drift The current drift on the minute to hour timescale is presented in figure 65. Over the first hour under load, the current drifts by $4 \cdot 10^{-5} I$. After this phase, it stabilizes and remains stable to about $1 \cdot 10^{-5} I$. This drift is clearly correlated with the warm–up of the heatsinks, as R_M and the IRF630 dissipate power. We observe that the temperature of the heatsinks rises by about 20K during such a run, while the temperature in the housing rises by about 10K. For these temperature changes, the components should fluctuate by the following values:

R_M	±40ppm
internal resistors	±120ppm
OP27	±11ppm
LT1128	±4ppm ± unspecified bias current drift
INA134	±10ppm typ., ±100ppm max.

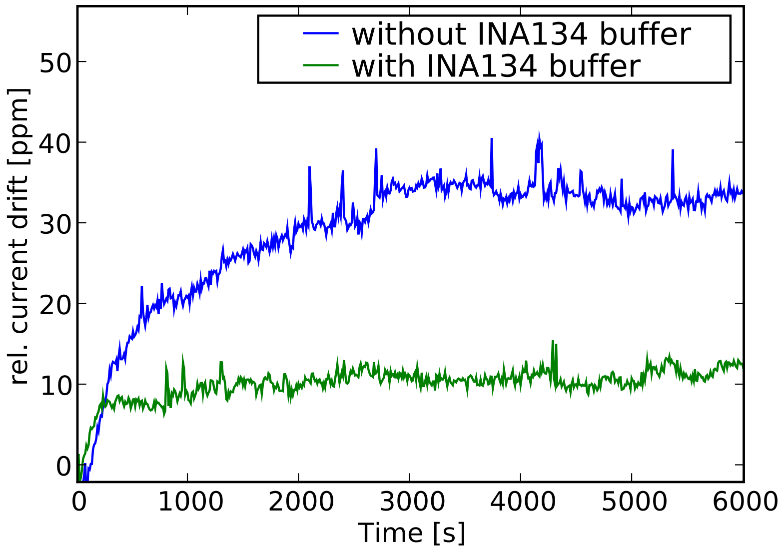

Figure 65: Current drift after a step from 0 to 2.2A output current at $t = 0$.

To compute the drift of the internal resistors, we have assumed the worst–case scenario that each resistor has a drift of ±2ppm/K and that the drift of all resistors is corellated in the most unfortunate way (e.g. that the resistors of each pair of 1k resistors around the LT1028 drift perfectly anticorellated). In practice, the temperture coefficients of the resistors may be correlated, which would significantly reduce the drift. If all internal resistors have the same temperature coefficients of resistance (TCR), the resulting total TCR will cancel.

Our measurement (figure 65) agrees well with this calculation. The data without the INA134 buffer shows a drift, which starts immediately at $t = 0$. This indicates that the dominant source of drift is indeed the VFP4Z measurement resistor, since the other components will heat only later on. Enabling the buffer reduces the drift by the same order of magnitude, suggesting that, for this particular source, the INA134 drifts opposite to the other components. We confirmed this by locally heating it in a separate measurement.

In total, the source meets our specification. We can always perform our experiment in the heated steady state, by running the source on a dummy load before taking data. In this state, the fluctuations are lower than the required 10ppm over 15min. In addition, the low duty cycle of our experiment greatly reduces the effective dissipated power.

A major concern, however, is the reproducibility of these results for a series of current sources. The component TCRs can vary in a given interval, so that the TCR of different sources may vary considerably over one production batch. A last ressort would be to include a ventilator on the heatsink. This would solve this problem with near certainty, albeit at the price of acoustic noise.

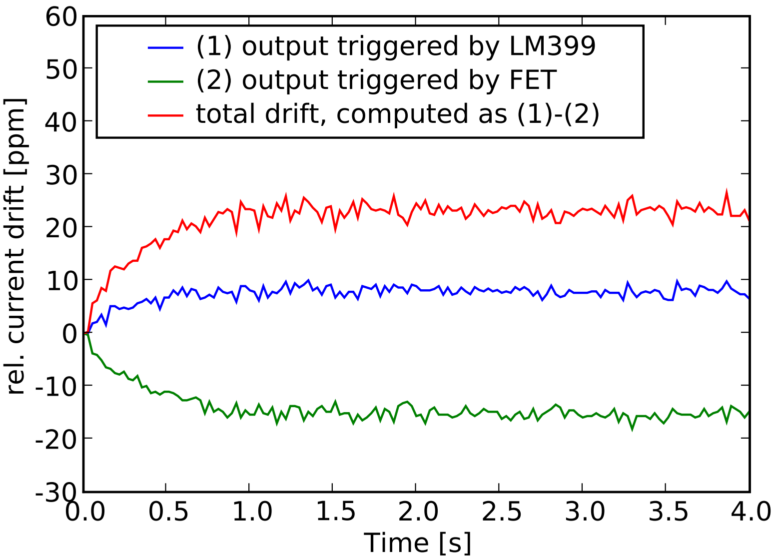

Figure 66: Current drift after a step from 0 to 2.2A output current at $t = 0$. In all measurements, the INA134 buffer was enabled.

Power drift We measured the power drift of the source with the same setup. Here, however, the drift of the load resistor cannot be neglected, since its heatsink does not play a role on short timescales. We calibrate its drift by performing two measurements: In one measurement, the output current is switched on at $t = 0$ by connecting the LM399H reference to the analog programming input. In a second measurement, the LM399H is continuously connected and we trigger the output current with the FET switch. For negative times, we short–circuit the output with the FET switch and open it at $t = 0$. In this way, the measurement resistance dissipates a constant power, so that the drift after $t = 0$ stems only from the drift of the load resistor. The latter measurement can then be used to correct the former for the drift of the load resistor. We verified that the LM399H reference drifted on these timescales by less than 10ppm.

The result of such a measurement is shown in Fig. 66. We observe a drift of ≈ 20ppm over the first second under load, both for the load and the measurement resistance. This corresponds to a wattage coefficient of resistance (WCR) of 4ppm/W. This drift is in excellent agreement with the specification of the VFP4Z resistors, which indeed states a max. WCR of ±4ppm/W.

As for the temperature drift, we can operate the source in the steady state by running it on a dummy load, e.g. the closed FET switch, before taking data. In the steady state, the source drifts less than 10ppm over the 1s period of measurement. In contrast to the temperature drift, however, this problem is intrinsic to the measurement resistor and cannot be alleviated by a better heatsink. A solution would be to use a better measurement resistor, but we are not aware of a better solution than the Vishay VFP4Z.

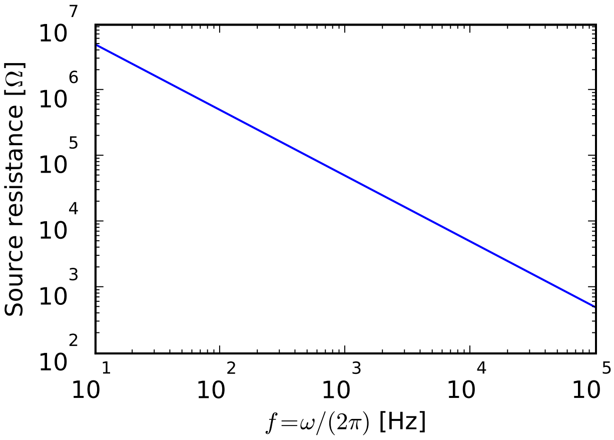

Figure 67: Source resistance of our source for the experimentally relevant frequencies.

6.1.7 Source resistance

In the real world, noise can couple into the output branch of the current source. This is modelled by a voltage source V_N in series with the load. Depending on the quality of the current source, the noise will translate into a small but finite current $I_N = V_N/R_{\text{sc}}$, with R_{sc} being the small-signal source resistance of the current source. An ideal current source would completely suppress this noise (cf. equation 116), corresponding to $R_{\text{sc}} = \infty$.

The source resistance of our source can be evaluated from equation 116. We note that, in absence of the feedback loop, V_N would source a current $S_f = V_N/(R_M + R_L)$ in the output branch. In presence of the feedback loop, this current is partly suppressed. The source resistance is computed from eq. 116 to be

$$R_{\text{sc}} = (R_M + R_L)\left(1 + \frac{iR_M}{\omega C(R_M + R_L)R_S}\right).$$

A plot of this source resistance is shown in figure 67. We speculate that the extremely high source resistance at low frequencies might have been the motivation for prefering an I–regulator over a P–regulator.

However, another imperfection must be taken into account. The absolute values of the 1k resistors around the LT1128 can vary. In particular, resistor pairs of nominally equal resistances might not be balanced. This compromises the common–mode–rejection of the LT1128 differential amplifier. The finite common–mode gain couples some of the noise into the feedback loop and thus into the output current. A tolerance of σ on the resistors will give rise to a common–mode gain of the order of σ, yielding a source resistance of

$$R_{\text{sc}} \approx \frac{R_M}{\sigma}$$

Our resistors have $\sigma = 0.01\%$, yielding an upper limit for the source resistance of $R_{\text{sc}} = 10\text{k}\Omega$. This is still good enough to attenuate a $V_N = 10\text{mV}$ noise to the μA level.

However, the performance of figure 67 is significantly degraded. In particular, in presence of these tolerances, the I–regulator does not present a sigificant advantage over a P–regulator.

6.1.8 Conclusion

The current source clearly reaches our specifications in terms of noise. The specifications in terms of drift are also reached, but still require the attention of the user, who has to insert suitable pre–heat cycles into his protocol.

The biggest concern clearly is the low bandwidth on inductive loads. This problem could be solved by switching the feedback gain G from an integrator to a proportional gain, which has 90° more phase margin.

A minor concern is that, in order to reach our targets in terms of thermal drift, we had to replace all critical resistors in the core by fairly expensive precision resistors having a low TCR. This problem could be solved by choosing a simpler core, requiring less resistors (or none at all). This would also resolve the problem of resistor tolerances and thus increase the source resistance.

Concluding, we therefore recommend to change the core to a simpler design, such as the ones proposed in [165] or [166]. The other components developed and selected for this source – such as the display, the buffer, the housing or the measurement resistance – could be conserved as they are. The change of the core would therefore present only a minor effort, but possibly a huge gain.

6.2 The microwave chain

6.2.1 Architecture

The microwave pulses for the interrogation are produced by a homebuilt synthesis chain. This chain receives as input the 100MHz reference signal of a cryogenic oscillator. It produces a signal at the clock frequency ($f = 6.834$GHz), which is phase–locked to the reference signal.

Basically, the chain implements the standard layout used in our lab [44]. Its block diagram is presented in figure 68. The signal is generated by a dielectric resonator oscillator (DRO). It runs at 6.434GHz, 400MHz below the clock frequency and is upmixed to the clock frequency at the output. This is done to avoid that radiation from the DRO could drive atomic transitions. The signal of the DRO drives the (saturated) LO input of the output mixer. The output power comes from the IF input, which is driven by the 400MHz signal.

The DRO as well as the 400MHz signal are stabilized to the 100MHz reference signal. The reference signal itself is buffered by a phase–locked quartz. This reduces its amplitude noise and protects the distributed signal. To lock the DRO, we generate a comb of multiples of 200MHz by an NLTL comb generator. The DRO is then locked to the 6.4GHz peak, with a 34MHz offset provided by a DDS synthesizer, which is also locked to the reference signal.

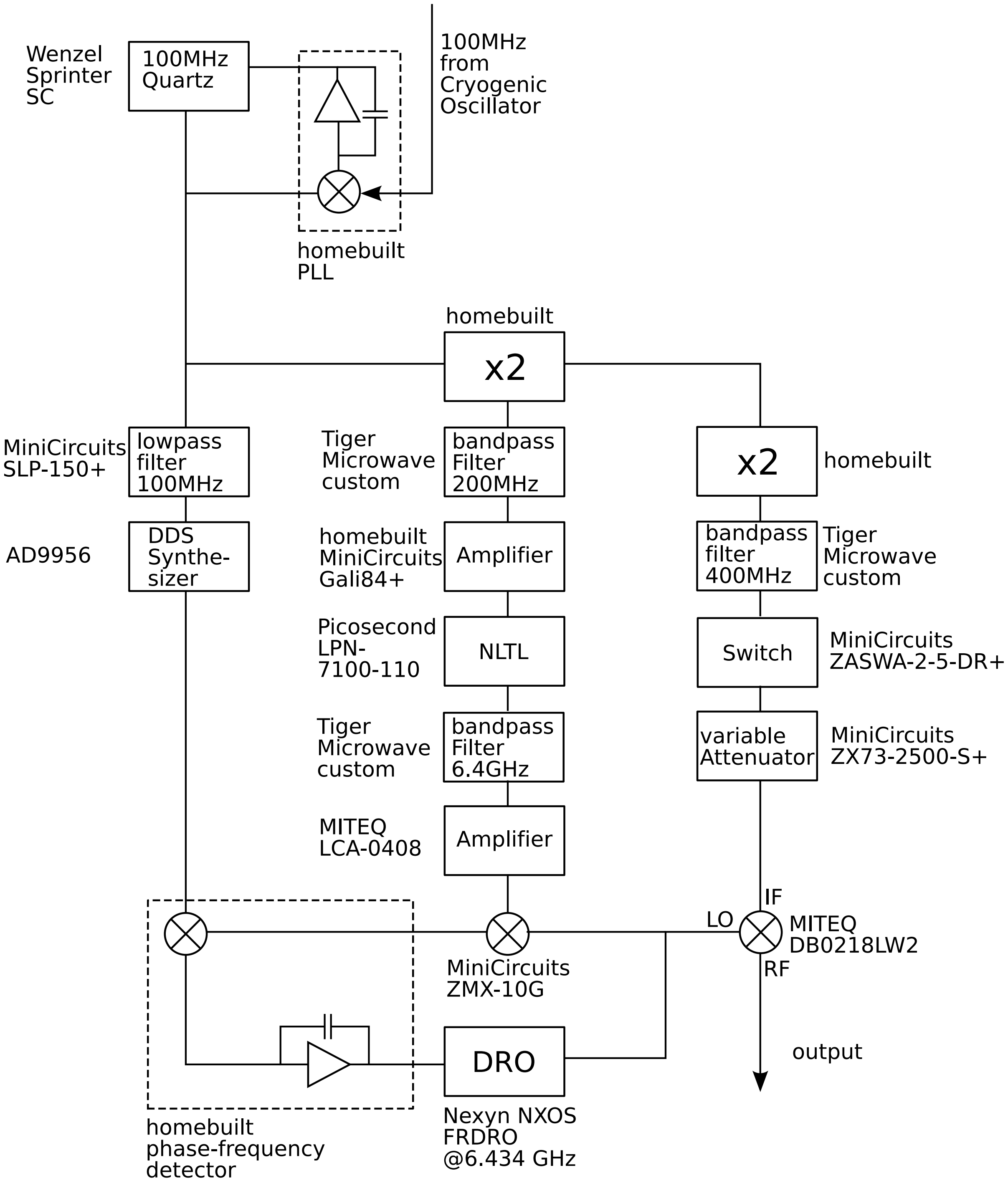

Figure 68: The microwave synthesis chain. The 100MHz reference signal drives a nonlinear transmission line (NLTL) comb generator (center) and a DDS synthesizer (left). A DRO is locked to 6.434GHz by mixing it with the 6.4GHz comb line and the DDS output. The resulting signal is upshifted by 400MHz to produce the clock frequency (right). Unspecified splits are performed by power splitters.

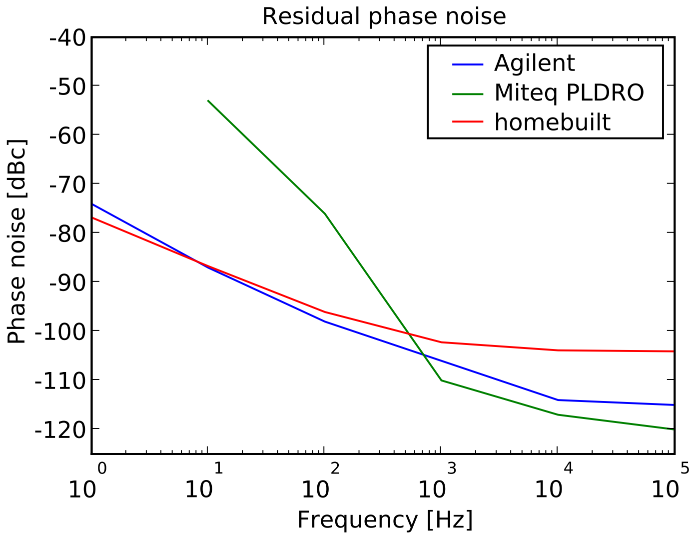

Figure 69: Residual phase noise of a homemeade synthesis chain (data from [44]) compared to a commercial microwave frequency synthesizer (Agilent E8257D PSG with option UNX) and a phase–locked DRO (Miteq PLDRO). The phase noise of the PLDRO is the total phase noise, including the phase noise of an unknown low–noise reference.

The user has control over the frequency and the amplitude of the output signal. The frequency can be changed by changing the offset frequency provided by the DDS, in either discrete steps or continuous ramps. The amplitude can be controlled by controling the power in the 400MHz RF line (right line in figure 68). This can be performed either continuously by the voltage variable attenuator or in a discrete step by the RF switch.

6.2.2 Comparison to commercial solutions

The residual phase noise of a typical homebuilt synthesis chain is presented in figure 69. It consists of a white–noise floor at -105dBc for high frequencies and a 1/f contribution at low frequencies. Comparable performance is achieved only by high–end microwave synthesizers (like the Agilent synthesizer cited in the figure, costing $\approx$ 50kEUR). In other experiments of our group, we use ready–made phase–locked DROs to generate the microwave signal [108]. A specification of their residual phase noise is generally not available. Instead, manufacturers specify the total phase noise of the DRO, when it is locked to an unspecified “ultra–low–noise” reference. We estimate that this specification comes close to the residual noise, since it is in the interest of the manufacturer to quote the best figure possible. Judging from this specification, the performance of a phase–locked DRO is considerably inferior to our chain.

In conclusion, a homebuilt chain is indeed the best solution for our task. In terms of performance, as is clear from figure 69, and in terms of cost, having consumed only $\approx$ 6kEUR of components and six manmonths of work.

7 Experimental results

The implementation of the whole setup except the interrogation microwave has been finished in the beginning of 2008 and led to the first observation of cold atoms in february 2008. Subsequently, besides work on the electronics and most notably the current source of the previous chapter, we have optimized the laser cooling and the loading of the magnetic trap. Since summer 2008, the evaporative cooling is in place and our work has since been steered towards the production of the first condensate, which we have obtained on 12/20/2008.

Even at this early stage, there are some experimental results, which we consider worth mentioning in this thesis and which we will discuss in this chapter: We present lifetime measurements in the magnetic trap, which indicate that the lifetime of the atoms is limited by background collisions and not by noise of the driver electronics. Furthermore, the experiment is found to be more stable than comparable setups. We quantify this empiric observation by analysing the fluctuation of the atom number over a typical experimental session of several hours. Finally, another subsection is devoted to the achievement of Bose–Einstein condensation in our setup.

7.1 Experimental cycle

To date the experimental cycle has been optimized up to the evaporative cooling and it is depicted in figure 70. The initial MOT is found to yield an atom number in excess of 10^7. This compares well with other setups of our group and is an indication that the performance of the macroscopic U has not been degraded by the implementation of the macroscopic I. After molasses cooling, we transfer $8 \cdot 10^6$ of these atoms into the magnetic trap. We subsequently compress the trap and apply evaporative cooling by RF radiation. All traps behave as expected from the chip design. The trap frequencies and the background fields correspond well to our design, if we correct for a fabrication

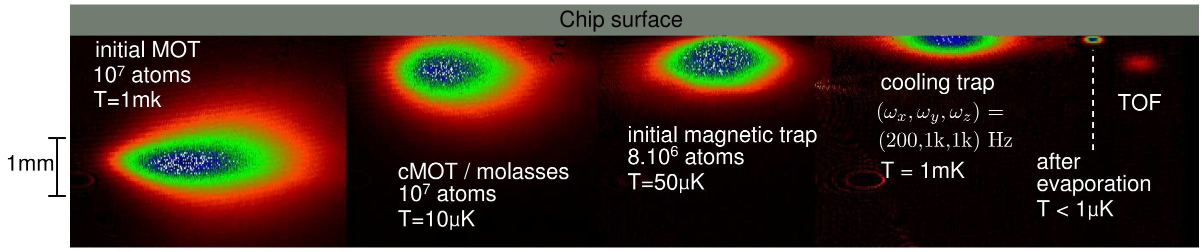

Figure 70: A stroboscopic image of a typical experimental cycle. Each phase of the cycle is artificially shifted to the right. During a real sequence, the cloud shifts only perpendicular to the chip. Atoms are collected in a magneto–optical trap (MOT) and subsequently cooled by optical molasses. After this preparation, they can be magnetically trapped. By applying an RF knife, we cool the cloud down to sub–microkelvin temperatures, before we drop it from the trap and destructively image it after a variable time of flight (TOF).

artefact, namely that the film of glue between the base chip and science chip is thicker than expected.

7.2 Loading and decay of a cloud

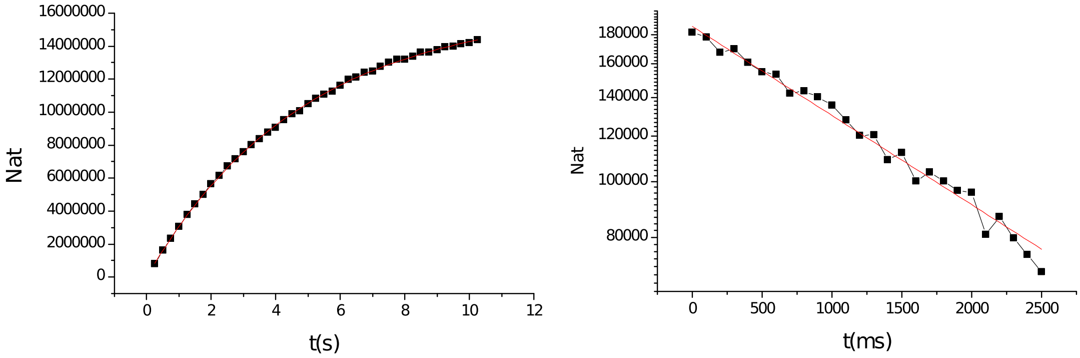

Figure 71: Loading of the initial MOT (left) and decay of a thermal cloud in a magnetic trap (right). The fits have time constants of 4.8 ± 0.2s (loading) and 2.8 ± 0.1s (decay). Both measurements have been carried out at a dispenser current of $I_{\text{disp}} = 3.95$A. The lifetime in the magnetic trap has been measured in a magnetic trap of frequencies $(\omega_x, \omega_{y/z}) = 2\pi(60, 300)$Hz after evaporative cooling had reduced its temperature to 10μK.

The quality of the vacuum and the electronics can be estimated by a measurement of the lifetime of the atoms. This can be performed in two ways, either by measuring the time constant of the loading of the initial MOT or, more directly, by measuring the decay of a trapped atomic cloud.

The former method is used in the left plot of figure 71. The loading of the MOT follows an exponential function

$$N(t) = N_0(1 - e^{-t/\tau})$$

where τ is the lifetime of an atom in the MOT, which is limited by collisions with the background gas. The dominant contribution of background particles comes from the Rubdium dispenser. It releases several species of “dirt” particles, which cannot be trapped by the MOT and reduce the atomic lifetime by collisions: ^{87}Rb atoms which are too fast to be captured by the MOT, ^{85}Rb and other chemical compounds. τ therefore depends on the dispenser current. For our typical experimental value $I_{\text{disp}} = 3.95$A, we measure a lifetime of $\tau = 4.8$s.

A more direct access to the loss rate is provided by a measurement of the decay of an atomic cloud in a magnetic trap. Ideally, the lifetime of an atom in a magnetic trap is limited by collisions with the background gas. It can be shortened below this limit, however, by inelastic collisions in the trap and losses due to magnetic field noise. In our setup, we measure a value of $\tau = 2.8$s.

The apparent disagreement between these values has also been observed in other experiments. A straightforward explanation is that a MOT is more likely to recapture an atom that has undergone a collision than is a magnetic trap. To make a sound statement, one therefore has to compare this data to similar setups. Data of a nearly identical setup is presented in [166]. For the same parameters, this data agrees with ours to within 10%. We therefore conclude that losses in our setup are mainly limited by collisions with the background gas.

Generally, we have observed that the lifetime increased over the first months of operation. Apparently, the dispenser is cleaned by use. Alternatively, the Rubidium might gradually coat the walls of the cell, which otherwise act as a pump for freshly released atoms.

7.3 Stability of the setup

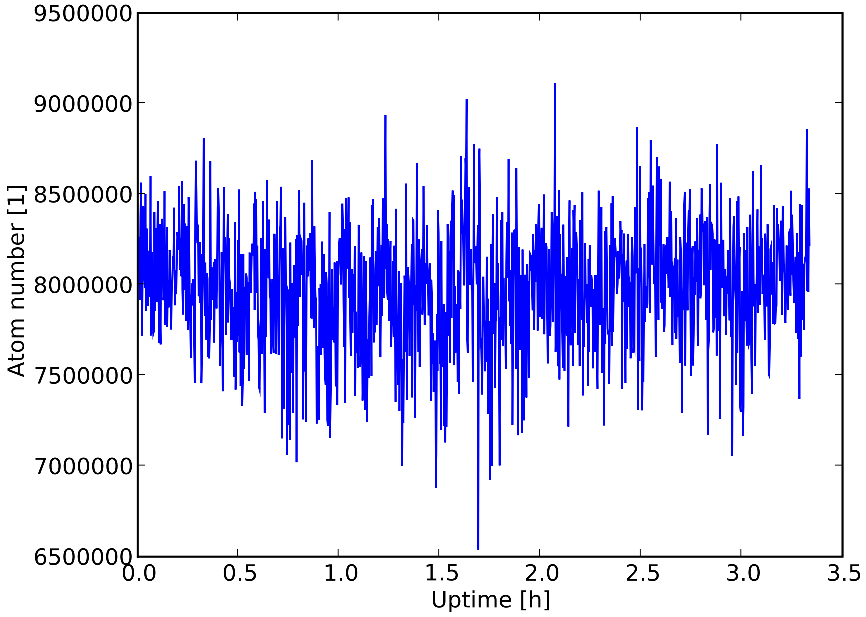

Figure 72: Stability of our setup: We repeatedly load the initial magnetic trap. The experiment runs autonomously for several hours and the atom number is constant to within 3.2%. The run was terminated on purpose and could have been continued for an even longer time.

Ultimately, when working as a clock, our setup will have to run quasi–continuously over several hours our even days. Therefore, we have taken great care to construct it in the most stable way possible: The master and repumper laser are mounted in temperature–stabilized housings. All optical paths are short and the optical components are mounted on short mounts, which are directly glued to the optical table. The chip–side optics is mounted in a rigid fashion (see section 4.4.2) and all power supplies have been chosen to provide a long–term stability of at least relative 10^{-3}. This effort has clearly payed off: The experiment is much more stable than comparable setups are reported to be. To quantify this observation, we have measured the fluctuation of the atom number in the initial magnetic trap over several hours, The resulting data is presented in figure 72. The high stability is demonstrated already by the fact that we can run this experiment for hours without any human intervention. Even more, however, the number of atoms fluctuates very little, about 3.2% over the whole experimental session of fig. 72.

7.4 Bose–Einstein condensation

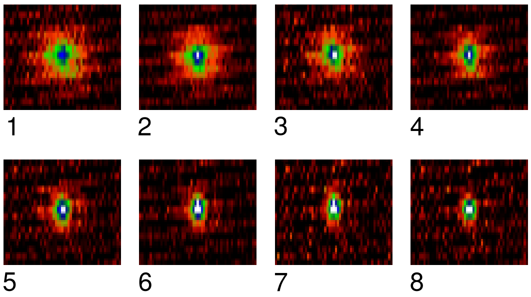

Figure 73: The BEC phase transition. All images are taken after a time of flight of 20ms. The final RF knife is subsequently lowered from image 1 to image 8. The change from a thermal cloud to a sharp peak is clearly visible as is the alignment of the coldest clouds along the vertical direction. The best shot (7) contains a nearly pure condensate of $2 \cdot 10^3$ atoms.

By evaporative cooling, our setup is able to cool the trapped cloud below the BEC phase transition. Absorption images of clouds above and below this transition are shown in figure 73. Imaging the cloud after a long time of flight, we clearly observe the emergence of a bimodal distribution. A dense core of condensed atoms emerges, which is surrounded by a dilute cloud of thermal atoms (figure 74).

A second signature of BEC is the anisotropy of the cloud. After a long time of flight, a thermal cloud has a spherical shape, reflecting its isotropic momentum distribution. In contrast, the kinetic energy of a condensate is anisotropic, since it stems from the quantum–mechanical zero–point motion of the ground state of the anisotropic trap. It is higher for the strongly confining direction, along which the trapped cloud is smaller. Consequently, the aspect ratio of a dropped condensate reverses during the time of flight. Indeed, the condensates (e.g. figure 73, 7) are aligned along the vertical direction of the absorption images, whereas the weak trap axis extends along the horizontal direction.

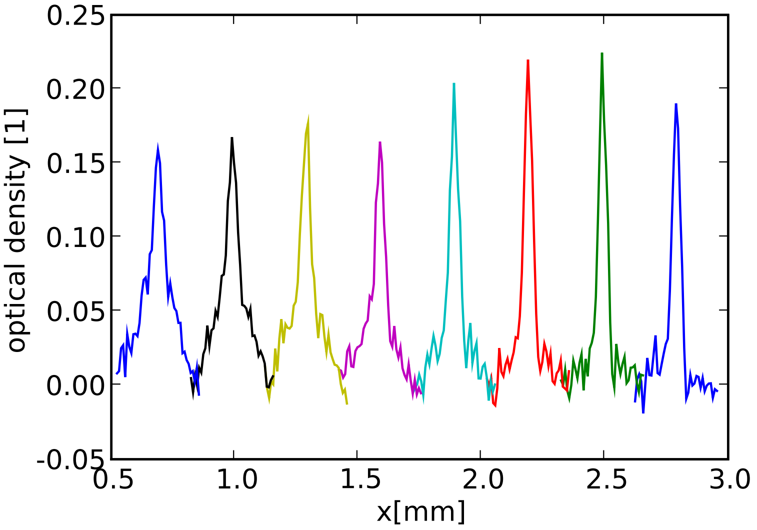

Figure 74: Bimodal distribution near the BEC phase transition. Each plot presents a profile of the optical density over a slice through the center of each of the clouds of figure 73. Temperature decreases to the right and subsequent plots are separated by an artificial offset of 0.3mm. The emergence of the central peak and the reduction of the thermal wings is clearly visible.

Conclusion and Outlook

A dedicated setup for clock measurements on a chip With this work, we have delivered a BEC machine which is tailored to the specific needs of an atomic clock on an atom chip. To get there, we have studied the relevant physical effects which influence the clock transition of a magnetically trapped cloud of ^{87}Rb atoms in our clock states. These are most notably the Zeeman shift and the mean–field shift arising from cold collisions in the cloud. We have estimated their influence on the clock stability and the coherence time of the cloud. We conclude from this analysis that a clock stability of few $10^{-13}\sqrt{s}$ is a realistic goal for a chip clock, but that there exist critical experimental parameters, which have to be controlled with high precision. Most notably, the best coherence times seem to lie in a parameter region where the magnetic field would have to be controlled to the level of several 10μG in order to reach a stability of $10^{-13}\sqrt{s}$.

This analysis has had direct implications for the design of the apparatus: We have implemented a double–layer Mumetal shield and developed a dedicated current source in order to reach these specifications. Furthermore, we have developed a dedicated atom chip. Compared to the proof–of–principle experiment, we have added an integrated microwave transmission line, to be able to produce well–controlled interrogation pulses with little microwave power.

The resulting setup is now operational and has been demonstrated to work as expected. The stable construction of the experiment pays off already now: The setup is able to run for hours without any human intervention.

Future developments With BEC being an accomplished task, the next step of our work clearly will be the implementation of the clock interrogation. The microwave chain is nearly ready and the experiment is prepared to accept it without significant modifications. Also, we are about to mount a second, low–noise, camera for the clock measurements. The first clock interrogation seems very close.

More interesting is the question, where this experiment will be heading in the long term. The straightforward objective is, of course, to achieve the best possible stability figure. We have shown in section 3.3 that the setup as it is should be able to reach a stability of the order of $10^{-12}\sqrt{\mathrm{s}}$. To reach a better level, the number of atoms has to be increased by one order of magnitude from the projected 10^4 to 10^5 and the cycle time will have to be reduced to the order of several seconds. As things look today, this will require an extension of the setup. We have started to explore several ways to load more atoms in less time. An obvious way to do this would be a 2D–MOT [167]. This, however, is a bulky device, a clear contradiction to our goal of building a compact setup. Therefore, we focus on a different approach, to find a way to modulate the Rubidium pressure in the vacuum chamber on a sub–second timescale.

We note, however, that there is the possibility of a lucky strike: We cannot yet exclude that a coherence time of the order of seconds can be achieved even with a hot cloud. If this was the case, we could afford to apply less evaporative cooling, which is a costly process in terms of atom number. To give an example, we can produce clouds of 10^5 atoms even in our current setup, if we allow for a temperature of $T = 5\mu$K.

This hints towards a second topic which is likely to be one of the first goals of the experiment: An analysis of the coherence time of the cloud as a function of the trap parameters. This will allow to refine our rough model and to correctly treat the effect of motional and collisional averaging. At the moment, a precise model for the coherence time is the missing link to predict the optimal operating parameters and the ultimate stability that can be reached by an atomic clock on a chip.

Let us assume that one of these approaches works – that the atom number can be increased as expected or that we find favourable trap parameters, which enable us to work with hotter atoms and/or to have a longer coherence time – so that the experiment indeed reaches the projected stability of few $10^{-13}\sqrt{\mathrm{s}}$. At this point, at most half of the work can be considered to be done, the other half being the further miniaturization from a breadboard–scale laboratory setup to a liter–sized, portable and ultimately commercial device. A lot of this work has already been done by others: A number of groups are pursueing research to miniaturize the essential components of our setup for similar applications. Compact laser sources, capable of producing all the light for a MOT, have already been developed for droptower experiments [89] and even spaceborne applications (see, e.g. the PHARAO optical bench, [81]). These systems typically occupy the size of a 19" rack, and further miniaturization seems possible. The situation is similar for the vacuum system. The size of our current vacuum system is limited by the pumps. However, comparable setups have already been run on smaller pumps [88, 81] or even exclusively on getter pumps [31], so that the vacuum system including the cell could probably be reduced to the liter scale.

It remains the chip–side optics and the components handling the magnetic field: The beam expanding optics could be nearly removed by switching to a pyramide MOT configuration [168], which requires only one beam. The cameras are a convenient but dispensable feature, since all the relevant information for a clock measurement could be equally obtained from photodiodes. The size of the offset coils could in principle be reduced up to the size of a MOT beam, of the order of centimeters. With this improvement, the magnetic shield could be reduced to the scale of ≈ 10cm. Alternatively, the shield could be replaced by an active compensation [169], which could in principle be implemented directly on the chip. Ultimately, it could be made obsolete by multiple parallelized clocks on the chip as outlined in section 3.3.5.

In summary, we are confident that a second or third generation of this clock can indeed be of the size of several liters and we emphasize the fact that a lot of the technology for this miniaturization is already available.

It is worth noting, moreover, that this experiment can also make qualitatively new contributions beyond a mere hunt for the best stability in the smallest possible package. An example is the possibility of parallelisation, which we have sketched in chapter 3. On a future chip, multiple clocks could be implemented. They could then operate in parallel and measure external parameters like fluctuations of the magnetic field along with the clock measurement. Here, a chip clock is truly complementary to other compact clocks, which cannot exploit the potential of such a highly integrated setup.

Another intriguing direction is to develop the experiment towards an atomic interferometer. This setup lends itself to this application, since the chip is able to manipulate external states with the flexible trapping potential as well as internal states with the integrated microwave. With these tools, we could implement on the chip a Ramsey–Bordé–like interferometer. Such an interferometer can be understood as a Ramsey–type atomic clock, in which the two clock populations are spatially separated during the interrogation time. Thereby, the clock signal becomes sensitive to potential gradients, e.g. of the gravitational potential. On our chip, we could implement such a state–sensitive splitting with the help of state–selective microwave potentials, in much the same way as it has been proposed for an atomic phase gate in [22].

We conclude that the setup has a clear potential beyond the intended application of a compact clock. This can also be told from the fact that the research on the $|1,-1\rangle \rightarrow |2,1\rangle$ transition in trapped ^{87}Rb is pursued by a larger community of experiments. In particular, we are aware of work in Munich (the group of Th. Hänsch and P. Treutlein), Swinburne (the group of P. Hannaford and A. Sidorov) and Amherst (in the group of D.S. Hall). We have no doubt that our experiment can yield an important and complementary contribution to this field, most notably because of its excellent control of the magnetic background field, the ability to use microwave near–fields and the ability to perform precision spectroscopy using the signal of the SYRTE frequency standards. The preparation of these features may have consumed some time, but the result clearly is a powerful tool.

A Exact diagonalization of the coupling Hamiltonian

This appendix is a complement to section 3.1.3. Again, we derive the lightshift of the RF and microwave coupling by taking into account the full coupling Hamiltonian. This derivation, however, does not rely on perturbation theory. Instead, we present an exact analytical solution.

The system We consider the electronic ground state of ^{87}Rb, labeling the states by the usual quantum numbers F, m_F. The clock transition is excited by a two-photon drive, consisting of a microwave field with frequency ω_{MW} and an RF field with ω_{RF}, both polarized to equal parts along σ_+ and σ_-. These fields create the two–photon coupling for the clock states, but also one–photon couplings between any pair of levels with adjacent m_F. The strength of these couplings can be read off from eq. 47 and fig.23. All couplings involving the clock states are summarized in fig. 75.
The goal of the following paragraphs is to prove that these couplings indeed give rise to two–photon Rabi flopping between the levels $|1,-1\rangle$ and $|2,1\rangle$, with negligible population of other states, and to calculate the Rabi frequency and lightshift.

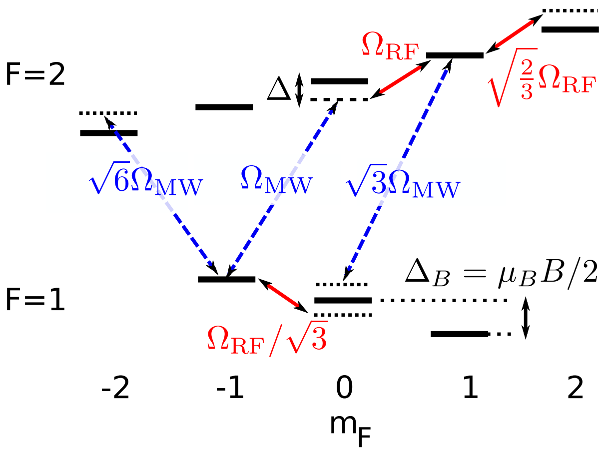

Figure 75: Couplings of the RF and microwave photons involving the clock states.

To treat all couplings exactly, we introduce three simplifications:

1. We adopt the theorist convention $\hbar = 1$
2. We map the eight–level system to the complex vector space $\mathbb{C}^8$ in the following way: $|F=1, m_F=-1\rangle$ is mapped to the canonical unit vector $|0\rangle$, $|F=1, m_F=0\rangle$ to $|1\rangle$, $|F=1, m_F=1\rangle \to |2\rangle$, $|F=2, m_F=-2\rangle \to |3\rangle$, $\ldots$, $|F=2, m_F=2\rangle \to |7\rangle$. By this convention, the coupling Hamiltonian can be visualized as an 8x8 matrix.
3. We rotate the system into the rotating frame of the two–photon transition: The level $|F=1, m_F=-1\rangle$ is defined to have zero energy. The remaining $F=1$ levels are rotated up by $(m_F-1)\cdot\omega_{\mathrm{RF}}$ The energy of the $F=2$ levels is rotated

down by $\omega_{\mathrm{MW}} + (m_F - 1) \cdot \omega_{\mathrm{RF}}$. In this frame, the clock states $|F_1, m_F = -1\rangle$ and $|F = 2, m_F = 1\rangle$ are split by δ and all adjacent m_F sublevels are split by the one–photon detuning Δ (see fig. 76).

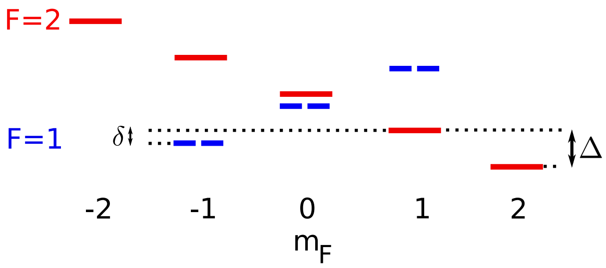

Figure 76: Levels in the rotating frame

With these conventions, the coupling Hamiltonian takes the form

$$H_t = \tag{118}$$
$$\begin{pmatrix}
0 & \frac{\Omega_{\mathrm{RF}}}{2\sqrt{3}} & 0 & \sqrt{\frac{3}{2}}\Omega_{\mathrm{MW}} e_t^{-1} & 0 & \frac{1}{2}\Omega_{\mathrm{MW}} & 0 & 0 \\
\frac{\Omega_{\mathrm{RF}}}{2\sqrt{3}} & \Delta - \delta & \frac{\Omega_{\mathrm{RF}}}{2\sqrt{3}} & 0 & \frac{\sqrt{3}}{2}\Omega_{\mathrm{MW}} & 0 & \frac{\sqrt{3}}{2}\Omega_{\mathrm{MW}} e_t^{-1} & 0 \\
0 & \frac{\Omega_{\mathrm{RF}}}{2\sqrt{3}} & 2\Delta - 2\delta & 0 & 0 & \frac{1}{2}\Omega_{\mathrm{MW}} e_t^{-1} & 0 & \sqrt{\frac{3}{2}}\Omega_{\mathrm{MW}} e_t^{-2} \\
\sqrt{\frac{3}{2}}\Omega_{\mathrm{MW}} e_t & 0 & 0 & 3\Delta - \delta & \frac{1}{\sqrt{6}}\Omega_{\mathrm{RF}} & 0 & 0 & 0 \\
0 & \frac{\sqrt{3}}{2}\Omega_{\mathrm{MW}} & 0 & \frac{1}{\sqrt{6}\Omega_{\mathrm{RF}}} & 2\Delta - \delta & \frac{1}{2}\Omega_{\mathrm{RF}} & 0 & 0 \\
\frac{1}{2}\Omega_{\mathrm{MW}} & 0 & \frac{1}{2}\Omega_{\mathrm{MW}} e_t & 0 & \frac{1}{2}\Omega_{\mathrm{RF}} & \Delta & \frac{1}{2}\Omega_{\mathrm{RF}} & 0 \\
0 & \frac{\sqrt{3}}{2}\Omega_{\mathrm{MW}} e_t & 0 & 0 & 0 & \frac{1}{2}\Omega_{\mathrm{RF}} & \delta & \frac{1}{\sqrt{6}}\Omega_{\mathrm{RF}} \\
0 & 0 & \sqrt{\frac{3}{2}}\Omega_{\mathrm{MW}} e_t^2 & 0 & 0 & 0 & \frac{1}{\sqrt{6}}\Omega_{\mathrm{RF}} & 2\delta - \Delta
\end{pmatrix} \approx$$

$$\begin{pmatrix}
0 & \frac{\Omega_{\mathrm{RF}}}{2\sqrt{3}} & 0 & 0 & 0 & \frac{1}{2}\Omega_{\mathrm{MW}} & 0 & 0 \\
\frac{\Omega_{\mathrm{RF}}}{2\sqrt{3}} & \Delta - \delta & \frac{\Omega_{\mathrm{RF}}}{2\sqrt{3}} & 0 & \frac{\sqrt{3}}{2}\Omega_{\mathrm{MW}} & 0 & 0 & 0 \\
0 & \frac{\Omega_{\mathrm{RF}}}{2\sqrt{3}} & 2\Delta - 2\delta & 0 & 0 & 0 & 0 & 0 \\
0 & 0 & 0 & 3\Delta - 2\delta & \frac{1}{\sqrt{6}}\Omega_{\mathrm{RF}} & 0 & 0 & 0 \\
0 & \frac{\sqrt{3}}{2}\Omega_{\mathrm{MW}} & 0 & \frac{1}{\sqrt{6}}\Omega_{\mathrm{RF}} & 2\Delta - \delta & \frac{1}{2}\Omega_{\mathrm{RF}} & 0 & 0 \\
\frac{1}{2}\Omega_{\mathrm{MW}} & 0 & 0 & 0 & \frac{1}{2}\Omega_{\mathrm{RF}} & \Delta & \frac{1}{2}\Omega_{\mathrm{RF}} & 0 \\
0 & 0 & 0 & 0 & 0 & \frac{1}{2}\Omega_{\mathrm{RF}} & \delta & \frac{1}{\sqrt{6}}\Omega_{\mathrm{RF}} \\
0 & 0 & 0 & 0 & 0 & 0 & \frac{1}{\sqrt{6}}\Omega_{\mathrm{RF}} & 2\delta - \Delta
\end{pmatrix} = H \tag{119}$$

The time–dependent terms $e_t = \exp\left[2i(\Delta + \Delta_B - \delta)t\right]$ result from couplings that are detuned from resonance by at least Δ_B (like, e.g. the coupling $|1, 0\rangle \rightarrow |2, 1\rangle$). We will justify later that, due to this large detuning, they can be neglected in the step (118)→(119). First, however, we turn to the analysis of the Hamiltonian 119: We compute its eigenenergies and eigenstates and prove that these indeed describe two–photon Rabi oscillations between the clock states. Throughout this derivation, we make use of the approximations $\Omega_{\mathrm{RF}} \ll \Delta, \Omega_{\mathrm{MW}} \ll \Delta$ and compute all quantities to first order in $1/\Delta$ and to second order in $\Omega_{\mathrm{RF}}, \Omega_{\mathrm{MW}}$.

Eigenenergies, lightshift and Rabi frequency The secular equation of Hamiltonian 119 is an eighth–order polynomial. To solve it, one makes use of the fact that the eigenenergies are approximately known: Two eigenenergies will be close to zero, corresponding to the dressed states emerging from the two clock states. Two others will be approximately Δ, corresponding to the dressed states which emerge from the $|1,0\rangle$ and $|2,0\rangle$ levels. By expanding the secular equation around these values, one can find the precise eigenenergies, which are

$$\mathrm{eva}_{0,-} = -\frac{3\Omega_{\mathrm{MW}}^2 + \Omega_{\mathrm{RF}}^2}{12\Delta}; \qquad \mathrm{eva}_{0,+} = -\frac{4\delta(7\delta - 3\Delta) + \Omega_{\mathrm{RF}}^2}{12\Delta}.$$

This result contains the lightshift and the Rabi frequency of the two–photon transition. The former is the difference of the eigenenergies in the limit of resonant drive $\delta = 0$ and weak drive power $\Omega_{\mathrm{RF}}, \Omega_{\mathrm{MW}} \ll \Delta$. Numerically, we find

$$\mathrm{eva}_{0,-} - \mathrm{eva}_{0,+} = -\frac{\Omega_{\mathrm{MW}}^2}{4\Delta} + \mathcal{O}(1/\Delta^2)$$

which reproduces the result of perturbation theory, eq. 50.

In practice, the detuning δ will be chosen such as to cancel this lightshift. In this situation, the energy difference of the dressed clock states is precisely the two–photon Rabi frequency, which is therefore

$$\mathrm{eva}_{0,-} - \mathrm{eva}_{0,+} \overset{\delta=-\Omega_{\mathrm{MW}}^2/4\Delta}{=} \frac{\Omega_{\mathrm{MW}}\Omega_{\mathrm{RF}}}{2\Delta}.$$

again in agreement with perturbation theory.

The eigenenergies near Δ can be found in the same way:

$$\mathrm{eva}_{\Delta,+} = \Delta - \frac{\Omega_{\mathrm{MW}}^2}{8\Delta} - \frac{\Omega_{\mathrm{MW}}\Omega_{\mathrm{RF}}}{2\sqrt{3}\Delta}, \mathrm{eva}_{\Delta,-} = \Delta - \frac{\Omega_{\mathrm{MW}}^2}{8\Delta} + \frac{\Omega_{\mathrm{MW}}\Omega_{\mathrm{RF}}}{2\sqrt{3}\Delta}$$

Eigenstates The eigenstates for the eigenvalues near zero energy are symmetric and antisymmetric combinations of the clock states, augmented by terms of order Ω/Δ

$$\begin{aligned} |\mathrm{ev}_{0,+}\rangle &= \frac{1}{\sqrt{2}}(1,0,0,0,0,0,1,0)^T + \mathcal{O}(\Omega/\Delta) \\ |\mathrm{ev}_{0,-}\rangle &= \frac{1}{\sqrt{2}}(1,0,0,0,0,0,-1,0)^T + \mathcal{O}(\Omega/\Delta) \end{aligned}$$

where Ω denotes either Ω_{MW} or Ω_{RF}.

The eigenstates near Δ are symmetric and antisymmetric combinations of $|1,0\rangle$ and $|2,0\rangle$. They are mixed by the two–photon transition $|1,0\rangle \rightarrow |2,-1\rangle \rightarrow |2,0\rangle$, which is resonant with the two–photon drive.

$$\begin{aligned} |\mathrm{ev}_{0,+}\rangle &= \frac{1}{\sqrt{2}}(0,1,0,0,0,1,0,0)^T + \mathcal{O}(\Omega/\Delta) \\ |\mathrm{ev}_{0,-}\rangle &= \frac{1}{\sqrt{2}}(0,1,0,0,0,-1,0,0)^T + \mathcal{O}(\Omega/\Delta) \end{aligned}$$

For exact expressions of the $\mathcal{O}(\Omega/\Delta)$ terms, we refer to the paragraph "Mathematica code".

This result proves that the drive indeed creates Rabi oscillations between $|1,-1\rangle$ and $|2,1\rangle$, with a population of other states of at most order Ω/Δ.

Analysis of the rapidly rotating terms It remains to prove that the rapid time–dependent terms containing $e_t = \exp\left[2i(\Delta + \Delta_B - \delta)t\right]$ in the Hamiltonian 118 do not contribute to the time evolution. This is best shown by computing the matrix elements between the dressed clock states and the remaining bare states $|F, m_F\rangle \notin \{|1,-1\rangle, |2,1\rangle\}$. Performing the calculation, one finds that all these matrix elements can be expressed in the form

$$\begin{aligned} \langle \mathrm{ev}_{0,+}|H_t|F, m_F\rangle &= \textstyle\sum_i a_i e_t^{x_i} \\ \langle \mathrm{ev}_{0,-}|H_t|F, m_F\rangle &= \textstyle\sum_i a_i e_t^{x_i} \\ \langle \mathrm{ev}_{0,-}|H_t|\mathrm{ev}_{0,+}\rangle &= \textstyle\sum_i a_i e_t^{x_i} \end{aligned}$$

where $x_i \in \{1, 2\}$ and a_i is a polynomial in $\Omega_{\mathrm{RF}}, \Omega_{\mathrm{MW}}, \Delta$ satisfying $|a_i| < \Omega_{\mathrm{MW}}$.
All these couplings rotate at least with Δ_B. At the same time, the above analysis has shown that the eigenenergies of the bare and dressed states are at most of order Δ. Since $\Delta, \Omega_{\mathrm{MW}} \ll \Delta_B$, the rotating terms cannot significantly contribute to the time evolution. The dressed clock states $|\mathrm{ev}_{0,+}\rangle, |\mathrm{ev}_{0,-}\rangle$ are indeed decoupled from the remaining bare states.

Mathematica code The explicit evaluation of the above procedure is best done using a computer algebra system. In the language Mathematica, it can be performed using the following code:

$$H = \begin{pmatrix} 0 & \frac{\Omega_{\mathrm{RF}}}{2\sqrt{3}} & 0 & 0 & 0 & \frac{\Omega_{\mathrm{MW}}}{2} & 0 & 0 \\ \frac{\Omega_{\mathrm{RF}}}{2\sqrt{3}} & -\delta+\Delta & \frac{\Omega_{\mathrm{RF}}}{2\sqrt{3}} & 0 & \frac{\sqrt{3}\Omega_{\mathrm{MW}}}{2} & 0 & 0 & 0 \\ 0 & \frac{\Omega_{\mathrm{RF}}}{2\sqrt{3}} & -2\delta+2\Delta & 0 & 0 & 0 & 0 & 0 \\ 0 & 0 & 0 & -2\delta+3\Delta & \frac{\Omega_{\mathrm{RF}}}{\sqrt{6}} & 0 & 0 & 0 \\ 0 & \frac{\sqrt{3}\Omega_{\mathrm{MW}}}{2} & 0 & \frac{\Omega_{\mathrm{RF}}}{\sqrt{6}} & -\delta+2\Delta & \frac{\Omega_{\mathrm{RF}}}{2} & 0 & 0 \\ \frac{\Omega_{\mathrm{MW}}}{2} & 0 & 0 & 0 & \frac{\Omega_{\mathrm{RF}}}{2} & \Delta & \frac{\Omega_{\mathrm{RF}}}{2} & 0 \\ 0 & 0 & 0 & 0 & 0 & \frac{\Omega_{\mathrm{RF}}}{2} & \delta & \frac{\Omega_{\mathrm{RF}}}{\sqrt{6}} \\ 0 & 0 & 0 & 0 & 0 & 0 & \frac{\Omega_{\mathrm{RF}}}{\sqrt{6}} & 2\delta-\Delta \end{pmatrix};$$

$\mathrm{SecEq} = \mathrm{Simplify}[\mathrm{Det}[H - \ \mathrm{SparseArray}[\mathrm{Band}[\{1,1\}] \to \lambda, \{8,8\}]]];$

(*expand around $\lambda = 0$ to find the eigenenergies of the dressed clock states *)
$\mathrm{Normal}[\mathrm{Series}[\mathrm{SecEq}, \{\lambda, 0, 2\}]//\mathrm{Simplify}];$
$\mathrm{Sol0} = \mathrm{Solve}[\% == 0, \lambda];$
$\mathrm{eva0} = \mathrm{FullSimplify}[\mathrm{Normal}[\mathrm{Series}[\lambda/.\mathrm{Sol0}, \{\Delta, \infty, 1\}]], \mathrm{Assumptions} \to \delta < 0]$

$\left\{-\frac{3\Omega_{\mathrm{MW}}^2+\Omega_{\mathrm{RF}}^2}{12\Delta}, -\frac{4\delta(7\delta-3\Delta)+\Omega_{\mathrm{RF}}^2}{12\Delta}\right\}$

(*calculation of the lightshift*)
ls = Normal[Series[eva0[[1]] − eva0[[2]]/.$\delta \to 0, \{\Delta, \infty, 1\}$]]
$-\frac{\Omega_{\mathrm{MW}}^2}{4\Delta}$

(*calculation of the Rabi frequency*)
eva0 = FullSimplify [Normal[Series[λ/.Sol0/.$\delta \to$ ls, $\{\Delta, \infty, 1\}$]], Assumptions $\to \{\Omega_{\mathrm{MW}} > 0, \Omega_{\mathrm{RF}} > 0\}$]
$\Omega_{2\Phi}$ = FullSimplify[eva0[[1]] − eva0[[2]]]
$\frac{\Omega_{\mathrm{MW}}\Omega_{\mathrm{RF}}}{2\Delta}$

(*expand around $\lambda = \Delta$ to find the next pair of eigenenergies *)
Normal[Series[SecEq/.$\delta \to$ ls/.$\lambda \to \Delta + \mathrm{d}\lambda, \{\mathrm{d}\lambda, 0, 2\}$]//Simplify];
SolΔ = Solve[% == 0, dλ];
evaΔ = Δ + Normal [Simplify [Series [dλ/.SolΔ, $\{\Delta, \infty, 1\}, \{\Omega_{\mathrm{MW}}, 0, 2\}, \{\Omega_{\mathrm{RF}}, 0, 2\}$]]]
$\left\{\Delta - \frac{\Omega_{\mathrm{MW}}^2}{8\Delta} - \frac{\Omega_{\mathrm{MW}}\Omega_{\mathrm{RF}}}{2\sqrt{3}\Delta}, \Delta - \frac{\Omega_{\mathrm{MW}}^2}{8\Delta} + \frac{\Omega_{\mathrm{MW}}\Omega_{\mathrm{RF}}}{2\sqrt{3}\Delta}\right\}$

(*eigenstates corresponding to the eigenvalues around E=0*)
ev0s = $\left\{\{1\}, \left\{-\frac{\Omega_{\mathrm{RF}}}{2\sqrt{3}\Delta}\right\}, \left\{\frac{\Omega_{\mathrm{RF}}^2}{24\Delta^2}\right\}, \{0\}, \left\{\frac{\Omega_{\mathrm{MW}}\Omega_{\mathrm{RF}}}{4\Delta^2} + \frac{\Omega_{\mathrm{RF}}^2}{8\Delta^2}\right\}, \left\{-\frac{\Omega_{\mathrm{MW}}}{2\Delta} - \frac{\Omega_{\mathrm{RF}}}{2\Delta}\right\}, \{1\}, \left\{\frac{\Omega_{\mathrm{RF}}}{\sqrt{6}\Delta}\right\}\right\}$;
ev0a = $\left\{\{1\}, \left\{-\frac{\Omega_{\mathrm{RF}}}{2\sqrt{3}\Delta}\right\}, \left\{\frac{\Omega_{\mathrm{RF}}^2}{24\Delta^2}\right\}, \{0\}, \left\{\frac{\Omega_{\mathrm{MW}}\Omega_{\mathrm{RF}}}{4\Delta^2} - \frac{\Omega_{\mathrm{RF}}^2}{8\Delta^2}\right\}, \left\{-\frac{\Omega_{\mathrm{MW}}}{2\Delta} + \frac{\Omega_{\mathrm{RF}}}{2\Delta}\right\}, \{-1\}, \left\{-\frac{\Omega_{\mathrm{RF}}}{\sqrt{6}\Delta}\right\}\right\}$;

(*prove that these are indeed eigenstates*)
(Normal[Series[H.ev0s/.$\delta \to$ ls, $\{\Delta, \infty, 1\}$]]−Normal[Series[eva0[[2]]∗ev0s, $\{\Delta, \infty, 1\}$]])//FullSimplify
(Normal[Series[H.ev0a/.$\delta \to$ ls, $\{\Delta, \infty, 1\}$]]−Normal[Series[eva0[[1]]∗ev0a, $\{\Delta, \infty, 1\}$]])//FullSimplify
$\{\{0\}, \{0\}, \{0\}, \{0\}, \{0\}, \{0\}, \{0\}, \{0\}\}$
$\{\{0\}, \{0\}, \{0\}, \{0\}, \{0\}, \{0\}, \{0\}, \{0\}\}$

(*eigenstates corresponding to the eigenvalues around E=Δ*) evΔs = $\left\{\left\{\frac{9\sqrt{3}\Omega_{\mathrm{MW}}^2-168\Omega_{\mathrm{MW}}\Omega_{\mathrm{RF}}-32\sqrt{3}\Omega_{\mathrm{RF}}^2}{576\Delta\Omega_{\mathrm{RF}}}\right\}\right.$
$\left\{-\frac{-27\Omega_{\mathrm{MW}}^3+72\sqrt{3}\Omega_{\mathrm{MW}}^2\Omega_{\mathrm{RF}}+96\Omega_{\mathrm{MW}}\Omega_{\mathrm{RF}}^2+32\sqrt{3}\Omega_{\mathrm{RF}}^3}{1152\sqrt{2}\Delta^2\Omega_{\mathrm{RF}}}\right\}, \left\{\frac{-9\sqrt{3}\Omega_{\mathrm{MW}}^3+72\Omega_{\mathrm{MW}}^2\Omega_{\mathrm{RF}}+32\sqrt{3}\Omega_{\mathrm{MW}}\Omega_{\mathrm{RF}}^2+32\Omega_{\mathrm{RF}}^3}{192\Delta\Omega_{\mathrm{RF}}^2}\right\}, \left\{-\frac{1}{3}\right\},$
$\left.\left\{-\frac{\Omega_{\mathrm{RF}}}{6\Delta}\right\}, \left\{-\frac{\Omega_{\mathrm{RF}}^2}{12\sqrt{6}\Delta^2}\right\}\right\}$;
evΔa = $\left\{\left\{-\frac{9\sqrt{3}\Omega_{\mathrm{MW}}^2+168\Omega_{\mathrm{MW}}\Omega_{\mathrm{RF}}-32\sqrt{3}\Omega_{\mathrm{RF}}^2}{576\Delta\Omega_{\mathrm{RF}}}\right\}, \left\{\frac{1}{3} - \frac{\Omega_{\mathrm{MW}}\left(3\Omega_{\mathrm{MW}}+8\sqrt{3}\Omega_{\mathrm{RF}}\right)}{32\Omega_{\mathrm{RF}}^2}\right\}, \left\{\frac{9\sqrt{3}\Omega_{\mathrm{MW}}^2+72\Omega_{\mathrm{MW}}\Omega_{\mathrm{RF}}-32\sqrt{3}\Omega_{\mathrm{RF}}^2}{576\Delta\Omega_{\mathrm{RF}}}\right\},\right.$
$\left\{-\frac{27\Omega_{\mathrm{MW}}^3+72\sqrt{3}\Omega_{\mathrm{MW}}^2\Omega_{\mathrm{RF}}-96\Omega_{\mathrm{MW}}\Omega_{\mathrm{RF}}^2+32\sqrt{3}\Omega_{\mathrm{RF}}^3}{1152\sqrt{2}\Delta^2\Omega_{\mathrm{RF}}}\right\}, \left\{\frac{9\sqrt{3}\Omega_{\mathrm{MW}}^3+72\Omega_{\mathrm{MW}}^2\Omega_{\mathrm{RF}}-32\sqrt{3}\Omega_{\mathrm{MW}}\Omega_{\mathrm{RF}}^2+32\Omega_{\mathrm{RF}}^3}{192\Delta\Omega_{\mathrm{RF}}^2}\right\}, \left\{-\frac{1}{3}\right\}, \left\{-\frac{\Omega_{\mathrm{RF}}}{6\Delta}\right\},$

(*prove that these states are indeed the eigenvectors corresponding to evΔa and evΔs*)
calc = Normal [Series [H.evΔs/.$\delta \to$ ls, $\{\Delta, \infty, 1\}, \{\Omega_{\mathrm{RF}}, 0, 2\}, \{\Omega_{\mathrm{MW}}, 0, 2\}$]] ;
ref = Normal [Series [evaΔ[[1]] ∗ evΔs/.$\delta \to$ ls, $\{\Delta, \infty, 1\}, \{\Omega_{\mathrm{RF}}, 0, 2\}, \{\Omega_{\mathrm{MW}}, 0, 2\}$]] ;
Simplify[calc − ref]
$\{\{0\}, \{0\}, \{0\}, \{0\}, \{0\}, \{0\}, \{0\}, \{0\}\}$
calc = Normal [Series [H.evΔa/.$\delta \to$ ls, $\{\Delta, \infty, 1\}, \{\Omega_{\mathrm{RF}}, 0, 2\}, \{\Omega_{\mathrm{MW}}, 0, 2\}$]] ;
ref = Normal [Series [evaΔ[[2]] ∗ evΔa/.$\delta \to$ ls, $\{\Delta, \infty, 1\}, \{\Omega_{\mathrm{RF}}, 0, 2\}, \{\Omega_{\mathrm{MW}}, 0, 2\}$]] ;

```
Simplify[calc − ref]
{{0}, {0}, {0}, {0}, {0}, {0}, {0}, {0}}
```

References

[1] M. H. Anderson, J. R. Ensher, M. R. Matthews, C. E. Wieman, and E. A. Cornell. Observation of Bose-Einstein Condensation in a Dilute Atomic Vapor. *Science*, 269(5221):198–201, 1995.

[2] K. B. Davis, M. O. Mewes, M. R. Andrews, N. J. van Druten, D. S. Durfee, D. M. Kurn, and W. Ketterle. Bose-Einstein condensation in a gas of Sodium atoms. *Phys. Rev. Lett.*, 75(22):3969–3973, Nov 1995.

[3] J. D. Weinstein and K. G. Libbrecht. Microscopic magnetic traps for neutral atoms. *Phys. Rev. A*, 52:4004–4009, 1995.

[4] Dirk Müller, Dana Z. Anderson, Randal J. Grow, Peter D. D. Schwindt, and Eric A. Cornell. Guiding neutral atoms around curves with lithographically patterned current-carrying wires. *Phys. Rev. Lett.*, 83(25):5194–5197, Dec 1999.

[5] N. H. Dekker, C. S. Lee, V. Lorent, J. H. Thywissen, S. P. Smith, M. Drndić, R. M. Westervelt, and M. Prentiss. Guiding neutral atoms on a chip. *Phys. Rev. Lett.*, 84(6):1124–1127, Feb 2000.

[6] J. Reichel, W. Hänsel, and T. W. Hänsch. Atomic micromanipulation with magnetic surface traps. *Phys. Rev. Lett.*, 83(17):3398–3401, Oct 1999.

[7] Ron Folman, Peter Krüger, Donatella Cassettari, Björn Hessmo, Thomas Maier, and Jörg Schmiedmayer. Controlling cold atoms using nanofabricated surfaces: Atom chips. *Phys. Rev. Lett.*, 84(20):4749–4752, May 2000.

[8] Wolfgang Hänsel, Peter Hommelhoff, Theodor W. Hänsch, and Jakob Reichel. Bose–Einstein condensation on a microelectric chip. *Nature*, 413:498–501, 2001.

[9] H. Ott, J. Fortagh, G. Schlotterbeck, A. Grossmann, and C. Zimmermann. Bose-Einstein condensation in a surface microtrap. *Phys. Rev. Lett.*, 87(23):230401, Nov 2001.

[10] J.-B. Trebbia, J. Esteve, C. I. Westbrook, and I. Bouchoule. Experimental evidence for the breakdown of a Hartree-Fock approach in a weakly interacting bose gas. *Physical Review Letters*, 97(25):250403, 2006.

[11] J. Esteve, J.-B. Trebbia, T. Schumm, A. Aspect, C. I. Westbrook, and I. Bouchoule. Observations of density fluctuations in an elongated bose gas: Ideal gas and quasicondensate regimes. *Physical Review Letters*, 96(13):130403, 2006.

[12] A.H. van Amerongen, I.J.P. van Es, P. Wicke, K.V. Kheruntsyan, and N.J. van Druten. Yang-Yang thermodynamics on an atom chip. *Phys. Rev. Lett.*, 100(090402), 2008.

[13] Ying-Ju Wang, Matthew Eardley, Svenja Knappe, John Moreland, Leo Hollberg, and John Kitching. Magnetic resonance in an atomic vapor excited by a mechanical resonator. *Physical Review Letters*, 97(22):227602, 2006.

[14] Philipp Treutlein, David Hunger, Stephan Camerer, Theodor W. Hänsch, and Jakob Reichel. Bose-Einstein condensate coupled to a nanomechanical resonator on an atom chip. *Physical Review Letters*, 99(14):140403, 2007.

[15] M. P. A. Jones, C. J. Vale, D. Sahagun, B. V. Hall, and E. A. Hinds. Spin coupling between cold atoms and the thermal fluctuations of a metal surface. *Phys. Rev. Lett.*, 91(8):080401, Aug 2003.

[16] Yu-ju Lin, Igor Teper, Cheng Chin, and Vladan Vuletić. Impact of the Casimir–Polder potential and Johnson noise on Bose-Einstein condensate stability near surfaces. *Phys. Rev. Lett.*, 92(5):050404, Feb 2004.

[17] D.M. Harber, J.M. McGuirk, J.M. Obrecht, and E.A. Cornell. Thermally induced losses in ultra–cold atoms magnetically trapped near room–temperature surfaces. *Journal of Low Temperature Physics*, 133(3–4):229–238, 2003.

[18] J. Fortágh, H. Ott, S. Kraft, A. Günther, and C. Zimmermann. Surface effects in magnetic microtraps. *Phys. Rev. A*, 66(4):041604, Oct 2002.

[19] J. Estève, C. Aussibal, T. Schumm, C. Figl, D. Mailly, I. Bouchoule, C.I. Westbrook, and A. Aspect. The role of wire imperfections in micro magnetic traps for atoms. *Phys. Rev. A*, 70:043629, 2004.

[20] S. Aigner, L. Della Pietra, Y. Japha, O. Entin-Wohlman, T. David, R. Salem, R. Folman, and J. Schmiedmayer. Long-Range Order in Electronic Transport Through Disordered Metal Films. *Science*, 319(5867):1226–1229, 2008.

[21] T. Calarco, E. A. Hinds, D. Jaksch, J. Schmiedmayer, J. I. Cirac, and P. Zoller. Quantum gates with neutral atoms: Controlling collisional interactions in time-dependent traps. *Phys. Rev. A*, 61(2):022304, Jan 2000.

[22] Philipp Treutlein, Theodor W. Hänsch, Jakob Reichel, Antonio Negretti, Markus A. Cirone, and Tommaso Calarco. Microwave potentials and optimal control for robust quantum gates on an atom chip. *Physical Review A (Atomic, Molecular, and Optical Physics)*, 74(2):022312, 2006.

[23] Igor Teper, Yu-Ju Lin, and Vladan Vuletić. Resonator-aided single-atom detection on a microfabricated chip. *Physical Review Letters*, 97(2):023002, 2006.

[24] Y. Colombe, T. Steinmetz, G. Dubois, F. Linke, D. Hunger, and J. Reichel. Strong atom–field coupling for Bose–Einstein condensates in an optical cavity on a chip. *Nature*, 450(7167):272–276, 2007.

[25] David P. DiVincenzo. The physical implementation of quantum computation. *quant-ph/0002077*, 2000.

[26] T. Schumm, S. Hofferberth, L.M. Andersson, S. Wildermuth, S. Groth, I. Bar-Joseph, J. Schmiedmayer, and P. Krüger. Matter–wave interferometry in a double well on an atom chip. *Nature Physics*, 1, 2005.

[27] Ying-Ju Wang, Dana Z. Anderson, Victor M. Bright, Eric A. Cornell, Quentin Diot, Tetsuo Kishimoto, Mara Prentiss, R. A. Saravanan, Stephen R. Segal, and Saijun Wu. Atom Michelson interferometer on a chip using a Bose-Einstein condensate. *Physical Review Letters*, 94(9):090405, 2005.

[28] G.-B. Jo, Y. Shin, S. Will, T. A. Pasquini, M. Saba, W. Ketterle, D. E. Pritchard, M. Vengalattore, and M. Prentiss. Long phase coherence time and number squeezing of two Bose-Einstein condensates on an atom chip. *Phys. Rev. Lett.*, 98(030407), 2007.

[29] Philipp Treutlein, Peter Hommelhoff, Tilo Steinmetz, Theodor W. Hänsch, and Jakob Reichel. Coherence in microchip traps. *Phys. Rev. Lett*, 92(203005), 2004.

[30] S. Knappe, P.D.D. Schwindt, V. Gerginov, V. Shah, H.G. Robinson, L. Hollberg, and J. Kitching. Microfabricated atomic clocks and magnetometers. In *Proceedings of the International Conference on Laser Spectroscopy*. ICOLS, 2005.

[31] J.D. Prestage, S. Chung, T. Le, L. Lim, and L. Maleki. Liter–sized ion clock with 10^{-15} stability. In *Proceedings of the 36th precise time and time interval (PTTI) systems and applications meeting*, 2005.

[32] F.X. Esnault, S. Perrin, D. Holleville, S. Guerandel, N. Dimarcq, and J. Delporte. Reaching a few $10^{-13}\tau^{-1/2}$ stability level with the compact cold atom clock HORACE. In *Proceedings of the Frequency Control Symposium*. IEEE, 2008.

[33] T. Rosenband, D.B. Hume, P.O. Schmidt, C.W. Chou, A. Brusch, L. Lorini, W.H. Oskay, R.E. Drullinger, T.M. Fortier, J.E. Stalnaker, S.A. Diddams, W.C. Swann, N.R. Newbury, W.M. Itano, D.J. Wineland, and J.C. Bergquist. Frequency ratio of Al^+ and Hg^+ single–ion optical clocks; metrology at the 17th decimal place. *Science*, 319(5871):1808–1812, 2008.

[34] A.D. Ludlow, T. Zelevinsky, G.K. Campbell, S. Blatt, M.M. Boyd, M.H.G. de Miranda, M.J. Martin, J.W. Thomsen, S.M. Foreman, Jun Ye, T.M. Fortier, J.E. Stalnaker, S.A. Diddams, Y. LeCoq, Z.W. Barber, N. Poli, and N.D. Lemke. Sr lattice clock at 1×10^{-16} fractional uncertainty by remote optical evaluation with a Ca clock. *Science*, 319(5871):1805–1808, 2008.

[35] D. S. Hall, M. R. Matthews, C. E. Wieman, and E. A. Cornell. Measurements of relative phase in two-component Bose-Einstein condensates. *Phys. Rev. Lett.*, 81(8):1543–1546, Aug 1998.

[36] D. S. Hall, M. R. Matthews, J. R. Ensher, C. E. Wieman, and E. A. Cornell. Dynamics of component separation in a binary mixture of Bose-Einstein condensates. *Phys. Rev. Lett.*, 81(8):1539–1542, Aug 1998.

[37] H. J. Lewandowski, D. M. Harber, D. L. Whitaker, and E. A. Cornell. Observation of anomalous spin-state segregation in a trapped ultracold vapor. *Phys. Rev. Lett.*, 88(7):070403, Jan 2002.

[38] J. M. McGuirk, H. J. Lewandowski, D. M. Harber, T. Nikuni, J. E. Williams, and E. A. Cornell. Spatial resolution of spin waves in an ultracold gas. *Phys. Rev. Lett.*, 89(9):090402, Aug 2002.

[39] D. M. Harber, H. J. Lewandowski, J. M. McGuirk, and E. A. Cornell. Effect of cold collisions on spin coherence and resonance shifts in a magnetically trapped ultracold gas. *Phys. Rev. A*, 66(053616), 2002.

[40] David W. Allan, Neil Ashby, and Clifford C. Hodge. The science of timekeeping. `http://literature.agilent.com/litweb/pdf/5965-7984E.pdf`, 1997. Agilent Application Note 1289.

[41] A. Scheibe and U. Adelsberger. Schwankungen der astronomischen Tageslänge und der astronomischen Zeitbestimmung mit den Quarzuhren der Phys.-Techn. Reichsanstalt. *Phys. Z.*, 37:185–203, 1936.

[42] J Terrien. News from the international bureau of weights and measures. *Metrologia*, 4(1):41–45, 1968.

[43] Joseph H. Taylor. Binary pulsars and relativistic gravity. *Rev. Mod. Phys.*, 66(3):711–719, Jul 1994.

[44] Sebastian Bize. *Tests fondamentaux à l'aide d'horloges à atomes froids de Rubidium et de Césium.* PhD thesis, Université de Paris VI, 2001.

[45] Jacques Vanier and Claude Audoin. *The quantum physics of atomic frequency standards.* IOP Ltd., Adam Hilger, Bristol, Philadelphia, 1989.

[46] Giovanni Busca, Laurent-Guy Bernier, Pascal Villiers, and Marin Rochat. Active Hydrogen maser atomic frequency standard. U.S. Patent N°5,838,206.

[47] X. Baillard. *Horloge à réseau optique à atomes de Strontium.* PhD thesis, Université Paris VI, 2008.

[48] Pierre Uhrich. Charactérisation de la stabilité en temps/fréquence. application aux comparaisons d'horloges. *Cours 2004/2005 de l'unité "Relativité et Temps" Formation M1 du "Master de Sciences de l'Univers et Technologies Spatiales" de l'Observatoire de Paris*, 2004.

[49] G. Santarelli, Ph. Laurent, P. Lemonde, A. Clairon, A. G. Mann, S. Chang, A. N. Luiten, and C. Salomon. Quantum projection noise in an atomic fountain: A high stability Cesium frequency standard. *Phys. Rev. Lett.*, 82(23):4619–4622, Jun 1999.

[50] Masahiro Kitagawa and Masahito Ueda. Squeezed spin states. *Phys. Rev. A*, 47(6):5138–5143, Jun 1993.

[51] M. Schleier-Smith, Ian D. Leroux, and V. Vuletic. Reduced–quantum–uncertainty states for an atomic clock. *arxiv:0810.2582v1 [quant-ph]*, 2008.

[52] A. Clairon, C. Salomon, S. Guellati, and W. D. Phillips. Ramsey resonance in a Zacharias fountain. *EPL (Europhysics Letters)*, 16(2):165–170, 1991.

[53] S. Bize, P. Laurent, M. Abgrall, H. Marion, I. Maksimovic, L. Cacciapuoti, J. Grünert, C. Vian, F. Pereira dos Santos, P. Rosenbusch, P. Lemonde, G. Santarelli, P. Wolf, A. Clairon, A. Luiten, M. Tobar, and C. Salomon. Advances in atomic fountains. *Comptes rendus physique*, 5:829–843, 2004.

[54] S.R. Jefferts, T.P. Heavner, T.E. Parker, and J.H. Shirley. NIST Cesium fountains – curent status and future prospects. *Proc. SPIE*, 6673(667309), 2007.

[55] R Wynands and S Weyers. Atomic fountain clocks. *Metrologia*, 42(3):S64–S79, 2005.

[56] R. Holzwarth, Th. Udem, T. W. Hänsch, J. C. Knight, W. J. Wadsworth, and P. St. J. Russell. Optical frequency synthesizer for precision spectroscopy. *Phys. Rev. Lett.*, 85(11):2264–2267, Sep 2000.

[57] Ch. J. Bordé, Ch. Salomon, S. Avrillier, A. van Lerberghe, Ch. Bréant, D. Bassi, and G. Scoles. Optical Ramsey fringes with traveling waves. *Phys. Rev. A*, 30(4):1836–1848, Oct 1984.

[58] Hidetoshi Katori, Masao Takamoto, V. G. Pal'chikov, and V.D. Ovsiannikov. Ultrastable optical clock with neutral atoms in an engineered light shift trap. *Physical Review Letters*, 91(17), 2003.

[59] Mark Murray and Maurizio Battaglia. Lecture notes of the gamit workshop. `http://seismo.berkeley.edu/~battag/GAMITwrkshp/wrkshp.html#Units`.

[60] R.B. Langley. The GPS error budget. *GPS World*, 8(3):51–56, 1997.

[61] J Ray and K Senior. IGS/BIPM pilot project: GPS carrier phase for time/frequency transfer and timescale formation. *Metrologia*, 40(3):S270–S288, 2003.

[62] Jim Ray and Ken Senior. Geodetic techniques for time and frequency comparisons using GPS phase and code measurements. *Metrologia*, 42(4):215–232, 2005.

[63] James Camparo. The Rubidium atomic clock and basic research. *Physics Today*, November:33–39, 2007.

[64] G. Mileti, C. Affolderbach, F. Droz, and E. Murphy. Navigating more precisely with laser clocks. *ESA Bulletin*, 122:53, 2005.

[65] R. Beard, J. Buisson, F. Danzy, M. Largay, and J. White. GPS block IIR Rubidium frequency standard life test results. *IEEE International Frequency Control Symposium and PDA Exhibition*, 2002.

[66] Perkin Elmer. RAFS datasheet. `http://optoelectronics.perkinelmer.com/content/Datasheets/DTS_RAFS.pdf`, 2007.

[67] Perkin Elmer. RFS-IIF datasheet. `http://optoelectronics.perkinelmer.com/content/RelatedLinks/Brochures/BRO_rfs2f.pdf`, 2007.

[68] P. Rochat et. al. The onboard GALILEO Rubidium and passive maser, status & performance. In *Proceedings of the Frequency Control Symposium and Exhibition, 2005. Proceedings of the 2005 IEEE International*, pages 26–32. IEEE, 2005.

[69] C. Affolderbach and G. Mileti. Development of new Rb clocks in Observatoire de Neuchâtel. In *Proceedings of the 35th Annual Precise Time and Time Interval (PTTI) Meeting*. U.S. Naval Observatory, 2003.

[70] Aldo Godone, Salvatore Micalizio, Filippo Levi, and Claudio Calosso. Physics characterization and frequency stability of the pulsed Rubidium maser. *Physical Review A*, 74(043401), 2006.

[71] Salvatore Micalizio, Aldo Godone, Filippo Levi, and Claudio Calosso. Pulsed optically pumped vapor cell clock: towards the optical detection. In *Proceedings of the European Forum on Time and Frequency*. EFTF, 2008.

[72] R. Boudot, S. Guérandel, E. De Clercq, N. Dimarcq, and A. Clairon. Current status of a pulsed CPT Cs cell clock. In *Proceedings of the Conference on Precision Electromagnetic Measurements (CPEM)*. NIST, 2008.

[73] Aldo Godone, Filippo Levi, Salvatore Micalizio, and Claudio Calosso. Coherent-population-trapping maser: Noise spectrum and frequency stability. *Phys. Rev. A*, 70(1):012508, Jul 2004.

[74] Mikko Merimaa, Thomas Lindvall, Ilkka Tittonen, and Erkki Ikonen. All-optical atomic clock based on coherent population trapping in ^{85}Rb. *J. Opt. Soc. Am. B*, 20(2):273–279, 2003.

[75] T. Zanon, S. Guerandel, E. de Clerq, D. Holleville, N. Dimarcq, and A. Clairon. High contrast Ramsey fringes with coherent-population-trapping pulses in a double lambda atomic system. *Phys. Rev. Lett.*, 94(193002), 2005.

[76] S. Knappe, P.D.D. Schwindt, V. Shah, L. Hollberg, J. Kitching, L. Liew, and J. Moreland. A chip–scale atomic clock based on ^{87}Rb with improved frequency stability. *Optics Express*, 13(4), 2005.

[77] L. Mattioni et. al. The development of a passive Hydrogen maser clock for the Galileo navigation system. In *Proceedings of the 34th Annual Precise Time and Time Interval (PTTI) Meeting*. U.S. Naval Observatory, 2002.

[78] J.D. Prestage, S. Chung, L. Lim, and T. Le. Miniaturized Mercury ion clock for ultra–stable deep space applications. In *Proceedings of the 38th precise time and time interval (PTTI) systems and applications meeting*, 2006.

[79] J.D. Prestage, S.K. Chung, L. Lim, and A. Matevosian. Compact microwave Mercury ion clock for deep–space applications. In *Proceedings of the Frequency Control Symposium, 2007 Joint with the 21st European Frequency and Time Forum*, 2007.

[80] Y. LeCoq, C. Oates, and L. Hollberg. Ultra–stable compact optical atomic clock. In *International Conference on Atomic Physics, Poster A.143*, 2006.

[81] Ph. Laurent, M. Abgrall, Ch. Jentsch, P. Lemonde, G. Santarelli, A. Clairon, L. Maksimovic, S. Bize, Ch. Salomon, D. Blonde, J.F. Vega, O. Grosjean, F. Picard, M. Saccoccio, M. Chaubet, N. Ladiette, L. Guillet, I. Zenone, Ch. Delaroche, and Ch. Sirmain. Design of the cold atom pharao space clock and initial test results. *Appl. Phys. B.*, 84:683–690, 2006.

[82] C. Lämmerzahl, G. Ahlers, N. Ashby, M. Barmatz, P.L. Biermann, H. Dittus, V. Dohm, R. Duncan, K. Gibble, J. Lipa, N. Lockerbie, N. Mulders, and C. Salomon. Review: Experiments in Fundamental Physics Scheduled and in Development for the ISS. *General Relativity and Gravitation*, 36(3), 2004.

[83] P. Wolf et. al. Quantum physics exploring gravity in the outer solar system: The SAGAS project. *gr-qc/0804.4593*, 2007.

[84] Wolfgang Hänsel. *Magnetische Mikrofallen für Rubidiumatome*. PhD thesis, LMU Munich, 2000.

[85] V.V. Vladimirskiĭ. Magnetic mirrors, channels and bottles for cold neutrons. *Soviet Physics JETP*, 12(740), 1961.

[86] K. J. Kügler, W. Paul, and U. Trinks. A magnetic storage ring for neutrons. *Physics Letters B*, 72(3):422 – 424, 1978.

[87] Alan L. Migdall, John V. Prodan, William D. Phillips, Thomas H. Bergeman, and Harold J. Metcalf. First observation of magnetically trapped neutral atoms. *Phys. Rev. Lett.*, 54(24):2596–2599, Jun 1985.

[88] Shengwang Du, Matthew B. Squires, Yutaka Imai, Leslie Czaia, R. A. Saravanan, Victor Bright, Jakob Reichel, T. W. Hänsch, and Dana Z. Anderson. Atom-chip Bose-Einstein condensation in a portable vacuum cell. *Phys. Rev. A*, 70(5):053606, Nov 2004.

[89] A. Vogel et. al. Bose–Einstein condensates in microgravity. *Applied Physics B: Lasers and Optics*, 84(4), 2006.

[90] W. Hänsel, J. Reichel, P. Hommelhoff, and T. W. Hänsch. Magnetic conveyor belt for transporting and merging trapped atom clouds. *Phys. Rev. Lett.*, 86(4):608–611, Jan 2001.

[91] P Hommelhoff, W Hänsel, T Steinmetz, T W Hänsch, and J Reichel. Transporting, splitting and merging of atomic ensembles in a chip trap. *New Journal of Physics*, 7:3, 2005.

[92] R. Long, T. Rom, W. Hänsel, T.W. Hänsch, and J. Reichel. Long distance magnetic conveyor for precise positioning of ultracold atoms. *The European Physical Journal D - Atomic, Molecular, Optical and Plasma Physics*, 35(1), 2005.

[93] T. Nirrengarten, A. Qarry, C. Roux, A. Emmert, G. Nogues, M. Brune, J.-M. Raimond, and S. Haroche. Realization of a superconducting atom chip. *Physical Review Letters*, 97(20):200405, 2006.

[94] T. Mukai, C. Hufnagel, A. Kasper, T. Meno, A. Tsukada, K. Semba, and F. Shimizu. Persistent supercurrent atom chip. *Physical Review Letters*, 98(26):260407, 2007.

[95] C. Roux, A. Emmert, A. Lupascu, T. Nirrengarten, G. Nogues, M. Brune, J.-M. Raimond, and S. Haroche. Bose-Einstein condensation on a superconducting atom chip. *EPL (Europhysics Letters)*, 81(5):56004 (6pp), 2008.

[96] S. Aubin, S. Myrskog, M.H.T. Extavour, L.J. LeBlanc, D. McKay, A. Stummer, and J.H. Thywissen. Rapid sympathetic cooling to Fermi degeneracy on a chip. *cond-mat/0512518*, 2005.

[97] C. D. J. Sinclair, E. A. Curtis, I. Llorente Garcia, J. A. Retter, B. V. Hall, S. Eriksson, B. E. Sauer, and E. A. Hinds. Bose-Einstein condensation on a permanent-magnet atom chip. *Physical Review A (Atomic, Molecular, and Optical Physics)*, 72(3):031603, 2005.

[98] T. Fernholz, R. Gerritsma, S. Whitlock, I. Barb, and R. J. C. Spreeuw. Fully permanent magnet atom chip for Bose-Einstein condensation. *Physical Review A (Atomic, Molecular, and Optical Physics)*, 77(3):033409, 2008.

[99] P. Krüger, X. Luo, M. W. Klein, K. Brugger, A. Haase, S. Wildermuth, S. Groth, I. Bar-Joseph, R. Folman, and J. Schmiedmayer. Trapping and manipulating neutral atoms with electrostatic fields. *Phys. Rev. Lett.*, 91(23):233201, Dec 2003.

[100] Wolfgang Petrich, Michael H. Anderson, Jason R. Ensher, and Eric A. Cornell. Stable, tightly confining trap for evaporative cooling of neutral atoms. *Physical Review Letters*, 74(17), 1995.

[101] J.-B. Trebbia, C. L. Garrido Alzar, R. Cornelussen, C. I. Westbrook, and I. Bouchoule. Roughness suppression via rapid current modulation on an atom chip. *Physical Review Letters*, 98(26):263201, 2007.

[102] S. Gupta, K. W. Murch, K. L. Moore, T. P. Purdy, and D. M. Stamper-Kurn. Bose-Einstein condensation in a circular waveguide. *Physical Review Letters*, 95(14):143201, 2005.

[103] Igor Lesanovsky and Wolf von Klitzing. Spontaneous emergence of angular momentum josephson oscillations in coupled annular Bose-Einstein condensates. *Phys. Rev. Lett.*, 98(050401), 2007.

[104] I. Lesanovsky and W. v. Klitzing. Time-averaged adiabatic potentials: Versatile traps and waveguides for ultracold quantum gases. *cond-mat/0612213*, 2007.

[105] W. Ketterle, D.S. Durfee, and D.M. Stamper-Kurn. Making, probing and understanding Bose-Einstein condensates. *cond-mat/9904034v2*, 1999.

[106] I. Lesanovsky, S. Hofferberth, J. Schmiedmayer, and P. Schmelcher. Manipulation of ultracold atoms in dressed adiabatic radio-frequency potentials. *Physical Review A (Atomic, Molecular, and Optical Physics)*, 74(3):033619, 2006.

[107] T. Schumm, S. Hofferberth, L.M. Andersson, S. Wildermuth, S. Groth, I. Bar-Joseph, J. Schmiedmayer, and P. Krüger. Matter-wave interferometry in a double well on an atom chip. *Nature Physics*, 1(57), 2006.

[108] Philipp Treutlein. *Coherent manipulation of ultracold atoms on atom chips.* PhD thesis, LMU Munich, 2008.

[109] G. Birkl, F.B.J. Buchkremmer, R. Dumke, and W. Ertmer. Atom optics with microfabricated optical elements. *Optics Communications*, 191:67–81, 2001.

[110] M. Trupke, F. Ramirez-Martinez, E.A. Curtis, J.P. Ashmore, S. Eriksson, E.A. Hinds, Z. Moktadir, C. Gollasch, M. Kraft, G. Vijaya Prakash, and J.J. Baumberg. Pyramidal micromirrors for microsystems and atom chips. *Appl. Phys. Lett.*, 88(071116), 2006.

[111] József Fortágh and Claus Zimmermann. Magnetic microtraps for ultracold atoms. *Reviews of Modern Physics*, 79(1):235, 2007.

[112] E. A. Hinds, C. J. Vale, and M. G. Boshier. Two-wire waveguide and interferometer for cold atoms. *Phys. Rev. Lett.*, 86(8):1462–1465, Feb 2001.

[113] G. Lewis, Z. Moktadir, C. Gollasch, M. Kraft, S. Pollock, F. Ramirez-Martinez, J.P. Ashmore, A. Laliotis, M. Trupke, and E.A. Hinds. Fabrication of magneto-optical atom traps on a chip. *atom-ph/0804.4593*, 2008.

[114] P. W. H. Pinkse, A. Mosk, M. Weidemüller, M. W. Reynolds, T. W. Hijmans, and J. T. M. Walraven. Adiabatically changing the phase-space density of a trapped bose gas. *Phys. Rev. Lett.*, 78(6):990–993, Feb 1997.

[115] H.J. Metcalf and P. van der Straten. *Laser Cooling and Trapping.* Springer, Heidelberg, 1999.

[116] J. Dalibard. Atomes ultra–froids. *Lecture notes of the Master 2 of the ENS*, 2006.

[117] Peter Hommelhoff. *Bose-Einstein-Kondensate in Mikrochip-Fallen.* PhD thesis, LMU Munich, 2002.

[118] Ron Folman and Jörg Schmiedmayer. Mastering the language of atoms. *Nature*, 413:466–467, 2001.

[119] Heather Jean Lewandowski. *Coherences and correlations in an ultracold Bose gas.* PhD thesis, University of Colorado, 2002.

[120] M. Ö. Oktel, T. C. Killian, D. Kleppner, and L. S. Levitov. Sum rule for the optical spectrum of a trapped gas. *Phys. Rev. A*, 65(3):033617, Feb 2002.

[121] M. Ö. Oktel and L. S. Levitov. Collective dynamics of internal states in a Bose-Einstein gas. *Phys. Rev. A*, 65(6):063604, May 2002.

[122] Franco Dalfovo, Stefano Giogini, Lev P. Pitaevskii, and Sandro Stringari. Theory of Bose–Einstein condensation in trapped gases. *Reviews of Modern Physics*, 71(3):463–512, 1999.

[123] Anthony J. Legett. Bose–Einstein condensation in the alkali gases. *Reviews of Modern Physics*, 73(2):307–356, 2001.

[124] S. Haroche. Intrication et information quantiques avec des atomes froids, Cours 2006-2007 Collège de France. `http://www.cqed.org/college/2007/Cours\_2006-2007-2.pdf`, 2006.

[125] C.J. Pethick and H. Smith. *Bose–Einstein–Condensation in Dilute Gases.* Cambridge University Press, 2nd edition, 2008.

[126] K.M. Mertes, J.W. Merrill, R. Carretero-González, D.J. Frantzeskakis, P.G. Kevrekidis, and D.S. Hall. Nonequilibrium dynamics and superfluid ring excitations in binary Bose-Einstein condensates. *Phys. Rev. Lett.*, 99(190402), 2007.

[127] J.N. Fuchs, D.M. Gangardt, and F. Laloe. Large amplitude spin waves in ultracold gases. *The European Physical Journal D*, 25:57–75, 2003.

[128] G. Breit and I. I. Rabi. Measurement of nuclear spin. *Phys. Rev.*, 38(11):2082–2083, Dec 1931.

[129] Daniel A. Steck. Rubidium 87 D–line data, rev. 1.6. `http://steck.us/alkalidata/rubidium87numbers.pdf`, 2001.

[130] Thomas R. Gentile, Barbara J. Hughey, Daniel Kleppner, and Theodore W. Ducas. Experimental study of one- and two-photon Rabi oscillations. *Phys. Rev. A*, 40(9), 1989.

[131] Michael R. Matthews. *Two-Component Bose-Einsten Condensation.* PhD thesis, University of Colorado, 1999.

[132] Kurt Gibble. Difference between a photon's momentum and an atom's recoil. *Phys. Rev. Lett.*, 97(073002), 2006.

[133] Enrico Fermi. Quantum theory of radiation. *Rev. Mod. Phys.*, 4(1):87, Jan 1932.

[134] R. H. Dicke. The effect of collisions upon the doppler width of spectral lines. *Phys. Rev.*, 89(2):472–473, Jan 1953.

[135] Ruoxin Li and Kurt Gibble. Phase variation in microwave cavities for atomic clocks. *Metrologia*, 41:376–386, 2004.

[136] E. A. Burt, R. W. Ghrist, C. J. Myatt, M. J. Holland, E. A. Cornell, and C. E. Wieman. Coherence, correlations, and collisions: What one learns about Bose-Einstein condensates from their decay. *Phys. Rev. Lett.*, 79(3):337–340, Jul 1997.

[137] Kurt Gibble. Decoherence and collisional frequency shifts of trapped bosons and fermions. `http://www.citebase.org/abstract?id=oai:arXiv.org:0908.3147`, to appear in PRL, 2009.

[138] Martin W. Zwierlein, Zoran Hadzibabic, Subhadeep Gupta, and Wolfgang Ketterle. Spectroscopic insensitivity to cold collisions in a two-state mixture of fermions. *Phys. Rev. Lett.*, 91(25):250404, Dec 2003.

[139] P. Rosenbusch. Magnetically trapped atoms for compact atomic clocks. *Applied Physics B: Lasers and Optics*, 95(2):227–235, May 2009.

[140] E. L. Hahn. Spin echoes. *Phys. Rev.*, 80(4):580–594, Nov 1950.

[141] J.J.P. van Es, A.H. van Amerongen, and N.J. van Druten. Bose gas in a box on a chip. In *International Conference on Atomic Physics, Poster A.92*, 2006.

[142] Giorgio Santarelli. *Contribution à la Réalisation d'une Fontaine atomique.* PhD thesis, Université de Paris VI, 1996.

[143] Hui Yan, Guo-Qing Yang, Tao Shi, Jin Wang, and Ming-Sheng Zhan. Experimental demonstration of controllable double magneto-optical traps on an atom chip. *J. Opt. Soc. Am. B*, 25(10):1667–1672, 2008.

[144] Christine Aussibal. *Réalisation d'un condensat de Bose-Einstein sur une microstructure*. PhD thesis, Université Paris XI Orsay, 2003.

[145] Peter D.D. Schwindt. *Magnetic Traps and Guides for Bose–Einstein Condensates on an Atom Chip: Progress toward a Coherent Atom Waveguide Beamsplitter*. PhD thesis, University of Colorado Boulder, 2003.

[146] Dana Z. Anderson and Jakob G.J. Reichel. Cold atom system with atom chip wall, 2006. U.S. Patent US 7,126,112 B2.

[147] Romain Long. *Couplage d'une microsphère accordable et d'une "Puce à atomes"*. PhD thesis, Université Paris VI, 2003.

[148] Immanuel Bloch. Skript zur Vorlesung Atomphysik, WS 06/07, Universität Mainz. `http://www.quantum.physik.uni-mainz.de/de/lectures/2006/ws0607_atomphysik/Atomphysik_Skript_Teil1.pdf`, 2006.

[149] T.J. Sumner, J.M. Pendlebury, and K.F. Smith. Conventional magnetic shielding. *J. Phys. D: Appl. Phys.*, 20:1095–1101, 1987.

[150] A. Mager. Magnetic shielding efficiencies of cylindrical shells with axis parallel to the field. *Journal of Applied Physics*, 39(3):1914–1914, 1968.

[151] Vacuumschmelze GmbH. Mumetal product data. `http://www.vacuumschmelze.de/dynamic/de/home/produkte/halbzeugampteile/weichmagnetisch/nickeleisen/mumetall.php`.

[152] Vacuumschmelze GmbH. Weichmagnetische Werkstoffe und Halbzeuge. `http://www.vacuumschmelze.de/dynamic/docroot/medialib/documents/broschueren/htbrosch/Pb-pht-0.pdf`, 2002. Brochure PHT-001.

[153] Sophocles J. Orfanidis. Electromagnetic waves and antennas. `http://www.ece.rutgers.edu/~orfanidi/ewa/`.

[154] Stephen A. Maas. *The RF and Microwave Circuit Design Cookbook*. Artech House Publishers, Boston, London, 1998.

[155] Jakob Reichel. Microchip traps and Bose-Einstein condensation. *Appl. Phys. B*, 75:469–487, 2002.

[156] François Ziadé. *Faisabilité d'un étalon calculable de puissance hautes fréquences*. PhD thesis, École Normale Supérieure des Télécommunications, 2008.

[157] Circuit Sage. Impedance matching with transmission lines. `http://www.circuitsage.com/matching/transmatch.pdf`.

[158] R.W. Klopfenstein. A transmission line taper of improved design. *Proceedings of the IRE*, pages 31–35, 1956.

[159] Microwaves101. A simple bias tee. `http://www.microwaves101.com/encyclopedia/quarterwave.cfm#biastee`.

[160] S. Wildermuth, P. Krüger, C. Becker, M. Brajdic, S. Haupt, A. Kasper, R. Folman, and J. Schmiedmayer. Optimized magneto-optical trap for experiments with ultracold atoms near surfaces. *Phys. Rev. A*, 69(3):030901, Mar 2004.

[161] T. Schumm, J. Estève, C. Figl, J.-B. Trebbia, C. Aussibal, H. Nguyen, D. Mailly, I. Bouchoule, C.I. Westbrook, and A. Aspect. Atom chips in the real world: the effect of wire corrugations. *Eur. Phys. J. D*, 35(141), 2005.

[162] Stanford Research Systems. SR760 datasheet. `http://www.thinksrs.com/downloads/PDFs/Catalog/SR760770c.pdf`.

[163] Paul Horowitz and Winfield Hill. *The Art of Electronics.* Cambridge University Press, second edition, 1989.

[164] Joachim Franz. *EMV. Störungssicherer Aufbau elektronischer Schaltungen.* Teubner B.G. GmbH, 2. edition, 2005.

[165] K.G. Libbrecht and J.L. Hall. A low-noise high-speed diode laser current controller. *Rev. Sci. Instr.*, 64(8):2133–2135, 1993.

[166] Johannes Hoffrogge, 2007. Diplomarbeit, LMU München.

[167] K. Dieckmann, R. J. C. Spreeuw, M. Weidemüller, and J. T. M. Walraven. Two-dimensional magneto-optical trap as a source of slow atoms. *Phys. Rev. A*, 58(5):3891–3895, Nov 1998.

[168] K. I. Lee, J. A. Kim, H. R. Noh, and W. Jhe. Single-beam atom trap in a pyramidal and conical hollow mirror. *Opt. Lett.*, 21(15):1177–1179, 1996.

[169] C.J. Dedman, R.G. Dall, L.J. Byron, and A.G. Truscott. Active cancellation of stray magnetic fields in a Bose-Einstein condensation experiment. *Rev. Sci. Instr.*, 78(024703), 2007.